



**HAL**  
open science

# Seismic analysis of a liquefiable soil foundation-embankment system : life cycle performance and mitigation

Christina Khalil

► **To cite this version:**

Christina Khalil. Seismic analysis of a liquefiable soil foundation-embankment system : life cycle performance and mitigation. Civil Engineering. Université Paris-Saclay, 2021. English. NNT : 2021UPAST027 . tel-04046872

**HAL Id: tel-04046872**

**<https://theses.hal.science/tel-04046872v1>**

Submitted on 27 Mar 2023

**HAL** is a multi-disciplinary open access archive for the deposit and dissemination of scientific research documents, whether they are published or not. The documents may come from teaching and research institutions in France or abroad, or from public or private research centers.

L'archive ouverte pluridisciplinaire **HAL**, est destinée au dépôt et à la diffusion de documents scientifiques de niveau recherche, publiés ou non, émanant des établissements d'enseignement et de recherche français ou étrangers, des laboratoires publics ou privés.

Analyse sismique d'un remblai et sa  
fondation liquéfiable:  
Cycle de vie et Mitigation

Seismic analysis of a liquefiable soil  
foundation-embankment system:  
Life Cycle performance and Mitigation

Thèse de doctorat de l'Université Paris-Saclay

École doctorale n° 579, sciences mécaniques et énergétiques,  
matériaux et géosciences (SMEMAG)

Spécialité de doctorat: Génie Civile

Unité de recherche: Université Paris-Saclay, CentraleSupélec, CNRS, Laboratoire de  
Mécanique des Sols, Structures et Matériaux,  
91190, Gif-sur-Yvette, France

Référent: : CentraleSupélec

Thèse présentée et soutenue à Paris-Saclay, le 26/03/2021, par

**Christina KHALIL**

Composition du Jury:

<b>Frédéric Ragueneau</b> Professeur, Université Paris-Saclay, ENS	Président
<b>Kyriazis Pitilakis</b> Professeur, Aristotle University of Thessaloniki	Rapporteur et Examineur
<b>Gopal Madabhushi</b> Professeur, Cambridge University	Rapporteur et Examineur
<b>Adrian Rodriguez-Marek</b> Professeur, Virginia Polytechnic Institute and State University	Examineur
<b>Fabian Bonilla</b> Directeur de Recherche, University Gustave Eiffel	Examineur
<b>Jean Francois Semblat</b> Directeur de Recherche, ENSTA-ParisTech	Examineur
<b>Arezou Modaresi</b> Professeur, Université Paris-Saclay, CentraleSupélec	Directrice
<b>Fernando Lopez-Caballero</b> Maître de Conférences, Université Paris-Saclay, Centrale-Supélec	Coencadrant



*To my nephew and niece, my important source of joy and happiness.*

*I love you.*

*To my brother, my first idol and supporter since I was a child.*

*I miss you*

*To my parents, the invisible hands that keep holding mine to cross over all life's obstacles.*

*Thank you, I love you.*

*To my grandparents, your spirits were pushing me forward through these three years.*

*May you rest in peace, I miss you.*



# Acknowledgment

This thesis would have not been achieved without the encouragement and support of my supervisors, whom I would like to acknowledge. As my mentors, they have prepared me in scientific contexts and to each one of them I express here my gratitude. First I thank Fernando Lopez Caballero for trusting me from the very beginning when I was doing my internship for my master degree, for his advice and instructions in both human and scientific fields, for encouraging me to participate in national and international conferences and projects, for giving me the chance to teach and guide master students in their research works, from which I have learned lots of pedagogic skills, for listening to me every time I had a problem, for his patience during low motivation periods. I am lucky and glad to have an advisor, a mentor and a friend like him. I will never forget his famous sentence “*C’est la vie!*” when it comes to solve a problem in life. A person like him cannot be forgotten.

To Arezou Modaresi, I am grateful for the scientific help you proposed to me when you realized that I was in need, for making sure that I am progressing and for your support. I am glad I had the opportunity to know you, to share with you some social and artistic ideas and to help you in your course. More importantly, I thank you for accepting my master’s application in 2015, without that moment I wouldn’t be having all the opportunities and experiences I have now.

I would also like to address my gratitude to all the jury members to accept judging my work during these exceptional pandemic situations and to simplify the enrollment of the evaluation. First of all, I would like to thank the reviewers for taking time to read and comment my work. I would like to thank Professor Pitilakis for his fruitful engineering questions that are going to help me project any work into the practical life. I address my gratitude to Professor Madabhushi for his constructive questions about the soil behavior and the clarifications about my work. I also thank him for helping me several times in answering or understanding questions of other jury members. As for the examiners, I would like to thank Professor Rofriguez-Marek for his suggestions on my work and for his questions that were partly clarifications and other corrections. I address my gratitude to Fabian Bonilla for the time he took to answer my questions and explain to me scientific problems I had during my thesis, and for his evaluation at the end. A special thanks to Jean Francois Semblat who gave me the opportunity to apply on the new job I started on april 2021, and also for evaluating my work as a jury member. And finally, I would like to thank the president of the jury for simplifying the enrollment of the

evaluation and for his clarification questions.

Other than the jury members, I would like to specially thank Denis Aubry for his support and the time he took to discuss with me about my work or to participate in the small events we used to organize. I also thank all the members of the ISOLATE project with whom I had meetings and discussions.

To my friends from MSSMAT laboratory, I am so happy to meet every single person of you and I have very good memories with all of you. I would like to thank: Michael Darche, Sara Touhami, Martin Colvez, Michail Korres, Hélène Moustacas, Claudia Aristizabal, Filippo Gatti, Andrea Riano Escandon, David Castro, Christian Noubissi, Valeria Soto Moncada. Specially, I would express my gratitude to Romain Ruysen for his help and his encouragement. And I would like to thank all the colleagues in this laboratory.

I would also like to acknowledge here the support and help of the laboratory staff at MSSMat, and specially Martine Lavabre and Fleur Litoust. Without it I could have not been able neither to register nor to travel to attend conferences.

To my friends, I express my gratitude for their friendships. Each one of you have helped me, encouraged me and supported me. You have been a family more than friends. I would like to express my gratitude to my childhood friends Rita Ibrahim, Farah Rifai, Elie Rachkidi and Bassel Merabi. A special thank to Nauf Khoury for meeting me in the airport the first day I arrived to France, and to introduce me this country in its happy and bad details. A big thank to Diana Salem who I met by chance in the lab and we became close friends since that. I thank her for the smile she put on my face every time we meet. I am very lucky and happy that the destination to all of us was France.

Finally, I adress my gratitude and love to all my family members all over the world and specially my uncle Khaled Khalil, who encouraged me to do a thesis, who helped me arrive to France and who supported me in all the stages of my life. You have always been my favorite uncle.

# Abstract

One of the main goal of the performance-based design is the probabilistic evaluation of the system-level performance of structures due to earthquakes. To this aim, a framing equation was proposed by the Pacific Earthquake Engineering Research Center based on the convolution of all levels of ground motion, structural damage and loss. A key issue in this methodology is the reliable assessment of the seismic damage potential. However, this methodology still presents a weakness in assessing a Life-Cycle analysis for structures because the potential damage is calculated from independent major events. Thus, this thesis assesses numerically a life-cycle seismic analysis of an earth structure. For this purpose, an embankment model is used, and the soil behavior is represented with an elasto-plastic multimechanism model. The finite element method in time domain is used as numerical tool.

As an initial and a mandatory step for engineering design, *virtual* laboratory tests are conducted as to identify the soil behavior, localize its critical state and calculate its resistance. Loads were applied similarly to typical laboratory tests (monotonic, cyclic). In addition, a dynamic analysis on a soil column is assessed in order to identify the *in-situ* response of the soil and compare the liquefaction triggering between the laboratory results and the numerical ones observed in field.

As this thesis deals with non-linear behavior of the soil, a large database in order to estimate the potential embankment failure is needed. Thus, a key study in this thesis is the use of real and synthetic earthquakes as inputs for dynamic analysis to examine the response of the embankment. These earthquakes were chosen to be mainshocks only in order to be consistent with the Performance Based Earthquake Engineering (PBEE) methodology. The potential embankment failure is also assessed from global and local damage indices. Site and structure specific approaches were interpreted.

However, in reality, a structure is not subjected to one event during its lifetime, but to multiple dependent events. For this reason, a life-cycle analysis is conducted in order to calculate the probability of survival of the embankment due to sequential events of mainshocks. For this purpose, synthetic ground motion models were used to represent the hazard analysis of the concerned site. The effect of different types of sequences and models was also assessed in this part of the study.

Moreover, to approach realistic scenarios, the effects of aftershocks in the life-cycle analysis is also assessed. The potential failure and the survival probability were calculated. More

importantly, the evolution in time of the fragility functions were also calculated. Finally, it was assumed all over this thesis that the embankment was not subjected to repairs or soil amelioration. For this reason, a natural biological mitigation method (i.e. MICP) was applied on the embankment. The evolution of its performance as well as the change in the soil behavior was also analyzed.

This thesis is part of a national French project called ISOLATE. It can be considered as a reference case study for seismic assessment of embankment-type structures subjected to earthquake and provides a high-performance computational framework accessible to engineers.

**Keywords:** life cycle, PBEE, mainshocks, aftershocks, potential failure

# Résumé

Pour la conception d'une structure, et dans le but de considérer sa capacité à résister des tremblements de terre, le Pacific Earthquake Engineering Research Center a proposé une méthodologie probabiliste prenant en compte les caractéristiques sismiques du site, l'évolution du dommage de la structure et sa vulnérabilité. L'élément essentiel de cette méthodologie est l'évaluation fiable du potentiel de dommages sismiques. Cependant, cette méthodologie présente encore une faiblesse concernant l'analyse du cycle de vie d'une structure à cause de la quantification des dommages à partir des événements indépendants. Ainsi, cette thèse cherche à simuler numériquement le cycle de vie d'une structure. Pour cela, un modèle de remblai est utilisé ainsi qu'un modèle élasto-plastique multi-mécanisme afin de représenter le sol.

Etant une étape indispensable en ingénierie, des essais en laboratoire *virtuel* ont été réalisés pour identifier le comportement du sol, localiser son état critique et déterminer sa résistance. Ces essais virtuels cherchaient à reproduire des essais effectués en laboratoire *réel* (considération de chargements monotones et cycliques) sur des réel échantillons de sol. De plus, la réponse dynamique d'une colonne de sol a été évaluée afin de comparer la précision entre les prédictions issues des tests de laboratoire et celles obtenues sur le terrain concernant la résistance des sols.

Cette thèse traitant le comportement non linéaire du sol, une base de donnée sismique importante est nécessaire pour estimer précisément la défaillance potentielle du remblai. Pour cela, des signaux réels et synthétiques ont été générés et utilisés pour l'analyse dynamique. Ces signaux ont été choisis comme chocs principaux uniquement afin de suivre la méthodologie de Performance Based Earthquake Engineering (PBEE). La rupture potentielle du remblai a été évaluée à partir d'indices de dommages globaux et locaux. Une approche spécifique considérant la structure et le site a été développée.

En réalité, une structure n'étant pas soumise, au cours de sa vie, qu'à un seul mais plusieurs évènements sismiques dépendants, une analyse du cycle de vie du remblai a été menée afin d'estimer la distribution de la durée de vie du remblai et de calculer sa probabilité de survie suite aux évènements séquentiels de chocs principaux. Pour ce faire, des modèles synthétiques de mouvement du sol ont été utilisés, tenant compte des aléas sismiques du site considéré. Les effets des différents types de séquences sismiques et de modèles ont été évalués.

De plus, afin de s'approcher de scénarios réalistes, les effets des répliques sont prises en compte dans l'analyse du cycle de vie. Le risque de dommage ainsi que la probabilité de survie ont été calculés. Aussi, l'évolution temporelle des fonctions de fragilité a également été évaluée. Finalement, une hypothèse de cette thèse était que le remblai ne subissait aucune réparation et le sol aucune amélioration. Pour revenir sur cette hypothèse, une méthode d'amélioration naturelle (MICP) a été appliquée au remblai. L'évolution de sa performance ainsi que le changement de comportement du sol ont été analysés.

Cette thèse entre dans le cadre d'un projet national français appelé ISOLATE. Elle peut être vue comme une étude référence pour l'évaluation sismique de structures de type remblai soumises à des séismes et fournir un cadre de calcul performant accessible aux ingénieurs.

**Mots clés:** cycle de vie, PBEE, chocs principaux, répliques, potentiel de dommages

# Contents

<b>Introduction</b>	<b>1</b>
<b>1 Virtual laboratory tests to characterize the soil behavior and identify the <i>in-situ</i> response</b>	<b>9</b>
1.1 Introduction . . . . .	10
1.2 Soil constitutive model . . . . .	12
1.3 Laboratory tests simulations . . . . .	12
1.3.1 Defining the soil behavior . . . . .	13
1.3.2 Effect of regular cyclic loading . . . . .	14
1.4 Effect of initial soil state . . . . .	16
1.5 Soil stability . . . . .	18
1.6 Local safety factor estimation through soil residual strength . . . . .	20
1.7 Post liquefaction behavior . . . . .	23
1.7.1 Concept of liquefaction resistance factor . . . . .	25
1.7.2 Liquefaction resistance factor and local safety factor . . . . .	26
1.8 Effect of irregular cyclic loading . . . . .	27
1.9 <i>In-situ</i> response - Study on a column . . . . .	30
1.9.1 Geometry and finite element model . . . . .	30
1.9.2 Analysis of the <i>in-situ</i> soil response . . . . .	31
1.9.3 Accuracy of the laboratory tests with respect to the <i>in-situ</i> tests . . . . .	33
1.10 Concluding remarks . . . . .	35
<b>2 The use of real and synthetic earthquakes as input to dynamic analysis</b>	<b>37</b>
2.1 Introduction . . . . .	38
2.2 Geometry and soil model . . . . .	41
2.2.1 Geometry . . . . .	41
2.2.2 Soil constitutive model . . . . .	41
2.2.3 Finite element model . . . . .	42
2.2.4 Boundary conditions . . . . .	43
2.2.5 Elastic behavior . . . . .	43
2.3 Input ground motion . . . . .	44

2.4	Distribution of Intensity Measures IM . . . . .	46
2.5	Damage measure and soil mechanical behavior . . . . .	49
2.6	Link between EDP and IM . . . . .	54
2.7	Fragility curves . . . . .	57
2.8	Concluding remarks . . . . .	59
<b>3</b>	<b>Survival analysis of a liquefiable soil foundation-embankment system sub- jected to sequential earthquakes</b>	<b>61</b>
3.1	Introduction . . . . .	63
3.2	Overview of the survival analysis . . . . .	66
3.2.1	Kaplan-Meier estimator . . . . .	67
3.2.2	Cox Proportional Hazards model . . . . .	68
3.2.3	Parametric models . . . . .	68
3.3	Geometry and soil numerical model . . . . .	68
3.3.1	Geometry . . . . .	68
3.3.2	Soil Constitutive Model . . . . .	69
3.3.3	Finite Element Model . . . . .	71
3.3.4	Boundary Conditions . . . . .	71
3.4	Assumptions of this chapter . . . . .	72
3.5	Input ground motions . . . . .	72
3.6	Site-specific seismic analysis . . . . .	75
3.7	Survival analysis of the Levee . . . . .	76
3.7.1	Crest settlement in the sequences . . . . .	77
3.7.2	Survival analysis . . . . .	80
3.8	Influence of various parameters on the survival analysis . . . . .	83
3.8.1	Effect of the loading history . . . . .	83
3.8.2	Importance of the recovery time between the sequences . . . . .	84
3.8.3	Effect of different synthetic ground motion models . . . . .	85
3.9	Concluding remarks . . . . .	86
3.10	Complements to this chapter . . . . .	87
<b>4</b>	<b>Lifetime evolution of the performance of an embankment subjected to se- quences of mainshocks and aftershocks</b>	<b>95</b>
4.1	Introduction . . . . .	96
4.2	Assumptions of this chapter . . . . .	99
4.3	Model to generate aftershocks . . . . .	99
4.3.1	Distribution of the magnitude-frequency . . . . .	100
4.3.2	Distribution of the occurrence time . . . . .	101
4.3.3	Location of the aftershocks . . . . .	102
4.3.4	Description of the generated aftershocks . . . . .	102

4.4	Damage measure during sequential clusters . . . . .	104
4.4.1	Relative crest settlement for sequential earthquakes . . . . .	105
4.4.2	Damage index from the soil residual strength . . . . .	107
4.5	Survival functions of the tested sequences . . . . .	109
4.6	Fragility curves evolution . . . . .	111
4.7	Concluding remarks . . . . .	115
<b>5</b>	<b>Application of a mitigation method to reduce the earthquake-induced liquefaction of an embankment</b>	<b>117</b>
5.1	Introduction . . . . .	118
5.2	Geometry and numerical model . . . . .	123
5.2.1	Geometry . . . . .	123
5.2.2	Finite Element model . . . . .	124
5.2.3	Boundary conditions . . . . .	124
5.3	Soil constitutive model . . . . .	124
5.4	Injection technique . . . . .	125
5.4.1	Location of the injection . . . . .	126
5.4.2	Injected material . . . . .	126
5.4.3	Method for injection . . . . .	127
5.5	Input ground motion . . . . .	128
5.6	Comparison of the treated and untreated cases . . . . .	128
5.6.1	Comparison based on the number of the injection zones . . . . .	129
5.6.2	Comparison based on the injected material . . . . .	130
5.6.3	Comparison based on the stress - strain evolution . . . . .	130
5.7	Amelioration ratio of the crest settlement . . . . .	132
5.8	Fragility curves of the tested cases . . . . .	134
5.9	Sensitivity analysis of the crest settlement amelioration ratio . . . . .	136
5.10	Concluding remarks . . . . .	138
	<b>Conclusions</b>	<b>139</b>
	<b>A ECP multimechanism model</b>	<b>145</b>
	<b>B Soil parameters for the ECP model</b>	<b>149</b>
	<b>C Concept of confusion matrices</b>	<b>153</b>
	<b>D The distribution of the ground motions used in Chapter 2</b>	<b>155</b>
	<b>E Analytical fragility curves</b>	<b>159</b>
	<b>F Evaluation of a statistical test from the <i>p-value</i></b>	<b>163</b>

**G Thesis summary in french****165**

# List of Figures

1	The probabilistic definition of the risk assessment according to the PBEE methodology (Porter, 2003) . . . . .	2
2	The thesis framework and outline . . . . .	5
1.1	The stress path of a) <i>Mat.1</i> and b) <i>Mat.2</i> from the simulated undrained monotonic triaxial tests . . . . .	14
1.2	The variation of the volumetric strain with respect to the mean effective stress for a) <i>Mat.1</i> and b) <i>Mat.2</i> from the simulated drained monotonic triaxial tests . . . . .	14
1.3	a) The variation of $\Delta p_w$ (top) and $\varepsilon_1$ (bottom) and b) the stress path of the regular loading for <i>Mat.1</i> . . . . .	15
1.4	The Variation of the Cyclic Stress Ratio <i>CSR</i> as function of the number of cycles $N_f$ for a) <i>Mat.1</i> and b) <i>Mat.2</i> . . . . .	16
1.5	a) An example of the applied load on the soil specimen and b) its stress paths in $p' - q$ plan . . . . .	17
1.6	a) the Cyclic stress ratio <i>CSR</i> for different values of initial deviatoric stresses and b) the Cyclic Resistance Ratio <i>CRR</i> as function of the Static Stress Ratio <i>SSR</i> for <i>Mat.1</i> . . . . .	18
1.7	The second increment of the work $d^2W$ for <i>Mat.1</i> for monotonic load . . . . .	19
1.8	The second increment of the work $d^2W$ for <i>Mat.1</i> for cyclic load . . . . .	19
1.9	a) The shear stress-strain of <i>Mat.1</i> and b) the variation of the parameter $r_{apt}$ as function of the shear strain $\gamma$ . . . . .	21
1.10	a) The shear stress-strain of <i>Mat.2</i> and b) the variation of the parameter $r_{apt}$ as function of the shear strain $\gamma$ . . . . .	22
1.11	The evolution of the parameter $r_{apt}$ for <i>Mat.1</i> after a monotonic and cyclic load in terms of the maximum shear strain $\gamma_{max}$ . . . . .	22
1.12	a) A loading path example of the conducted test and b) The stress path in $s' - t$ space for <i>Mat.1</i> . . . . .	23
1.13	The stress key points during a monotonic load alone and the sequence of cyclic+monotonic load . . . . .	24
1.14	a) Variation of the normalized peak strength and b) Variation of the normalized strength at steady state as function of the deviatoric stress . . . . .	24

1.15	The resistance factor against liquefaction $F_L$ for the normalized a) peak and at b) steady state shear stress . . . . .	25
1.16	The parameter $r_{apt}$ for a) <i>No Resistance</i> zone, b) <i>Intermediate</i> zone and c) <i>Resistance</i> zone for $N_{cyc} = 20$ . . . . .	27
1.17	An example of an applied loading with earthquake shape . . . . .	28
1.18	a) The variation of $\Delta p_w$ (top) and $\varepsilon_1$ (bottom) and b) the stress path of the irregular loading of <i>Mat.1</i> . . . . .	28
1.19	The different methods for the number of cycles . . . . .	29
1.20	Cyclic stress ratio CSR* for the case of irregular loading for a) <i>Mat.1</i> and b) <i>Mat.2</i> . . . . .	30
1.21	The column geometry . . . . .	31
1.22	The results analysis of the weak motion ( $a_{max,out} = 0.1$ g) . . . . .	32
1.23	The results analysis of the strong motion ( $a_{max,out} = 0.7$ g) . . . . .	33
1.24	The values of $r_{apt}$ at 3m depth for two seismic inputs . . . . .	33
1.25	a) The cyclic stress ratio of the tested motions and b) the confusion matrix of the tested motions . . . . .	34
2.1	The steps of the Performance Based Earthquake Engineering methodology . . . . .	38
2.2	Geometry of the embankment inspired by Rapti et al. (2018); Lopez-Caballero and Khalil (2018) . . . . .	41
2.3	a) The CPU time of two different levee models and b) the damage index for the types of meshes (to be explained later on in this chapter) . . . . .	42
2.4	a) The transfer function and b) the variation in depth of the shear wave velocity of the embankment . . . . .	44
2.5	The median spectral responses of the tested ground motions . . . . .	46
2.6	a) The cumulative distribution function and b) the density distribution function of the real and synthetic ground motions . . . . .	47
2.7	The logarithmic distribution of some ground motion parameters ( $PGV$ , $I_a$ and $1/T_{va}$ ) of the real and synthetic ground motions . . . . .	47
2.8	The logarithmic distribution of some ground motion parameters ( $PGV$ , $I_a$ and $1/T_{va}$ ) for the group of a) & b) $CAx$ , $CAy$ , $RM$ and $RL$ and c) $RZx$ , $BKx$ . . . . .	48
2.9	The example a) ground motion of this section and b) the evolution in time the relative crest settlement $u_{z,rel}$ and the excess pore water pressure ratio $r_u$ (i.e. = $\Delta p_w/p'_0$ ) . . . . .	50
2.10	Enlarged view of typical vertical co-seismic displacement contours at the end of the shaking . . . . .	50
2.11	The values of $r_{apt}$ in the domain of interest for three time intervals: 3, 7 and 40 seconds . . . . .	51
2.12	The distribution of $r_{apt} \geq 0.75$ from the IPs (black points) for the example ground motion . . . . .	52

2.13	a) The CCDF of the parameter $r_{apt}$ during the co-seismic duration of the example ground motion and b) the dependency of the parameter $r_{apt}$ with the crest settlement of the embankment . . . . .	53
2.14	The potential failure of the embankment for a) one type of real ground motions and b) one type of synthetic ground motions . . . . .	53
2.15	Box plot of the relative crest settlement for the tested real and synthetic motions	55
2.16	Percentage crest settlement for the groups of real and synthetic ground motions	55
2.17	The link between the chosen EDP and several IMs for a) $BKx$ , $RZx$ and b) $Cax$ , $CAy$ , $RL$ and $RM$ . . . . .	56
2.18	The link between the chosen IMs and the damage levels for the a) real and b) synthetic earthquakes . . . . .	57
2.19	Fragility curves of the real and synthetic motions for <i>Moderate</i> damage level . .	58
3.1	Schema of the used methodology to estimate the lifecycle of an embankment . .	66
3.2	Geometry and behavior of the soil (Lopez-Caballero and Khalil, 2018) . . . . .	69
3.3	a) The magnitude-frequency distribution curve for 50,000 years catalog (Aristizábal et al., 2018) along with b) the PGA hazard curve of the generated synthetic ground motions . . . . .	73
3.4	The response spectral of a) <i>Mod.R</i> and b) <i>Mod.B</i> . . . . .	74
3.5	The distribution of some ground motion parameters of the two models: a) <i>Mod.R</i> and b) <i>Mod.B</i> . . . . .	75
3.6	The variation of the crest settlement with respect to the outcrop acceleration of the two models: a) <i>Mod.R</i> and b) <i>Mod.B</i> and c) the obtained crest settlement hazard curve. . . . .	76
3.7	The excess pore water pressure of one mainshock a) under the center of the embankment and b) at free-field . . . . .	78
3.8	The relative crest settlement of the sequential signals a) for all the sequences and b) in form of box-plots . . . . .	78
3.9	The complementary cumulative distribution function (CCDF) of the relative crest settlement . . . . .	79
3.10	The damage levels of <i>Mod.R</i> with respect to the magnitude and distance of the seismic motions . . . . .	81
3.11	The survival probability of the levee for <i>Mod.R</i> . . . . .	82
3.12	The relative crest settlement with No loading history a) in the form of box-plot and b) its survival analysis . . . . .	84
3.13	The survival analysis of the different sequence types for a) Moderate damage and b) Serious damage . . . . .	85
3.14	The survival analysis of <i>Mod.B</i> in back-to-back form for a) DL2 and b) DL3 . .	86
3.15	The PMF of $M_w$ and $R$ . . . . .	87
3.16	The compatible IM with the GMPE for $M_w = 5.0$ conditioned on $S_a$ of 0.41g . .	88

3.17	a) The logarithmic distribution of some ground motion parameters of <i>Mod.R</i> for the tested time windows and b) The survival analysis for a time window of 50, 75 and 100 years, adapted from the data of Lopez-Caballero et al. (2020) . . . . .	89
3.18	The relative crest settlement of one subset but different permutation: a) perm1 and b) perm2 . . . . .	90
3.19	Comparison of the logarithmic distribution of some ground motion parameters for Seed 1 and 2 of <i>Mod.R</i> . . . . .	91
3.20	Comparison of the survival functions for each seed record for a) <i>Moderate</i> and b) <i>Serious</i> damage levels . . . . .	92
3.21	a) The density distribution function and b) the CCDF of $M_w$ for three example sequences . . . . .	92
4.1	The methodology presented in this chapter . . . . .	98
4.2	a) The response spectral of the generated aftershocks and b) a section of a sequence . . . . .	103
4.3	Scatter plots of some ground motion parameters of mainshocks and aftershocks with respect to a) $M_w$ and b) $M_w$ and $R$ . . . . .	103
4.4	The logarithmic distribution of some ground motion parameters of the Mainshocks (MS) and the Aftershocks (AFS) . . . . .	104
4.5	Comparison of the percentage relative crest settlement for an example of mainshock (MS) sequences and mainshocks - aftershocks (MS - AFS) sequences . . . . .	106
4.6	Median value of the crest settlement for the MS and MS-AFS sequences . . . . .	106
4.7	The time evolution of $\delta u_{z,rel}/H$ and $\rho_{r_{apt} \geq 0.75}$ for a a) MS sequence and b) a MS-AFS sequence . . . . .	108
4.8	The time evolution of $\rho_{r_{apt} \geq 0.75}$ for two examples of MS or MS-AFS sequences . . . . .	109
4.9	Survival functions of the two types of sequences used in this study for a) <i>Moderate</i> damage (DL3) and b) <i>Serious</i> damage (DL4) . . . . .	110
4.10	The methodology presented in this section . . . . .	111
4.11	The MS-AFS sequence example and the time interval after which the fragility curves will be calculated . . . . .	112
4.12	The time evolution of the crest settlement $\delta u_{z,rel}/H$ and the density parameter $\rho_{r_{apt}}$ . . . . .	113
4.13	The evolution in time of the probability of exceeding the a) <i>Moderate</i> and b) the <i>Serious</i> damage level . . . . .	114
4.14	The evolution in time of the probability of exceeding the <i>Serious</i> damage level for different sequence examples . . . . .	115
5.1	The a) deviator stress, b) excess pore pressure and c) stress ratio from undrained testing of specimens at an initial relative density of 40% and a confining stress of 100 kPa, extracted and adapted from O'Donnell (2016) . . . . .	119
5.2	Geometry and behavior of the soil (Lopez-Caballero and Khalil, 2018) . . . . .	123

5.3	Deviatoric strain $\varepsilon_d$ at the end of the ground motion (Rapti et al., 2018) . . . . .	126
5.4	The soil behavior of the tested materials for $p'_0 = 50$ kPa . . . . .	127
5.5	The mesh elements and the different zones of injections . . . . .	128
5.6	Comparison of a) the co-seismic relative crest settlement of the embankment as function of the number of the injection zones and b) the response spectral of each case . . . . .	129
5.7	Comparison of the co-seismic relative crest settlement of the embankment as function of the injected material . . . . .	130
5.8	The ratio of the maximum shear a) stress and b) strain between the treated and untreated cases . . . . .	131
5.9	The ratio of the a) excess pore water pressure and b) the volumetric strain between the treated and untreated cases . . . . .	132
5.10	The crest settlement analysis with respect to the outcropping acceleration ( $a_{max,out}$ ) for each case study . . . . .	133
5.11	The reduction ratio of the relative crest settlement as function of a) $a_{max,out}$ and $1/T_{va}$ and b) $PGV$ . . . . .	134
5.12	Fragility curves of two damage levels: a) $\delta u_{z,rel}/H = 0.1$ and b) $\delta u_{z,rel}/H = 1$ . . . . .	135
5.13	The correlation between a) the chosen input ground motion parameters and b) with respect to the reduction of the crest settlement . . . . .	137
C.1	Summary of the confusion matrix and its classification . . . . .	153
D.1	The logarithmic distribution of some ground motion parameter ( $PGA$ , $D_{595}$ and $CAV$ ) of the real and synthetic ground motions . . . . .	156
D.2	The logarithmic distribution of some ground motion parameter ( $PGA$ , $D_{595}$ and $CAV$ ) for the group of a) & b) $CAX$ , $CAY$ , $RM$ and $RL$ and c) $RZx$ , $BKx$ . . . . .	157
G.1	Le modèle de remblai utilisé dans le cadre de cette thèse . . . . .	165
G.2	Figure qui résume les différentes thématiques abordées dans cette thèse . . . . .	167



# Introduction

## Background and rationale

The standard definition of *Risk*, from a broad range of fields, is the probability that a certain set of consequences occur given a hazardous scenario. Risk analysis is the process of determining the probability of occurrence and consequences as well as evaluating the determined risks. Then, risks are judged as acceptable or tolerable on the basis of exceeding a defined threshold level. Risk management will then be determined from decision makers.

In earthquake related problems, the Pacific Earthquake Engineering Research (PEER) Center developed a performance-based methodology for risk assessment. This methodology, called the Performance Based Earthquake Engineering (PBEE), addresses the performance of the engineering model in terms of levels of the design (risk of collapse, repair costs and post-earthquake loss) (Porter, 2003; Baker and Allin Cornell, 2005; National Academies of Sciences and Medicine, 2016; De Silva, 2020, among others). The objective of this methodology is to estimate the frequency of a particular performance to exceed various levels of the design. This can be translated into conducting a risk analysis in which the probability of collapse is determined from the convolution integral of the probability of hazard and the consequent losses related to it, such as:

$$P(\text{collapse}) = \int P(\text{consequent losses related to the hazard}) \cdot P(\text{hazard}) \quad (1)$$

According to the PBEE, four stages of the analysis should be determined. Each stage has its own relation with the design model through a performance parameter that is linked to the previous stage. Figure 1 frames schematically the required stages for a performance-based assessment of a design. It should be mentioned that  $P(X|Y)$  is the probability of  $X$  conditioned on the knowledge of  $Y$  and  $\lambda(X|Y)$  is the occurrence frequency of  $X$  given  $Y$ .

Thus, Equation 1 can be framed mathematically into Equation 2 in order to take into account all the different stages of the analysis.

$$\lambda(DV|D) = \int \int \int P(DV|DM, D) \cdot P(DM|EDP, D) \cdot P(EDP|IM, D) \cdot \lambda(IM|D) \cdot dIMdEDPdDM \quad (2)$$

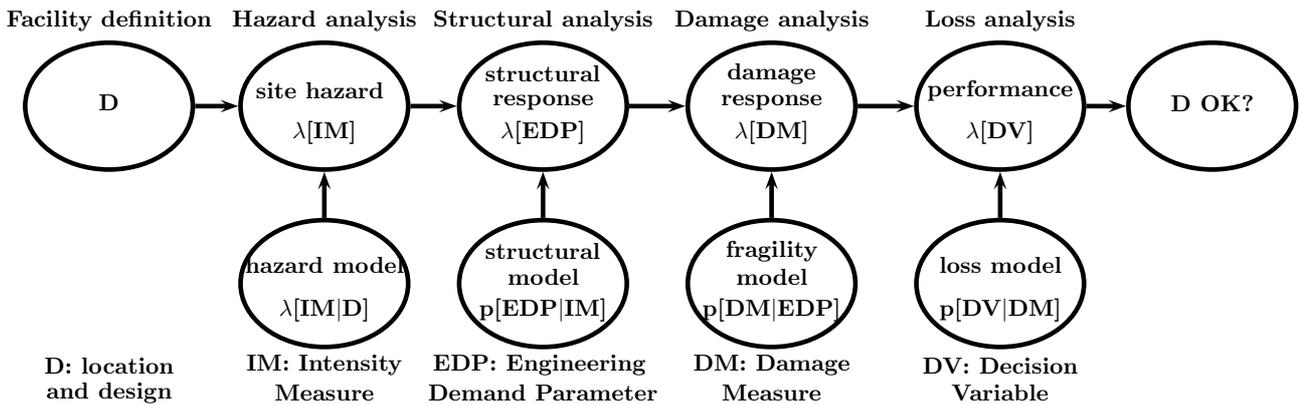


Figure 1: The probabilistic definition of the risk assessment according to the PBEE methodology (Porter, 2003)

The first stage of the PBEE requires a *Hazard Analysis* that involves the quantitative estimation of the ground motion hazards of the precised location. For this purpose, an Intensity Measure (IM) parameter that characterizes the excitation is identified. In this stage, the knowledge of the geologic evidence, the fault activity, the magnitude and the historical seismicity of the studied region is required (Kramer, 1996; Bommer, 2002). The uncertainties in the earthquake size, location and occurrence time are accounted for through a Probabilistic Seismic Hazard Analysis (PSHA) to obtain the probability that any IM will be exceeded at a particular time period. The level of shaking produced from the seismic hazard analysis comes from the contribution of the magnitude  $M_w$ , the source-to-site distance  $R$  and often the deviation of the GM from the predicted value ( $\varepsilon$ ) (Bazzurro and Allin Cornell, 1999).

After defining the main aspects that characterize the local seismic hazard, it is possible to proceed with the selection of time histories considered as mainshocks. This later step is important for geotechnical earthquake engineering problems because it is strongly related to the nonlinear dynamic analysis. An adequate definition of the seismic input is needed in order to choose the nonlinear time history dynamic analysis (Schwab and Lestuzzi, 2007). Nevertheless, a large number of database is required in order to conduct such analysis. Moreover, sometimes, available data resources are not available (i.e. not enough data for high magnitudes ground motions) or inadequate to characterize the models due to several problems (i.e. near-fault ground motions, basin effects) (Stewart et al., 2002; Luco and Cornell, 2007; Seyedi et al., 2010; Sáez et al., 2011; Wang et al., 2020, among others). For these reasons, artificial or synthetic earthquakes could be used. They are conducted based on several methods (i.e. stochastic ground motion model, the composite source method, among others) and are useful in order to represent particular conditions. Thus, both recorded and synthetic mainshock events can be used.

The second stage of the PBEE methodology is the *Structural Analysis*, in which a structural model of the facility is created, and an estimation of its structural response is measured in terms of an Engineering Demand Parameter (EDP) conditioned on the seismic excitation and design  $p[EDP|IM, D]$ . The structural model does not need to be deterministic as it sometimes

include uncertainties in the characteristics of the model (i.e. mass, damping, deformations) (Porter, 2003). As a primary cause of damages to the soil and the structures, liquefaction is still considered as a disastrous phenomenon. It is defined as the loss of the soil of its shear strength due to the excess of pore water pressure (Casagrande, 1936; Roscoe et al., 1958; Castro et al., 1982; Sladen et al., 1985; Been and Jefferies, 1985; Ishihara, 1993, among others). In the context of risk analysis, the damage of structures caused by liquefaction is assessed based on the properties of materials, the pore water pressure generation and also the occurred damage measures during and after the seismic event. The damage indices used to measure the potential structural failure are either defined for each structural element (local) or related to the entire structure (global) (Cosenza and Manfredi, 2000). As to account for the EDP, the damage quantification depends on the type of the studied structure. For an embankment for example, the crest settlement is the mode of failure usually studied to identify the structural response (Swaisgood, 2003; Wu, 2014; Rapti et al., 2018; Gomez-Martinez et al., 2018; Lopez-Caballero and Khalil, 2018, among others). Since the IM affects the seismic response of the studied structure, the EDP is linked with it through damage levels. According to that, the damage measures are related to the seismic inputs and the seismic vulnerability can be calculated from the third stage of the PBEE.

After the accomplishment of the first two stages of the performance-based methodology, the third stage can be conducted (i.e. *Damage Analysis*). The EDP is the input to a set of fragility functions that model the probability of various Damage Measures (DM) conditioned on the structural response and the design  $p[DM|EDP, D]$ . Fragility curves are functions that represent the probability of exceeding a damage state (a value of DM) as a function of EDP for a given IM (Shinozuka et al., 2000; Porter et al., 2007; Sáez et al., 2011; Zentner, 2017; Oblak et al., 2020, among others). The final stage of the PBEE is the definition of the Decision Variable parameter to estimate the probability of the performance conditioned on the damage measure and the design  $p[DV|DM, D]$ . After all these stages, the risk assessment of the design will be evaluated as acceptable or not.

Otherwise, structures, during their lifetime, are subjected to multiple earthquake events. Conventionally, earthquakes are divided into clusters of mainshocks and aftershocks. In practice, from the PBEE methodology, structures are designed to resist the first damaging earthquake scenario. So this framework neglects the cumulative damage and the evolution of the material properties issued from each occurring event (Iervolino et al., 2020). In addition, the commonly used PSHA to select the corresponding ground motions, is intended to evaluate the hazards from discrete independent events (i.e. mainshocks). Thus, for the aftershock occurrence, empirical scaling laws (i.e. Gutenberg-Richter, modified Omori's law, Bath's law) have been proposed (Shcherbakov et al., 2005; Ruiz-García, 2012; Trevlopoulos et al., 2020). As for the seismic vulnerability conducted from this methodology, the classical fragility curves represent the failure probability of one event of a given intensity only. More importantly, and in liquefaction related problems, the initial state of the soil and its history of loading condition its

future behavior (Ishihara et al., 1975; Been and Jefferies, 1985; Sica et al., 2008; Lopez-Caballero et al., 2016, among others). In this case, in order to calculate the cumulative damage induced from multiple events, these aspects in the soil should be taken into account. On the opposite to the structural response where scaling of the seismic inputs can be applied (i.e. incremental dynamic analysis) (Vamvatsikos and Cornell, 2002; Iervolino et al., 2015, 2020).

On the other hand, when drastic damages occur as a consequence of liquefaction, there is a need to develop various methods to improve the soil resistance. The typical methods for liquefaction mitigation require the densification or compaction of the soil with mechanical energy (Brennan and Madabhushi, 2002; Mitrani and Madabhushi, 2012; Montoya-Noguera and Lopez-Caballero, 2016, among others). The disadvantage of these methods is that they may be disruptive to existing facilities and cause extensive settlements. For this purpose, the step change of the existing geotechnical practices is to improve the soil against liquefaction with the use of natural biological solutions. Such processes are called *Bio-mediated* or *Bio-inspired* processes and they provide somehow a sustainable ground improvement solution (Montoya and DeJong, 2015; O'Donnell, 2016; Lin et al., 2016; Gomez and DeJong, 2017; Cui et al., 2017; Lee et al., 2020; Zhang et al., 2020; Yu et al., 2020, among others).

According to the state of the art in the assessment of the earthquake-induced soil liquefaction performed by the National Academies of Sciences and Medicine (2016), it is necessary to “refine, develop, and implement performance-based approaches to evaluating liquefaction, including triggering, the geotechnical consequence of triggering, structural damage, and economic loss models to facilitate performance-based evaluation and design.” In this context, several European or French projects have been initiated in order to emphasize the liquefaction related problems. Recently, the European project LIQUEFACT, addresses the mitigation of risks due to earthquakes induced liquefaction events in European communities with a holistic approach. The project deals with the resistance of structures to earthquake events and the resilience of the collective urban community in relation to their quick recovery. This project set seven objectives starting from developing a European liquefaction hazard map (Lai et al., 2019a,b) and analyzing, with the aid of seismic centrifuge tests and field trials, the appropriate mitigation techniques adapted in the selected areas for the project (Da Fonseca et al., 2019; Ramos et al., 2019; Fasano et al., 2019; Rios et al., 2020). Finally, defining the vulnerability, resistance and resilience that can be applicable across the varying tested regions (Borozan et al., 2017; Ferreira et al., 2020).

On the other hand, the ongoing national French project, ISOLATE, from which this thesis is a part, aims at characterizing and improving the soil against liquefaction. Moreover, conducting physical and numerical models in order to assess the response of actual geo-structures (Semblat et al., 2019). It set four objectives starting from a soil sampling characterization and *in-situ* response to characterizing the effect of liquefaction on geo-structure and possible mitigation techniques.

## Objectives of the thesis

The following thesis combines the essential and eventual steps required to conduct a seismic analysis of a liquefiable soil foundation-embankment system, starting from a soil sampling interpretation to a life cycle performance. Figure 2 represents the framework of this thesis and its outline. The dynamic analysis is conducted on a particular geo-structures and an application (sometimes an adaptation) of the PBEE methodology is assessed in this work. For this purpose, an embankment model is used, and the soil behavior is represented from an elasto-plastic multi-mechanism model. The finite element method in time domain is used as numerical tool.

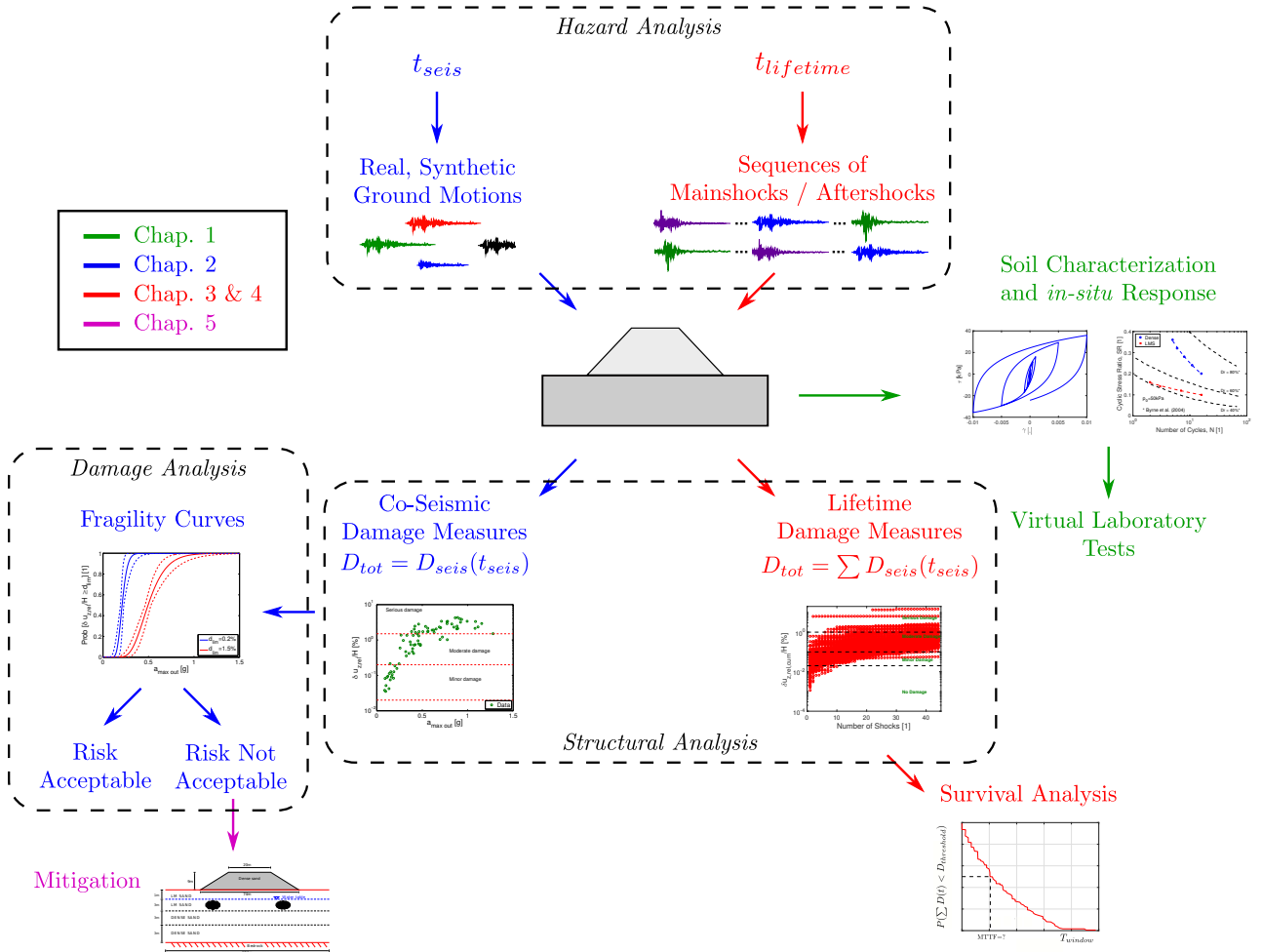


Figure 2: The thesis framework and outline

The significant questions that this work is trying to answer are the following:

- 1) What are the characteristics and the *in-situ* response of the soil used in this study?
- 2) Given a predefined seismic hazard, what is the co-seismic response of the concerned structure? Is it affected by the type of seismic inputs used? In consequence, what will be its fragility exposure?
- 3) After the co-seismic analysis, what would be the lifetime seismic analysis of the concerned

structure? Should the multiple seismic inputs consists of mainshocks only or mainshocks-aftershocks? How the fragility curves would evolve in this case?

- 4) Given an unacceptable risk, and thus a mitigation solution, does the response of the geo-structure change after the mitigation application? Is the vulnerability also affected?

Each presented question develops a chapter that is briefed in the coming section. It should be mentioned that in order to maintain focus on the conducted numerical study, the employed FE formulations are briefed in each chapter but detailed in Appendix A.

## Outline of the thesis

This thesis is arranged in five chapters, each self-contained as a journal paper (some already published, under review or under preparation). The chapters are connected in sequence and they can be classified under the evaluation of the seismic response of a geostructure (i.e. embankment). An application or an adaptation of the PBEE framework is established.

**Chapter 1.** develops a fundamental and essential procedure for seismic analysis that consists of the identification of the soil behavior. This chapter is a preliminary step before the extension to a structure-foundation system in the other chapters. For this purpose, a soil sampling interpretation and the *in-situ* soil response are conducted through *virtual* laboratory tests. Consistency with the laboratory experiments is taken into consideration in terms of the type of loading (i.e. regular and irregular loads) and the liquefaction resistance of the tested samples is identified. In addition, a study on a soil column is conducted in order to compare the behavior of the soil after the propagation of several seismic inputs. Finally, a statistical approach is conducted in order to find the accuracy between the predicted laboratory results and observed numerical results.

**Chapter 2.** studies the level of performance of the embankment in terms of the use of real and synthetic seismic inputs. The intensity measure of the tested motions was analyzed, the engineering demand parameter was calculated and linked with the mechanical soil behavior. And finally, the fragility exposure of the concerned structure is evaluated. The reason behind this study is to explore how the probability of failure of a structure can depend on selecting real or synthetic motions.

**Chapter 3.** quantifies, for a defined working life of the embankment, the liquefaction-induced damage due to sequential earthquakes (i.e. mainshocks). Because of the problematic of the nonlinear behavior, the need of a large number of seismic inputs is required. In addition, due to the findings of Chapter 2 that deduced only a slight difference in the response between real and synthetic ground motions, two stochastic ground motion models, compatible with the

PSHA of the site of concern, were used in this chapter. The probability of survival of the embankment is calculated through non-parametric survival functions. These later estimate the lifetime distribution as well as the Mean Time To Failure (i.e. failure being the exceedance of a damage level) during the working life of the concerned geostructure.

**Chapter 4.**, studies, for the same working life, the response of the embankment subjected to sequences of mainshocks-aftershocks. This chapter is a continuity of Chapter 3, which means that the same stochastic ground motion model is used to generate the mainshocks and the methodology to calculate the survival probability is also the same. As for the generation of the aftershocks, the Branching Aftershock Sequence (BASS) model is used. As a complement to the survival probability, and to be compatible with the PBEE framework, a methodology is proposed to calculate the fragility exposure of the embankment over its lifetime.

**Chapter 5.** aims to combine, from a phenomenological viewpoint, experimental and numerical results to assess a mitigation application on a liquefiable foundation of the embankment. The improvement requires the replacement of a treated material within an injection zone. The effect of the number and type of the material, and the potential of liquefaction of the embankment are discussed. The fragility curves are also drawn. Finally, a sensitivity analysis is conducted to identify the ground motion parameter that controls the amelioration ratio of the crest settlement. This chapter opens the perspective of the use of mitigation methods for a lifetime analysis, and hence a connection with the previous chapters.



# Chapter 1

## Virtual laboratory tests to characterize the soil behavior and identify the *in-situ* response

### Contents

---

<b>1.1</b>	<b>Introduction</b>	<b>10</b>
<b>1.2</b>	<b>Soil constitutive model</b>	<b>12</b>
<b>1.3</b>	<b>Laboratory tests simulations</b>	<b>12</b>
1.3.1	Defining the soil behavior	13
1.3.2	Effect of regular cyclic loading	14
<b>1.4</b>	<b>Effect of initial soil state</b>	<b>16</b>
<b>1.5</b>	<b>Soil stability</b>	<b>18</b>
<b>1.6</b>	<b>Local safety factor estimation through soil residual strength</b>	<b>20</b>
<b>1.7</b>	<b>Post liquefaction behavior</b>	<b>23</b>
1.7.1	Concept of liquefaction resistance factor	25
1.7.2	Liquefaction resistance factor and local safety factor	26
<b>1.8</b>	<b>Effect of irregular cyclic loading</b>	<b>27</b>
<b>1.9</b>	<b><i>In-situ</i> response - Study on a column</b>	<b>30</b>
1.9.1	Geometry and finite element model	30
1.9.2	Analysis of the <i>in-situ</i> soil response	31
1.9.3	Accuracy of the laboratory tests with respect to the <i>in-situ</i> tests	33
<b>1.10</b>	<b>Concluding remarks</b>	<b>35</b>

---

## Abstract

Laboratory tests with the association to *in-situ* tests are essential to characterize and identify the soil behavior. But sometimes, these tests are not available or cannot take place. In addition, due to their limitations, laboratory tests are sometimes not compatible with the field conditions (i.e. heterogeneity, spatial variability, systematic errors). Thus, *virtual* laboratory tests can be used as an alternative or a supplement to physical labs.

This chapter simulates *virtual* laboratory results on two soil specimens with a consistency with the conditions of real experiments. The purpose behind this step is to characterize and identify the soil behavior of specimens that will be used in field simulations. Thus, the response of *in-situ* tests was assessed from a soil column composed of one of the tested samples. The accuracy between the findings of laboratory tests and numerical response in terms of the liquefaction triggering is developed through a sensitivity analysis.

This chapter is considered as an essential step that will allow the extension to structure-foundation system in the following chapters. It is adapted and improved from a conference paper cited as:

*Khalil, C., and Lopez-Caballero, F. (2019). The effect of liquefaction-induced damage on an embankment: “virtual” laboratory tests. In 3rd meeting of EWG Dams and Earthquakes. An international Symposium, May 2019, Lisboa, Portugal.*

## 1.1 Introduction

Liquefaction is one of the most devastating and complex behaviors that affect the soil and causes damage to earth structures and foundations (Papadopoulou and Tika, 2016). It is used in conjunction with variety of aspects that involve soil deformations and volume change, but the generation of excess pore water pressure under undrained loading is kept as a common basic definition of this phenomena (Kramer, 1996; Ueng et al., 2000).

The determination of liquefaction has been studied by several researchers since longtime. First, it was introduced by Casagrande (1936), the concept of the *critical void ratio*, then its formalized design procedure termed as the *steady state approach* and developed by Castro et al. (1982). Then, an analogous concept of this later was the *critical state concept* (Roscoe et al., 1958). Sladen et al. (1985) proposed an extension of the steady state concepts known as the *collapse surface*. In addition, Been and Jefferies (1985) developed the so-called *state parameter* for sands that combines the influence of the void ratio and the stress level with a reference to an ultimate state to represent the soil behavior. It was agreed from all the workers on this subject that the behavior of the soil is mainly governed by its volume change. When soils are sheared, they increase in volume if they are initially “dense” or contract if they are initially “loose”.

Otherwise, for a structure to be resistant to seismic activities, its performance is analyzed from a soil sampling interpretation until a site response analysis (Koutsourelakis et al., 2002;

Elgamal et al., 2002; Sextos et al., 2003; Pitilakis, 2004; Bonilla et al., 2005; Pousse et al., 2006; López-Querol and Blázquez, 2006; Lopez-Caballero et al., 2007; Huang et al., 2008; Xia et al., 2010; Lopez-Caballero and Modaressi-Farahmand-Razavi, 2010, 2013; Ramirez et al., 2018; Oblak et al., 2020, among others). In practice, laboratory (i.e. triaxial test, direct shear test) (Ladd, 1974; Seed et al., 1976; Kokusho, 1980; Dobry et al., 1982; Xenaki and Athanasopoulos, 2003; Byrne et al., 2004; Yasuda et al., 2017; Pan and Yang, 2018, among others), centrifuge (DeAlba et al., 1975; Brennan and Madabhushi, 2002; Zeybek and Madabhushi, 2019; Elgamal et al., 2002; Maharjan and Takahashi, 2014; Tiznado et al., 2020, among others) or *in-situ* tests (i.e. CPT, SPT) (Tatsuoka et al., 1980; Seed et al., 1983; Cruz et al., 2004; Da Fonseca et al., 2010; Chandra et al., 2015, among others) identify the soil properties by collecting data from definite experimental or field conditions. For these reasons, the findings of these tests are sometimes not compatible with the realistic response in the field, or when structures take place. For example, the cyclic stress-based liquefaction resistance is influenced by factors such as the soil fabric, the age, the stress-strain history (Ishihara, 1993). These factors can be destroyed by sampling and are difficult to replicate in the laboratory (Kramer, 1996). In consequence, the interpretation of the soil behavior might be affected. Moreover, *in-situ* tests collect data from sites that are gently sloped or not geographically complicated (Zhao et al., 2018; Montoya-Noguera et al., 2019). Thus, the results of the soil behavior will be affected by site conditions or restrictions (Youd and Idriss, 2001).

In order to overcome the challenges presented from experimental or *in-situ* tests and in case of absence of these data (i.e. heterogeneity, sampling extraction), the application of modern technologies to develop *virtual laboratories* can be valid from powerful numerical models. The advantage behind this application is the absence of the laboratory systematic errors (i.e. fabrication, instrumentation, observation) and *in-situ* errors (i.e. anisotropy, stratigraphic irregularities, spatial variability). Nevertheless, numerical models, if they do not project the real case scenarios, they can also present numerical uncertainties (i.e. choice of boundary conditions, initial conditions).

This chapter develops a fundamental and essential procedure for seismic analysis that allows the determination of the soil behavior in order to extend the work to a structure-foundation system. This procedure consists in conducting a soil sampling interpretation and identifying the likelihood *in-situ* response. For this purpose, *virtual* laboratory tests are simulated on two soil samples (*Mat.1* and *Mat.2*) such as typical triaxial tests or shear tests. The effect of the loading type is studied, hence regular and irregular loads are applied on each soil sample and their liquefaction resistance is identified. Concerning the *in-situ* response, a study on a soil column is conducted in order to compare the behavior of the soil after the propagation of a seismic input. For this purpose, several number of real input ground motions are used. Finally, a statistical approach is conducted in order to find the accuracy between the predicted laboratory results and the observed numerical results on the liquefaction triggering.

## 1.2 Soil constitutive model

The *Ecole Centrale Paris (ECP)* elastoplastic multi-mechanism model (also known as Hujeux model) is the soil constitutive model chosen for this work and is written in terms of effective stress (Aubry et al., 1986). The non-linearity of this model is represented by four coupled elementary plastic mechanism: three plane-strain deviatoric plastic strain mechanism in three orthogonal planes ( $k$  - planes) and an isotropic plane. The model follows a Coulomb type failure criterion, contemplates the existence of dilatancy/contractancy phenomena, and uses the critical state concept. The cyclic behavior is taken into account by a kinematical hardening that is based on the state variables at the last load reversal. The model is written in the concept of the incremental plasticity which divides the total strain into an elastic and a plastic part. Refer to Aubry et al. (1982), Hujeux (1985) or Lopez-Caballero et al. (2003), among others (or Appendix A) for further details about the ECP model. The soil parameters of each sample are shown also in Appendix B. For the sake of brevity only, some model definitions will be developed in this discussion.

Considering the well-known sign convention of the soil mechanics which sets the positive sign to the compression forces, the yield surface of this numerical model is written in the  $k$  plane as follows:

$$f_k(\sigma, \varepsilon_v^p, r_k) = q_k - \sin \phi'_{pp} \cdot p'_k \cdot F_k \cdot r_k \quad , \quad (1.1)$$

where  $p'_k$  and  $q_k$  are the effective mean and deviatoric values of the stress tensors. The parameters that control the behavior of the soil are  $F_k$ , which controls the isotropic hardening associated with the plastic volumetric strain and  $r_k$ , which controls the isotropic hardening generated by the plastic shearing. These two parameters represent progressive friction mobilization in the soil. At perfect plasticity, the product  $F_k \cdot r_k$  reaches unity.

## 1.3 Laboratory tests simulations

The behavior of the soil is mainly governed by its volume change. When soils are sheared, they increase in volume if they are initially dense or contract if they are initially loose. In order to validate this behavior, Casagrande (1936) conducted shear tests and found that “loose” sands contracted and “dense” sands dilated until approximately the same void ratio was attained at large strains. This latter was termed as the *critical void ratio*, and is affected by the mean effective stress, becoming smaller as the stress level increases. The relationship between the critical void ratio and the mean effective stress is called the *Critical State Line (or locus)* (CSL). The critical state is the state at which a soil continues to deform at constant stress and constant void ratio (Roscoe et al., 1958; Schofield and Wroth, 1968; Sladen et al., 1985; Been and Jefferies, 1985; Ishihara, 1993, among others).

In the development of the constitutive models, a capture of the large-scale experience is

essential. A basic assumption that a proper constitutive model for soils should adopt, is its ability to represent the changes in the soil behavior caused by the changes in density (Been and Jefferies, 1985). However, the relative density (or the void ratio) is rarely included as a variable to model the soil behavior. For this purpose, the critical state concept has been the preferred starting point of soil constitutive models (Been and Jefferies, 1985). According to this concept, the macroscopic behavior of sand is related to the proximity of its initial state to the critical state or steady-state rather than to the absolute measurements of its density (Been and Jefferies, 1985; Ishihara, 1993). The soil state is defined in the  $e - p' - q$  space where  $e$  is the void ratio,  $p'$  (i.e.  $= (\sigma'_1 + 2 \cdot \sigma'_3)/3$ ) is the mean effective stress and  $q$  (i.e.  $= \sigma'_1 - \sigma'_3$ ) is the deviatoric stress. The point where the stress path turns its direction in this space is called the transformation phase because it defines a transient state in which the change from contractive to dilative behavior occurs in the sand (Ishihara, 1993). In the work of Sladen et al. (1985), the peak points of undrained effective stress paths in terms of the major  $s'$  (i.e.  $= (\sigma'_1 + \sigma'_3)/2$ ) and minor  $t$  (i.e.  $= (\sigma'_1 - \sigma'_3)/2$ ) stresses is called the Collapse Surface (lately also called Instability Line (Ishihara, 1993; Lade, 1994; Lade and Ibsen, 1997)). For liquefaction to occur, the soil state has to reach the collapse surface and the shear stress must exceed the steady state shear strength.

The purpose of this section is to *simulate* laboratory tests in order to represent the soil behavior of two sand materials. Typical laboratory tests conditions and loads are going to be applied.

### 1.3.1 Defining the soil behavior

Similar to any common laboratory test, first, monotonic triaxial tests are conducted in order to understand the type of the material and estimate its behavior once subjected to different types of loading. Hence, drained and undrained monotonic triaxial tests were simulated on the tested materials. It should be mentioned that the triaxial test has been a preferred method to determine the soil parameters because its apparatus is widely available, and the sample behavior will always be determined because of the minimization of the non-uniformities in case of a contractive or dilative soil (Sladen et al., 1985). Different initial values of the mean effective stresses were chosen ( $p'_0 = 20, 50$  and  $70$  kPa) for both materials. From the conducted test, the stress path represented by the major and minor stresses (i.e.  $s', t$ ) from the undrained monotonic triaxial tests is shown in Figure 1.1, and the variation of the volumetric strain from drained monotonic triaxial tests is shown in Figure 1.2.

It can be seen from Figure 1.1 that the stress paths show a peak value before reaching the CSL (or the line of maximum resistance). The collapse surface is therefore represented. From Figure 1.2, the volumetric strain decreases to reach the CSL in the case of *Mat.1* whereas it increases towards the CSL in the case of *Mat.2*. From these “*experimental*” results, it can be viewed that *Mat.1* is a “normally consolidated” sand whereas *Mat.2* is an “overconsolidated” sand. It is true that the consolidation nomination is only applied for clay soils and is difficult to

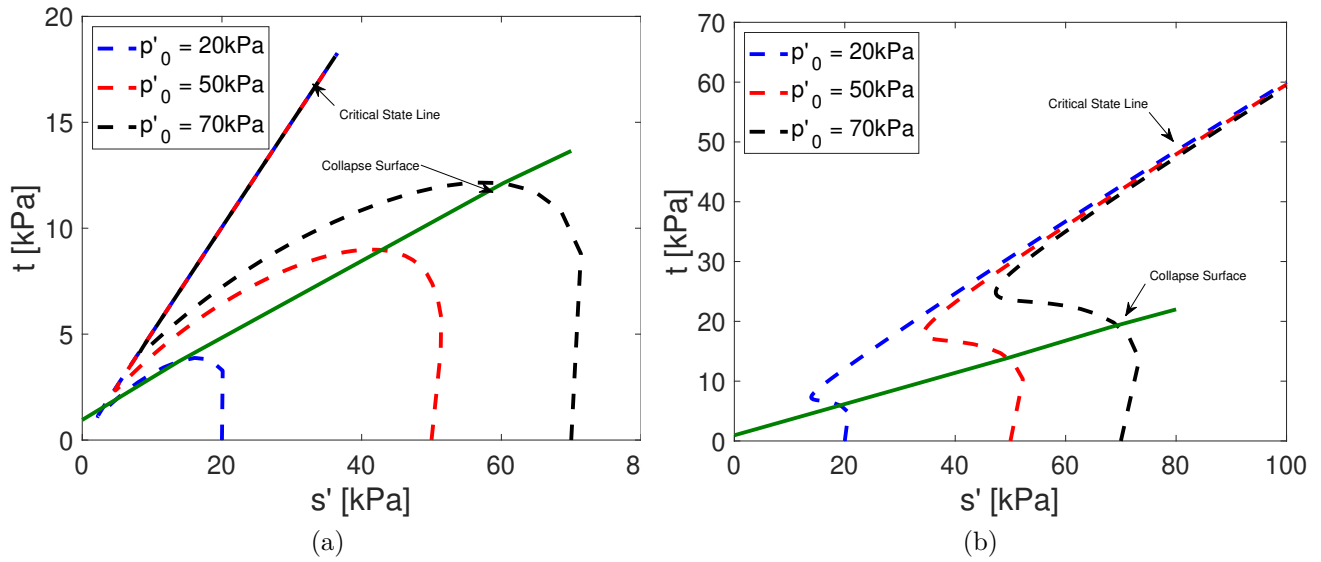


Figure 1.1: The stress path of a) *Mat.1* and b) *Mat.2* from the simulated undrained monotonic triaxial tests

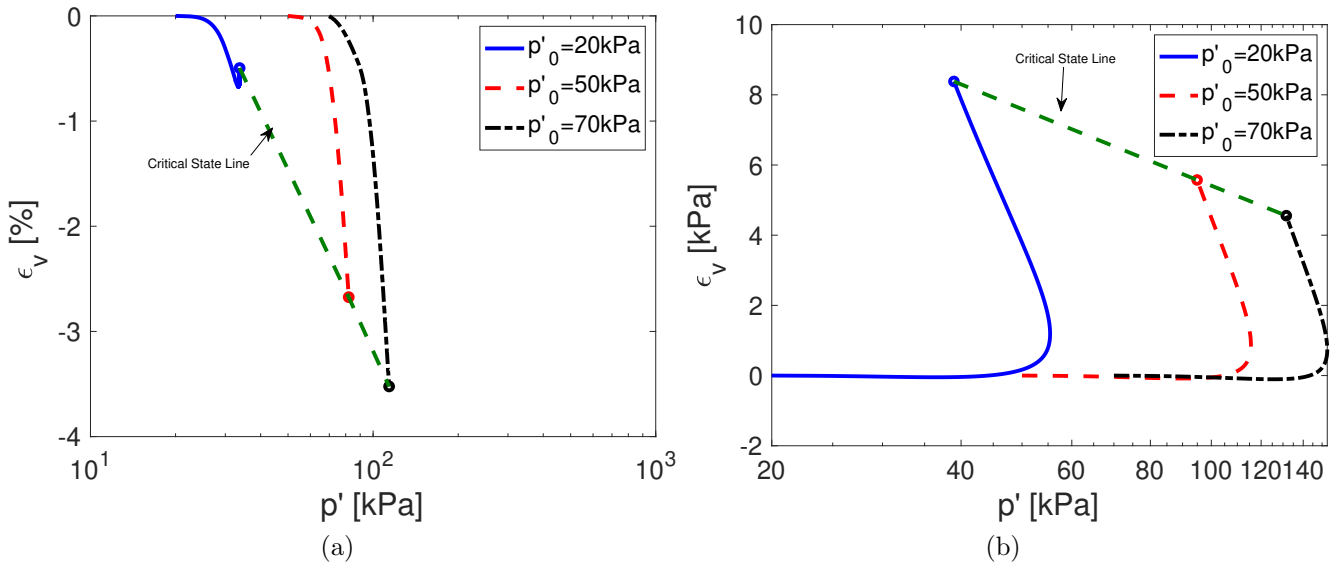


Figure 1.2: The variation of the volumetric strain with respect to the mean effective stress for a) *Mat.1* and b) *Mat.2* from the simulated drained monotonic triaxial tests

adopt for sands except for some cases (Biarez and Hicher, 1994). In this study, the nomination of “loose” and “dense” sand will be related to the relative density  $D_r$ , as will be shown later in this section.

### 1.3.2 Effect of regular cyclic loading

In practice, the liquefaction charts are used to quantify the liquefaction triggering. These charts are characterized by the severity of the earthquake loading and the soil resistance for liquefaction (Seed and Idriss, 1971; Youd and Idriss, 2001; Sassa and Yamazaki, 2016, among others). The level of the loading is characterized by the cyclic stress ratio defined by the ratio

of the maximum cyclic shear stress to the initial effective confining pressure (i.e.  $CSR = q_{cyc}/2 \cdot p'_0$ ). For the soil resistance, it can be identified by field measurements (i.e. N-values of the SPT test, q-values of the CPT test and shear wave velocity) or laboratory tests (triaxial tests; monotonic or cyclic, drained or undrained). In the case of regular loading, which is best compatible with the laboratory experiments, different values of the cyclic shear stress were considered in order to find the soil resistance. For *Mat.1*, the tested shear stresses are 8, 9, 10, 11 and 12 kPa, whereas 10, 11, 12, 15 and 20 kPa were tested for *Mat.2*. For the sake of brevity only, one initial confining pressure is considered ( $p'_0 = 50$  kPa) and one example material is shown for interpretation. The variation of the excess pore water pressure  $\Delta p_w$  and the axial deformation  $\varepsilon_1$ , in addition to the stress path of the regular load are shown in Figure 1.3.

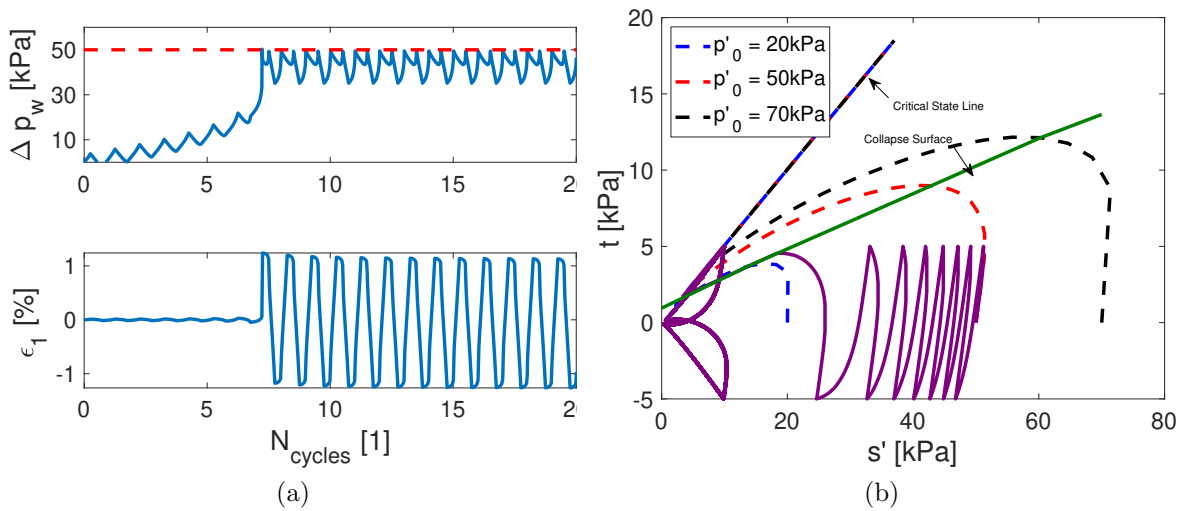


Figure 1.3: a) The variation of  $\Delta p_w$  (top) and  $\varepsilon_1$  (bottom) and b) the stress path of the regular loading for *Mat.1*

It can be seen, that the excess pore water pressure increases until reaching the value of the initial confining stress (50 kPa) for a certain number of cycles  $N_{cycles}$  indicating the liquefaction occurrence. In consequence, axial deformation started to occur for the same  $N_{cycles}$ . As for the stress path in Figure 1.3b, once the specimen reached the collapse surface, *butterfly shapes* start to occur until reaching the CSL.

Concerning the level of loading for all the tested regular loads, the cyclic resistance is represented in Figure 1.4 in terms of the cyclic stress ratio  $CSR$  and the number of cycles  $N_f$  that generates an axial strain of 2% double-amplitude (DA) (Ishihara, 1993). It should be mentioned that in theory, the generation of 5% DA is considered for liquefaction. But based on recent studies, the occurrence of 2% or 3% DA axial strain can also be acceptable (Cubrinovski, 2011; Pan and Yang, 2018).

In Figure 1.4, a reference to an experimental study conducted by Byrne et al. (2004) on Nevada sand for different values of relative densities is represented. Comparing the referenced results to the ones simulated in this study, it can be deduced that *Mat.1* has  $D_r \approx 40\%$  whereas *Mat.2* has  $D_r \approx 50\%$ . Hence, *Mat.1* is shown to behave as a loose sand, so it will contract if

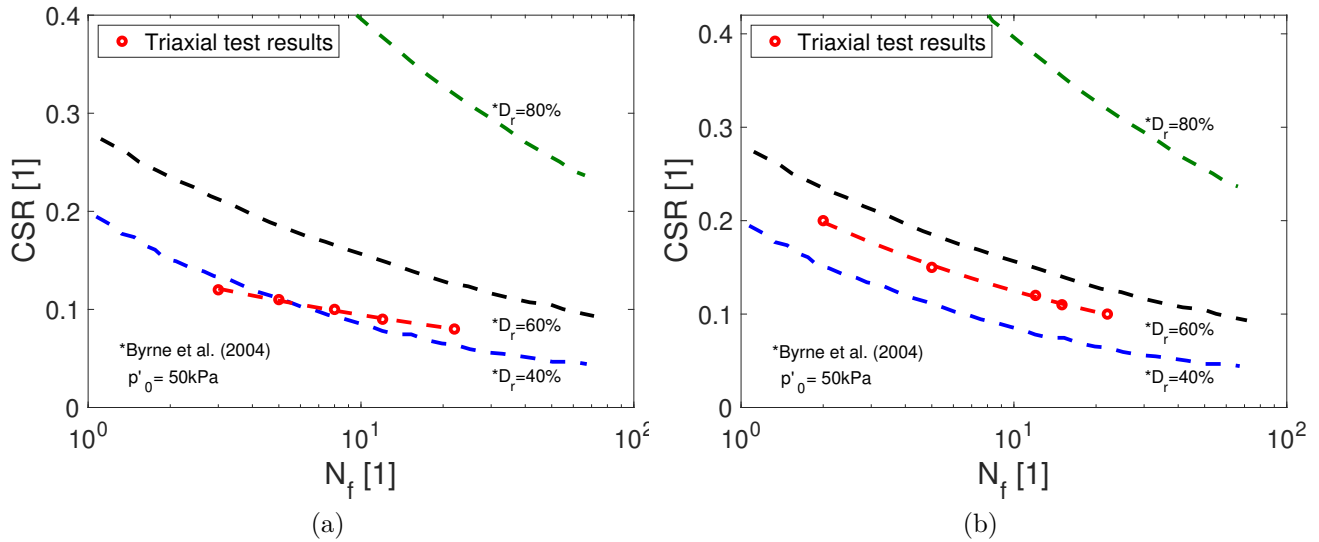


Figure 1.4: The Variation of the Cyclic Stress Ratio  $CSR$  as function of the number of cycles  $N_f$  for a) *Mat.1* and b) *Mat.2*

sheered, whereas *Mat.2* behaves as a dense sand, so it will dilate when sheered for lower  $p'_0$ . The results of the cyclic resistance for regular loading will be used in the continuity of this chapter as a boundary to identify the liquefaction apparition.

## 1.4 Effect of initial soil state

It is known that liquefaction susceptibility depends essentially on the initial state of the soil (Ishihara et al., 1975; Sladen et al., 1985; Been and Jefferies, 1985). It was presented so far the behavior of two soil samples based on regular cyclic loading. The resistance of each sample was represented in terms of their cyclic stress ratio  $CSR$ . This section will examine the change in the  $CSR$  values considering different initial states. For this purpose, one soil sample will be analyzed in order to maintain focus on the objective of this section. Hence, a drained monotonic triaxial test is first conducted after which an undrained cyclic triaxial test will take place. According to Pan and Yang (2018), in order to compare the different test configuration, the initial confining pressure for all the cyclic tests is always  $p'_0 = 50$  kPa. It means that only for the cases without preloading, the confining pressure is isotropic. For the other cases it is anisotropic (i.e.  $q \neq 0$ ). Figure 1.5a shows an example of the applied load. In this case, the initial isotropic confining pressure of the static load is 48 kPa. The stress path of the conducted test is shown in Figure 1.5b. It can be seen from this Figure that the soil specimen reached the critical state during the cyclic load.

The cyclic resistance of the soil is taken into consideration with a reference to a recent study conducted by Pan and Yang (2018). They conducted a series of undrained triaxial tests on Toyoura sand at varying levels of initial deviatoric stresses to investigate the combined effect of the static and cyclic shear. The cyclic stress ratio in this case will be  $CSR = q_{tot}/2p'_0$  where

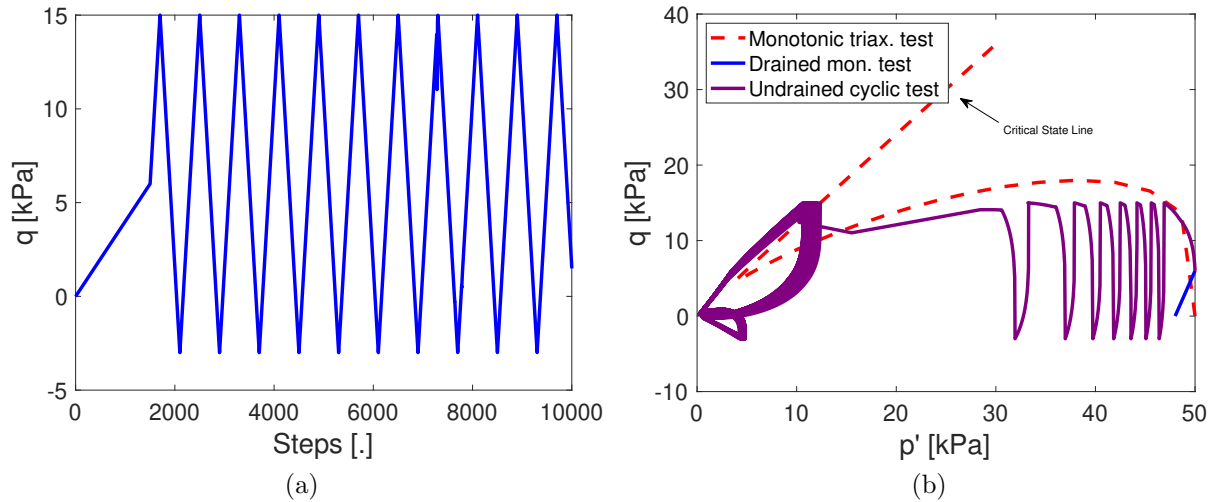


Figure 1.5: a) An example of the applied load on the soil specimen and b) its stress paths in  $p' - q$  plan

$q_{tot} = q_s + q_{cyc}$ . In addition, the cyclic resistance could be quantified by the Cyclic Resistance Ratio  $CRR$  that is the  $CSR$  required for failure at  $N_f = 10$  ( $N_f$  being the number of cycle that induced liquefaction) (Pan and Yang, 2018).

In the scope of this study, similar work is conducted on *Mat.1* in order to calculate the cyclic stress ratio for different values of initial deviatoric stresses. Thus  $q_s = 3, 6, 9, 10$  kPa and  $q_{cyc} = 7, 8, 9$  and 10 kPa. The results are shown in Figure 1.6a. It should be noted that  $SSR$  is the Static Stress Ratio and is equal to  $SSR = q_s/2p'_0$ . Clearly from this figure, when the initial load increases (static in this case), the soil resistance increases. The effect of the variation of the cyclic load affected the number of cycles such that when  $q_{cyc}$  increases, less cycles  $N_f$  are needed to reach liquefaction.

Moreover, a comparison with the results of the study conducted by Pan and Yang (2018) is shown in Figure 1.6b. The  $CRR$  as function of the  $SSR$  is represented. The present study shows compatible results with the cited one such that the  $CRR$  increases when  $SSR$  is between 0 and 0.1.

Finally, it can be concluded from this work that the initial state of the soil affects its behavior as it increases its resistance to liquefaction. In addition, it was emphasized that the used numerical model takes into account the history of the soil when sequential loads are applied (an idea that will have lights in Chapter 3 and 4).

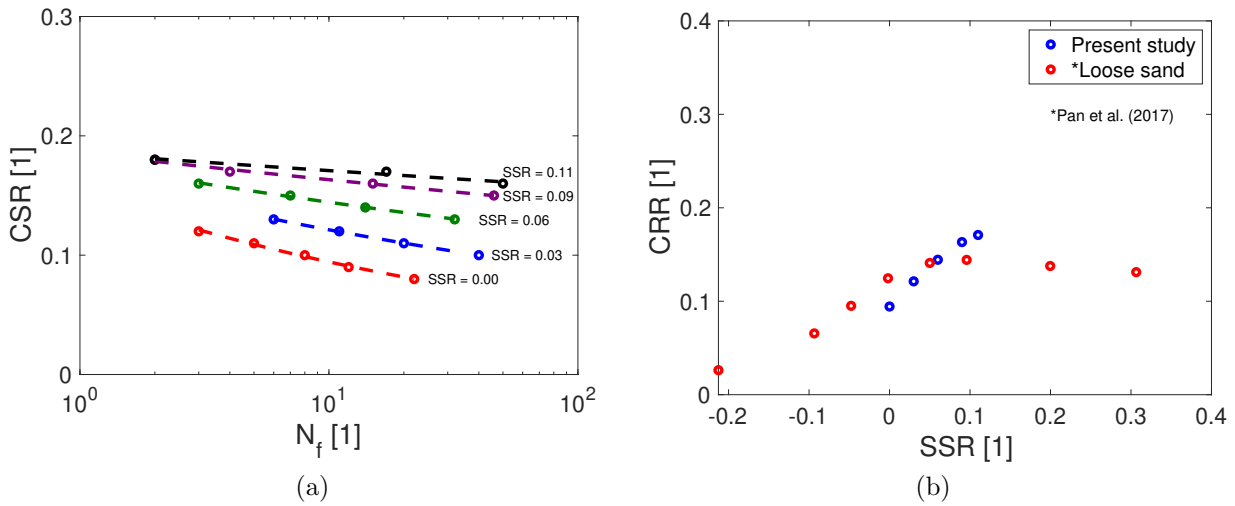


Figure 1.6: a) the Cyclic stress ratio  $CSR$  for different values of initial deviatoric stresses and b) the Cyclic Resistance Ratio  $CRR$  as function of the Static Stress Ratio  $SSR$  for *Mat.1*

## 1.5 Soil stability

Liquefaction is sometimes considered as the consequence of the collapse of a metastable arrangement of soil particles (Been and Jefferies, 1985). The transition from stable hardening behavior to sudden strength loss in undrained tests is represented from the Collapse Surface that is sometimes considered as an Instability Line. For undrained conditions and compressive material, the instability is self-sustaining and unconditional, whereas in drained conditions, the instability is conditional and depends on the position of the stress state with respect to the yield surface (Lade, 1994). It is important to mention that the instability of a soil might be an initiation to liquefaction but it is not the only factor, since the shear stress has to exceed the soil shear strength in addition to an excess of pore water pressure. Based on the sufficient condition of stability predicted by Hill (1958), a stress-strain state is called “stable” if for any increment in the stress and in its corresponding strain, the second increment of the plastic work is strictly positive as shown in Equation 1.2 (Hill, 1958; Hamadi et al., 2008a,b, among others). Because soils are non-associated plasticity materials, the instability is reached inside the plastic limit, so the normalized second order increment of the work calculated based on Equation 1.3 will facilitate the detection of instability zones (Darve and Laouafa, 2000).

$$\forall(d\underline{\underline{\sigma}}', d\underline{\underline{\varepsilon}}), \quad d^2W = d\sigma'_{ij}d\varepsilon_{ij} > 0 \quad , \quad (1.2)$$

$$\forall(d\underline{\underline{\sigma}}', d\underline{\underline{\varepsilon}}), \quad d^2W_{normalized} = \frac{d\sigma'_{ij}d\varepsilon_{ij}}{\|d\underline{\underline{\sigma}}'\| \|d\underline{\underline{\varepsilon}}\|} \quad . \quad (1.3)$$

In order to verify if the collapse line is the transition to instability behavior, the second increment of the work  $d^2W$  is calculated for *Mat.1* for monotonic loads with three initial confining pressures and a cyclic load with  $p'_0 = 50$  kPa. The material is considered unstable when  $d^2W$  is negative

(opposite of Equation 1.2). This variable was drawn in the major and minor stresses  $s' - t$  plan. The results are shown in Figure 1.8, and when  $d^2W$  is negative, it is designated with circles on the stress paths.

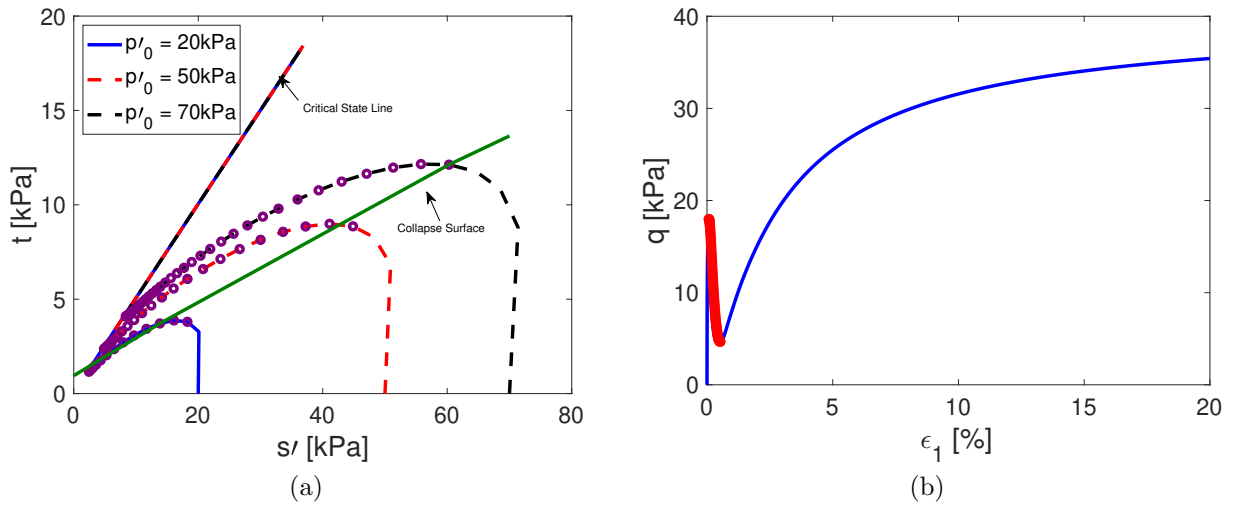


Figure 1.7: The second increment of the work  $d^2W$  for *Mat.1* for monotonic load

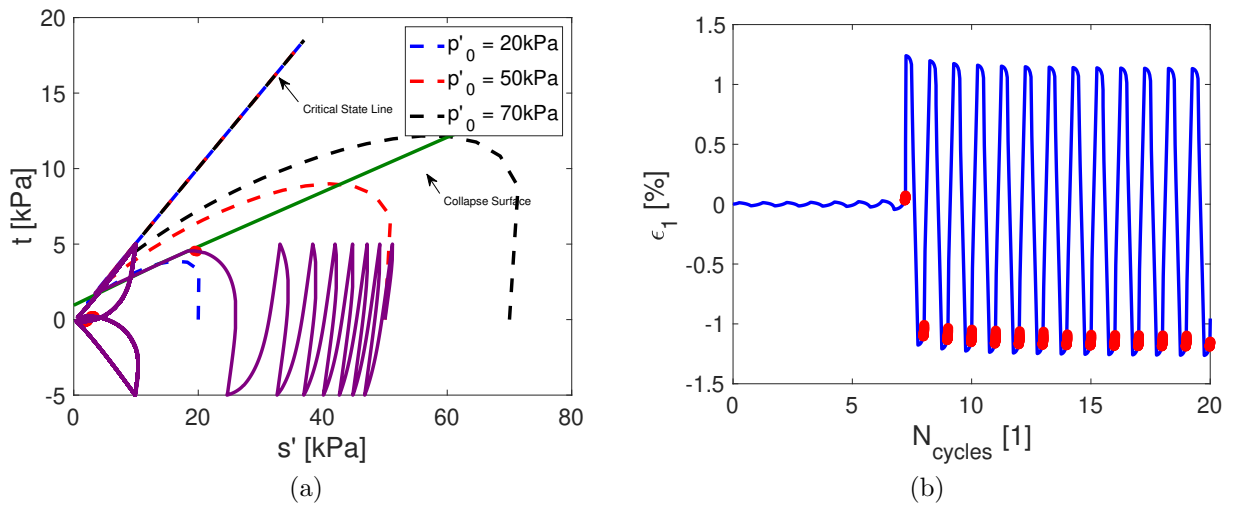


Figure 1.8: The second increment of the work  $d^2W$  for *Mat.1* for cyclic load

For the monotonic loads in Figure 1.7a and for the tested confining pressures  $p'_0$ ,  $d^2W$  shows negative values when the effective stress path reaches the collapse surface until the CSL. Thus, the collapse surface designates the failure initiation state, above which, the material is not stable. On the contrary, for the cyclic load (Figure 1.8a), the condition of stability predicted by Hill (1958) is misleading as it only predicts the initiation of the soil instability but does not correctly localize it. In addition, as shown in the work of Rapti (2016), this criterion is not cumulative and gives only an image of instability at specific instants of the loading.

Thus, for engineering practices, in order to localize the seismic instability of structures, a recall to stability analysis methods (i.e. limit equilibrium, pseudo-static analysis) is more

general than the condition of Hill (1958) (Rapti, 2016). In Section 1.6, a parameter based on the numerical model is going to be introduced as an instability indicator.

## 1.6 Local safety factor estimation through soil residual strength

Stability analysis, in static or dynamic loads, is developed through traditional methods such as the limit equilibrium or the pseudo-static analysis (Duncan, 1996; Lu et al., 2012). These methods require the identification of the soil physical characteristics in addition to the location and the geometry of the structure of concern through laboratory test results and field investigations. Without these information, the stability analysis will require some hypotheses that will expose it to uncertainties (Huang and Yamasaki, 1993). These uncertainties are more important when dealing with dynamic loads (Duncan, 1996; Kramer, 1996). For this purpose, non linear finite element methods are proven to be more efficient in assessing numerical stability analysis and identify the failure surface of an element at-risk.

It was seen in the previous section that the stability condition of (Hill, 1958) is only applicable for monotonic loads. Since dynamic stability analysis is more realistic, the common approach of the existing stability analysis is to identify or assume a failure surface and assess its factor of safety  $FS$ . In some cases, when developed FE models exist, the  $FS$  is assigned on each point in a domain of interest in order to represent a failure surface and thus, it is designated as a local safety factor  $LFS$ . The  $LFS$  is an indicator of how far from failure the current state of stress is (Lu et al., 2012).

In the case of this study, the used ECP numerical model provides for any soil state, a parameter that gives a direct measure of the “distance to reach the critical state”. Taking into consideration the soil mechanics sign convention, the yield surface of the model written in the  $k$  plane is presented in Equation 1.1.

The function  $F_k$  controls the isotropic hardening associated with the plastic volumetric strain, whereas  $r_k$  accounts for the isotropic hardening generated by plastic shearing. They represent progressive friction mobilization in the soil and their product reaches unity at perfect plasticity. Therefore, it is possible to define an apparent friction angle  $\phi_{apt}$  as follows:

$$F_k = 1 - b \ln \left( \frac{p'_k}{p_c} \right) , \quad (1.4)$$

$$p_c = p_{co} \exp(\beta \varepsilon_v^p) . \quad (1.5)$$

$$\sin \phi'_{apt} = \frac{q_k}{p'_k \cdot F_k} . \quad (1.6)$$

$$r_{apt} = \frac{\sin \phi'_{apt}}{\sin \phi'_{pp}} . \quad (1.7)$$

$r_{apt}$  varies between 0 and 1 where perfect plasticity is reached and could be defined as the

inverse of a local safety factor ( $r_{apt} = 1/LFS$ ). Thus, the potential mean stress is evaluated from the friction angle at the critical state  $\phi'_{pp}$  and the current mean stress from the apparent friction angle  $\phi'_{apt}$ . A threshold value of the damage measure is taken as 0.75 (i.e. corresponds to  $LFS \approx 1.33$ ) (Lopez-Caballero and Modaressi-Farahmand-Razavi, 2013; Rapti et al., 2018).

Since the behavior of the soil is mainly governed by its volume change, in order to explain the meaning of the parameter  $r_{apt}$ , drained cyclic shear tests were conducted on the tested materials for an initial confining pressure  $p'_0$  equals to 50 kPa. The results of *Mat.1* are shown in Figure 1.9.

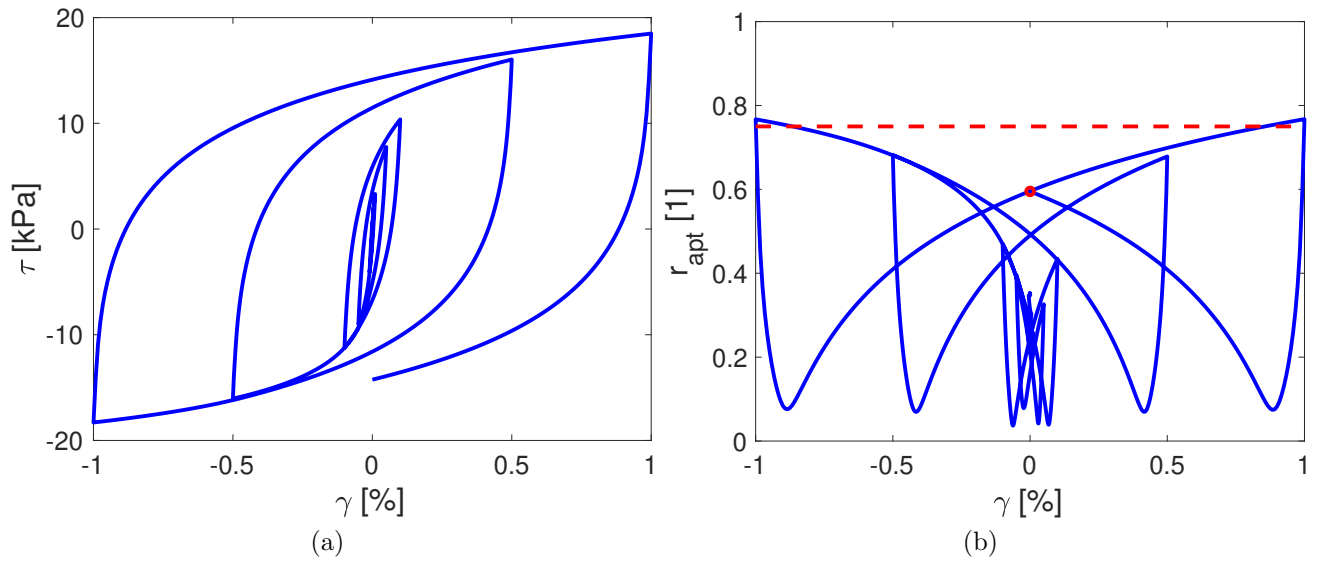


Figure 1.9: a) The shear stress-strain of *Mat.1* and b) the variation of the parameter  $r_{apt}$  as function of the shear strain  $\gamma$

The non linear behavior is clear from the shear stress  $\tau$  and shear strain  $\gamma$  curve in Figure 1.9. As function of the shear strain, the parameter  $r_{apt}$  increases when the shearing increases. At higher shear,  $r_{apt}$  slightly increases its threshold limit and instability occurs. Clearly, the soil state did not recover to its initial state since  $r_{apt}$ , at the end of loading (red circle in Figure 1.9b) is not zero.

Similar interpretations can be conducted to *Mat.2* in Figure 1.10. However, it is clear that higher values of shear stress were applied comparing to *Mat.1*. This is due to the higher resistance of this soil sample comparing to the previous one. Otherwise,  $r_{apt}$ , at the end of loading (red circle in Figure 1.10b) show that the soil did not recover.

In order to examine the values of  $r_{apt}$  in terms of each cycle of load, Figure 1.11a shows the evolution of this parameter as function of the maximum shear strain  $\gamma_{max}$  at each cycle of load for *Mat.1*. It is clear that  $r_{apt}$  increases as the cycles of loads and the maximum shear strain increase. Moreover, in Figure 1.11b it is shown the values of  $r_{apt}$  for a monotonic load and a cyclic shear test at the end of the cycle and the maximum values. It can be seen from this figure that *Mat.1* is exposed to failure rapidly when subjected to cyclic load rather than monotonic load. In addition,  $r_{apt}$  increases at the beginning of the load and then it tends to

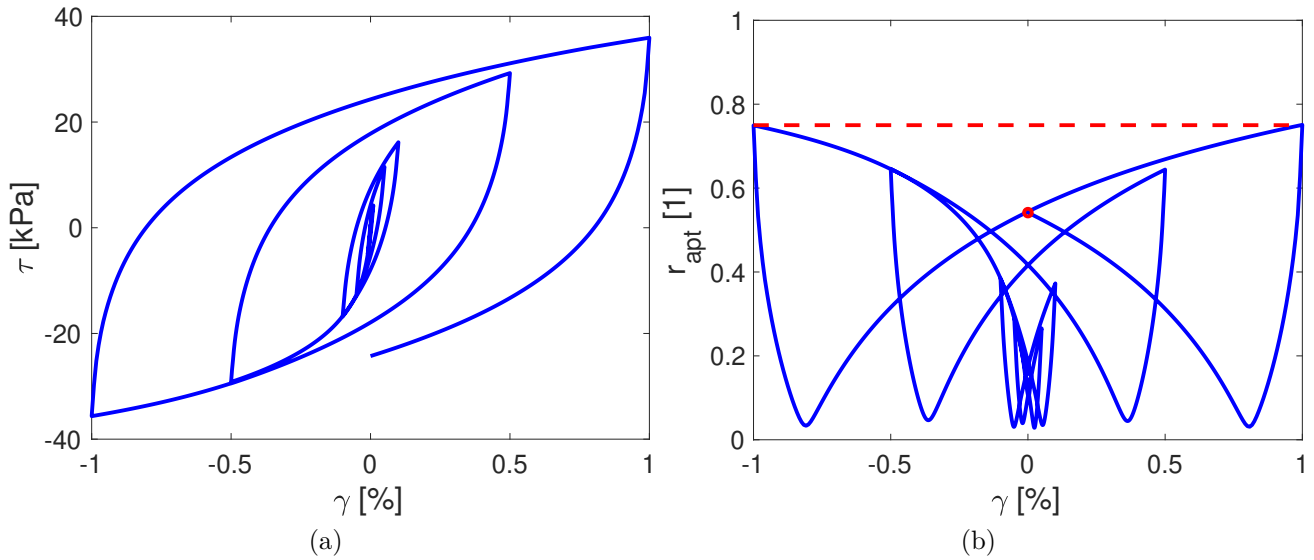


Figure 1.10: a) The shear stress-strain of *Mat.2* and b) the variation of the parameter  $r_{apt}$  as function of the shear strain  $\gamma$

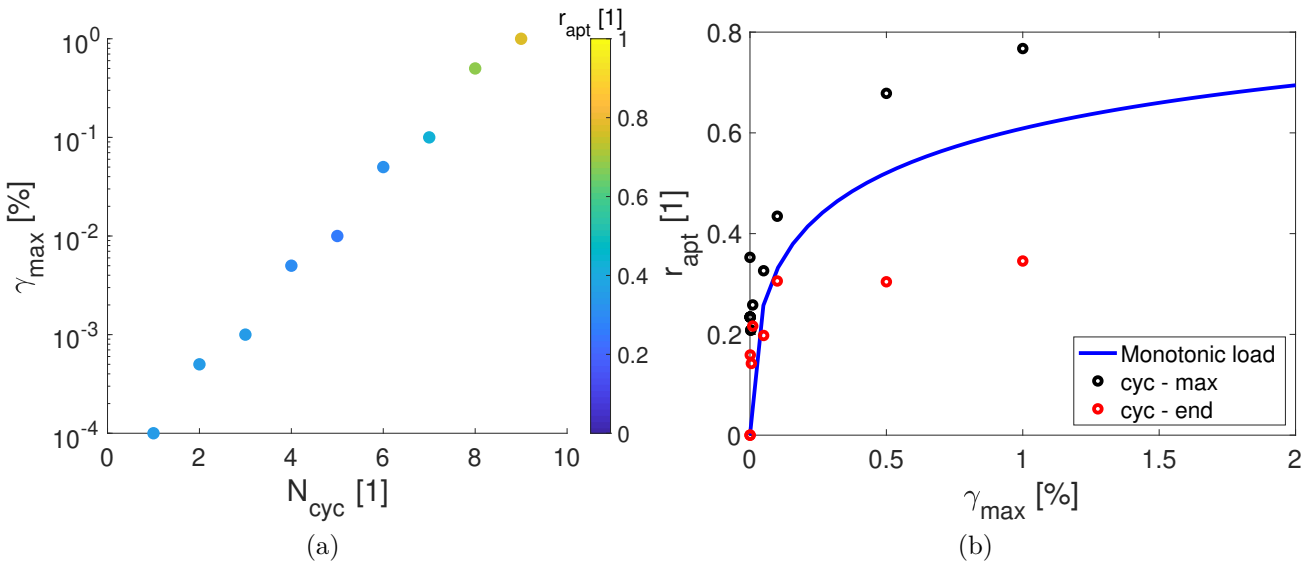


Figure 1.11: The evolution of the parameter  $r_{apt}$  for *Mat.1* after a monotonic and cyclic load in terms of the maximum shear strain  $\gamma_{max}$

stabilize, independently of the loading type.

It was shown in this section that the parameter  $r_{apt}$  can represent the instability localization for cyclic loads. Thus, the ratio of apparent to critical friction angle represented by the parameter  $r_{apt}$  provides a reliable measure of soil strength, which takes into account the loading history and can be used as a criterion for estimating the local state of soil for cyclic loads.

## 1.7 Post liquefaction behavior

From the conducted virtual experimental tests, it was seen that the soil behavior can be represented with the critical state concept, for a monotonic and a cyclic load. In addition, the stability theory of Hill (1958) can be misleading for a cyclic load, thus it was presented a model parameter to represent the soil residual strength and was considered as an indicator of the local safety factor. In this section, in order to track the liquefaction behavior of the soil, a sequence of cyclic undrained tests followed by monotonic undrained tests will be conducted on one tested material (*Mat.1*), for the sake of brevity only. Such tests will also give an idea about the post-liquefaction behavior of the tested soil to estimate the bearing capacity of the soil after the liquefaction. Figure 1.12a shows a loading type example of the conducted test. The stress path in major and minor stresses  $s' - t$  plane is shown in Figure 1.12b.

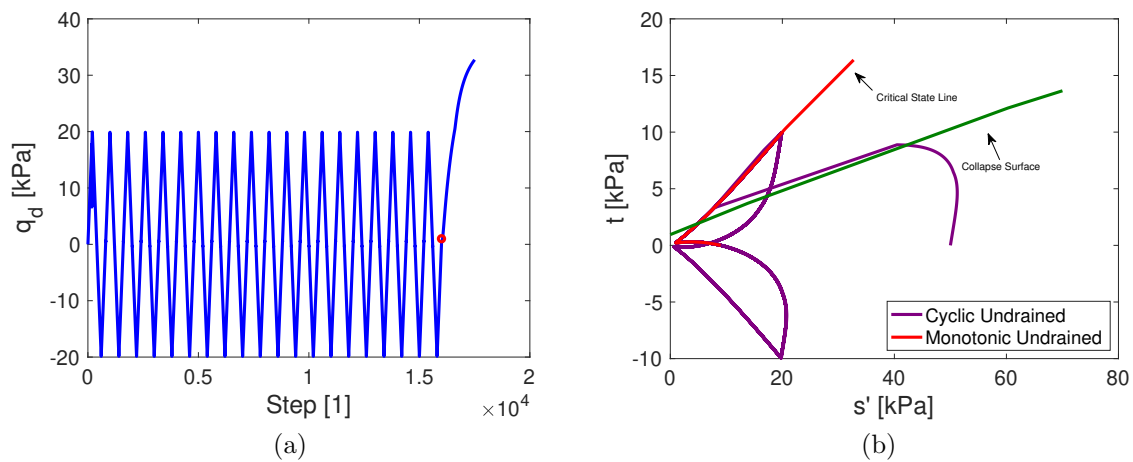


Figure 1.12: a) A loading path example of the conducted test and b) The stress path in  $s' - t$  space for *Mat.1*

From the stress path in Figure 1.12b, and after few cycles, the soil reaches the collapse surface and enters the instability zone to continue in a butterfly shape till the end of the cyclic loading (purple path in the figure). Once the monotonic shaking starts to occur (blue path), the soil reached the critical state rapidly.

Otherwise, Been and Jefferies (1985) developed the so-called *state parameter* for sands that combines the influence of the void ratio and the stress level with a reference to an ultimate state to represent the soil behavior. This reference should be independent of the test conditions and it can be represented by the steady state (Casagrande, 1936; Schofield and Wroth, 1968; Been and Jefferies, 1985, among others). For sands, it is measured after liquefaction and it is defined as the locus of all points in  $e - p' - q$  space at which the soil deforms under constant effective stress and void ratio. It is interesting to note that both concepts (i.e. critical and steady state) are similar for sands. Some stresses at key points are related to the state index which are the peak strength  $q_p$  and the strength at steady state  $q_s$  (Been and Jefferies, 1985; Ishihara, 1993, among others). These two stress key points are shown in Figure 1.13 for a monotonic load alone

(blue) and the sequence of cyclic+monotonic load (red). The chosen initial confining stress  $p'_0$  is 50 kPa. As seen from this figure and for this case,  $q_{p,mon}$  is 18 kPa and  $q_{s,mon}$  is 4 kPa. Clearly,  $q_p$  and  $q_s$  are smaller than the ones for monotonic loads alone, which means that the soil changes its behavior after the cyclic loading.

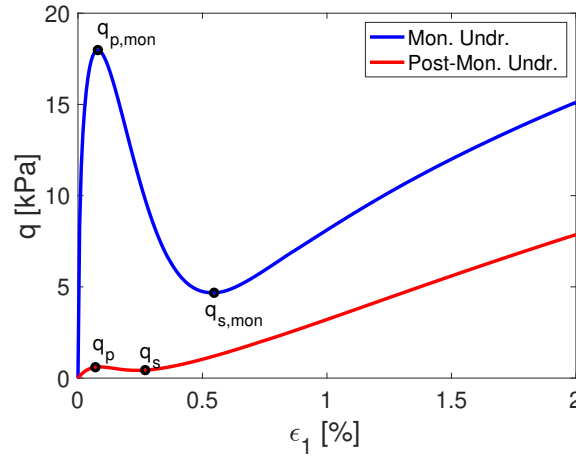


Figure 1.13: The stress key points during a monotonic load alone and the sequence of cyclic+monotonic load

Hence, in order to track the liquefaction occurrence, several values of deviatoric stress  $q_d$  were taken, in addition to different number of cycles  $N_{cyc}$ . Figure 1.14a shows the variation of the normalized peak strength  $q_{p,cyc}/q_{p,mon}$  and Figure 1.14b shows the variation of the normalized strength at the steady state  $q_{s,cyc}/q_{s,mon}$  as function of the deviatoric stress for different number of cycles.

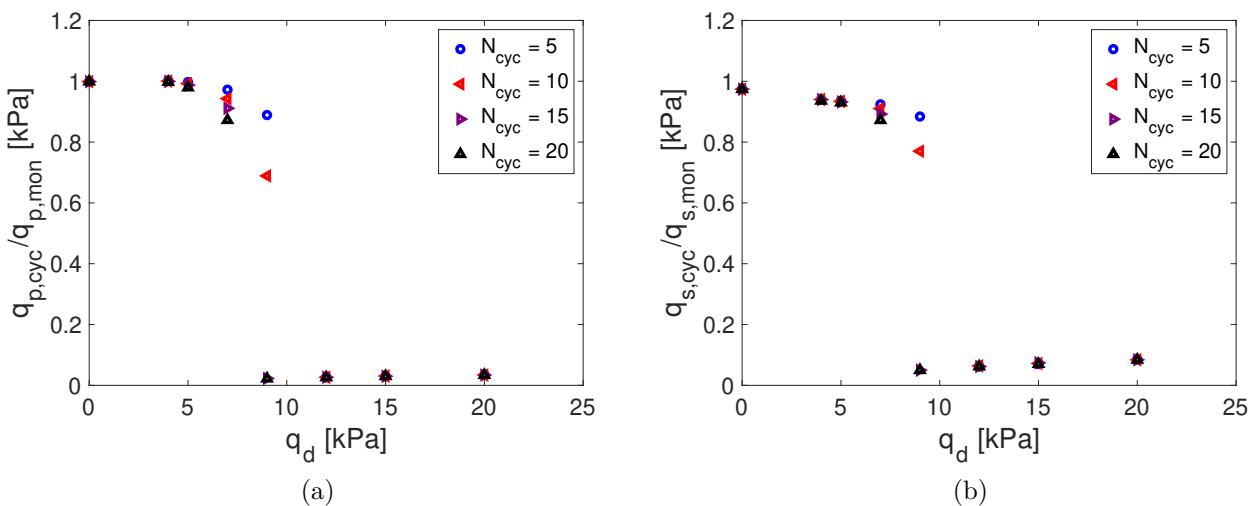


Figure 1.14: a) Variation of the normalized peak strength and b) Variation of the normalized strength at steady state as function of the deviatoric stress

It can be seen from Figure 1.14a that with respect to the deviatoric stress, the soil does not show resistance when subjected to high values of  $q_d$  (i.e.  $q_d > 10$  kPa) independently to the

number of cycles of the cyclic loading. Whereas for  $q_d$  values less than 6 kPa, the soil shows resistance due to values of  $q_{p,cyc}/q_{p,mon}$  close to unity. There is an interval where  $q_d$  is between 6 to 10 kPa in which the number of cycles affects the response of the soil. When the number of cycles increases the soil tends to lose its resistance. Notice that the same interpretation can be done for the normalized strength at steady state in Figure 1.14b.

### 1.7.1 Concept of liquefaction resistance factor

The resistance factor against liquefaction  $F_L$  expresses the severity of liquefaction (Yasuda et al., 2017). It is a factor that takes place at post-liquefaction for a critical number of cycles that is usually 15 (Stamatopoulos et al., 2015; Karimi et al., 2018). This factor  $F_L$  is the ratio between the cyclic stress that generates liquefaction (i.e.  $CSR$  for 15 cycles) to the applied cyclic stress  $CSR$ . The  $F_L$  factor was drawn for the tested material subjected to different values of deviatoric shear stress with respect to the normalized peak shear stress and the one at steady state. The results are shown in Figure 1.15. The critical values of  $F_L$  are 0.8 and 1.25 and are drawn as dashed lines in this figure (Yasuda et al., 2017).

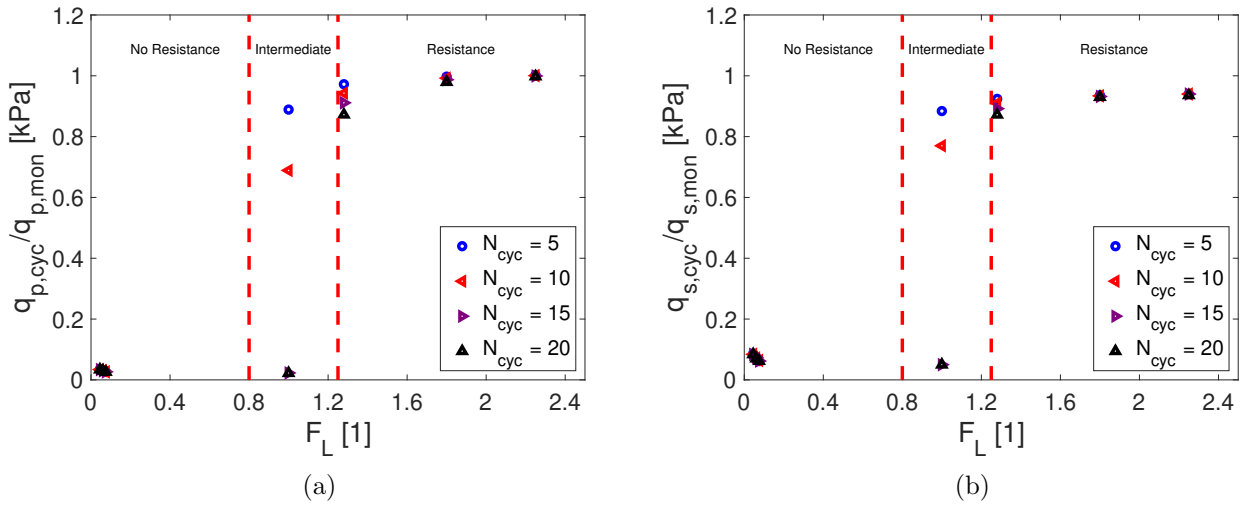


Figure 1.15: The resistance factor against liquefaction  $F_L$  for the normalized a) peak and at b) steady state shear stress

It should be mentioned that the same interpretation can be done based on either the normalized peak strength or the strength at steady state (Figure 1.15a or 1.15b). It can be seen that when  $F_L$  is less than 0.8, the normalized strength is close to zero. This means that the soil was not resistant to liquefaction and that failure occurred. It is interesting to mention that these cases concern the high values of deviatoric stress hence the applied  $CSR$  is high. However, for  $F_L$  greater than 1.25, the normalized strength is close to unity. So the soil for these cases was resistant to liquefaction. Within the two critical values of  $F_L$ , there is an intermediate range in which the values of  $F_L$  are either small or high. Relating this variation to the number of cycles of the cyclic loading, it can be seen that when the number of cycles is small, the normalized

strength is close to unity and hence the soil is resistant. When the number of cycles increases, the soil tends to lose its resistance by reaching small values of the normalized strength (i.e. black triangular shape which corresponds to  $N_{cyc} = 20$ ).

### 1.7.2 Liquefaction resistance factor and local safety factor

It was mentioned in Section 1.6 that the parameter  $r_{apt}$  can be interpreted as the inverse of the local safety factor of the soil. The threshold value of this parameter after which instabilities occur is 0.75, and perfect plasticity is reached when  $r_{apt} = 1$ . In this section, it will be presented the link of this parameter with the aforementioned liquefaction resistance factor  $F_L$ . As developed before, three zones can be identified based on the values of  $F_L$ , which are *No Resistance*, *Intermediate* and *Resistance* zone. The parameter  $r_{apt}$  will be calculated for a case in each zone. For the sake of brevity only, one number of cycle will be chosen  $N_{cyc} = 20$ . The results are shown in Figure 1.16.

It can be seen from this figure that when the soil shows no resistance (Figure 1.16a), the parameter  $r_{apt}$  shows values that are greater than 0.75 during the cyclic shaking. For the zone where the soil resists liquefaction (i.e. Figure 1.16c), the parameter  $r_{apt}$  shows values less than 0.2, so the soil lies in the *Resistance* zone. However, after the cyclic load, the soil reached instabilities due to the post event and its history of loading. For the *Intermediate* zone (Figure 1.16b), the soil tries to resist at the beginning of the loading when the values of  $r_{apt}$  are small, but then, it fails since  $r_{apt}$  exceeded its threshold limit. Therefore, the interpretation developed above regarding the effect of the number of cycles is valid in this case as well; when the number of cycles increases, the soil tends to reach the critical state rapidly. Thus, it can be concluded from this work that the post liquefaction behavior of the soil is affected by its history of loading.

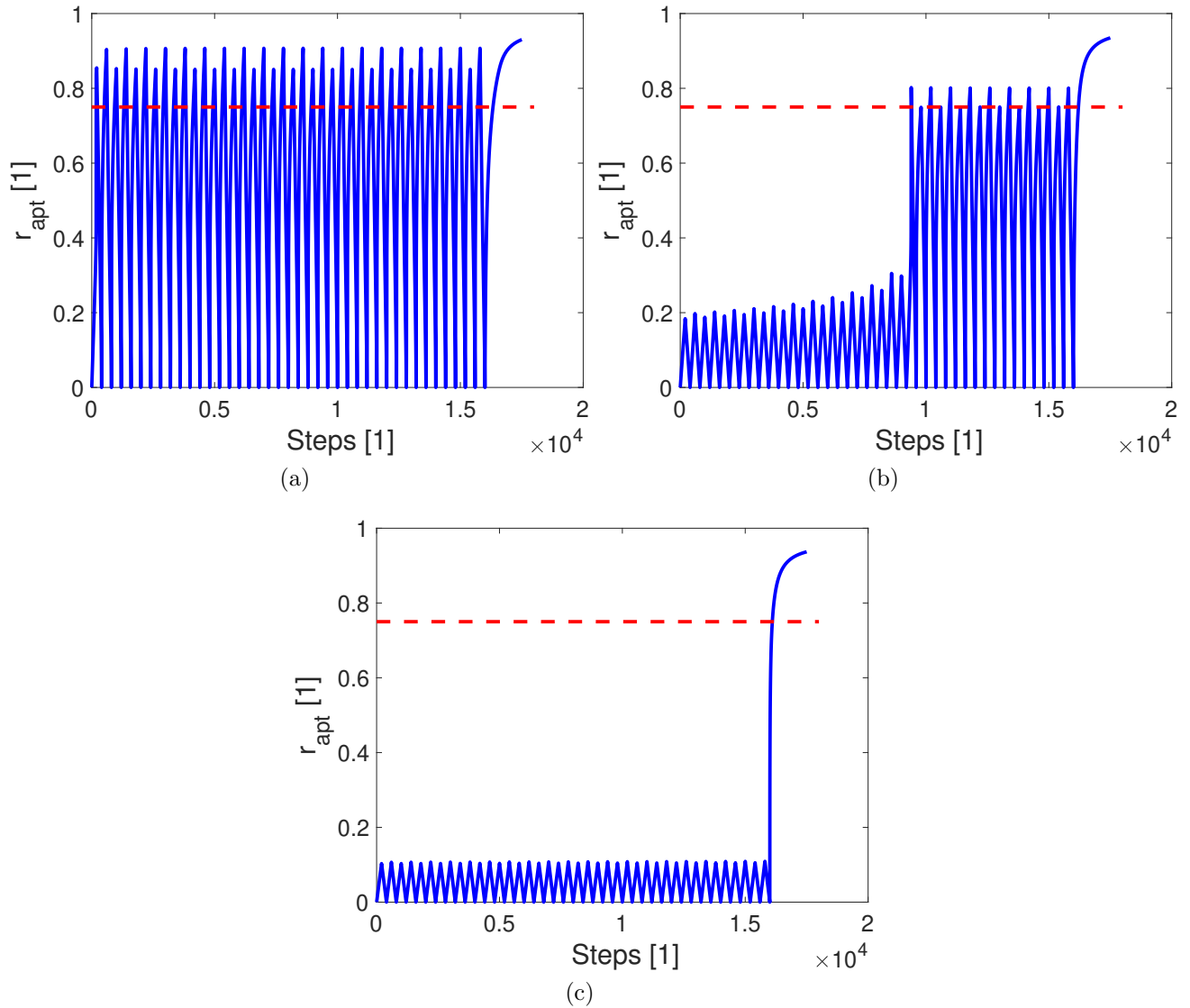


Figure 1.16: The parameter  $r_{apt}$  for a) *No Resistance zone*, b) *Intermediate zone* and c) *Resistance zone* for  $N_{cyc} = 20$

## 1.8 Effect of irregular cyclic loading

In practice, the liquefaction potential is assessed from laboratory testing. The usual laboratory tests only deal with uniform sinusoidal cycles of loading. However, in real scenarios, the earthquakes are not presented in these shapes. For this purpose, a recall to *virtual* laboratory tests will be assessed and undrained triaxial tests with irregular cyclic loading will be applied on the soil sample. An example of the used type of load is represented in Figure 1.17. In order to compare with typical laboratory tests conducted in Section 1.3, the same values of the cyclic shear stress will be considered which means that  $q_{cyc} = 8$  to 12 kPa, with some additional values to 20 kPa. Similar to the analysis method of Section 1.3, the generation of the excess pore water pressure  $\Delta p_w$  and the variation of the axial strain  $\varepsilon_1$  are found for the irregular loading. For the sake of brevity, only one tested motion for one material (*Mat.1*) will be interpreted. The results are shown in Figure 1.18.

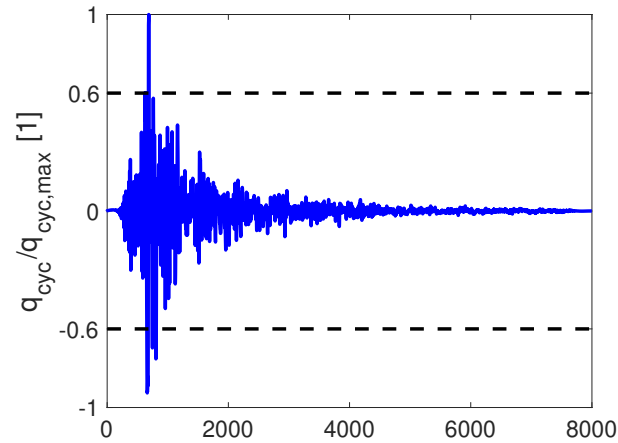


Figure 1.17: An example of an applied loading with earthquake shape

It can be seen from Figure 1.18 that the same interpretation for  $\Delta p_w$  and  $\varepsilon_1$  conducted in Section 1.3 can be valid for this section.  $\Delta p_w$  increases at the beginning of the loading until it reaches the value of the initial confining pressure of 50 kPa (i.e. the excess pore water pressure ratio  $r_u = \Delta p_w/p'_0 = 1$ ). For the stress paths of *Mat.1* (Figure 1.18b), the soil enters an instability phase once it reaches the collapse line after which butterfly loops start to occur until failure is reached.

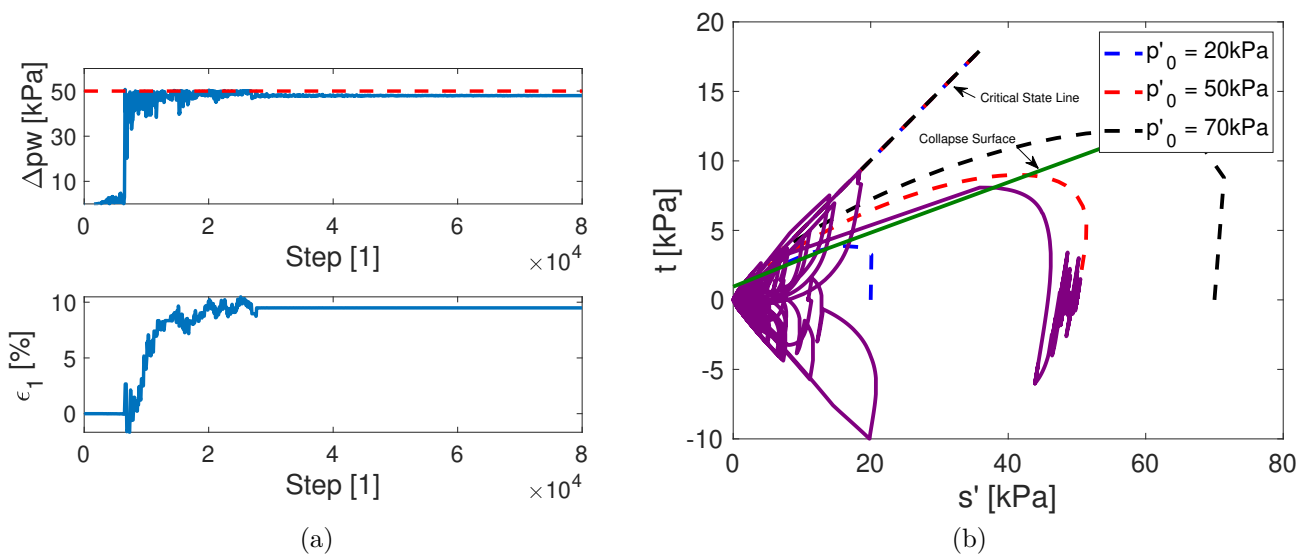


Figure 1.18: a) The variation of  $\Delta p_w$  (top) and  $\varepsilon_1$  (bottom) and b) the stress path of the irregular loading of *Mat.1*

In applications of earthquake engineering, for practical purposes, recorded seismic motions can be represented by an equivalent acceleration time history of a given amplitude that is generally equal to 60% of the peak acceleration level of the seismic signal, the specific frequency and the specific number of cycles (Seed and Idriss, 1971; Sladen et al., 1985; Kramer, 1996; Youd and Idriss, 2001; Hancock and Bommer, 2005; Castiglia and Santucci de Magistris, 2018, among others). Many researchers have proposed that the effective number of cycles of the ground

motion is a more robust indicator of the destructive capacity of the shaking than the duration (Hancock and Bommer, 2005). For this purpose, two approaches to calculate the number of cycles are proposed and shown in Figure 1.19. The effective number of cycles  $N_{eff}$  is the half the number of half waves above  $0.6 \tau_{max}$  inspired from Sassa and Yamazaki (2016). In addition, from the viewpoint of counting cycles in fatigue, the number of cycles of the irregular loading  $N_{equiv}$  is calculated (Rychlik, 1987; Nieslony, 2009). It is also called the rainflow counting because of its comparison to the flow of rain falling on a pagoda and running down the edges of the roof.

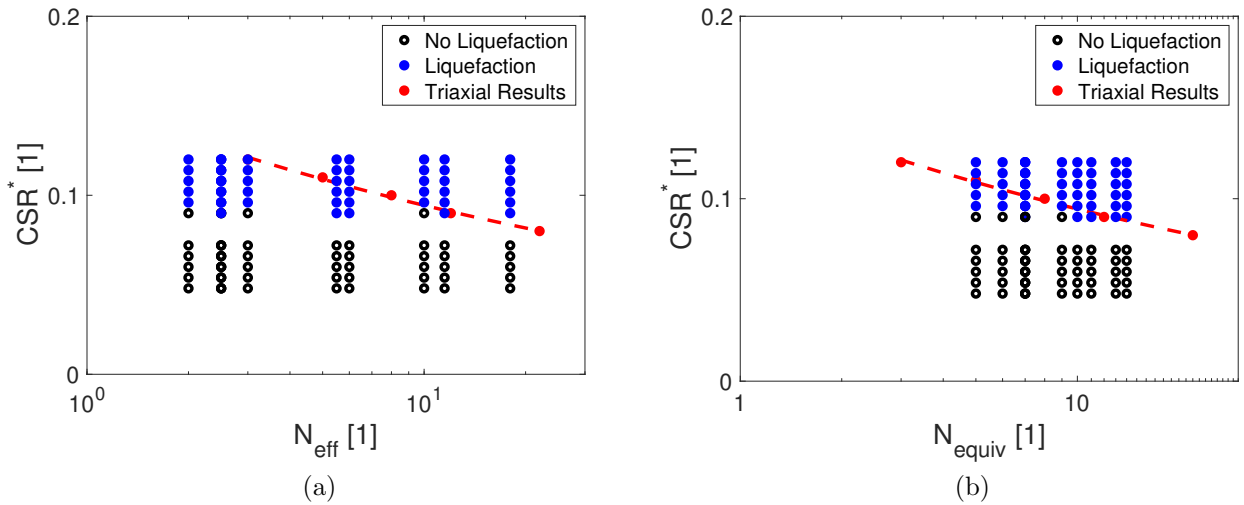


Figure 1.19: The different methods for the number of cycles

The results of this figure are in agreement of Hancock and Bommer (2005) that among the generic definitions of the number of cycles, the rainflow counting definition  $N_{equiv}$  has the merit considering as the number of cycle for an irregular load. Hence, the cyclic stress ratio becomes  $CSR^* = q_{cyc}/2 \cdot p'_0$  with  $q_{cyc} = 0.6 \cdot q_{cyc,max}$ . The results are shown in Figure 1.20a. The grey dots designate the non-liquefied cases on the opposite of the blue dots that designate the liquefied cases. The red curve on Figure 1.20a is the boundary generated by the experimental data results developed in Section 1.3. From Figure 1.20a, it can be seen that the increase in the cyclic stress affects the liquefaction occurrence for *Mat.1*. The cases that are below the boundary did not mostly liquefy, on the opposite to the cases above the boundary that shows liquefaction. However, the boundary of the experimental tests for *Mat.2* underestimated the resistance of the soil, since very few cases above the red curve liquefied.

It can be partially concluded that the laboratory tests may under-estimate the soil response because the cases that were predicted to liquefy, did not do as such in the actual scenario. To be more consistent with the realistic scenarios, in the next section, the *in-situ* soil response will be studied from a seismic analysis on a soil column. Moreover, the liquefaction triggering will also be examined in this case.

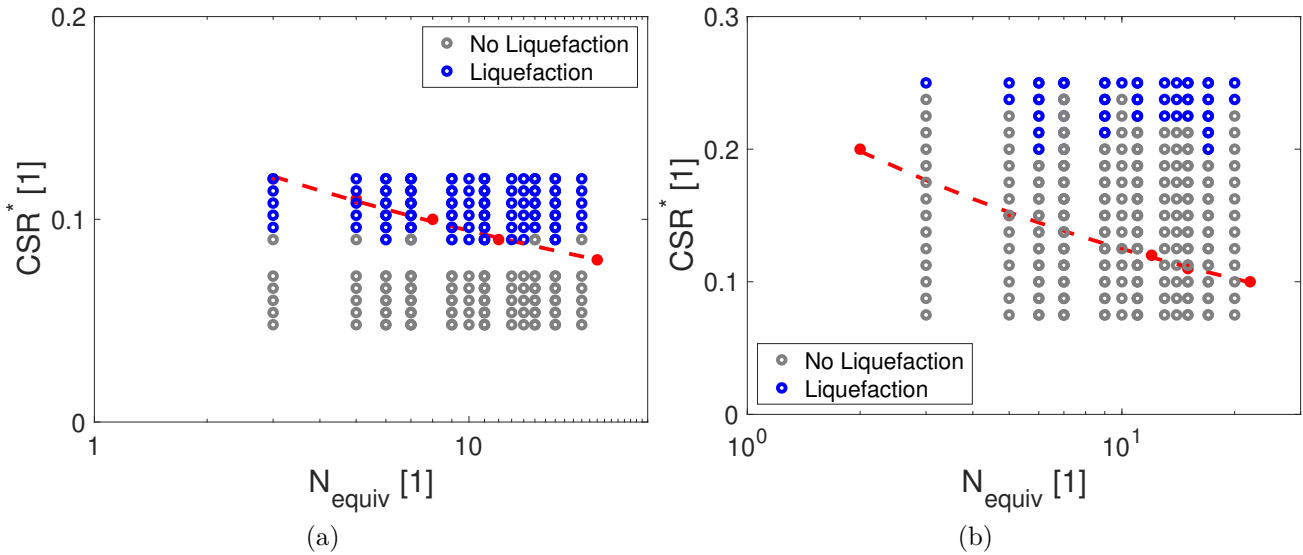


Figure 1.20: Cyclic stress ratio  $CSR^*$  for the case of irregular loading for a) *Mat.1* and b) *Mat.2*

## 1.9 *In-situ* response - Study on a column

In the previous sections, the behavior of two soil samples was studied from simulated laboratory experiments. The effect of irregular loading was taken into consideration in order to better approach the realistic case of a soil subjected to earthquake, and hence to characterize the liquefaction triggering. It was shown that *Mat.1* is more susceptible to liquefaction than *Mat.2*. Thus, this material will form the shallow layer of a 1D column and its behavior will be analyzed after several seismic inputs. To take into account the dynamic effect, 447 different recorded ground motions were used. The same elastoplastic multi-mechanism model is used to represent the soil behavior.

This section will develop the results issued from possible in-situ tests for two seismic inputs as an example. In addition, a comparison between the predicted and the observed results between the laboratory and the *in-situ* tests will be discussed.

### 1.9.1 Geometry and finite element model

The column geometry, shown in Figure 1.21, is composed of 4 m of *Mat.1* and 6 m of a dense sand. The numerical computations were conducted with a 2D coupled FE modelling with GEFDyn Code (Aubry et al., 1986), using a dynamic approach derived from the  $\underline{u} - p_w$  version of the Biot's generalized consolidation theory (Zienkiewicz, 1991). The FE model is composed of quadrilateral isoparametric elements with eight nodes for both solid displacements and fluid pressures. The element size is 0.5 m horizontally and 0.5 m vertically. An implicit Newmark numerical integration scheme with  $\gamma = 0.625$  and  $\beta = 0.375$  and a time step  $\Delta t = 10^{-3}$  was assumed in the dynamic analysis (Kuhl and Crisfield, 1999). Only vertically incident shear waves are introduced into the domain and as the response of an infinite semi-space is modelled, equivalent boundaries have been imposed on the nodes of lateral boundaries (i.e. the normal

stress on these boundaries remains constant and the displacements of nodes at the same depth in two opposite lateral boundaries are the same in all directions). For the half-space bedrock's boundary condition, paraxial elements simulating deformable unbounded elastic bedrock have been used (Modaressi and Benzenati, 1994). The incident waves, defined at the outcropping bedrock are introduced into the base of the model after deconvolution.

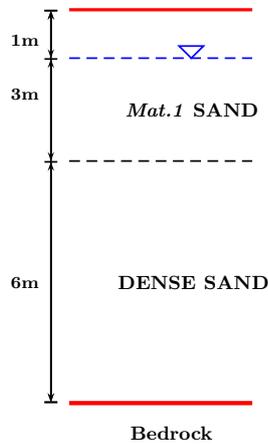


Figure 1.21: The column geometry

### 1.9.2 Analysis of the *in-situ* soil response

Typical to any conducted seismic analysis, the co-seismic damage and soil behavior will be evaluated. The damage index, represented by the vertical settlement  $u_z$ , is calculated as to evaluate possible structure existence. The behavior of the tested material is evaluated at 3 m depth, represented by the shear stress and strain  $\tau - \gamma$  curve. The liquefaction occurrence is evaluated all over the depth of the column and is represented by the excess pore water pressure ratio  $r_u$  (i.e.  $= \Delta p_w / p'_0$ ). As to take into consideration the cyclic mobility and the true liquefaction, it is assumed that liquefaction appears when  $r_u > 0.8$  (Rapti et al., 2018). The evolution in time of the parameter  $r_{apt}$  is also evaluated for the depth of the column. For the sake of brevity only, two ground motions will be taken as an example. The weak one has an outcrop acceleration  $a_{max,out}$  of 0.1 g (Figure 1.22) and the strong motion has  $a_{max,out}$  of 0.7 g (Figure 1.23).

For the co-seismic vertical settlement  $u_z$  of the weak motion in Figure 1.22, it increases with time until reaching a constant value at the end of the shaking. As for the soil behavior, and at 3 m depth, the shear stress and strain  $\tau - \gamma$  curve shows irregular shapes and an increase in the deformation during time. For the liquefaction occurrence of this seismic input example, it can be seen from the  $r_u$  values that the soil did not liquefy during time;  $r_u$  did not reach the value of 0.8. The parameter  $r_{apt}$  has also small values in the two soil layers, which indicates that instability did not occur during the co-seismic time of this example. It should be mentioned that for the dense sand, it appears to have weird values at the beginning of the motion, but after serious checks, those values are maybe due to the boundary conditions.

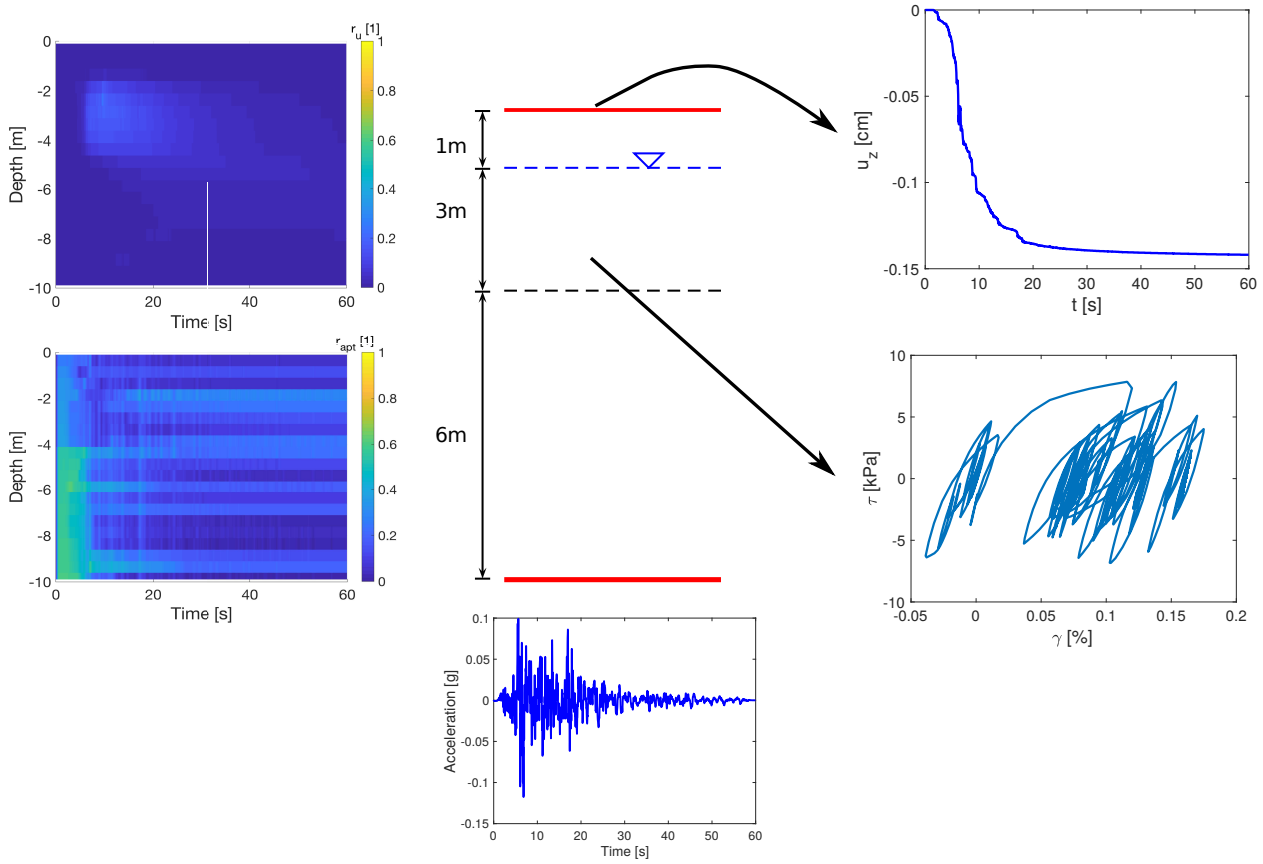


Figure 1.22: The results analysis of the weak motion ( $a_{max,out} = 0.1$  g)

For the strong ground motion represented in Figure 1.23, it is clear that the induced damage increases with time and the value of  $u_z$  reached is more important than the previous example. For the soil behavior at 3 m depth, the  $\tau - \gamma$  curve shows hysteresis loops. As for the liquefaction occurrence, it is clear from the values of  $r_u$  that the dense sand did not liquefy, however, for the loose sand,  $r_u$  surpassed 0.8 around 60 seconds. After reaching this peak,  $r_u$  decreases as a result of the dissipation of the excess pore water pressure. In parallel, the parameter  $r_{apt}$  was higher than its threshold limit during the co-seismic time indicating instability zones. However, at the end of the motion, this value decreases showing a “densification” of the soil.

In order to understand and examine the evolution in time of the parameter  $r_{apt}$  in the liquefiable layer, Figure 1.24 shows the values of  $r_{apt}$  at 3m depth for two seismic inputs. Clearly, in Figure 1.24a, instabilities did not occur since the threshold limit was not reached. However, in Figure 1.24b,  $r_{apt}$  exceeds 0.75 during time and the soil did not recover at the end of this example motion, as an indicator of an instability occurrence.

After understanding the co-seismic *in-situ* response of the soil, an evaluation of the *predicted* responses from the laboratory tests with that *observed* from the numerical model will be conducted in the coming section, as to compare the liquefaction triggering prediction of each test.

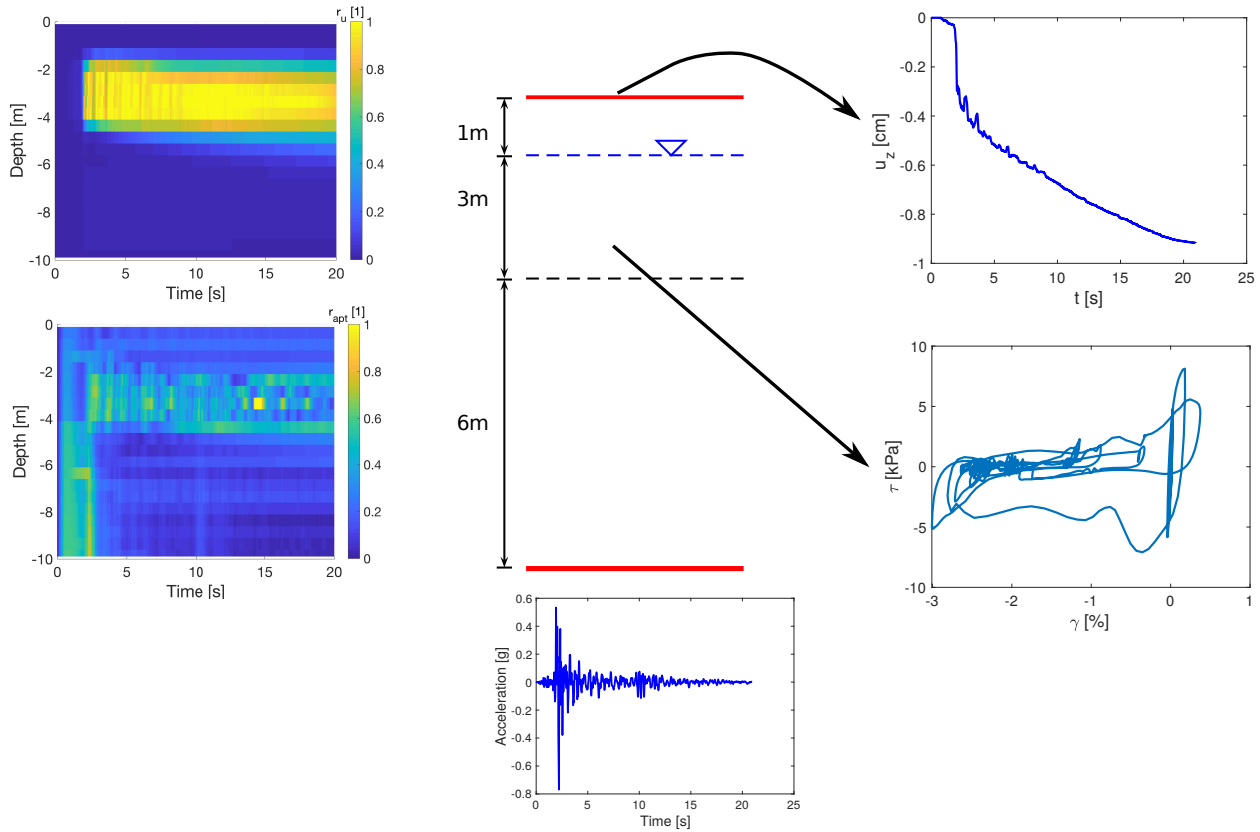


Figure 1.23: The results analysis of the strong motion ( $a_{max,out} = 0.7$  g)

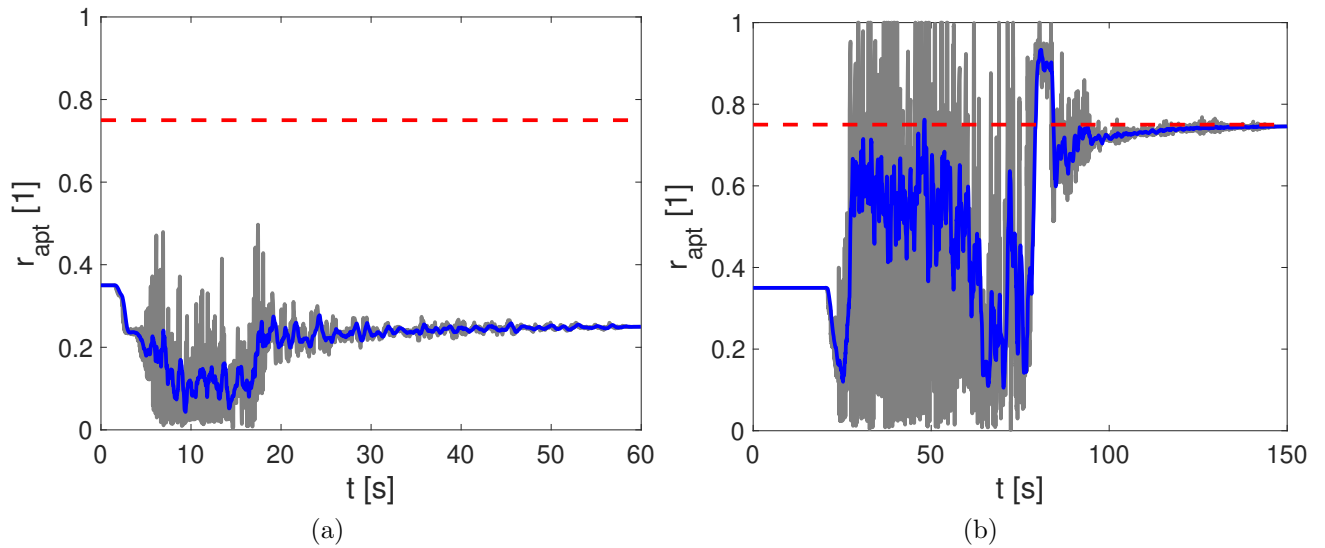


Figure 1.24: The values of  $r_{apt}$  at 3m depth for two seismic inputs

### 1.9.3 Accuracy of the laboratory tests with respect to the *in-situ* tests

In order to take into account all the tested ground motion and characterize the liquefaction occurrence from the *in-situ* test results, the cyclic stress ratio is calculated for 447 ground motions. Laboratory tests show that the cyclic shear stress required to trigger liquefaction

increases at high effective confining pressures (Kramer, 1996). Seed and Idriss (1971) and Youd and Idriss (2001) suggested correction factors to take into account the effect of the initial shear stress (i.e.  $K_\alpha$ ) and the effective overburden pressure (i.e.  $K_\sigma$ ). The field corrected cyclic stress ratio for the case of this study is shown as a green curve in Figure 1.25a. This curve will be considered as the new boundary for the coming tested cases. The cyclic stress ratio was calculated similar to the case of irregular loading described in Section 1.8, in addition to the same definition of the number of cycles (i.e.  $N_{equiv}$ ). Liquefaction triggering was identified from the excess pore water pressure ratio. The motions that did not liquefy are represented in grey and the ones that did, are shown in blue.

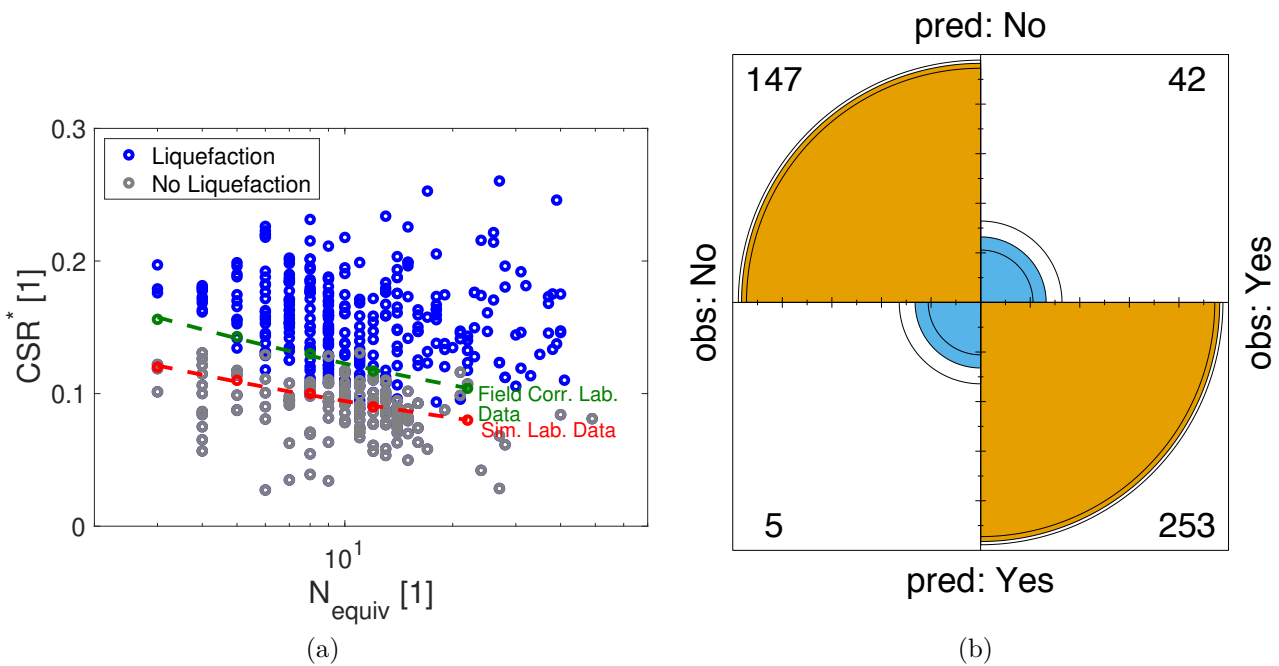


Figure 1.25: a) The cyclic stress ratio of the tested motions and b) the confusion matrix of the tested motions

It can be seen from Figure 1.25a that there exist some cases where liquefaction did not occur above the field corrected boundary. In addition to cases where liquefaction occurred below the boundary. Hence, in order to better understand the accuracy of the laboratory tests, confusion matrix is drawn and shown in Figure 1.25b. The concept of the confusion matrix and what it represents are explained in Appendix C.1. In this study, the purpose of this matrix is to summarize the performance of the soil based on both the actual observations (i.e. column finite element simulations) and the predicted observations (i.e. *virtual* laboratory tests). From Figure 1.25b, 147 cases are not supposed to liquefy based on the predicted laboratory test and actually, they did not liquefy. These cases are called the True Negative (TN) results. Also, 253 cases are supposed to liquefy, and they liquefied based on the actual observations. Hence, they are the True Positive (TP). On the contrary, 5 cases located above the field corrected boundary did not liquefy based on the actual observations and they are called the False Positive (FP)

data. And finally, the False Negative (FN) data (i.e. 42 cases) are the ones that were not supposed to liquefy since their cyclic stress ratio is below the field corrected boundary, but based on the actual observations, they liquefied. The FN data are considered as a dangerous case for the decision making. They underestimated the response of the soil because the soil that did not liquefy in the laboratory, had a different behavior in field. The FP data are also not beneficial for the decision maker since in the laboratory the soil sample liquefied whereas when the wave propagated in the realistic case, the soil did not liquefy. This means that unnecessary precautions could be set in field if there was a reference to laboratory tests only. The accuracy between the laboratory and the finite element method in this case is 89.49% (i.e.  $(TN+TP)/(TN+TP+FN+FP)$ ).

A partial conclusion can be deduced from this section is that the laboratory tests, in some cases, under-estimate the response of the soil. Validation between laboratory and numerical tests is an ideal procedure to represent the global behavior of the soil and the structure of concern. It is interesting to mention that the limitation to a 1D soil column is not fully representative, for this purpose, the coming chapters will develop the performance of a 2D model, composed from the aforementioned soil layers with a geo-structure.

## 1.10 Concluding remarks

Virtual laboratory tests were simulated in this chapter via an elastoplastic multi-mechanism soil behavior model with the help of a finite element code (GEFDyn). These tests are useful in case experimental data are not available or there is a need to predict the behavior of the soil in field. They can also validate the laboratory tests and help for a better understanding of the global response of the soil. Thus, two soil samples were tested. At the beginning their behavior was identified from simulated triaxial tests as well as regular loading to trigger liquefaction. The effect of the initial state of the soil and its history of loading were emphasized in this chapter. In addition, for a better estimation of the realistic scenarios, earthquake loading were applied on the soil samples and the change in the soil behavior was analyzed. In the final section, the *in-situ* response of the soil was simulated from a 1D column after the propagation of 447 real input motions. Finally, an accuracy study between the laboratory and the finite element methods was conducted with the help of confusion matrix.

The results have shown that the soil sample used later as a foundation (*Mat.1*) is loose and has an ability to liquefy rapidly on the contrary to the second sample that had a higher resistance to liquefaction. The cyclic resistance of the samples created a reference boundary for liquefaction triggering. It was shown based on the application of irregular loads that this boundary can sometimes underestimate the resistance of the soil sample (the case of *Mat.2* for example).

Concerning the *in-situ* response, the results of the soil resistance show that below a field corrected boundary, the soil may liquefy whereas above it, the response will also depend on the

severity of the earthquake.

As a conclusion, the laboratory tests in some cases, underestimate the soil response but they are somehow accurate with the finite element models. Hence, for a decision making and to a good estimation of the soil response, performing experimental and numerical tests together will be more accurate.

# Chapter 2

## The use of real and synthetic earthquakes as input to dynamic analysis

### Contents

---

<b>2.1</b>	<b>Introduction</b>	<b>38</b>
<b>2.2</b>	<b>Geometry and soil model</b>	<b>41</b>
2.2.1	Geometry	41
2.2.2	Soil constitutive model	41
2.2.3	Finite element model	42
2.2.4	Boundary conditions	43
2.2.5	Elastic behavior	43
<b>2.3</b>	<b>Input ground motion</b>	<b>44</b>
<b>2.4</b>	<b>Distribution of Intensity Measures IM</b>	<b>46</b>
<b>2.5</b>	<b>Damage measure and soil mechanical behavior</b>	<b>49</b>
<b>2.6</b>	<b>Link between EDP and IM</b>	<b>54</b>
<b>2.7</b>	<b>Fragility curves</b>	<b>57</b>
<b>2.8</b>	<b>Concluding remarks</b>	<b>59</b>

---

## Abstract

The Pacific Earthquake Engineering (PEER) Center has developed a framing equation to study the probabilistic evaluation of the system-level performance of structures due to earthquakes. The proposed framework is based on the convolution of all levels of seismic hazard, fragility and losses.

The purpose of this chapter is to evaluate the probability of the performance level of an embankment subjected to earthquakes. The use of real and synthetic seismic inputs is going to be tested. The engineering demand parameter as well as the fragility exposure of the structure of concern are going to be evaluated.

This chapter is partially adapted from two publications on a similar embankment:

*Khalil, C., Rapti, I., and Lopez-Caballero, F. (2017). Numerical Evaluation of Fragility Curves for Earthquake-Liquefaction-Induced Settlements of an Embankment. In Geo-Risk 2017 , GSP 283, 21-30*

*Khalil, C., and Lopez-Caballero, F. (2019). Effect of synthetic ground motions on the liquefaction induced settlements. In ICASP13: 13th International Conference on Applications of Statistics and Probability in Civil Engineering, page Paper 232, Seoul, South Korea*

## 2.1 Introduction

The seismic performance-based design requires the evaluation of the mean annual rate of exceeding different levels of loss due to the occurrence of earthquakes. For this purpose, a framing methodology is proposed by the Pacific Earthquake Engineering Research and is based on the convolution of all levels of ground motion, structural damage and loss (better known as seismic hazard, fragility and exposure). This methodology is called the Performance-Based Earthquake Engineering, PBEE and is presented in Figure 2.1.

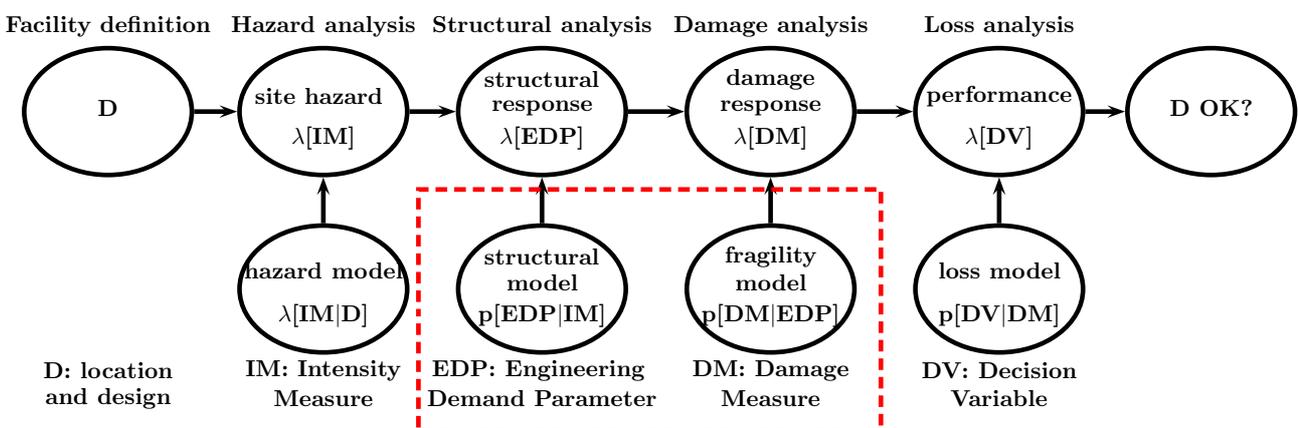


Figure 2.1: The steps of the Performance Based Earthquake Engineering methodology

In the scope of the PBEE, an identification of the Intensity Measure (IM) is essential in order to evaluate the performance of the concerned structure. For this purpose, a seismic

hazard analysis is needed in which the ground motion (GM) characteristics at a particular site are identified through a Probabilistic Seismic Hazard Analysis (PSHA). This method combines the uncertainties in the earthquake characteristics to obtain the probability that any IM will be exceeded at a particular time period. The level of shaking produced from this analysis comes from the contribution of the magnitude  $M$ , the source to-site distance  $R$  and often the deviation of the GM from the predicted value  $\varepsilon$  (Bazzurro and Allin Cornell, 1999; Watson-Lamprey and Abrahamson, 2006; Rathje and Saygili, 2011; Pitilakis et al., 2012; Causse et al., 2014a; Iervolino et al., 2015, among others). The mean annual rate of exceedance  $\lambda_{IM}$  at a site of specified level  $im$  takes the following form:

$$\lambda_{IM}(im) = \lambda(M \geq M_{min}) \int \int \int P[IM > im|m, r, \varepsilon] \cdot f(m, r, \varepsilon) \cdot dm dr d\varepsilon \quad , \quad (2.1)$$

where  $\lambda(M \geq M_{min})$  is the mean annual rate of occurrence of earthquakes with a magnitude greater than some specified lower bound  $M_{min}$ ,  $P[IM > im|m, r, \varepsilon]$  is the probability that IM will exceed  $im$  at a given location for a given set of source parameters  $(m, r, \varepsilon)$  and  $f(m, r, \varepsilon)$  is the joint probability density function of  $m$ ,  $r$  and  $\varepsilon$ . After defining the main aspects that characterize the local seismic hazard, it is possible to proceed with the selection of time histories. This later step is important for geotechnical earthquake engineering problems because it is strongly related to the nonlinear dynamic analysis. An adequate definition of the seismic input is needed in order to choose the nonlinear time history dynamic analysis (Schwab and Lestuzzi, 2007). Nevertheless, a large number of database is required in order to conduct such analysis. In this context, both recorded and synthetic earthquakes can be used. However, sometimes, recorded data resources are not available (i.e. not enough data for high magnitudes ground motions) or inadequate to characterize the site of concern (i.e. near-fault ground motions, basin effects) (Stewart et al., 2002; Luco and Cornell, 2007; Seyedi et al., 2010; Sáez et al., 2011; Wang et al., 2020). For this reason, calibrations can be used to adjust recorded ground motions and to make them more representative of the analysis conditions (Stewart et al., 2002; Schwab and Lestuzzi, 2007; Yamamoto and Baker, 2013, among others). Different ground motion models (i.e. stochastic, composite source method, among others) exist in order to create artificial or synthetic earthquakes that are able to represent particular conditions (Douglas et al., 2009; Yamamoto and Baker, 2013).

Once the hazard analysis is known, the performance of the structure is identified in terms of the probability distribution functions of the Engineering Demand Parameter (EDP). The mean annual rate of exceeding a given level  $z$  of EDP is  $\lambda_{EDP}(z)$  and is given by:

$$\lambda_{EDP}(z) = \int P[EDP \geq z|IM = im] \cdot \lambda_{IM}(im) \cdot dim \quad . \quad (2.2)$$

The term  $P[EDP \geq z|IM = im]$  represents the probability of exceeding a specified EDP level  $z$  given a specified level  $im$  of IM.

A key issue in the performance-based design is its credibility in assessing a seismic damage potential (Cosenza and Manfredi, 2000). Thus, a reliable definition of seismic intensity has to relate the effect of damage on structural behavior (Equation 2.2). This site-specific approach is important in order to assess the potential seismic hazard and to classify the seismic input.

On the other hand, the EDP should represent a structural damage measure. It corresponds to a quantifiable measurement of the damage that represents the global potential of system failure. Traditionally, the probability of failure for levels of EDP is calculated through fragility curves (Sáez et al., 2011; Sfahani et al., 2015; Khalil et al., 2017; Zentner, 2017; Oblak et al., 2020, among others). It is independent of the hazard analysis, thus, it is a structure-specific approach.

Furthermore, soil liquefaction problems have never been old-fashioned in engineering practices. Liquefaction is still a major source of damage to buildings and infrastructure after major earthquake events. The performance of geo-structures after this phenomena has been studied through experimental (Brennan and Madabhushi, 2002; Zeybek and Madabhushi, 2019; Byrne et al., 2004; Dashti et al., 2010; Maharjan and Takahashi, 2014; Tiznado et al., 2020, among others) or numerical approaches (Koutsourelakis et al., 2002; Elgamal et al., 2002; López-Querol and Blázquez, 2006; Huang et al., 2008; Xia et al., 2010; Lopez-Caballero and Modaressi-Farahmand-Razavi, 2010, 2013; Lopez-Caballero et al., 2016; Rapti et al., 2018; Oblak et al., 2020, among others). The principal conclusion of these works is that the characterization of the soil liquefaction depends on the input signal and the properties of the soil.

The purpose of this study is to evaluate the seismic response of a liquefiable foundation. A large number of seismic inputs is required, thus, the effect of both recorded and synthetic earthquakes is studied in this chapter. This analysis will consist of the seismic response rather than the seismic model. Thus, the effect of both types of motions will be analyzed by the calculation of the potential structural failure. To this end, the significant questions that this chapter is trying to answer are the following:

- a) Are the chosen synthetic ground motions representative of the chosen real motions ?
- b) How to calculate the global and local damage measures of the concerned structure?
- c) How does the ground motion type (real or synthetic) affect the global response of the concerned structure?
- d) Are the obtained fragility curves of the structure affected by the seismic inputs?

To answer these questions, the methodology of the PBEE is analyzed from the parts designated in red in Figure 2.1. The geometry model is an embankment and an elastoplastic multi-mechanism soil behavior model is used in the 2D finite element simulations.

## 2.2 Geometry and soil model

### 2.2.1 Geometry

The geometry of the model is a levee of 9 m high composed of dry dense sand. The foundation is formed of 4 m loose to medium sand (LMS) on the top of a 6 m dense sand. The bedrock is located under the dense sand. The water table is placed at 1 m below the surface to keep the embankment dry. The inclination of the levee is a slope of 1:3 (vertical: horizontal). The geometry in this work is inspired by [Rapti et al. \(2018\)](#); [Lopez-Caballero and Khalil \(2018\)](#), and is detailed in Figure 2.2.

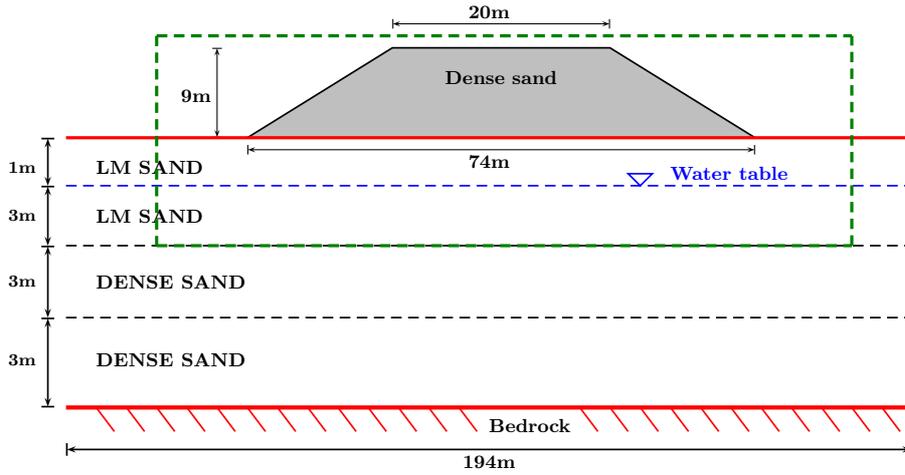


Figure 2.2: Geometry of the embankment inspired by [Rapti et al. \(2018\)](#); [Lopez-Caballero and Khalil \(2018\)](#)

### 2.2.2 Soil constitutive model

As for the constitutive model, the *Ecole Centrale Paris (ECP)* elastoplastic multi-mechanism model (also known as *Hujeux* model) is the one chosen for this study and is written in terms of effective stress. The non-linearity of this model is represented by four coupled elementary plastic mechanism: three plane-strain deviatoric plastic strain mechanism in three orthogonal planes ( $k$  - planes) and an isotropic plane. The model follows a Coulomb type failure criterion, contemplate the existence of dilatancy/contractancy phenomena, and use the critical state concept. The cyclic behavior is taken into account by a kinematical hardening that is based on the state variables at the last load reversal. The model is written in the concept of the incremental plasticity which divides the total strain into an elastic and a plastic part. For the sake of brevity only, the yield surface definition is presented in the following, however, more details are presented in Appendix A. Considering the well-known sign convention of the soil mechanics which sets the positive sign to the compression forces, the yield surface of this numerical model is written in the  $k$  plane as follows:

$$f_k(\sigma, \varepsilon_v^p, r_k) = q_k - \sin \phi'_{pp} \cdot p'_k \cdot F_k \cdot r_k, \quad (2.3)$$

where  $p'_k$  and  $q_k$  are the effective mean and deviatoric values of the stress tensors and  $\phi'_{pp}$  is the friction angle at the critical state. The variables that control the behavior of the soil are  $F_k$ , which controls the isotropic hardening associated with the plastic volumetric strain and  $r_k$ , which controls the isotropic hardening generated by the plastic shearing. These two parameters represent progressive friction mobilization in the soil.

### 2.2.3 Finite element model

The computations were conducted by the coupled FE modelling code GEFDyn (Aubry et al., 1986), using a dynamic approach derived from the  $\underline{u} - p_w$  version of the Biot's generalized consolidation theory (Zienkiewicz, 1991). The 2D FE model is composed of quadrilateral isoparametric elements with eight nodes for both solid displacements and fluid pressures. In this work, two different embankment models with different mesh sizes were selected in order to choose the one with the least computational time. For this purpose, varied earthquake scenarios were selected without care of their type or origin. The tested mesh sizes were  $0.5 \text{ m} \times 0.5 \text{ m}$  for the fine mesh and  $3.5 \text{ m} \times 1 \text{ m}$  for the coarse mesh. The CPU time per earthquake duration of each model is represented as boxplots in Figure 2.3a. Clearly, for the smaller model (i.e. less DOF), the CPU time varies between 1.3 and 1.5 min per seconds of earthquake duration. This means that for an earthquake with a typical duration of 30 seconds, the computational time is approximately 40 to 45 min. On the opposite, it takes 6 to 7 hours for a larger 2D model for an earthquake with the same duration. As for the response of the embankment (Figure 2.3b), it should be first mentioned that the details regarding the calculation and the choice of this parameter (i.e. relative crest settlement  $\delta u_{z,rel}/H$ ) will be explained later on in this work. It is clear from this figure that the damage index of both models is the same. Thus, for this work, the considered mesh sizes to conduct the necessary computations will be  $3.5 \text{ m} \times 1 \text{ m}$ .

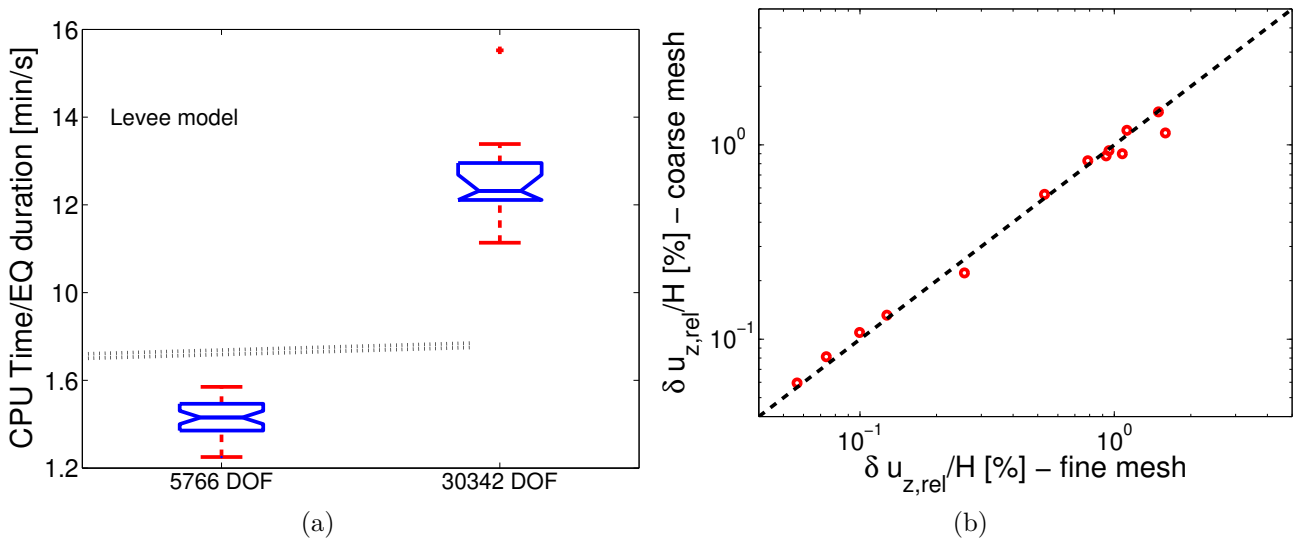


Figure 2.3: a) The CPU time of two different levee models and b) the damage index for the types of meshes (to be explained later on in this chapter)

An implicit Newmark numerical integration scheme with  $\gamma = 0.625$  and  $\beta = 0.375$  and a time step  $\Delta t = 10^{-3}$  was assumed in the dynamic analysis (Kuhl and Crisfield, 1999). The FE analysis is performed in three consecutive steps: i) a computation of the initial *in-situ* stress state due to gravity loads; ii) a sequential level-by-level construction of the embankment and iii) a sequential seismic loading analysis in the time domain.

## 2.2.4 Boundary conditions

In the analysis, equivalent boundaries have been imposed on the nodes of lateral boundaries (i.e., the normal stress on these boundaries remains constant and the displacements of nodes at the same depth in two opposite lateral boundaries are the same in all directions). They are the response of a modeled infinite semispace. Hence, only vertically incident shear waves are introduced into the domain. The model is wide enough (194 m) to ensure that the effect of the boundaries on the response of the model can be neglected and also to satisfy the free field condition at the lateral boundaries. For the half-space bedrock's boundary condition, paraxial elements simulating deformable unbounded elastic bedrock have been used (Modaressi and Benzenati, 1994). The incident waves, defined at the outcropping bedrock are introduced into the base of the model after deconvolution.

## 2.2.5 Elastic behavior

In order to examine the fundamental frequency of the soil-embankment system and its shear wave velocity  $V_s$  distribution (i.e.  $= \sqrt{\frac{G}{\rho}}$ ,  $G$  being the shear modulus and  $\rho$  the total mass density), a small amplitude ground motion propagated in the medium ( $PGA = 1.5 \cdot 10^{-5} \text{ m/s}^2$ ). The results are drawn under the crest of the embankment and at free field. The transfer function is drawn in Figure 2.4a and the variation in depth of  $V_s$  is represented in Figure 2.4b. Based on the represented transfer function, it can be seen that the presence of the embankment affected the response since the fundamental frequency is higher at the crest than at free field. The fundamental frequency of the whole system (red curve) is 4.44 Hz whereas that of the soil is 6.54 Hz. As for the variation in depth of  $V_s$ , the results show that the  $V_s$  increases with depth. It is higher under the embankment center due to its weight.

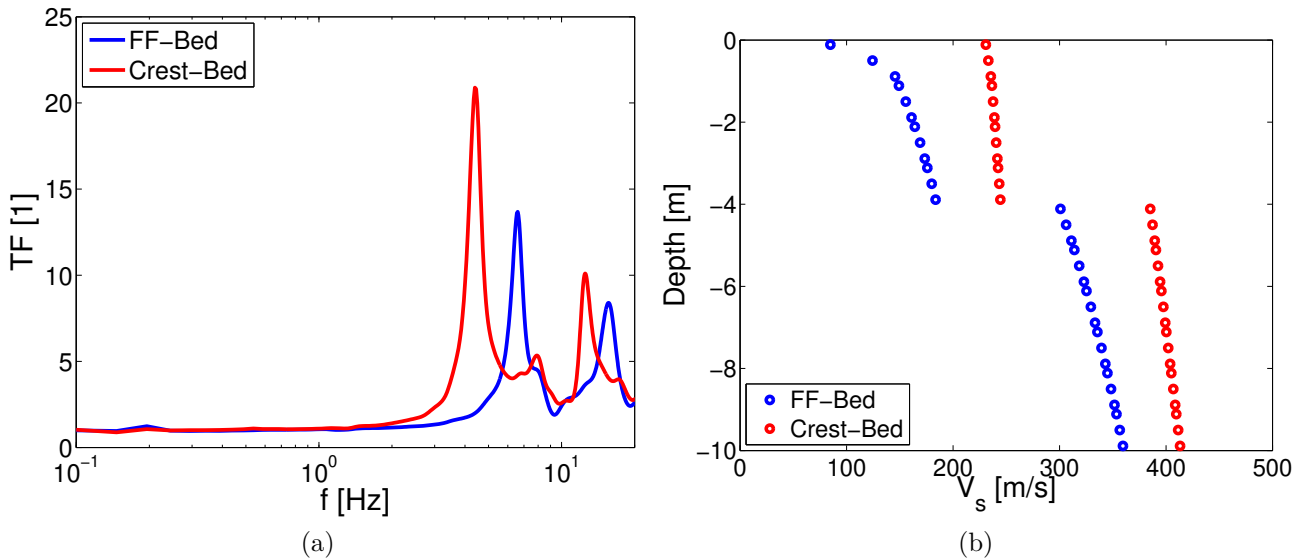


Figure 2.4: a) The transfer function and b) the variation in depth of the shear wave velocity of the embankment

## 2.3 Input ground motion

In order to analyze the non linear behavior of the soil, and in the scope of the performance-based design, large number of input ground motions (GMs) should be selected. Based on literature, several methods exist for calibrating synthetic motions for a specific earthquake scenarios. These calibrations are used to adjust recorded GMs to make them more representative of the analysis conditions or when actual recordings are sparse (Stewart et al., 2002; Yamamoto and Baker, 2013, among others). For the scope of this study, the stochastic simulation technique, conducted from different models, is the one used to generate synthetic GMs. This technique tends to directly simulate the recorded motions with varied characteristics including the variability of the GM (Sabetta and Pugliese, 1996; Boore, 1996; Pousse et al., 2006; Rezaeian and Der Kiureghian, 2012; Yamamoto and Baker, 2013, among others). In addition, it requires few parameters and is less expensive than other methods.

Three synthetic ground motion models (SGMM) were used for this study to develop the stochastic simulation technique: the one conducted by Yamamoto and Baker (2013), designated as “*BKx*”, the one of Rezaeian and Der Kiureghian (2012), designated as “*RZx*” and finally the SGMM of Zentner and Poirion (2012) designated as “*CAx*” and “*CAy*”. It is interesting to mention that the chosen codes are free access. The *BKx* SGMM, consists of the method of wavelet packet transform (WPT) to generate artificial ground response compatible with a target pseudovelocity response spectrum, and having non-stationary time-frequency (Yamamoto and Baker, 2013). This method requires the use of 13 parameters that are linked through regression analysis to the characteristics of the earthquake motion, such as the magnitude and distance. As for the *RZx* SGMM, the method consists in rotating the recorded ground motion pairs into their principal axes. The parameters of the model are identified by fitting to each recorded

pair in the new database (Rezaeian, 2010; Rezaeian and Der Kiureghian, 2012, among others). Concerning the  $CAx$  and  $CAy$  SGMM, the method consists in generating ground motion time histories that have statistical properties compatible with the recorded accelerograms based on the method of Karhunen-Loeve (Zentner and Poirion, 2012). For the sake of brevity, the details of each stochastic model are omitted, it is recommended to refer to each cited paper for more information.

Furthermore, to compare the accuracy of the synthetic ground motions on the structural response, real ground motions are also used. They are designated as  $RL$  and  $RM$ .  $RL$  are motions with a moment magnitude ( $M_w$ ) of 7.0 and a hypocentral distance ( $R$ ) of 40.0 km (Isbiliroglu, 2018). And  $RM$  are real motions of events ranged between 5.2 and 7.6 in magnitude with a site-to-source distances from 15 to 50 km. Table 2.1 summarizes the types and numbers of the motions used and generated for this work.

Name	Type	Number	Faulting	$V_{s,30}$ (m/s)
RM	Real	296	Strike-Slip	100-600
RL	Real	88	Strike-Slip	100-600
BKx	Synth	50	Strike-Slip	700
RZx	Synth	50	Strike-Slip	760
CAx	Synth	50	Strike-Slip	800
CAy	Synth	50	Strike-Slip	800

Table 2.1: The characteristics of the used ground motions for this study

Concerning the response spectra of input earthquake motions, Figure 2.5 shows the median of the response spectra curves (structural damping  $\xi = 5\%$ ) of the input motions. However, it is interesting to note that the response spectra of the selected motions are close. Nevertheless, to overcome the numerical uncertainties, all input signals have a baseline correction, a sampling time ( $\Delta t$ ) equal to 0.005 s and they are filtered using a non-causal 4th-order Butterworth bandpass filter (i.e. Zero-phase digital filtering) between 0.1-25 Hz.

After this small introduction about the real and synthetic ground motion models used in this chapter, the PBEE methodology will be applied as to first introduce an intensity measure (IM). Then, the distribution of the different IMs will be compared for all the used ground motions.

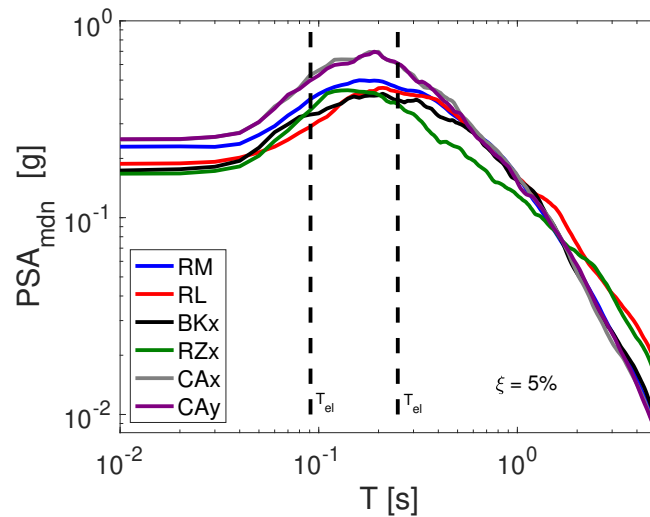


Figure 2.5: The median spectral responses of the tested ground motions

## 2.4 Distribution of Intensity Measures IM

According to the PBEE methodology, the distribution of the ground motion IMs is linked to the EDP through probabilistic approaches, to obtain a damage measure due to seismic events (Stewart et al., 2002; Porter, 2003, among others). As mentioned in Section 2.3, a series of real and synthetic ground motions was selected to compare the ground response. The choice of artificial ground motions should be consistent with the physical conditions and characteristics of the recorded ground motions (Yamamoto and Baker, 2013). First of all, a comparison of the peak ground acceleration (PGA) of the used GMs is conducted from the cumulative distribution function (CDF) in Figure 2.6a. Thus, “Real” motions in this figure refer to *RL* and *RM* whereas “Syn” motions refer to all the sets of synthetic motions used in this chapter.

It can be seen from the distribution of *PGA* in Figure 2.6a that the chosen real and synthetic motions are close for small values of *PGA* and slightly different for large values of *PGA*. Concerning the probabilistic distribution of each ground motion, Figure 2.6b shows the empirical density distribution function in terms of *PGA*. It is clear from this figure, that the ground motions can be divided into two groups based on the similarity of their distribution functions. Thus, *CAx*, *CAy*, *RM* and *RL* form one group and *RZx*, *BKx* form another group.

In order to take into account the distribution of different ground motion parameters (other than *PGA*), Figure 2.7 shows a matrix form of a logarithmic comparison of the peak ground velocity *PGV*, the Arias Intensity ( $I_a$ ) and the equivalent predominant frequency  $1/T_{va}$  of the real and synthetic GMs. These parameters are chosen exclusively because they control the response of the structure (Kawase, 2011; Lopez-Caballero and Modaressi-Farahmand-Razavi, 2013; Lopez-Caballero and Khalil, 2018, among others). As for the other parameters, they are presented in Appendix D. The comparison is conducted in terms of the density functions located in the diagonal of the matrix, the scatterplots and the histograms that are both located to the bottom left of the diagonal and finally, the boxplots that are located to the right.

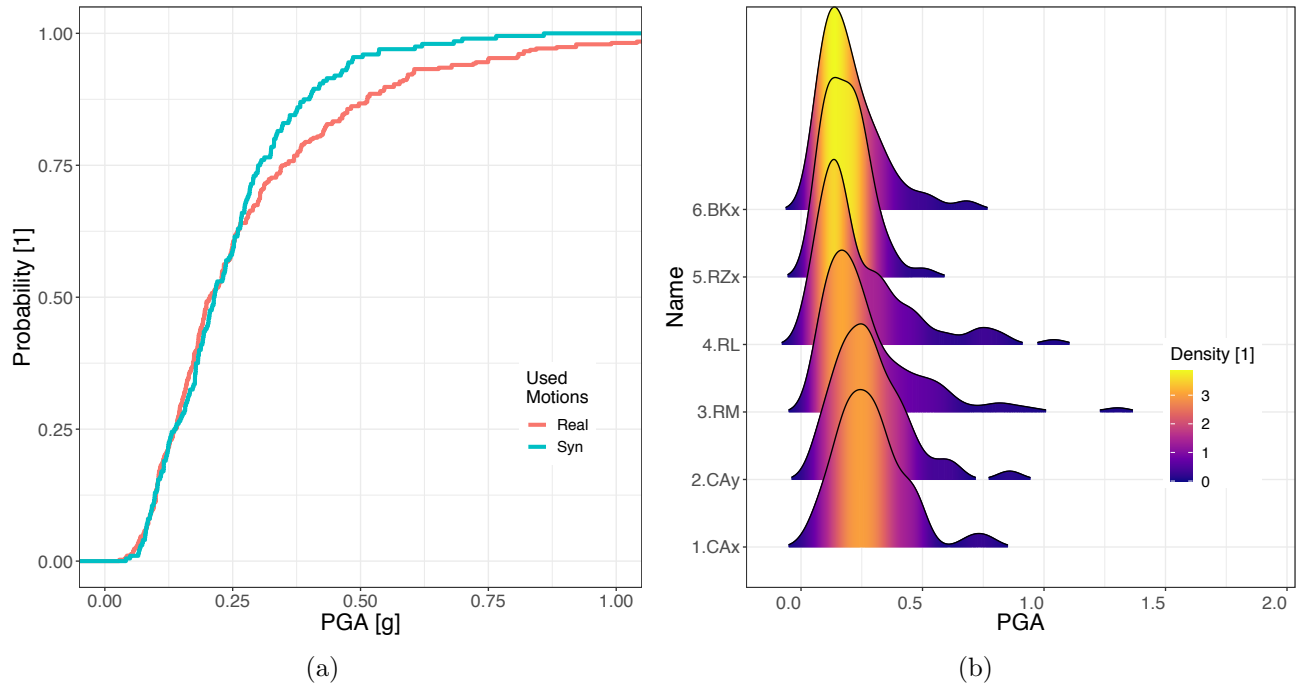


Figure 2.6: a) The cumulative distribution function and b) the density distribution function of the real and synthetic ground motions

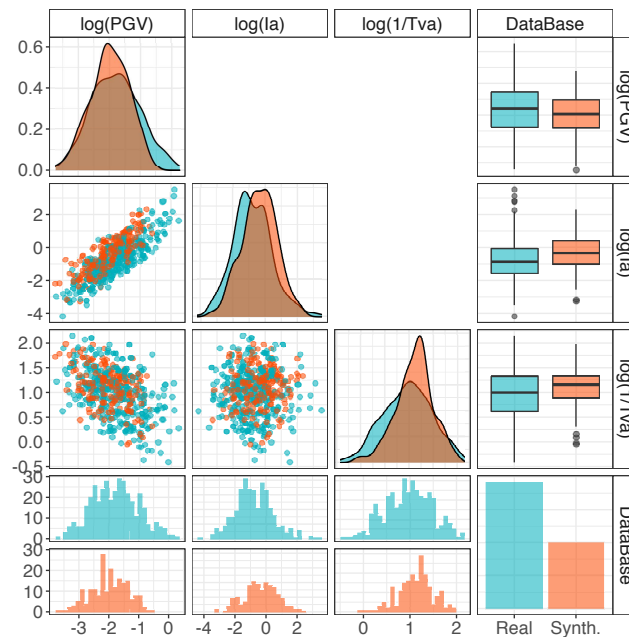


Figure 2.7: The logarithmic distribution of some ground motion parameters ( $PGV$ ,  $I_a$  and  $1/T_{va}$ ) of the real and synthetic ground motions

For the density distribution function of the chosen parameters, it can be seen that the real and synthetic motions overlap the same data intervals. However higher values of  $PGV$  and  $1/T_{va}$  are found in the synthetic motions. For the median value of each database, it can be seen from the boxplots, that it is almost close for the two ground motion types. Concerning the scatterplots and the histograms, they are useful to have an idea about the precise values or

the relation between each parameter.

For the two groups of motions classified from Figure 2.6b, the logarithmic distribution of their ground motion parameters is also plotted in Figure 2.8. It is interesting to mention that each group overlaps similar data intervals.

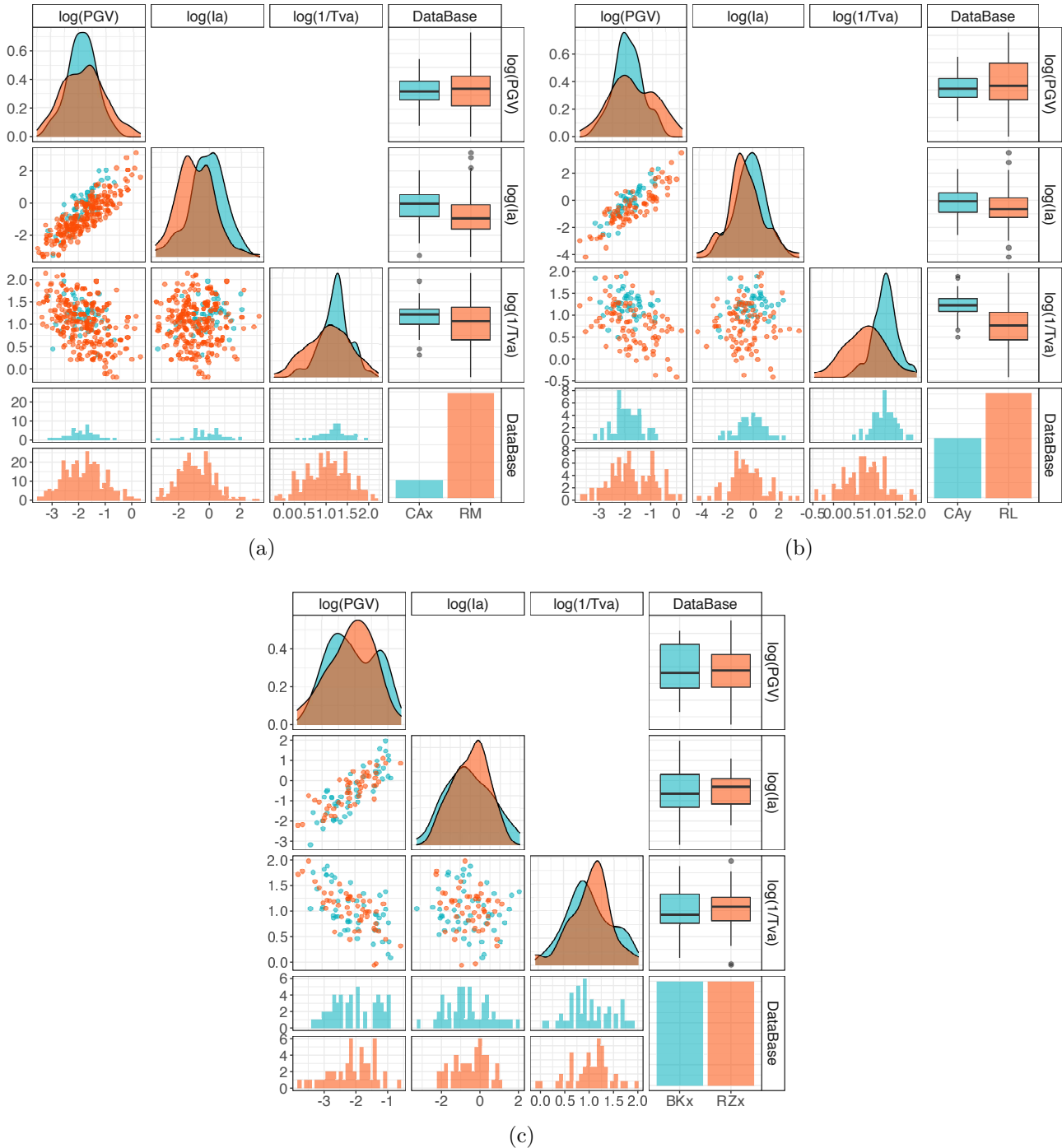


Figure 2.8: The logarithmic distribution of some ground motion parameters ( $PGV$ ,  $I_a$  and  $1/T_{va}$ ) for the group of a) & b)  $CAx$ ,  $CAy$ ,  $RM$  and  $RL$  and c)  $RZx$ ,  $BKx$

Finally, the first question in the Introduction section is answered. It was shown in this section that based on the distribution of the IMs, the chosen real and synthetic ground motions

are compatible. It will be seen in the coming section the potential damage of the embankment with global and local indices.

## 2.5 Damage measure and soil mechanical behavior

The assessment of seismic structural vulnerability has broadened the objectives of seismic design so that not only the safety against collapse is the required criteria but also the long term resistance of the structures. A great effort has been made to improve the current earthquake-resistant design methods in order not only to avoid collapse under a destructive earthquake, but also to limit the damage under moderate earthquakes (Cosenza and Manfredi, 2000). In engineering practices, a stability analysis is required in order to define a safety index above which the structure will reach failure. This later is commonly known by the factor of safety  $FS$ . It is typically defined as the ratio of the available shear strength to the shear stress required to maintain the equilibrium along the prescribed failure surface (Huang and Yamasaki, 1993; Kramer, 1996; Lu et al., 2012, among others). The basic idea for stability analysis, specially for soils, is to calculate at each point in a domain of interest, the so-called local factor of safety  $LFS$ . It is defined as the ratio of the potential mean stress to the current mean stress under the Mohr-Coulomb failure criterion (Lu et al., 2012).

Furthermore, the damage indices used to measure the potential structural failure are either defined for each structural element (local) or related to the entire structure (global) (Cosenza and Manfredi, 2000). In this study, the potential failure and damage state of the embankment are examined. For the sake of brevity only, one example ground motion will be analyzed in details. The acceleration time history at the bedrock for this example is shown in Figure 2.9a. Typically, the global structural failure for any similar structure is to calculate the relative crest settlement  $u_{z,rel}$ . Thus, Figure 2.9b shows the evolution of  $u_{z,rel}$  and the excess pore water pressure ratio  $r_u$  (i.e.  $= \Delta p_w / p'_0$ ) for a point placed under the center of the embankment, at 3 m depth. It should be mentioned that 30 seconds of zero values were added at the end of the ground motion in order to ensure the recovery time (i.e. the  $\Delta p_w$  dissipation) of the soil foundation. It is clear from Figure 2.9b that at the beginning of the motion,  $u_{z,rel}$  and  $r_u$  were zero. When the strong phase of the motion starts the relative crest settlement decreases rapidly, in parallel, the excess pore water pressure is generated which results in peak values for  $r_u$ . After the strong phase, the crest settlement is constant and the excess pore water pressure dissipates.

To define the liquefaction potential, Figure 2.10 shows a typical distribution of the vertical co-seismic displacement at the end of the earthquake loading. The results of this figure shows that the liquefaction induces settlements at the crest as a result of the damage of the soil foundation under the embankment towards the free field (Kramer, 1996; Kourkoulis et al., 2010; Sadeghi et al., 2014; Rapti, 2016, among others).

Concerning the potential failure of the embankment from a local damage index, a local safety

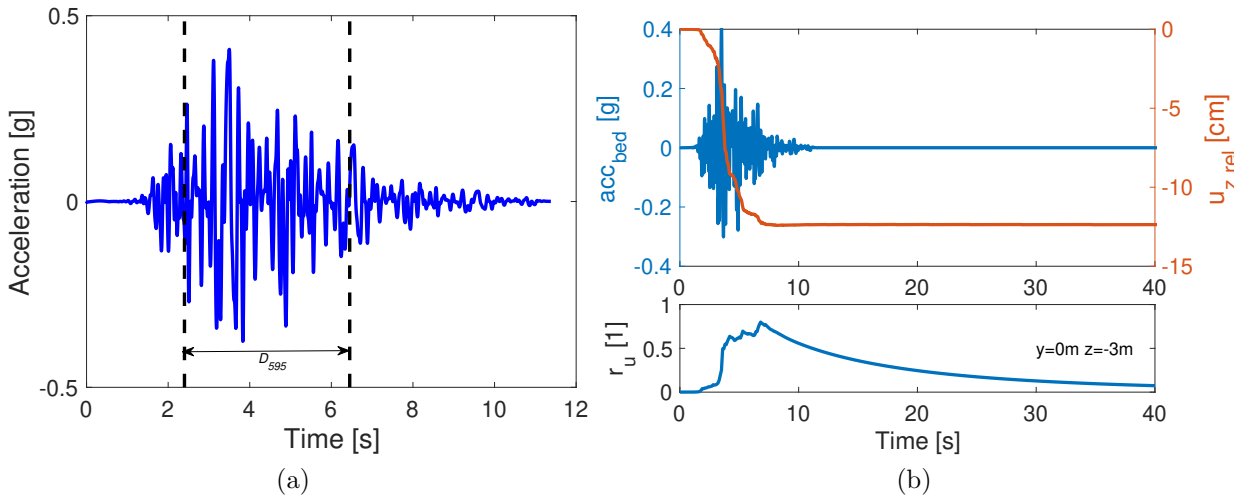


Figure 2.9: The example a) ground motion of this section and b) the evolution in time the relative crest settlement  $u_{z,rel}$  and the excess pore water pressure ratio  $r_u$  (i.e.  $= \Delta p_w / p'_0$ )

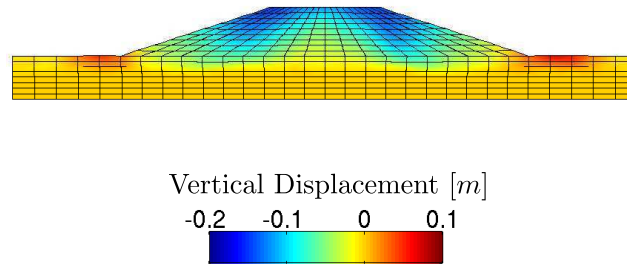


Figure 2.10: Enlarged view of typical vertical co-seismic displacement contours at the end of the shaking

factor  $LFS$  could be estimated by calculating the residual strength. The  $LFS$  discussed in this chapter is the one proposed by [Lopez-Caballero and Modaressi-Farahmand-Razavi \(2013\)](#); [Rapti et al. \(2018\)](#) and previously mentioned in Chapter 1 (Section 1.6). It provides, for any soil state, a direct measure of the “distance to reach the critical state”. The yield surface of the model (Equation 2.3) shows two parameters that control the behavior of the soil;  $F_k$  that controls the isotropic hardening associated with the plastic volumetric strain and  $r_k$  that controls the isotropic hardening generated by the plastic shearing. These two parameters represent progressive friction mobilization in the soil, such that:

$$F_k = 1 - b \ln \left( \frac{p'_k}{p_c} \right) , \quad (2.4)$$

$$p_c = p_{co} \exp(\beta \varepsilon_v^p) . \quad (2.5)$$

$$\sin \phi'_{apt} = \frac{q_k}{p'_k \cdot F_k} , \quad (2.6)$$

$$r_{apt} = \frac{\sin \phi'_{apt}}{\sin \phi'_{pp}} . \quad (2.7)$$

$r_{apt}$  varies between 0 and 1 where perfect plasticity is reached and could be defined as the

inverse of a local safety factor ( $r_{apt} = 1/LFS$ ). Thus, the potential mean stress is evaluated from the friction angle at the critical state  $\phi'_{pp}$  and the current mean stress from the apparent friction angle  $\phi'_{apt}$ . A threshold value of the damage measure is taken as 0.75 (i.e. corresponds to  $LFS \approx 1.33$ ) (Lopez-Caballero and Modaressi-Farahmand-Razavi, 2013; Rapti et al., 2018). The domain of interest in which the local damage  $r_{apt}$  is calculated is composed of the liquefied layer and the embankment (i.e. the green window in Figure 2.2). It was chosen vertically based on the depth of the liquefiable layer (4 m) and laterally from the possible zones where the failure pattern could occur.

Figure 2.11 shows the values of  $r_{apt}$  of the domain for three time intervals. It is clear from this figure that at 3 seconds, some high values of  $r_{apt}$  appear in the soil layer. It is interesting to notice that also when the strong phase of the motion ends (after  $D_{595}$  in Figure 2.9a), and at 7 seconds precisely, instability is indicated from high values of  $r_{apt}$  in the embankment. This is due to the peak value of the excess pore water pressure during this time (see description of Figure 2.9b). However, at the end of the shaking, and after the dissipation of the excess pore water pressure, values of  $r_{apt}$  of almost 0.6 appear in the domain.

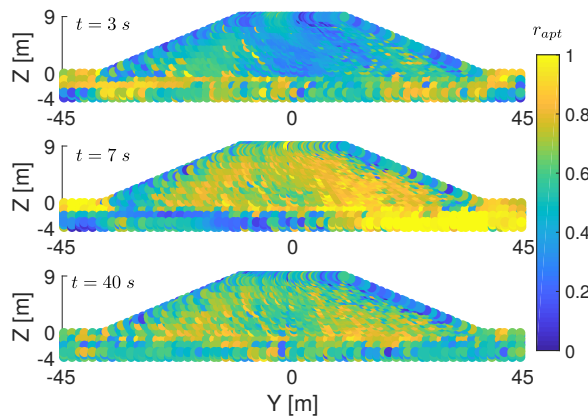


Figure 2.11: The values of  $r_{apt}$  in the domain of interest for three time intervals: 3, 7 and 40 seconds

In order to explain the function of this local damage measure, Figure 2.12 considers the threshold value of  $r_{apt}$  (i.e. 0.75). Thus, in this figure, for each integration point (IP) in the domain of interest, when  $r_{apt} < 0.75$ , red color is designated and when  $r_{apt} \geq 0.75$ , black color is attributed. Confirming to Figure 2.11, at the beginning of the ground motion, some instability points (black points) are shown in the foundation layer. However, at 7 seconds (Figure 2.12b), it can be seen that the increase in time resulted in more instability points that increase upwards towards the slope of the embankment.

In order to statistically represent the values of  $r_{apt}$  during the co-seismic duration of the example ground motion, Figure 2.13a shows the empirical Complementary Cumulative Distribution Function (CCDF) of this parameter. The limit value of 0.75 is also plotted as a dashed line in this figure. As expected, the CCDF of  $r_{apt}$  evolves with the increase in time. It may also be interpreted that the probability of exceeding the limit value of 0.75 increases with time.

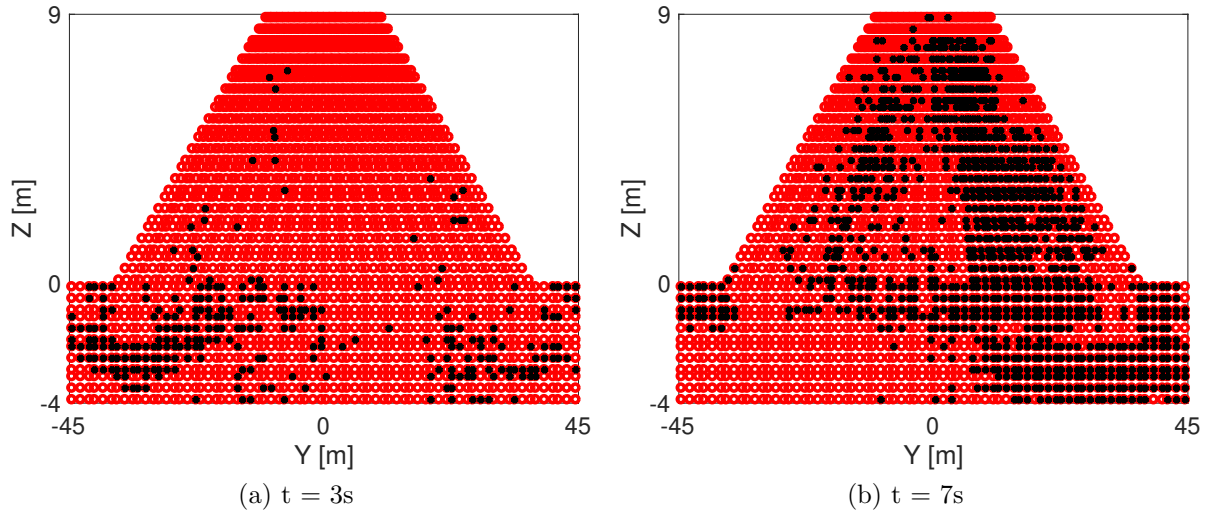


Figure 2.12: The distribution of  $r_{apt} \geq 0.75$  from the IPs (black points) for the example ground motion

Because  $r_{apt}$  can be interpreted as a *LFS*, the global damage measure is represented by the probability of exceeding the  $r_{apt}$  limit value, which is introduced in this chapter by the *failure density concept*, given in Equation 2.8. The failure density concept intends to give a measure of the failure extension in the embankment system:

$$\mathbb{P}(r_{apt}(t) \geq 0.75) = \int_{r_{apt} \geq 0.75} f(r_{apt}) \cdot dr_{apt} \approx \frac{N_{r_{apt} \geq 0.75}(t)}{N_T} = \rho_{r_{apt} \geq 0.75}(t) \quad (2.8)$$

$N_{r_{apt} \geq 0.75}(t)$  gives the number of IPs that surpassed the  $r_{apt}$  limit and  $N_T$  is the total number of IPs in the domain of interest.

Yet, it is important to compare the potential failure of the embankment from the two global damage indices:  $u_{z,rel}$  and  $\rho_{r_{apt}}$ . For this purpose, Figure 2.13b shows the variation in time of both  $u_{z,rel}$  and  $\rho_{r_{apt} \geq 0.75}$ . It is clear from this figure that both damage indices are linked. For example, around 5 seconds, the settlement increases when  $\rho_{r_{apt} \geq 0.75}$  increases. Once the settlement reaches a maximum value,  $\rho_{r_{apt} \geq 0.75}$  reaches a peak value of 0.4. This value means that 40% of the domain of interest had  $r_{apt} \geq 0.75$ . It is interesting to mention that around 10 seconds, even if  $u_{z,rel}$  was constant,  $\rho_{r_{apt} \geq 0.75}$  was decreasing. This is linked to the dissipation of the excess pore water pressure at this time (Figure 2.9b) and a proof that the soil tries to densify. At the end of the strong phase of the motion, the soil tries to recover where its settlement and  $r_{apt}$  are constants. Thus, for practical purposes,  $\rho_{r_{apt} \geq 0.75}$  at the end of the ground motion is able to represent the state of failure of the embankment. For simplicity of the notation in what proceeds in this chapter, the notation  $\rho_{r_{apt} \geq 0.75}$  means  $\rho_{r_{apt} \geq 0.75}(t = t_{end})$ .

It is demonstrated so far, the global (i.e.  $u_{z,rel}$  and  $\rho_{r_{apt}}$ ) and local damage (i.e.  $r_{apt}$ ) indices that represent the potential failure of the embankment for one example ground motion. It will be represented hereafter the results for a large number of ground motions. For the sake of simplicity and for less computational time, only one type of real (*RM*) and one type of

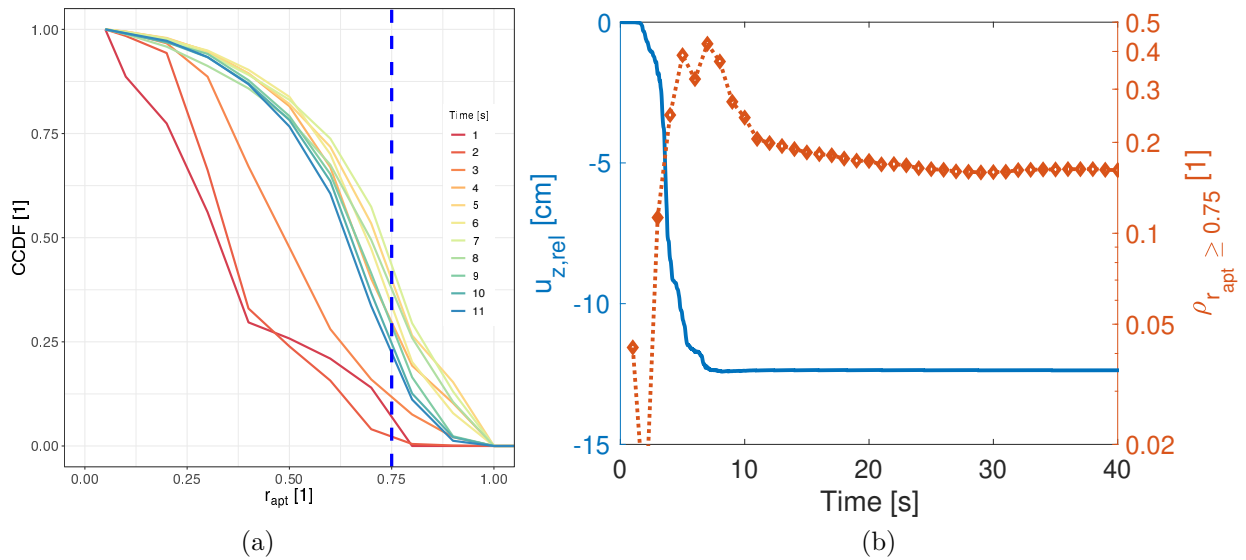


Figure 2.13: a) The CCDF of the parameter  $r_{apt}$  during the co-seismic duration of the example ground motion and b) the dependency of the parameter  $r_{apt}$  with the crest settlement of the embankment

synthetic (*BKx*) ground motion are taken into consideration. The results are shown in Figure 2.14 in terms of the percentage relative crest settlement is  $\delta u_{z,rel}/H$  where  $u_{z,rel}$  is the crest settlement and  $H$  is the height of the embankment with the foundation (i.e. 19 m in this case) (Lopez-Caballero and Khalil, 2018; Khalil and Lopez-Caballero, 2021). The damage levels are designated such that when  $\delta u_{z,rel}/H \leq 0.02\%$ , there is *No* damage, if  $0.02\% < \delta u_{z,rel}/H \leq 0.1\%$ , the damage is *Minor*, if  $0.1\% < \delta u_{z,rel}/H \leq 1\%$ , the damage is *Moderate* and finally if  $\delta u_{z,rel}/H > 1\%$ , the damage is *Serious*.  $\rho_{r_{apt} \geq 0.75}$  is also represented in this figure.

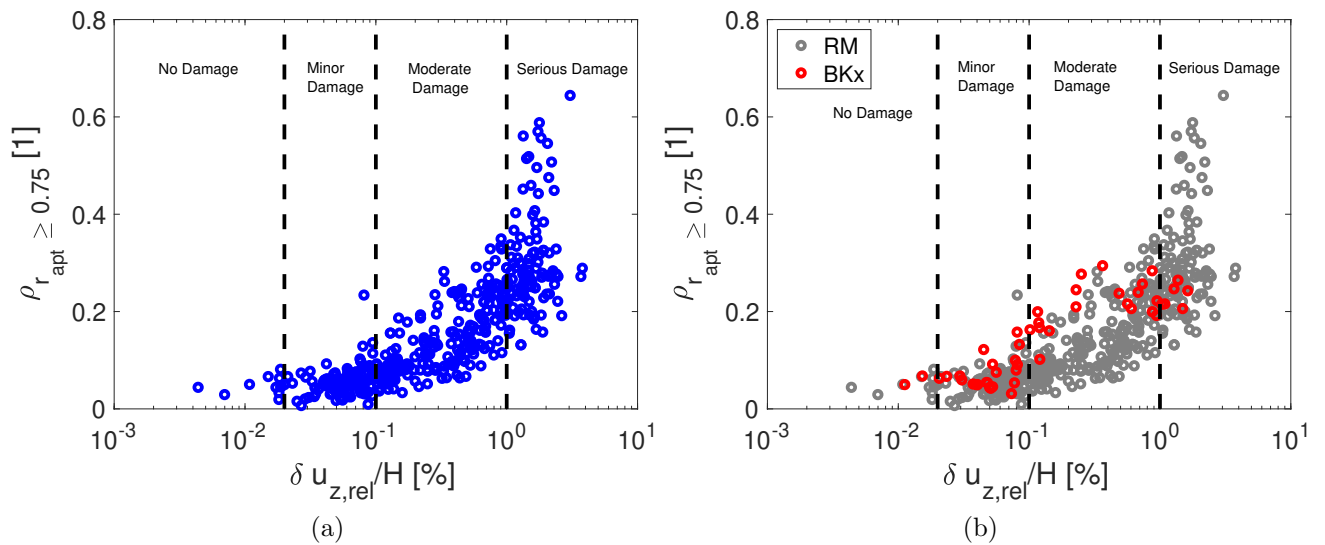


Figure 2.14: The potential failure of the embankment for a) one type of real ground motions and b) one type of synthetic ground motions

Concerning the recorded ground motion only (Figure 2.14a), for the first two damage levels

(i.e. *No* and *Minor*), small values of  $\delta u_{z,rel}/H$  and  $\rho_{r_{apt} \geq 0.75}$  are presented. However, for *Moderate* level,  $\rho_{r_{apt}}$  reached values of 0.3. Concerning the largest damage level,  $\rho_{r_{apt} \geq 0.75}$  had values from 20% to 70 % in addition to important values of  $\delta u_{z,rel}/H$ . For Figure 2.14b where a comparison of the synthetic ground motion is drawn, it can be seen that the synthetic motions give almost similar results as the recorded ones.

It can be partially concluded in this chapter that the damage measure represented by the relative crest settlement  $\delta u_{z,rel}/H$  is a global indicator of the potential failure of the embankment. In addition, the ratio of apparent to critical friction angle, designated as the parameter  $r_{apt}$ , provides a reliable measure of soil strength, which takes into account the loading history and can be used as a criterion for estimating the local state of soil for cyclic loads. The coming section will answer the third question in the introduction about the effect of the motion type on the response of the embankment. In other words, it will aim to find the link between the engineering demand parameter EDP and the intensity measure IM.

## 2.6 Link between EDP and IM

The structural analysis is the second stage of the performance-based engineering. This analysis consists in choosing an engineering demand parameter (EDP) that represents the global response of the structure after an earthquake (Stewart et al., 2002; Porter, 2003; Lopez-Caballero and Khalil, 2018, among others). For levees (or dams) under seismic activities, the mode of failure usually studied is the crest settlement because it is a quantifiable measurement. It was presented in the previous section, a description of two global damage measure. Practically, the damage index  $\rho_{r_{apt}}$  is difficult to calculate without numerical codes. Thus, the relative crest settlement  $\delta u_{z,rel}/H$  is going to represent the EDP of this case study. Swaisgood (2003) analyzes a historical database on the performance of dams during earthquakes and found that the crest settlement is directly related to some input ground motion characteristics (i.e. the peak ground acceleration and magnitude).

It was presented in Section 2.3 a selection of real and synthetic ground motions that were classified into two groups in Section 2.4. In this section, the link between the EDP and the IM of these motions will be evaluated. First, a comparison between the response after the real and the synthetic motions is conducted. The results are represented as box plots in Figure 2.15. The boxes represent 50% of the data and their boundaries consider the 25th and 75th percentile of the data respectively. The two extremes are 1.5 times the distance between the two percentiles, and the red dots above or below the box-plots are the outliers. It can be seen that the median value of the percentage relative crest settlement of the real and synthetic ground motions (Figure 2.15) is almost close. However, more dispersion was found for the real ground motions. Hence, in this specific case, the damage induced on the embankment is not affected by the type of the occurring ground motion.

In order to validate this interpretation, the relative crest settlement was drawn for each

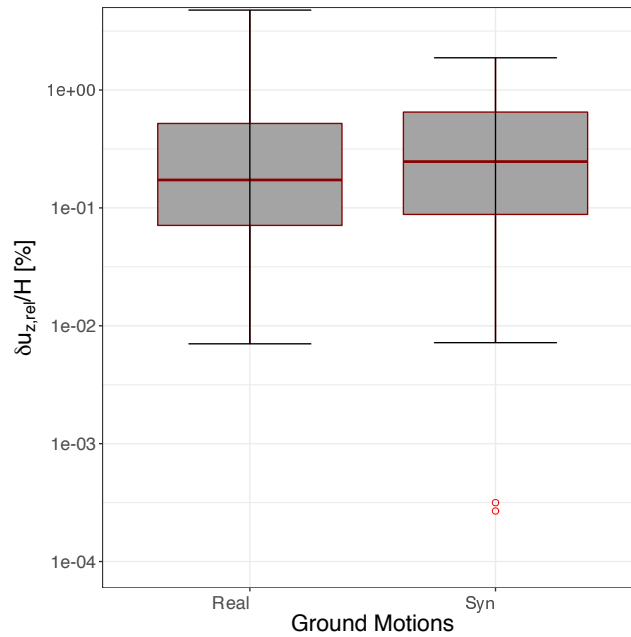


Figure 2.15: Box plot of the relative crest settlement for the tested real and synthetic motions

group of motions (classified from Figure 2.6b). The results are shown in Figure 2.16. Damage levels are also attributed to the relative crest settlement and appear in this figure as dashed lines. In addition in this figure, a reference to a study conducted by Lopez-Caballero and Khalil (2018) is also shown, where the global response of the embankment is shown after a larger number of real ground motions.

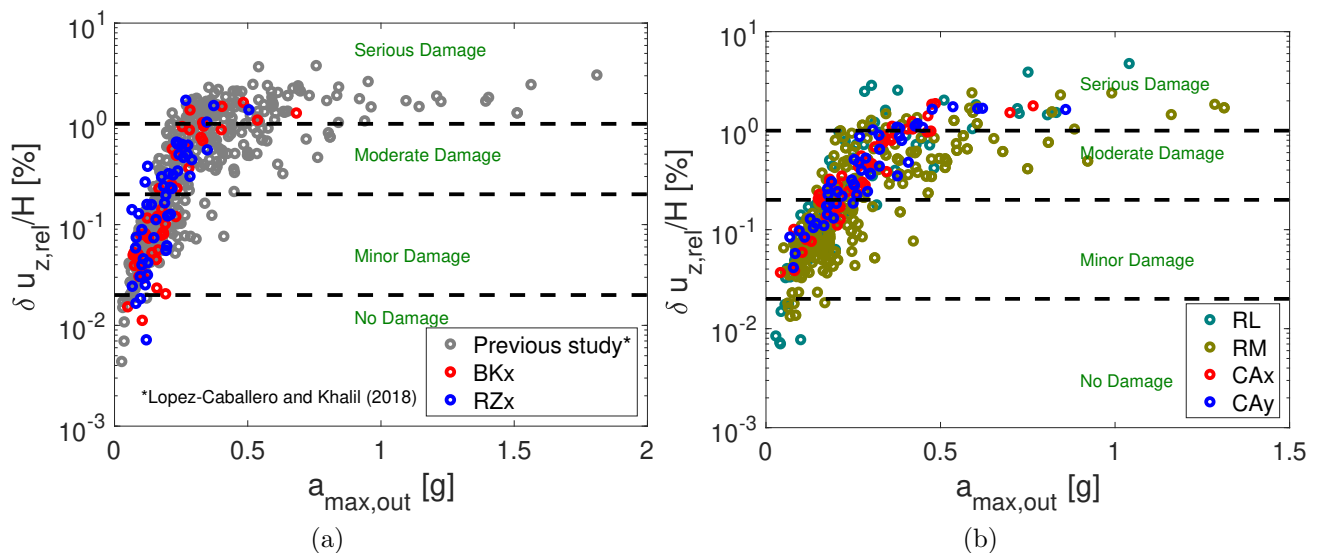


Figure 2.16: Percentage crest settlement for the groups of real and synthetic ground motions

Confirming to the referenced study, the synthetic ground motions shows that the percentage crest settlement increases when the PGA at the outcropping bedrock increases. Concerning the first group of motions (Figure 2.16a), the synthetic motions *BKx* and *RZx* show compatible results. Whereas for the second group of motions in Figure 2.16b, *CAx* and *CAy* show similar

results which is normal because they only differ in the spatial coordinates. In addition, the comparison with the real motions shows the same data intervals.

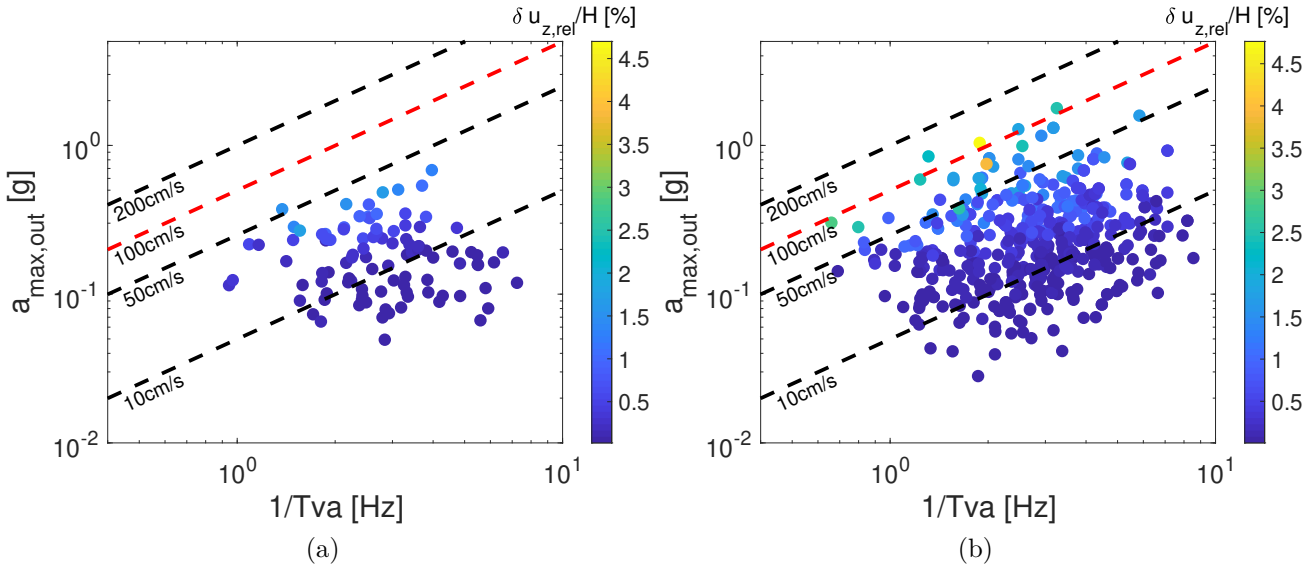


Figure 2.17: The link between the chosen EDP and several IMs for a)  $BKx$ ,  $RZx$  and b)  $CAx$ ,  $CAy$ ,  $RL$  and  $RM$

Furthermore, the response of the soil does not only depend on one IM but also on the entire motion. For this purpose, the variation of  $a_{max,out}$ , the equivalent predominant frequency  $1/Tva$  and the peak ground velocity  $PGV$  are shown in Figure 2.17. The dashed lines in this figure represent  $PGV$ . It can be seen for both groups of motions, that the crest settlement increases toward the upper left, which means proportional with the increase in  $PGV$ .

Similar to this interpretation, the variation of the aforementioned IMs with the damage levels of the relative crest settlement are shown in Figure 2.18 in order to evaluate the severity of chosen seismic inputs. It should be mentioned that  $DL1$  represents *No* damage,  $DL2$ , *Minor* damage,  $DL3$  *Moderate* damage and  $DL4$  *Serious* damage.

As expected and relatively to Figure 2.17, it can be seen from Figure 2.18 that the increase of the damage levels is proportional to the increase in  $PGV$ . It is interesting to mention that the synthetic earthquakes reached  $DL3$  or  $DL4$  before the real earthquakes. This result shows that the synthetic earthquakes could over estimate the damage level of the embankment.

Finally, it can be partially concluded that for the case of this study, the chosen synthetic ground motions give almost similar ground response as the real motions. However, they over estimate the level of damage in some cases. The purpose of the coming section is to calculate the probability of failure of the embankment through fragility curves, and verify if it is affected by the type of motion.

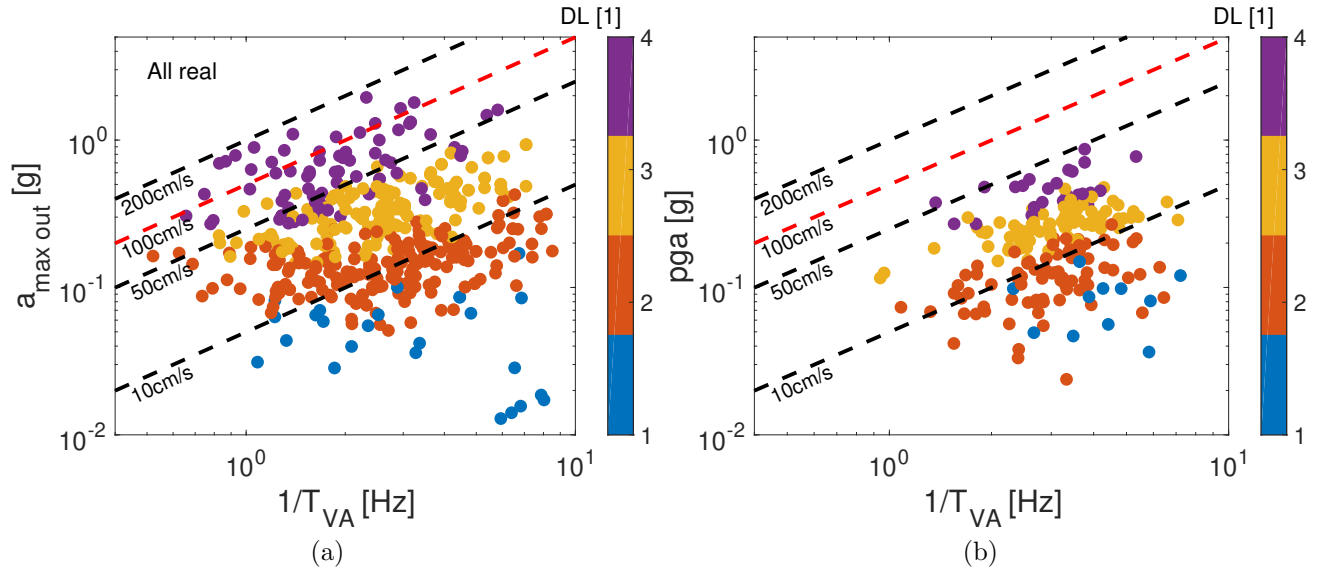


Figure 2.18: The link between the chosen IMs and the damage levels for the a) real and b) synthetic earthquakes

## 2.7 Fragility curves

In performing a seismic risk analysis of a structural system, it is essential to identify seismic vulnerability of component structures associated with damage levels (Shinozuka et al., 2000). The development of structural vulnerability in the form of fragility curves has been a practice specially when the information requires a set of uncertain sources (i.e. seismic hazard, soil-structure interaction, site conditions) (Shinozuka et al., 2000; Sáez et al., 2011; Argyroudis and Kaynia, 2015; Zentner, 2017, among others). Fragility curves are functions that express the conditional probability of the design to exceed a certain level of damage measure  $DM_0$  for given a IM of level  $im$ . It has the following form:

$$P(DM > DM_0 | IM = im) = \phi \left[ \frac{\ln im - \ln \eta_{DM|IM}}{\beta_{DM|IM}} \right] , \quad (2.9)$$

where  $\phi[\cdot]$  is the standardized normal distribution function.  $\eta_{DM|IM}$  is the median threshold value of IM required to cause the damage and  $\beta_{DM|IM}$  is the total lognormal standard deviation. One or more IMs can be used to represent the fragility curves or surfaces (Lopez-Caballero and Khalil, 2018). However, for simplicity, the mostly used IM is the *PGA*. Several analytical methods have been proposed to generate the fragility curves of structures, such as the probability-based scenario, the non linear seismic analysis of the model, among others (Sáez et al., 2011).

In this chapter, the fragility curves are developed from a statistical procedure that is based on two parameters log-normal distribution functions as proposed by Shinozuka et al. (2000). In addition, in the work of Sáez et al. (2011), the quality of fit and an estimation of the interval confidence for the two parameters controlling the fragility curves have been presented.

The details of the statistical procedure to calculate analytical fragility functions are developed in Appendix E. In the test case of this chapter, the damage state is taken as the *Moderate* damage level. Thus, fragility curves are drawn for the two groups of motions as function of the acceleration at the outcropping  $a_{max,out}$ . They are shown in Figures 2.19a and 2.19b.

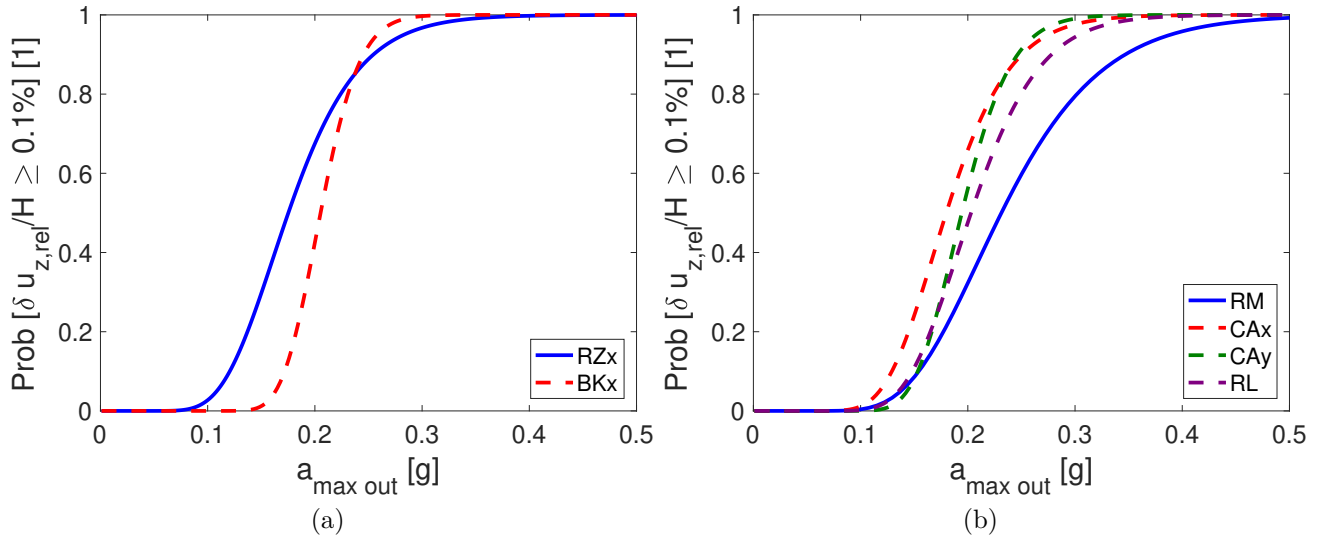


Figure 2.19: Fragility curves of the real and synthetic motions for *Moderate* damage level

From Figure 2.19a and for high values of  $a_{max,out}$ , the probability of reaching the tested damage state is close for *RZx* and *BKx*. On the contrary, for lower values of  $a_{max,out}$ , the probability to exceed the damage limit is different. For example, for an acceleration  $a_{max,out}$  equals to 0.2g, there is 55% chance that the damage is exceeded if the event that happened was *BKx* whereas for *RZx*, this chance increases to 75%. This difference in value should be taken into consideration because any change in the synthetic model can lead to a change in the structural response. Now in Figure 2.19b, it can be seen that the results of both the real and synthetic ground motions are almost close. It should be noted that there is a difference in the response between the two real motions (i.e. *RM* and *RL*). This could be due to the sampling number of each type used to compute the fragility curves. From Table 2.1, there is 296 motions of type *RM* whereas 88 motions of type *RL* (refer to Appendix E to see the importance of the number of sampling to draw fragility curves). For example, an acceleration  $a_{max,out}$  of 0.2g, there is a 30% chance (or 45% if small data sampling is compared) that the damage level is exceeded if the events of interest were real ground motions. Whereas for synthetic ground motions, the probability of exceeding increases to 55% and even 70% for some cases.

Finally, this section answered the fourth question in the introduction about the effect of the ground motion type on the fragility curve. It can be partially concluded from this chapter that a difference in the response between the real and synthetic ground motions appears when conducting fragility curves. From an engineering point of view, an overestimation can sometimes be positive as to consider a higher safety factor and a robust design. However, it might generate additional undesirable costs.

## 2.8 Concluding remarks

The performance-based earthquake engineering methodology was investigated through its stages in this chapter. A large number of real and synthetic ground motions was selected. The damage measure of an embankment was calculated from local and global indices. An elastoplastic multi-mechanism soil behaviour model integrated in a finite element code (GEFDyn) was used.

The answers to the questions presented in the introduction are the following:

- a) The chosen synthetic motions were based on the stochastic method to simulate artificial earthquakes. The distribution of some characteristics were drawn in order to verify complementary in the domains. The results show that the chosen synthetic motions were representative of the real ones.
- b) The damage measure represented by the relative crest settlement  $\delta u_{z,rel}/H$  is a global indicator of the potential failure of the embankment. In addition, the parameter  $r_{apt}$  can be used as a criterion for estimating the local damage measure. Moreover, the failure density concept represented by the probability of exceeding  $r_{apt} \geq 0.75$ , noted as  $\rho_{r_{apt} \geq 0.75}$ , shows that it can be a global damage index. The link between both indices was proven in this study. However, this later one is difficult to compute without powerful numerical models.
- c) The global response of the embankment is linked to the IMs of the ground motions. It is similar for real and synthetic ground motions; the relative crest settlement increases with respect to the peak ground acceleration for both groups of motions.
- d) The real and synthetic ground motions have close estimation of the level of performance.

Finally, when the recorded ground motion data are very sparse, synthetic ground motions can be used. But a good care should be made on this choice in order to closely represent the real case scenarios.



# Chapter 3

## Survival analysis of a liquefiable soil foundation-embankment system subjected to sequential earthquakes

### Contents

---

<b>3.1</b>	<b>Introduction</b>	<b>63</b>
<b>3.2</b>	<b>Overview of the survival analysis</b>	<b>66</b>
3.2.1	Kaplan-Meier estimator	67
3.2.2	Cox Proportional Hazards model	68
3.2.3	Parametric models	68
<b>3.3</b>	<b>Geometry and soil numerical model</b>	<b>68</b>
3.3.1	Geometry	68
3.3.2	Soil Constitutive Model	69
3.3.3	Finite Element Model	71
3.3.4	Boundary Conditions	71
<b>3.4</b>	<b>Assumptions of this chapter</b>	<b>72</b>
<b>3.5</b>	<b>Input ground motions</b>	<b>72</b>
<b>3.6</b>	<b>Site-specific seismic analysis</b>	<b>75</b>
<b>3.7</b>	<b>Survival analysis of the Levee</b>	<b>76</b>
3.7.1	Crest settlement in the sequences	77
3.7.2	Survival analysis	80
<b>3.8</b>	<b>Influence of various parameters on the survival analysis</b>	<b>83</b>
3.8.1	Effect of the loading history	83
3.8.2	Importance of the recovery time between the sequences	84

---

3.8.3 Effect of different synthetic ground motion models . . . . .	85
<b>3.9 Concluding remarks . . . . .</b>	<b>86</b>
<b>3.10 Complements to this chapter . . . . .</b>	<b>87</b>

---

## Abstract

In practice, the performance of the structure is studied from a seismic scenario composed of independent single earthquakes. But in real life, the structure is subjected to multiple earthquakes during its typical design working life, which will produce an evolution of damage with time.

The main purpose of this chapter is to quantify the liquefaction-induced damage of an embankment due to sequential earthquakes during a defined working life. Moreover, a non-parametric survival analysis is used to estimate the time (in years) until a defined damage level is reached during a specific time interval. For this purpose, a site was chosen where its seismicity and its Probabilistic Seismic Hazard Analysis (PSHA) were identified. First, a site-specific seismic analysis was assessed, that consists in finding the relation between the Intensity Measures (IM) and the Engineering Demand Parameter (EDP). Second, in order to estimate the lifetime distribution as well as the Mean Time To Failure (MTTF) of the embankment, survival functions were drawn. The used time histories were stochastically generated from synthetic ground motion models.

This chapter was published in the *Soil Dynamics and Earthquake Engineering* journal and cited as *Khalil, C. and Lopez-Caballero, F. (2021). Survival analysis of a liquefiable embankment subjected to sequential earthquakes. Soil Dynamics and Earthquake Engineering, 140, 106436.*

## 3.1 Introduction

Seismic hazard analysis involves the quantitative estimation of the ground motion (GM) hazards of a specific area. It requires the knowledge of the geologic evidence, the fault activity, the magnitude and the historical seismicity of the studied region (Kramer, 1996; Bommer, 2002). The *Probabilistic Seismic Hazard Analysis (PSHA)* considers the uncertainties in the earthquake size, location and occurrence time. It estimates the mean frequency of exceedance of any spectral acceleration at the site (Bazzurro and Allin Cornell, 1999). The level of shaking produced from this analysis comes from the contribution of the magnitude  $M_w$ , the source-to-site distance  $R$  and often the deviation of the GM from the predicted value ( $\varepsilon$ ) (Bazzurro and Allin Cornell, 1999). Given the aforementioned information, the Ground Motion Prediction Equations (GMPEs) create the relationship between the magnitude, distance, and other model parameters and the Intensity Measures (IM). In this context, the study of the non linear behavior of the structures needs a recall to a large number of acceleration time histories. In addition and for particular scenarios, available data resources are sometimes inadequate to characterize the models due to several problems (i.e. ground motions from very large magnitude earthquakes, near-fault ground motions, basin effects) (Stewart et al., 2002; Luco and Cornell, 2007; Seyedi et al., 2010; Sáez et al., 2011; Wang et al., 2020, among others). For this reason,

artificial or synthetic earthquakes could be used. They are conducted based on several methods (i.e. stochastic ground motion model, the composite source method, among others) and are useful when real motions are not available.

In practice, structures are designed to resist the first damaging earthquake scenario (Hu et al., 2018). But during their service life, the structures are not only exposed to a single seismic event but also to multiple or repeated earthquake shocks. Previous works in this context have been conducted on various structures like buildings or bridges (Hatzigeorgiou and Beskos, 2009; Ruiz-Garcia and Negrete-Manriquez, 2011; Ruiz-García, 2012; Goda, 2012; Zhai et al., 2013; Ruiz-García, 2014; Ghosh et al., 2015; Iervolino et al., 2015; Panchireddi and Ghosh, 2019; Iervolino et al., 2020; Di Sarno and Pugliese, 2020, among others). As a consequence of the latter, structural damage accumulation by consecutive earthquake loading will be produced. The damage accumulation according to Iervolino et al. (2015), is mainly due to two phenomena: i) continuous deterioration of the material which is called “aging” or ii) cumulative damage due to repeated load, also known as “*sequential earthquakes*”. The cumulative damage of the structure during its working life, is known as the *Life Cycle* of the structure (Yeo and Cornell, 2009; Sanchez-Silva et al., 2011; Ruiz-Garcia and Negrete-Manriquez, 2011; Iervolino et al., 2015; Riascos-Ochoa et al., 2016; Salami et al., 2019; Lopez-Caballero et al., 2020, among others). In another context, the life cycle of the structure can take lots of definitions. It can be considered as the cycle needed for a structure to be constructed, maintained and economically valued (i.e. LCSA (Jungmeier et al., 2016)). It can also be considered as the time length of the structure until the occurrence of an event of interest (i.e. equipment failure, damage, complex system), or in other words, the time-to-event study. The later is known as the *Survival Analysis*. It is generally defined as a set of statistical methods to analyze data that has the time of occurrence of an event of interest as the outcome. Such analysis is not a new subject in medicine precisely (Hosmer Jr and Lemeshow, 1999; Clark et al., 2003; Bradburn et al., 2003). For example, it is used to validate the impact of a certain disease on different types of patients, or the occurrence of specific symptoms after a drug. Reflecting this analysis in the geotechnical field, it is, to the knowledge of the authors, still a new topic (Nafday, 2010; Christodoulou and Fragiadakis, 2014; Diamoutene et al., 2016).

Otherwise, the behavior of the structure (e.g. reinforced concrete buildings) under seismic sequence loading is assessed based on the *Incremental Dynamic Analysis (IDA)*. It consists in subjecting the structural model to multiple ground motion records each scaled to different intensities (Vamvatsikos and Cornell, 2002). Then, a limit state is considered in which the structure reaches failure when it exceeds the limits. On the other hand, previous studies in structural analysis have shown that, for mid-rise buildings, ten to twenty records are enough to have an estimation of the seismic demand (Shome, 1999; Vamvatsikos and Cornell, 2002, among others). IDA in this case, is easily applied since it does not have a large set of earthquake scenarios to draw fragility curves. Whereas in earthquake geotechnical engineering and particularly in liquefaction related problems, this approach is not enough to represent the overall response of

the geo-structure due to i) the multi-physical aspects of the soil (solid, water and air), ii) its history of loading that will affect its future behavior (Sica et al., 2008; Lopez-Caballero et al., 2016) and iii) the correlation of the soil response with several intensity measures of the real seismic motions (i.e. Arias intensity, number of cycles) (Causse et al., 2014b).

The present work aims to quantify numerically the liquefaction-induced damage on an embankment due to sequential earthquake loading. Following the Performance Based Earthquake Engineering (PBEE) approach, a PSHA should be conducted in which the seismicity of the site and the occurrence rate of earthquake are identified. In this work, the site of concern is located in Mygdonia, Greece. The reference to the fully probabilistic hazard analysis in this study are based on the work of Aristizábal et al. (2018). A large number of time histories was generated using stochastic simulations from synthetic ground motion models (e.g. Rezaeian and Der Kiureghian (2012) and Boore (1996)). Nevertheless any other stochastic models are also suitable to be used under the proposed methodology. At the beginning of this work, the induced damage was quantified based on a set of GM records without sequences similarly to a site-specific seismic analysis. Concerning the sequential analysis, the methodology adopted in this study is shown in Figure 3.1. Assuming that the working life of the embankment ( $T_{window}$ ) is 100 years, and according to the PSHA and the catalog GM constructed for this site, the event rate of the mainshocks ( $\lambda_{earthquakes}$ ) is 0.44 events/year. Thus, 44 acceleration time histories ( $N_{shocks}$ ) should occur during this period. Then the sequential loading is obtained by a random permutation of the obtained number of mainshocks. In order to calculate the survival function ( $P(\sum D(t) < D_{threshold})$ ), a threshold damage  $D_{threshold}$  should be identified. Hence, the lifetime distribution of the embankment can be estimated as well as its Mean Time To Failure (MTTF, the expected time to failure for a non-repairable system). In this study, the survival analysis is computed based on a non parametric statistical method (Kaplan and Meier, 1958). The main advantage behind this method is that it does not require the assumptions of a particular probability distribution (i.e. Weibull, exponential, log-logistic) of the structure's survival function. Also in this work, a numerical parametric analysis is performed in order to quantify the impact of considering (or not) the loading history and the recovery time between each ground motion on the obtained MTTF of the embankment. This study points out the importance of the history of loading since it affects the overall performance of the embankment. Finally, two synthetic ground motions models are assessed in order to generalize, to a certain extent, this work. The 2D finite element calculations were performed using the GEFDyn code (Aubry et al., 1986). For the soil behavior, an elastoplastic multi-mechanism model that takes into consideration the history of loading was used.

This chapter is structured as follows. It starts by introducing the theory behind the survival analysis in Section 3.2. The geometry and the numerical model are shown in Section 3.3. The development of the used synthetic ground motion model is presented in Section 3.5. The site-specific seismic analysis of the embankment is developed in Section 3.6. Then, in Section 3.7, the sequential and the survival analysis are presented. Finally, the different types of sequential

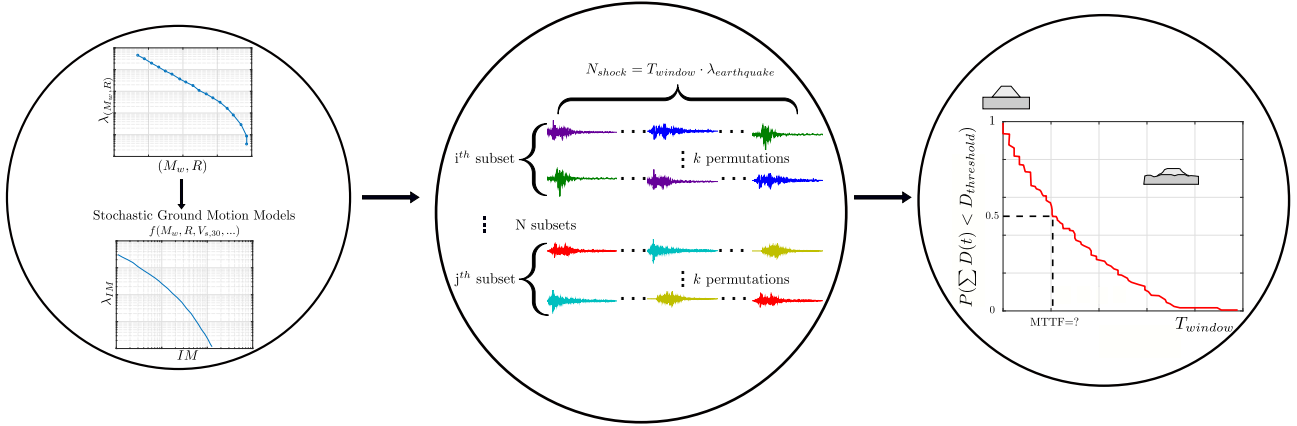


Figure 3.1: Schema of the used methodology to estimate the lifecycle of an embankment

analysis approaches are developed in Section 3.8, as well as the consideration of different synthetic GM models. The chapter is closed with conclusions.

## 3.2 Overview of the survival analysis

The survival analysis is the analysis of time-to-event data. These data describe the length of time until the occurrence of a well-defined end point of interest (Bradburn et al., 2003; Kartsonaki, 2016; Schober and Vetter, 2018, among others). Survival analysis is conducted via survival (or survivor) functions or hazard functions. Let  $T$  be a non-negative random variable that represents the surviving time. Denoting the duration of each event as  $t$ , the probability density function of  $T$  is  $f(t)$ , and its cumulative distribution is  $F(t) = P\{T < t\}$ . First, the survival function is:

$$S(t) = P\{T \geq t\} = 1 - F(t) = \int_t^{\infty} f(x)dx \quad (3.1)$$

The survival function is non increasing (i.e. at  $t = 0$ ,  $S(t) = 1$ ) and when the time increases, it tends to approach zero.

Second, the hazard function which represents the instantaneous rate of occurrence over time, is:

$$h(t) = \lim_{\Delta t \rightarrow 0} \frac{P(t \leq T < t + \Delta t | T \geq t)}{\Delta t} = \frac{f(t)}{S(t)} \quad (3.2)$$

Both, the survival and hazard functions are inversely proportional so that when the hazard increases, the survivor declines and vice versa (Kartsonaki, 2016; Schober and Vetter, 2018, among others). The survival time response are usually continuous. When they are not completely observed, they are called censored. Three methods exist to analyze the survival data and are developed in the following (Hosmer Jr et al., 2008; Kartsonaki, 2016):

- *Non-parametric method* is a widely used method. It consists in plotting the Kaplan-Meier

curve (Kaplan and Meier, 1958). The simplicity of this curve is that it does not need any assumptions for the distribution of the survival time, or the relationship between the covariates and the survival time.

- *Semi-parametric method*, in which there is also no assumption for the distribution of the survival time but assumes the relationship between the covariates and the hazard (also the survival) function. This method uses the Cox Proportional Hazard (Cox PH) model.
- *Parametric method* assumes the distribution of the survival time and the form of the covariates.

### 3.2.1 Kaplan-Meier estimator

The Kaplan-Meier (KM) estimator (or product-limit estimator)  $\hat{S}(t)$  incorporates information from censored and uncensored observations. It considers the survival function to any point in time as series of steps defined by the observed survival and censored times (Kaplan and Meier, 1958). The probability of surviving an event in time  $t_i$  is calculated from the probability of surviving the event at time  $t_{i-1}$ . Hence the KM estimator of the survival function is::

$$\hat{S}(t_i) = \prod_{t_i \leq t} \left[1 - \frac{d_i}{Y_i}\right] \quad , \quad (3.3)$$

with  $d_i$  is the observed cases that reached failure and  $Y_i$  is the cases that are still at risk. Normally, at  $t_0 = 0$ ,  $S(0) = 1$ . Several approaches are used to calculate the variance of the KM estimator. The commonly used approach is the *delta method*. The KM estimator is viewed as a product of two proportions. Hence, in order to calculate its variance, it is better to derive one for its logarithm since the variance of a sum is simpler to calculate than the variance of a product (Hosmer Jr and Lemeshow, 1999):

$$\ln(\hat{S}(t)) = \sum \ln\left(1 - \frac{d_i}{Y_i}\right) = \sum \ln\left(\frac{Y_i - d_i}{Y_i}\right) \quad (3.4)$$

$$= \sum \ln(\hat{p}_i) \quad , \quad (3.5)$$

where  $\hat{p} = (Y_i - d_i)/Y_i$ . The variance of Equation 3.4, given  $Y_i$  would be:

$$Var[\ln(\hat{S}(t))] = \sum Var[\ln(\hat{p}_i)] \quad (3.6)$$

$$= \sum \frac{1}{\hat{p}^2} \frac{\hat{p}_i(1 - \hat{p}_i)}{Y_i} \quad (3.7)$$

$$= \sum \frac{d_i}{Y_i(Y_i - d_i)} \quad , \quad (3.8)$$

Hence, the Greenwood formula for the variance of the survival function will be:

$$\text{Var}[S(t)] = \text{Var}[\exp[\ln(\hat{S}(t))] = [S(t)]^2 \sum \frac{d_i}{Y_i(Y_i - d_i)} \quad , \quad (3.9)$$

### 3.2.2 Cox Proportional Hazards model

The basic Cox PH model fits the survival data with the covariates  $z$  to a hazard function. Actually, this model does not directly estimate the survival functions, instead it attempts to fit it with the hazard function that has the form of

$$h(t | z) = h_0(t) \exp(\beta'z) \quad , \quad (3.10)$$

where  $h_0(t)$  is the baseline hazard and  $\beta$  is a parameter that represents the effect of covariate on the outcome. Assuming that one event occurs at a time  $t_i$ , the parameter  $\beta$  can be calculated by solving the partial likelihood:

$$PL(\beta) = \prod_{t_i} \frac{\exp(\beta z(t_i))}{\sum_{j:t_j \leq t_i} \exp(\beta z(t_j))} \quad . \quad (3.11)$$

### 3.2.3 Parametric models

It is possible to estimate the survival function by making parametric assumptions. Some commonly used distributions are the Weibull (or its special case the exponential) and the log-logistic distribution. The advantages of this model is its high efficiency when it deals with small sample size. However, it is difficult sometimes to find the best distribution that fits the given data which may mislead the analysis. For more details about each distribution as well as more developed information about the survival analysis, a reference to [Hosmer Jr and Lemeshow \(1999\)](#) is useful.

## 3.3 Geometry and soil numerical model

### 3.3.1 Geometry

The model's geometry is a levee of 9 m high composed of dry dense sand. The foundation is formed of 4 m loose to medium sand (LMS) on the top of a 6 m dense sand. The bedrock is located under the dense sand. The water table starts 1 m below the surface to keep the dam dry. The inclination of the levee is a slope of 1:3 (vertical: horizontal). The geometry in this work is inspired from [Rapti et al. \(2018\)](#); [Lopez-Caballero and Khalil \(2018\)](#), and is detailed in Figure 5.2.

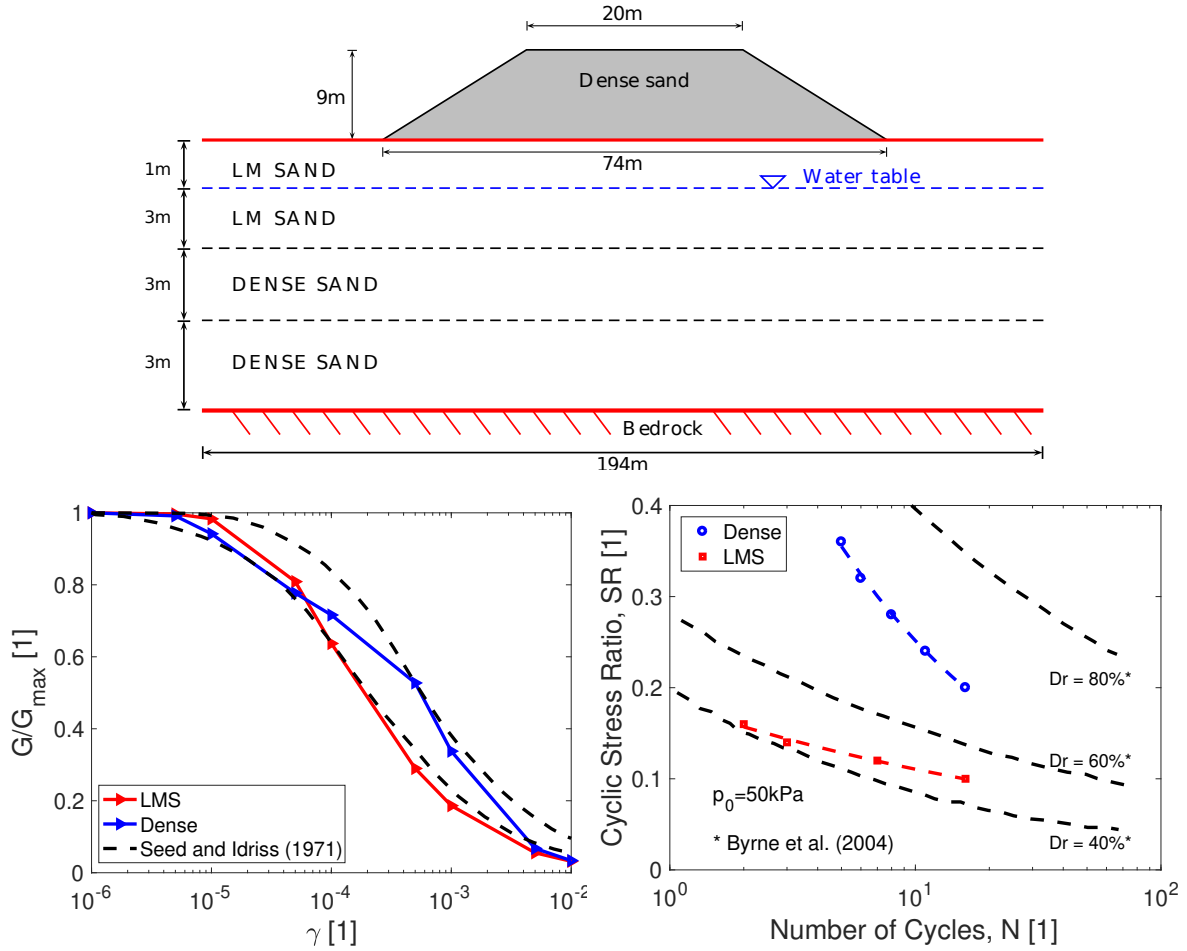


Figure 3.2: Geometry and behavior of the soil (Lopez-Caballero and Khalil, 2018)

### 3.3.2 Soil Constitutive Model

As for the constitutive model, the *Ecole Centrale Paris (ECP)* elastoplastic multi-mechanism model (also known as *Hujeux* model) is the one chosen for this study and is written in terms of effective stress. The non-linearity of this model is represented by four coupled elementary plastic mechanism: three plane-strain deviatoric plastic strain mechanism in three orthogonal planes ( $k$  - planes) and an isotropic plane. The model follows a Coulomb type failure criterion, contemplate the existence of dilatancy/contractancy phenomena, and use the critical state concept. The cyclic behavior is taken into account by a kinematical hardening that is based on the state variables at the last load reversal. The model is written in the concept of the incremental plasticity which divides the total strain into an elastic and a plastic part. Refer to (Aubry et al., 1982; Lopez-Caballero et al., 2007; Gomes et al., 2016, among others) for further details about the ECP model. For the sake of brevity only, some model definitions will be developed in the following. Considering the well-known sign convention of the soil mechanics which sets the positive sign to the compression forces, the yield surface of this numerical model is written in the  $k$  plane as follows:

$$f_k(\sigma, \varepsilon_v^p, r_k) = q_k - \sin \phi'_{pp} \cdot p'_k \cdot F_k \cdot r_k, \quad (3.12)$$

where  $p'_k$  and  $q_k$  are the effective mean and deviatoric values of the stress tensors and  $\phi'_{pp}$  is the friction angle at the critical state. The parameters that control the behavior of the soil are  $F_k$ , which controls the isotropic hardening associated with the plastic volumetric strain and  $r_k$ , which controls the isotropic hardening generated by the plastic shearing. These two parameters represent progressive friction mobilization in the soil. At perfect plasticity, the product  $F_k \cdot r_k$  reaches unity, and the Mohr-Coulomb criterion will be satisfied. The friction angle at the critical state and  $F_k$  depends on  $\varepsilon_v^p$  such that

$$F_k = 1 - b \ln \left( \frac{p'_k}{p_c} \right), \quad (3.13)$$

$$p_c = p_{c_0} \exp(\beta \varepsilon_v^p), \quad (3.14)$$

with  $\beta$  is the plasticity compression modulus and  $p_{c_0}$  is the critical stress that corresponds to the initial void ratio. The parameter  $b$  shapes the form of the yield surface in  $p' - q$  plane and varies between  $b = 0$  where it verifies the Mohr-Coulomb criterion and  $b = 1$  which will be the Cam-Clay criterion. The third variable of the yield surface which is the degree of mobilized friction angle  $r_k$  is linked to the plastic deviatoric strain  $\varepsilon^p$ . It shows the effect of the shear hardening and decomposes its behavior into pseudo-elastic, hysteretic and mobilized domains. It is given by:

$$\dot{r}_k = \dot{\lambda}_k^p \frac{(1 - r_k)^2}{a}, \quad (3.15)$$

where  $\dot{\lambda}_k^p$  is the plastic multiplier of  $k$  mechanism and

$$a = a_1 + (a_2 - a_1) \alpha_k(r_k), \quad (3.16)$$

with,

$$\begin{aligned} \alpha_k &= 0 && \text{if } r_k^{elas} < r_k < r_k^{hys}, \\ \alpha_k &= \left( \frac{r_k - r_k^{hys}}{r_k^{mob} - r_k^{hys}} \right)^m && \text{if } r_k^{hys} < r_k < r_k^{mob}, \\ \alpha_k &= 1 && \text{if } r_k^{mob} < r_k < 1. \end{aligned} \quad (3.17)$$

Notice that  $a_1$ ,  $a_2$  and  $m$  are model parameters and  $r_k^{hys}$  and  $r_k^{mob}$  designates when the domain shows hysteresis degradation. The isotropic yield surface is assumed to be :

$$f_{iso} = |p'| - d p_c r_{iso}, \quad (3.18)$$

with :

$$\dot{r}_{iso} = \dot{\varepsilon}_{v_{iso}}^p \frac{(1 - r_{iso})^2}{C_{mon} \frac{p_c}{p_{ref}}}, \quad (3.19)$$

where  $d$  is a model parameter representing the distance between the isotropic consolidation line and the critical state line in the  $(e - \ln p')$  plane and  $c_{mon}$  controls the volumetric hardening. In the model, an associated flow rule in the deviatoric  $k$  plane is assumed and the Roscoe's dilatancy law is used to obtain the increment of the volumetric plastic strain in terms of the characteristic angle  $\psi$  and a constant parameter  $\alpha_\psi$  such that:

$$\dot{\varepsilon}_{vk}^p = \dot{\lambda}_k^p \cdot \alpha_\psi \cdot \alpha_k(r_k) \left( \sin \psi - \frac{q_k}{p'_k} \right), \quad (3.20)$$

$\psi$  is the characteristic angle and  $\alpha_\psi$  a constant parameter. The density hardening is characterized by the critical stress  $p_c$  (Eq. 3.13) that considers all the mechanisms ( $k$  - planes and isotropic plane). This can be related to the plastic volumetric strain such that:

$$\varepsilon_v^p = \sum_{k=1}^3 (\varepsilon_v^p)_k + \varepsilon_v^{iso} = \frac{1}{\beta} \log \frac{p_c}{p_0} \quad (3.21)$$

### 3.3.3 Finite Element Model

The computations were conducted by the coupled FE modelling code GEFDyn (Aubry et al., 1986), using a dynamic approach derived from the  $\underline{u} - p_w$  version of the Biot's generalized consolidation theory (Zienkiewicz, 1991). The FE model is composed of quadrilateral isoparametric elements (3.5 m by 1 m) with eight nodes for both solid displacements and fluid pressures. An implicit Newmark numerical integration scheme with  $\gamma = 0.625$  and  $\beta = 0.375$  and a time step  $\Delta t = 10^{-3}$  was assumed in the dynamic analysis (Kuhl and Crisfield, 1999). The FE analysis is performed in three consecutive steps: i) a computation of the initial in-situ stress state due to gravity loads; ii) a sequential level-by-level construction of the embankment and iii) a sequential seismic loading analysis in the time domain. This computation is used in Section 3.6 and 3.8.1. For the computation of the sequential seismic loading developed in Section 3.7, and for the first motion precisely, the initial effective stresses, pore-water pressures and model history variables are stored to be used as initial state for the computation of the second ground motion. The storage of the history variable of the  $i$ th computation will be used as initial state of the  $i$ th+1 computation. More details regarding the calculation procedures are developed in each section.

### 3.3.4 Boundary Conditions

In the analysis, equivalent boundaries have been imposed on the nodes of lateral boundaries (i.e., the normal stress on these boundaries remains constant and the displacements of nodes at the same depth in two opposite lateral boundaries are the same in all directions). They are the response of a modeled infinite semispace. Hence, only vertically incident shear waves are introduced into the domain. The model is wide enough (194 m) to ensure that the effect of the boundaries on the response of the model can be neglected and also to satisfy the free field condition at the lateral boundaries. For the half-space bedrock's boundary condition,

paraxial elements simulating deformable unbounded elastic bedrock have been used (Modaressi and Benzenati, 1994). The incident waves, defined at the outcropping bedrock are introduced into the base of the model after deconvolution.

### 3.4 Assumptions of this chapter

For the study of the life-cycle of a levee subjected to sequential signals, basic assumptions are made:

- 1 The cumulative damage of the levee is due to the effect of the series of mainshocks only. The effect of aftershocks is not taken into account.
- 2 The effect of aging is not considered. For example, there is non consideration of the rain or sun, the wind load or any other type of loads that may be caused from external uncontrolled conditions. Also aging needs a deeper study about the material resistance, origin and age, which are not considered in this study.
- 3 At the beginning of the study, before the first seismic loading, the embankment is considered in its virgin and stable state. It does not have a history of earthquake loading.
- 4 The embankment is not subjected to any repairs during its lifetime.
- The constitutive model does not take into account the secondary consolidation or compression after each seismic loading.
- 5 The pore water pressure has dissipated after each seismic loading. It is ensured by adding a time-gap (recovery time) between each mainshock. This assumption is evaluated later in this chapter.

### 3.5 Input ground motions

The seismicity of the site requires the knowledge of the geographical location, the site characteristic and the magnitude-frequency distribution of the earthquakes. The seismic hazard analysis involves the quantitative estimation of the ground motion characteristic at a particular site with the help of deterministic or probabilistic approaches. The *Probabilistic Seismic Hazard Analysis (PSHA)* sets a predictive relationship for each ground motion parameter in each source. This method combines the uncertainties in the earthquake characteristics to obtain the probability that any IM will be exceeded at a particular time period. The hazard curve is used to identify the ground shaking level or the mean annual rate of exceedance ( $\lambda_{IM}$ ) (Rathje and Saygili, 2011). Once the main aspects that characterize the local seismic hazard are defined, it is possible to proceed with the selection of time histories. For this purpose, calibrations are used to adjust recorded ground motions and make them more representative of the analysis

conditions (Stewart et al., 2002; Yamamoto and Baker, 2013, among others).

Concerning the present work, the response of the embankment based on sequential seismic loading is the major focus of this chapter. The site of concern is a valley in Mygdonia that has an epicentral distance located about 30 km to the NE of the city of Thessaloniki in northern Greece. The magnitude  $M_w$  in this area is between 4.5 to 7.8. The fully probabilistic hazard analysis is adopted from the study of Aristizábal et al. (2018) on the same site. They generated a long catalog from 500 years to 50,000 years (equivalent to a probability of exceedance of 1% in 50 years). Hence, the magnitude-frequency distribution for 50,000 years catalog is shown in Figure 3.3a. More details regarding the PSHA are presented in the work of Aristizábal et al. (2018).

In the case of regions with lower seismicity, it is not easy to know with a higher level of accuracy, the expected ground motion scenarios. In practice, the effect of various GMPE's is studied. In addition, to generalize (to a certain extent) this work, two synthetic ground motion models were used: Rezaeian and Der Kiureghian (2012) and Boore (1996). They are designated as *Mod.R* and *Mod.B* accordingly. *Mod.R* uses an NGA database (Campbell and Bozorgnia, 2008) and for *Mod.B*, Aristizábal et al. (2018) adapted the Akkar et al. (2014) GMPE which provides a good representation of the European context. The hazard curve built from the generated catalog of the two synthetic ground motion models, is shown in Figure 3.3b. It can be seen from this figure that the 10% of exceedance for 100 years ( $\lambda_{IM} = 0.001$

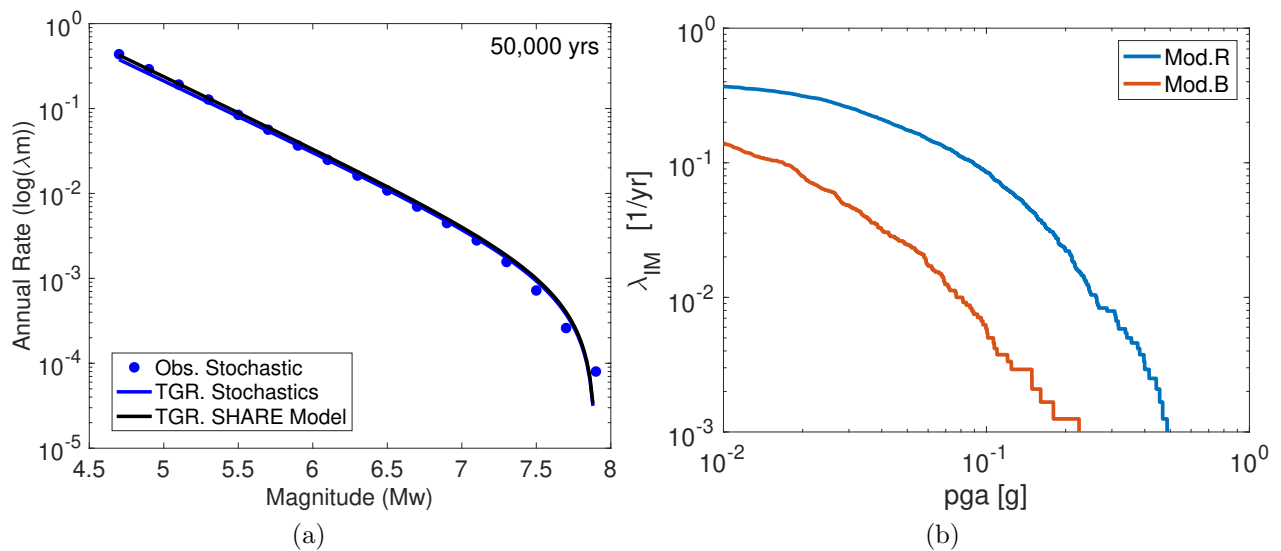


Figure 3.3: a) The magnitude-frequency distribution curve for 50,000 years catalog (Aristizábal et al., 2018) along with b) the PGA hazard curve of the generated synthetic ground motions

1/year) is 0.2 g for *Mod.B* and 0.5 g for *Mod.R*. Concerning the methods of each model, both are based on stochastic simulations. They tend to directly simulate the recorded ground motions with varied characteristics including the variability of the ground motion (Rezaeian and Der Kiureghian, 2012; Yamamoto and Baker, 2013, among others). For *Mod.R*, the method consists in rotating the recorded ground motion pairs into their principal axis and choosing only

the strong component. As for *Mod.B*, the stochastic method consists in distributing randomly the energy over a duration equal to the inverse of the low frequency corner. The different ground motion parameters can be obtained by using the random vibrating theory (Boore, 2003). For the sake of brevity, the deeper details and equations of each stochastic model are omitted, it is recommended to refer to each cited paper for more information. The spectral response of the two models is drawn in Figures 3.4a and 3.4b. It is clear that the spectral acceleration of *Mod.R* is higher than *Mod.B*.

Because it is difficult to understand the complexity of the earthquakes from one parameter

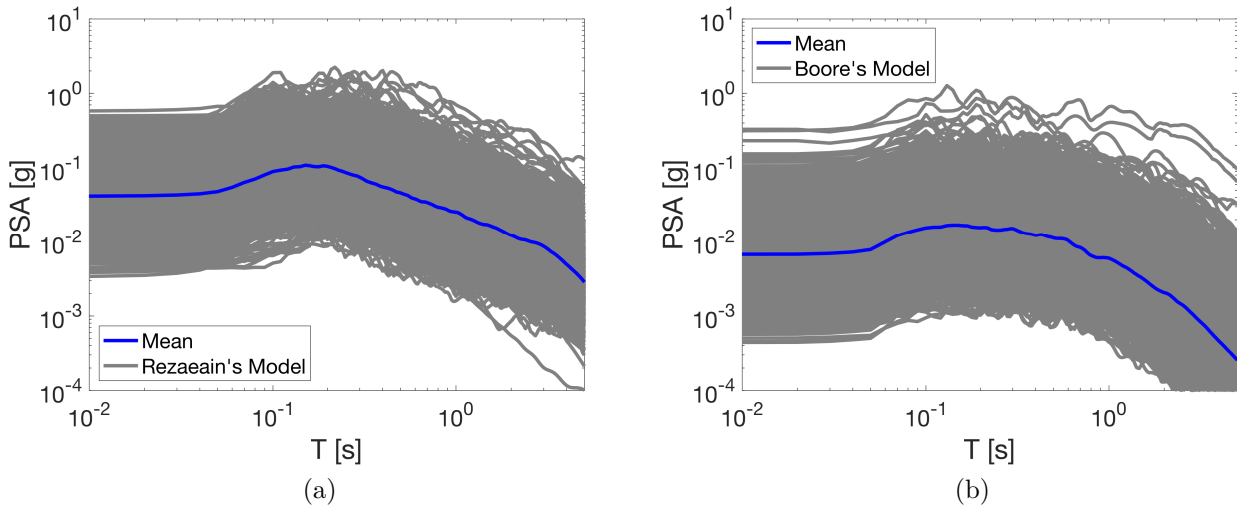


Figure 3.4: The response spectral of a) *Mod.R* and b) *Mod.B*

(Kramer, 1996), and based on Kawase (2011) there exists a proportional relation between the outcrop acceleration and the equivalent predominant frequency which is  $T_{v,a} = \alpha \cdot PGV / a_{max,out}$  with  $\alpha = 4.89$ . These three parameters are represented in Figure 5.11a. *PGV* is represented as dashed lines. Although the two models represent the same site, they use different relationships to determine their parameters and in consequence the corresponding IMs. This proves the difference in the results shown in Figure 5.11a. They are compatible in their frequency interval but not in their peak acceleration; *Mod.R* has a higher acceleration than *Mod.B*. Also, the majority of the motions of *Mod.B* have a *PGV* less than 10 cm/s which is not the case for *Mod.R*.

After identifying and presenting the different synthetic ground motion models used in this study, a site-specific seismic analysis will take place. The response of the embankment will be calculated after a set of unsequenced ground motion records.

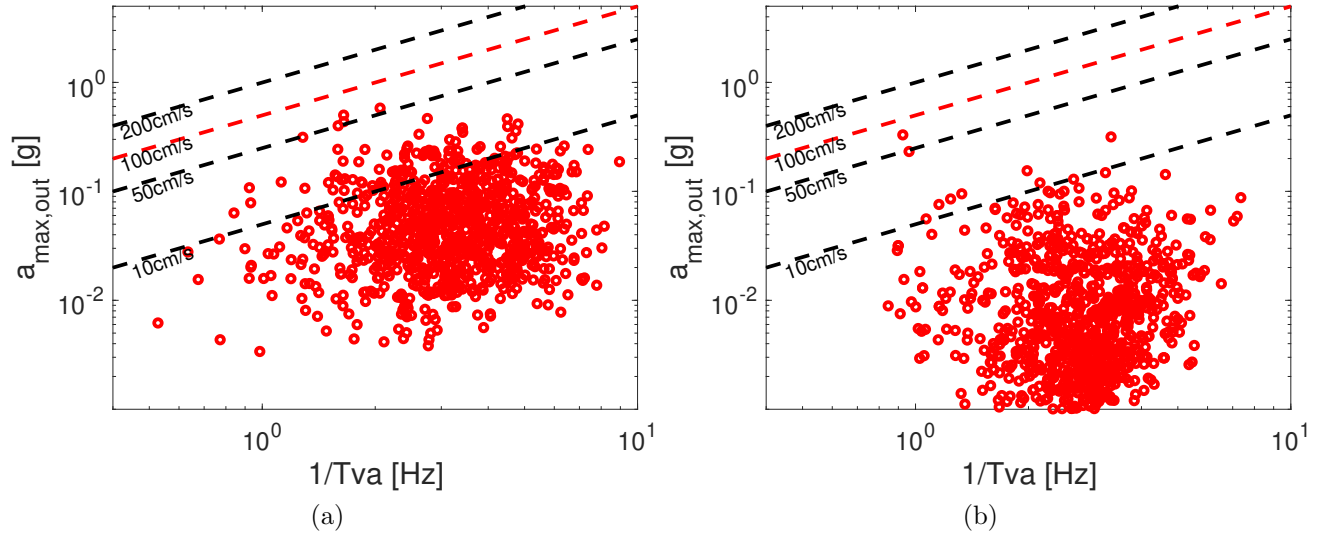


Figure 3.5: The distribution of some ground motion parameters of the two models: a) *Mod.R* and b) *Mod.B*

### 3.6 Site-specific seismic analysis

In Section 3.5, the used synthetic ground motions were presented. Two models were used (*Mod.R* and *Mod.B*). In this section, the response of the embankment based on each seismic load will be developed. Since the crest settlement is the mode of failure normally studied in case of embankments, it will be the parameter for the damage quantification. It is calculated by considering each ground motion as a single event. The percentage relative crest settlement as calculated by Swaisgood (2003) is the ratio of the vertical displacement of the crest to the height of the dam with its corresponding foundation:  $\delta u_{z,rel}/H$ , given that  $H$  in this study is 19 m. The relative crest settlement is divided into damage levels (Swaisgood, 2003; Lopez-Caballero and Khalil, 2018). The limit values of these levels is still debatable but the ones chosen for this study are shown as dashed lines in Figure 5.10a. When  $\delta u_{z,rel}/H \leq 0.02\%$ , there is *No* damage, if  $0.02\% < \delta u_{z,rel}/H \leq 0.1\%$ , the damage is *Minor*, if  $0.1\% < \delta u_{z,rel}/H \leq 1\%$ , the damage is *Moderate* and finally if  $\delta u_{z,rel}/H > 1\%$ , the damage is *Serious*. Figure 5.10a shows the relative crest settlement obtained using the two models: *Mod.R* and *Mod.B*. As expected and as seen in Figure 5.10a, the relative crest settlement  $\delta u_{z,rel}/H$  increases with the peak ground acceleration for both models. Since the acceleration of *Mod.R* is higher than *Mod.B* (proved in Section 3.5), *Mod.R* induces more damage than *Mod.B*. Comparing the damage levels, it can be seen that *Mod.B* in majority, did not show any damages; few values of  $\delta u_{z,rel}/H$  were in *Minor* damage and only one shows *Serious* damage. Whereas *Mod.R* shows more variability in the damage levels that lies in majority in *Minor* and *Major* damages. But on the contrary of Figure 3.6b, only four ground motions showed *Serious* damage for *Mod.R*. In addition, a hazard curve for the crest settlement was obtained using the two stochastic models (Figure 3.6c). The damage levels are also represented as dashed green lines in this figure. It can be seen for example that with a 10% of exceedance in 100 years, the obtained co-seismic settlement using *Mod.R* corresponds

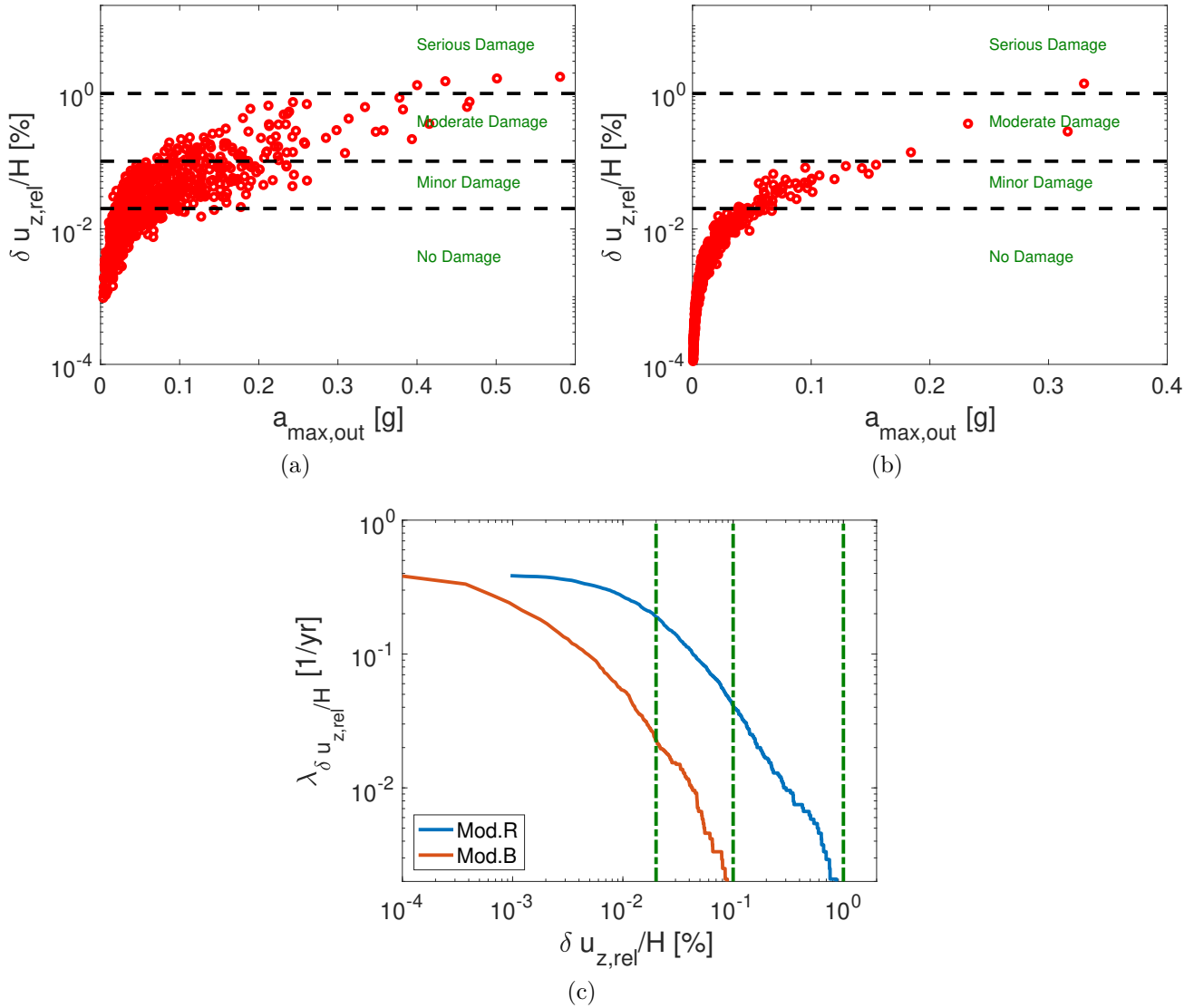


Figure 3.6: The variation of the crest settlement with respect to the outcrop acceleration of the two models: a) *Mod.R* and b) *Mod.B* and c) the obtained crest settlement hazard curve.

to the *Serious damage* level. Whereas for *Mod.B*, for the same probability, *Moderate damage* is the corresponding level.

It was seen in this section that the two synthetic ground motion models show different results in terms of the embankment performance. These results highlight the importance of the choice of the ground motion model.

### 3.7 Survival analysis of the Levee

Also in the scope of the PBEE methodology, the lifetime of the structure is the length of time until failure occurs. In order to calculate it, the degradation of the structure over time should be considered. Thus, the study of its performance due to sequential loading is required. In Section 3.6, it was shown that the two synthetic ground motion models gave different responses

and that  $Mod.R$  induced more damage. Thus, this model will be used to compute the seismic sequential loads as well as the survival life of the tested embankment. Assuming that the working life of the embankment (i.e.  $T_{window}$  in Figure 3.1) is 100 years, the occurrence rate of event during this life corresponds to 44 acceleration time histories (i.e.  $N_{shock} = 44$ ) which means  $\lambda_{earthquake} = 0.44$  events/year. In order to be statistically representative, a large number of subsets must be used. In this work, 21 subsets (i.e.  $N_{subset} = 21$  in Figure 3.1) compatible with the seismic hazard of the tested site were used. The 44 events were permuted randomly 10 times (i.e.  $k = 10$  in Figure 3.1) for each subset. In total, 210 sequences of ground motions were created for a serviceable life of 100 years. It should be reminded that for the sequential computation, the storage of the history variable of the  $i$ th computation will be used as initial state of the  $i+1$  computation.

This section is divided into two parts. The first part develops the quantification of the relative crest settlement of the embankment for each sequence. The second part develops its survival analysis.

### 3.7.1 Crest settlement in the sequences

Based on Iervolino et al. (2015), the damage accumulation is due to either the aging of the material or the sequential earthquakes. The first degradation model is called the deterioration-based: the system degrades progressively due to internal factors such as aging, corrosion in steel or wear (Nakagawa, 2007; Ranjkesh et al., 2019). The second degradation model is the shock-based model where the system is subjected to a sudden decrease in its performance due to an earthquake (Nakagawa, 2007; Ranjkesh et al., 2019). In this work, the aging is not taken into consideration because it needs a deeper understanding of the material origin, resistance and age. As explained in the introduction of this section, the event of interest is the occurrence time of different mainshocks sequences.

In order to ensure that the pore water pressure is dissipated completely after each mainshock (the sixth assumption in this study), a recovery time of 30 seconds is considered. It was chosen in a way to ensure the dissipation of  $\Delta p_w$  without the generation of expensive computational time. In order to validate if this recovery time is enough for the dissipation of  $\Delta p_w$ , one input ground motion is considered and a post-seismic loading is applied. The results are shown for a sample located at 3 m depth under the center of the embankment (Figure 3.7a) and at free field (Figure 3.7b). It is interesting to note that after the co-seismic loading, the excess pore water pressure is near zero in the two locations. The post-seismic loading, where the embankment is returned to its static case, proves that chosen recovery time can be enough since the two curves overlapped and follow the same path.

Concerning the damage quantification of each sequence, the relative crest settlement  $\delta u_{z,rel}/H$  is calculated based on the method developed Section 3.6. Figure 3.8a shows  $\delta u_{z,rel}/H$  and the corresponding damage levels for all the seismic sequences. To better visualize the results and conduct the analysis, Figure 3.8b shows  $\delta u_{z,rel}/H$  in the form of box-plots (aka Speaker style).

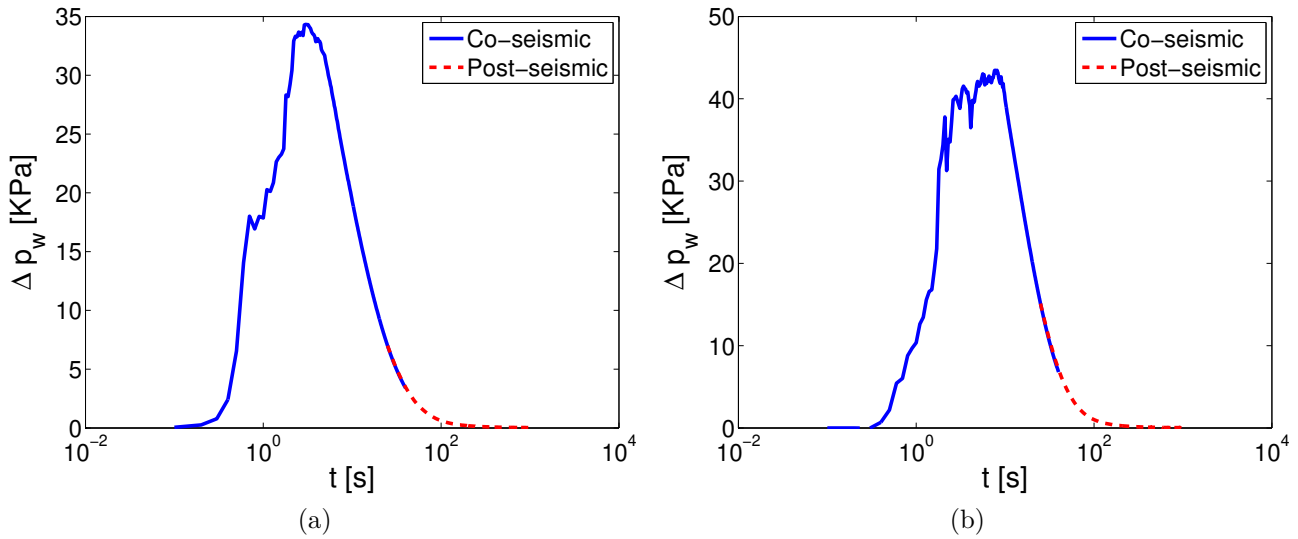


Figure 3.7: The excess pore water pressure of one mainshock a) under the center of the embankment and b) at free-field

A small explanation about this form of graph is discussed herein before proceeding in the discussion of the results. The median of the tested data is represented by the small bars in the boxes. The boxes represent 50% of the data and their boundaries considers 25th and 75th percentile of the data respectively. The two extremes are 1.5 times the distance between the two percentiles, and the red dots above or below the box-plots are the outliers.

Back to the analysis of the relative crest settlement of *Mod.R* sequences and as expected,

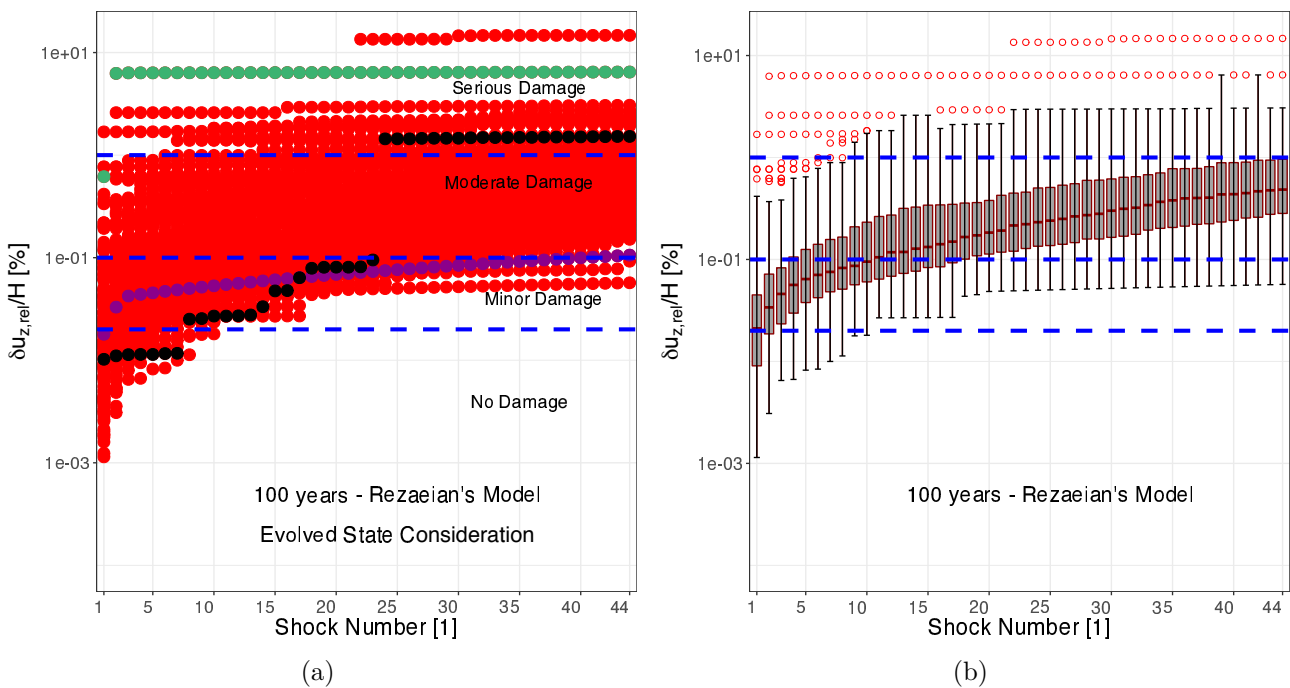


Figure 3.8: The relative crest settlement of the sequential signals a) for all the sequences and b) in form of box-plots

$\delta u_{z,rel}/H$  increases when the number of shocks increases (Figures 3.8). Based on these results, the increment was either progressive during the sequential load, or sudden after few mainshocks. For this purpose, three curves are selected for interpretation. For example, the purple curve in Figure 3.8a shows that after the first shock, the embankment had *No* damage. The relative crest settlement kept increasing during this sequence but in a small manner. At the end of this sequence, the embankment showed a damage level located in the interface between *Moderate* and *Minor* damage. This case can be considered “safe”, in the point of view that the cumulative damage did not lead to failure. On the opposite, the green path shows a *Moderate* damage directly after the first shock. The embankment was not able to resist the load repetition and hence it failed drastically after the second shock till the end. For the path in black, the damage was progressive. The embankment had *No* damage until the seventh shock. After it,  $\delta u_{z,rel}/H$  increased progressively until after the 23rd shock, the embankment was not able to resist and the induced damage was drastic. It should be mentioned that previously, in Section 3.6, only four ground motions showed *Serious* damage. The occurrence of these motions in the sequence, either led to a good densification of the soil and hence less damage or it increased the crest settlement to a severe case.

Another statistical way to visualize the results is found in Figure 3.8b. Based on the median value,  $\delta u_{z,rel}/H$  increases with the shock increment. For the first shock, 50% of the data showed *Minor* damage. But after the 44th shock, 50% of the data showed *Moderate* damage. The upper quarter of the data showed *Serious* damage. The outliers are presented in the upper part of the graph which proves that the embankment fails completely for some cases at the beginning of the sequences. An associated explanation is also represented in Figure 3.9

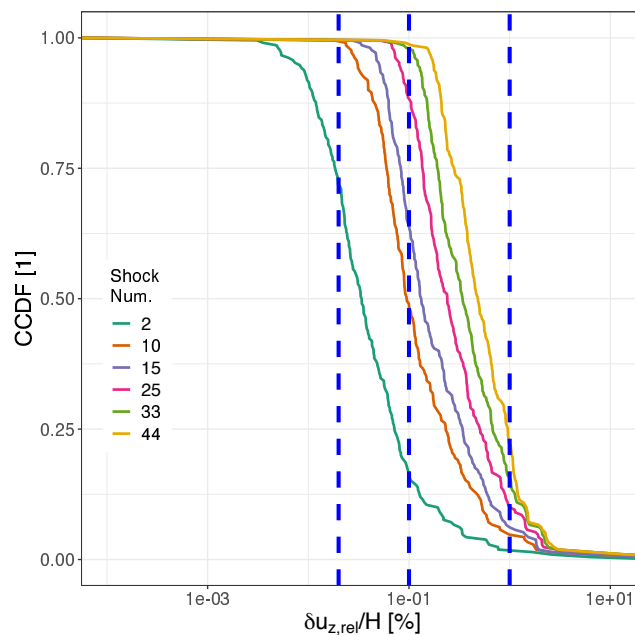


Figure 3.9: The complementary cumulative distribution function (CCDF) of the relative crest settlement

with the empirical Complementary Cumulative Distribution (CCDF). This figure shows the distribution of the relative crest settlement after a specified number of shocks. The damage levels are also represented by blue dashed lines. For the damage line 0.1% for example, the distribution of the relative crest settlement increases when the shock number increases. After the 10th shock, 50% of the tested sequences shows that the embankment will be deteriorated in a *Moderate* damage. Usually in engineering practices, the green curve in Figure 3.9, is similar to the ones conducted in Section 3.6 where the response of the embankment is calculated after the occurrence of independent earthquakes. It was shown so far in this work, that this curve can be misleading and may not represent the behavior of the embankment for a long term.

On the other hand, since the ground motions sequences are chosen for a working life of 100 years, the change in the damage levels between the years is interesting to identify. Figure 3.10 shows the Damage Level (DL) of the selected ground motion as function of the magnitude and the source-to-site distance. Since the acceleration time histories during the lifetime are permuted randomly, it is evident that the ground motions are not in the same position in the first, 50 and 100 years. The damage levels are numerated from 1 to 4 to represent *No* damage to *Serious* damage respectively. From Figure 3.10a, after the first ground motion, very few responses show damage level of class 3. The other responses were either 1 or 2. After 50 years of sequential ground motions (Figure 3.10b), it is clear that there is no damage level of class 1 and very few of class 2. Finally, at the end of the chosen working life (i.e. 100 years), more damage levels of class 4 are shown (Figure 3.10c), which means that the embankment has a high risk to fail at the end. This synthesis is similar to the one found previously in this section with a different type of analysis.

As a partial conclusion of this section, it is noted that the loading history of the embankment will definitely affect its behavior in the long term. Even if the embankment was intact after few shocks, the failure can be reached in the working life. In addition, some sequences showed that the embankment was drastically damaged after few shocks.

### 3.7.2 Survival analysis

The survival analysis is the analysis of data involving time needed for an event of interest to happen. It is also known as the time-to-event data. Detailed explanation about this analysis were developed in Section 3.2. The event of interest in the scope of this study, is the occurrence of mainshocks during a working life of 100 years. For this purpose, the survival function is calculated based on the Kaplan-Meier estimator (Kaplan and Meier, 1958). The estimated probability is usually a step function and is shown in Figure 3.11. The three damage levels are represented in this figure. An important quantity that can be derived from this figure, is the Mean Time To Failure (MTTF, the expected time to failure for a non-repairable system) that is also represented. After two years (i.e.  $MTTF = 2.27$  years), 50% of the cases survived the damage level of class 2 (i.e. *Minor* damage). Whereas the MTTF of class 3 (i.e. *Moderate* damage) is 25 years. At 100 years, the survival probability of this damage level is zero. For

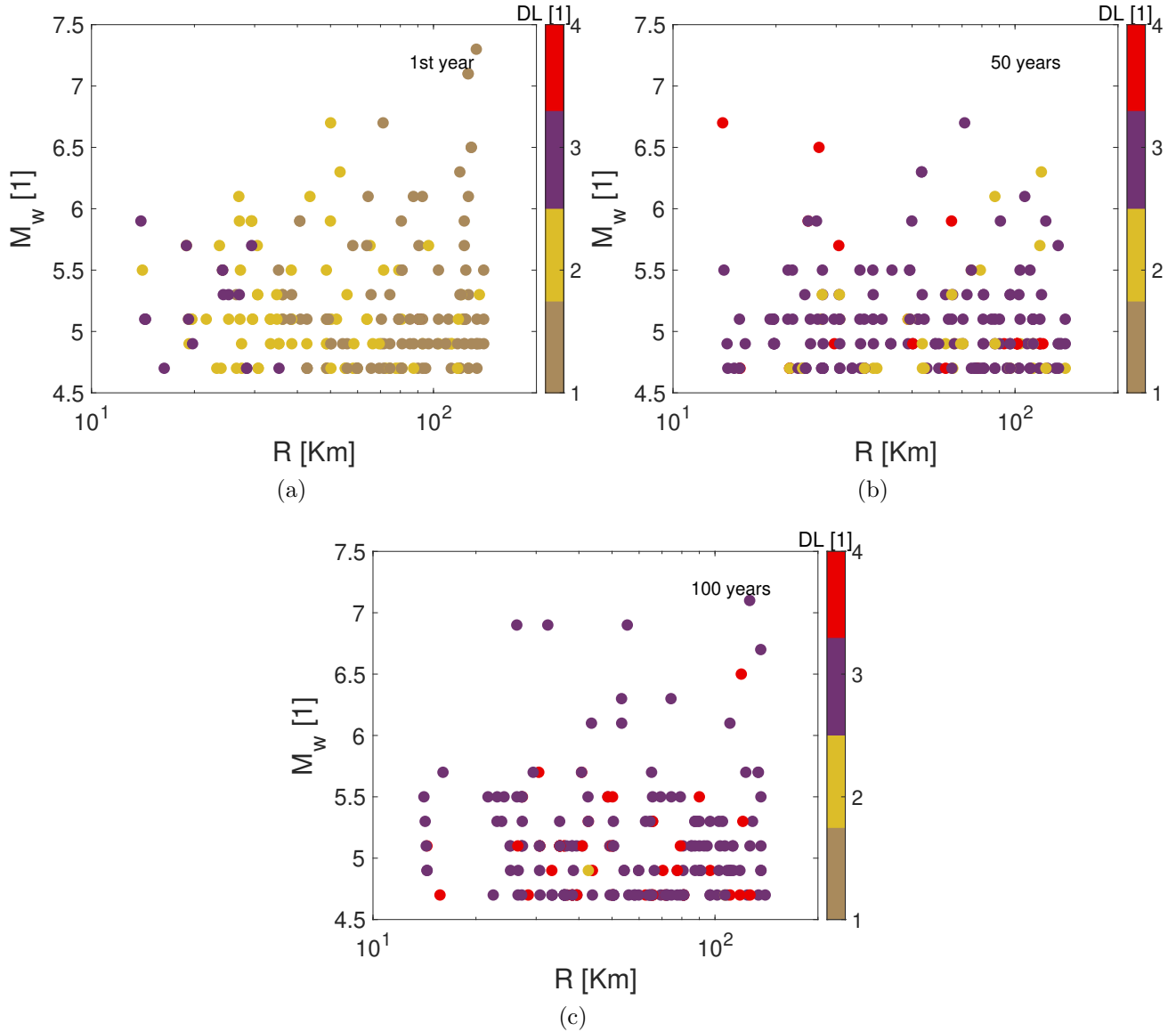


Figure 3.10: The damage levels of  $Mod.R$  with respect to the magnitude and distance of the seismic motions

*Serious* damage, 25% of the cases were not able to survive.

In all the preceding, the survival function was conducted based on a non parametric approach. It is important to mention that even when the parameters of the distribution are unknown, distributions such as Weibull, lognormal, exponential or others, can be fitted from results obtained from non parametric methods. The accuracy of this fitting is ensured by the Kolmogorov-Sminorv (KS) test (Lilliefors, 1967). It was carried out for each empirical distribution of the two critical damage levels. Both, the Weibull and its special case the exponential, could be considered according to the KS test. It should be noted that the distribution of the survival function in case of Weibull is  $S(t) = \exp(-\alpha t^\gamma)$  and in the case of exponential is  $S(t) = \exp(-\lambda t)$ . Table 3.1 shows the obtained parameter of each damage level from the survival function found in Figure 3.11. The interpretation of these results are pointing on the idea

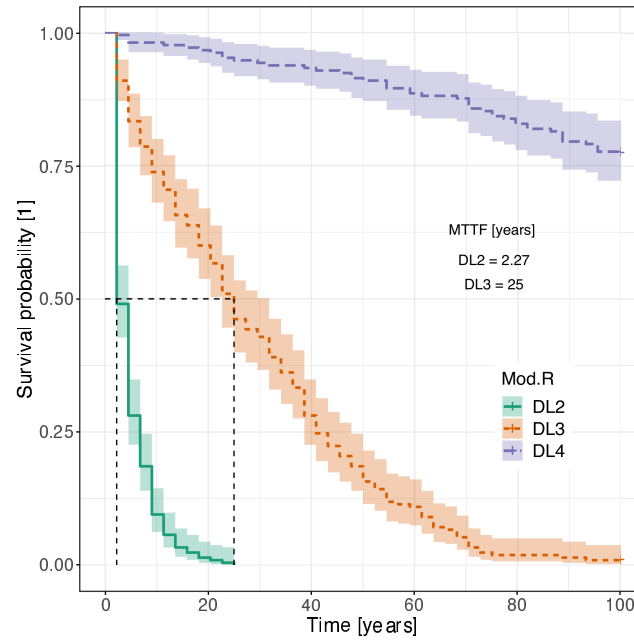


Figure 3.11: The survival probability of the levee for *Mod.R*

that the Weibull distribution is more appropriate to represent the slow deterioration overtime whereas the exponential distribution can be used to represent the deterioration after sudden shocks. Since the *Moderate* damage was mainly due to the progressive increase of the crest settlement, its distribution can be approximated to follow a Weibull distribution. Whereas *Serious* damage is more likely to follow the exponential distribution because the failure was sudden in most of the cases. Thus, the results obtained for both distributions confirm the biases that

	Weibull		Exponential
	$\alpha$ [1]	$\gamma$ [1]	$\lambda$ [1]
<i>With Recovery Time (Section 3.7.2)</i>			
<b>DL3</b>	0.058	0.909	0.037
<b>DL4</b>	$1.9 \cdot 10^{-3}$	1.057	$2.5 \cdot 10^{-3}$
<i>No Loading History (Section 3.8.1)</i>			
<b>DL3</b>	0.065	1.344	0.014
<b>DL4</b>	$5.77 \cdot 10^{-5}$	2.387	0.018
<i>No Recovery Time (Section 3.8.2)</i>			
<b>DL3</b>	0.024	1.175	0.044
<b>DL4</b>	$9.19 \cdot 10^{-5}$	1.961	0.007

Table 3.1: The distribution parameters of *Moderate* and *Serious* damages for the three tested cases of this work

could be introduced in a parametric approach when the survival function is not well known.

## 3.8 Influence of various parameters on the survival analysis

To this point of this article, it was represented an analysis of the relative crest settlement of an embankment after both, a single event and sequential events of mainshocks. This later considered sequences of 44 mainshocks with a recovery time between each. In addition, the survival function was calculated based on a non parametric approach. In this section, answers on the following questions will be discussed respectively:

- What if the loading history was not considered? Technically, what will happen if the embankment was returning to its initial state after each ground motion of each sequence.
- What if there was no recovery time between the GM which means that the mainshocks are sequenced in a back-to-back form?
- How the response will differ if the analysis was conducted based on a different synthetic ground motion model (e.g. *Mod.B*)?

### 3.8.1 Effect of the loading history

In soil precisely, the history of loading plays a major role for its future behavior. Many previous studies have been conducted to check the effect of past histories on the response of geo-structures (i.e. [Sica et al. \(2008\)](#); [Lopez-Caballero et al. \(2016\)](#)). Moreover, it was seen in the previous section, that even if the embankment was intact after few years, it might be damaged in a long time. Its state evolves based on the years of loading. Considering now the sequences are formed by simply adding the responses found in [Figure 3.6a](#) based on their occurrence, [Figure 3.12a](#) will be obtained. Based on this figure, the results did not show too much dispersion and few outliers, on the contrary of the results in [Figure 3.8b](#). The embankment started its cycle of life with a *Minor* damage, to attend a *Serious* damage after half of its lifetime. The difference between the response of the embankment with consideration of its evolved state ([Figure 3.8b](#)) and that presented in [Figure 3.12a](#) is that the last one over estimates the results. The embankment settles less when in its history, it was subjected to many loads: this is due to the consolidation of the soil and the evolution of its properties.

Concerning the survival analysis of this case ([Figure 3.12b](#)), after approximately 7 years (i.e.  $MTTF = 6.92$  years), the embankment will moderately survive the applied sequential loads. Whereas after almost half of its serviceable life (i.e.  $MTTF = 52.37$  years), it will be damaged drastically. These results are very different from the ones obtained in [Section 3.8.2](#). The parameters of the survival function distributions are shown in [Table 3.1](#).

Maybe this analysis satisfies the decision makers as they consider it “preventive” for security reasons, but besides the fact that it is not realistic, it could mislead the design and may generate additional useless costs.

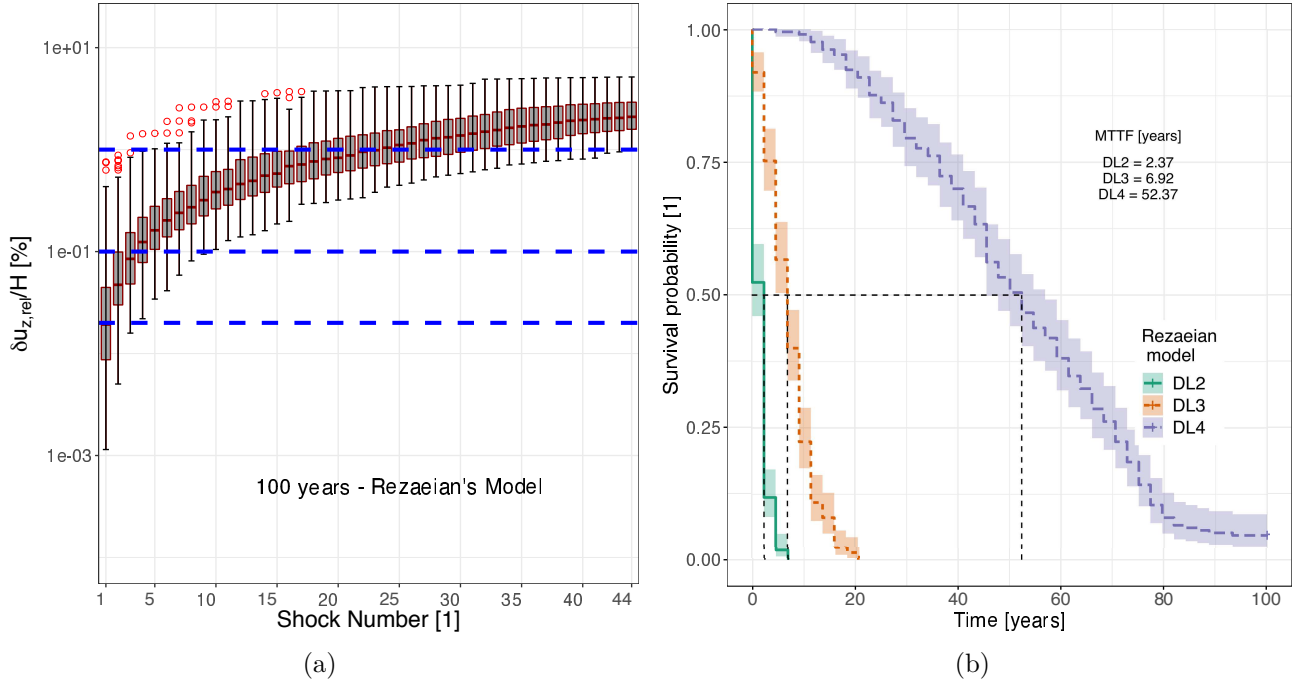


Figure 3.12: The relative crest settlement with No loading history a) in the form of box-plot and b) its survival analysis

### 3.8.2 Importance of the recovery time between the sequences

Based on codes and literature, a system is considered to fail when its cumulative damage due to shocks exceeds its capacity of resistance (Eurocode, 1994; Iervolino et al., 2015; Ranjkesh et al., 2019, among others). On the opposite of the structural systems, geotechnical systems have in majority, recovery times that if not considered in the analysis, it may lead to severe and over estimated damages. In this section, a comparison of the survival function of three different types of shock-based approaches is considered. The approaches are i) the consideration of the the recovery time between each shock (Section 3.7.2), ii) taking the shocks in a back-to-back form and iii) the consideration of the loading history (Section 3.8.1). The results are shown in Figure 3.13. The survival probability was analyzed for two damage levels: *Moderate* damage ( $0.1 < \delta u_{z,rel}/H < 1$ ) in Figure 3.13a and *Serious* damage ( $\delta u_{z,rel}/H > 1$ ) in Figure 3.13b.

For both damage levels, it can be seen that the loading history plays a major role in the response of the embankment: without its consideration, the relative settlement was over estimated. This over estimation may be beneficial if the region was of low seismic activity. But for some cases, it can be a result of high cost of construction/reparation. Considering the *Moderate* damage (Figure 3.13a) and comparing the orange and the green curves, it can be noticed that there are five years of survival life that are not taken into account if the recovery time was not ensured. In addition, it is clear, from the different values of the MTTF, that loading history has an important effect. Whereas for the *Serious* damage (Figure 3.13b), it is important to mention that the embankment did not reach the MTTF when the recovery time was ensured. The parameters of the survival function distribution are shown in Table 3.1.

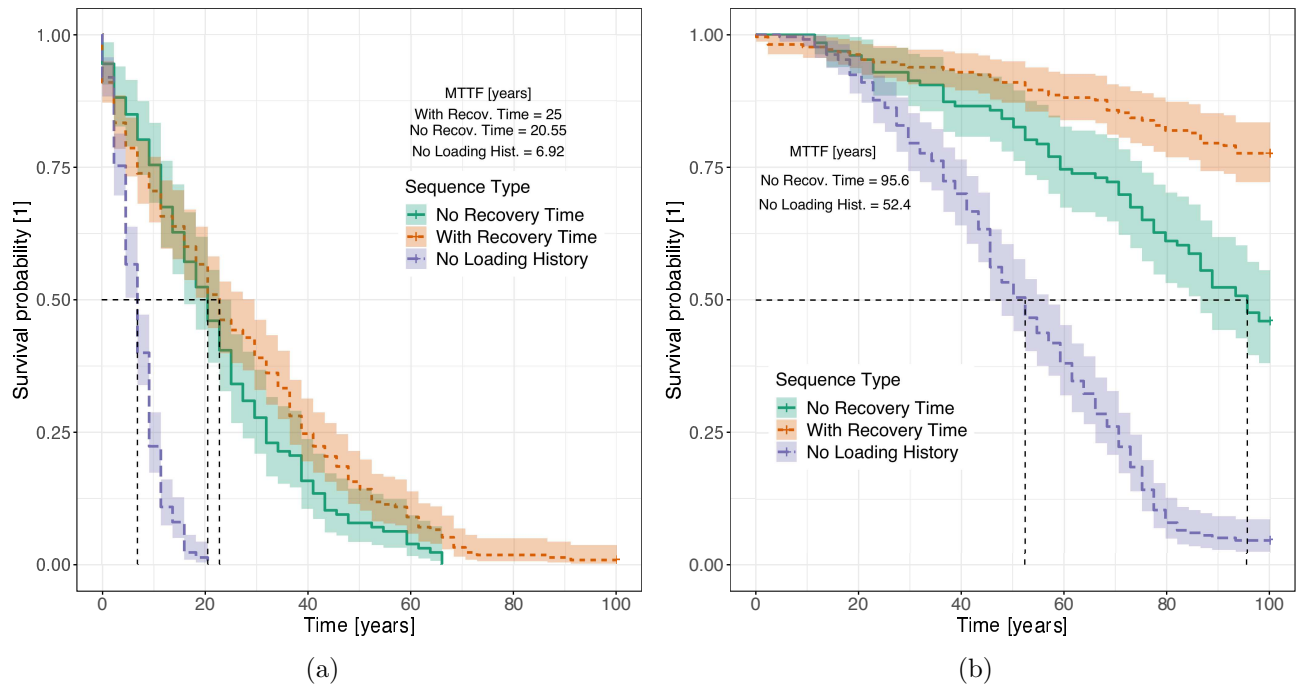


Figure 3.13: The survival analysis of the different sequence types for a) Moderate damage and b) Serious damage

### 3.8.3 Effect of different synthetic ground motion models

The survival analysis in this chapter was conducted based on the synthetic ground motion model called *Mod.R* since it showed more variety in the response of the embankment and its damage level (Section 3.6). This section will consider *Mod.B* in a back to back form (or with no recovery time) since this type of calculations needs less computational time. Adopting the same strategy developed in this chapter to calculate the survival functions, the results are obtained in Figure 3.14 as function of two damage levels: *Minor* damage (DL2) and *Moderate* damage (DL3). Also in this figure, a comparison of the survival function with *Mod.R* in back-to-back form is shown. It is clear how the survival function for *Mod.B* is very optimistic and shows that the embankment is able to resist the shocks during its lifetime. At 41 years for example, there is 50% chance that the embankment will survive a damage level of DL2 if it was subjected to *Mod.B*, whereas based on *Mod.R* it needs 2 years (Figure 3.14a). Also for DL3, based on *Mod.B*, the embankment have high chances to survive this damage level whereas based on *Mod.R*, after 20 years, it will have only 50 % chance to survive it (Figure 3.14b). It is evident that the response varies with the ground motion model, which points on the importance of the choice of the stochastic method to generate the ground motions.

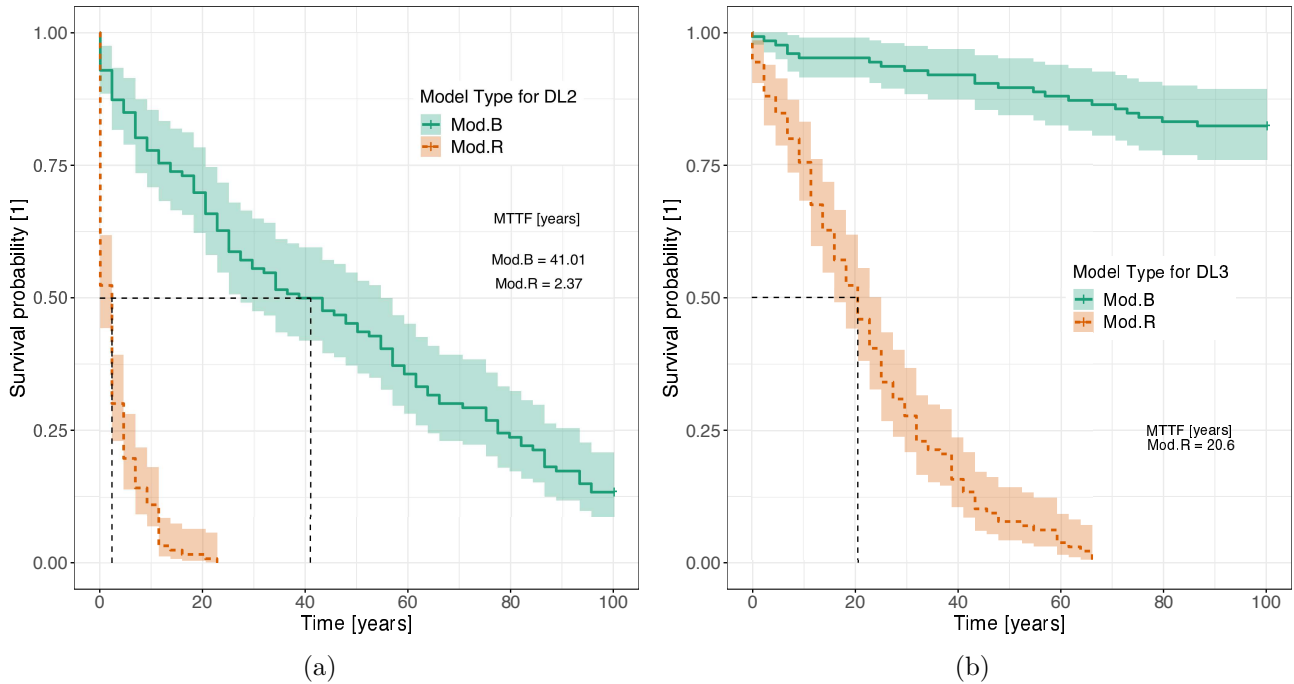


Figure 3.14: The survival analysis of *Mod.B* in back-to-back form for a) DL2 and b) DL3

### 3.9 Concluding remarks

This chapter presents the survival analysis of a liquefiable embankment subjected to sequential earthquakes. First, it started with a site-specific seismic analysis where the damage was quantified after a set of unsequenced ground motion records. To generalize this work, two synthetic ground motion models were used. They were extracted from the studies of [Rezaeian and Der Kiureghian \(2012\)](#) and [Boore \(1996\)](#) and were designated in this chapter as *Mod.R* and *Mod.B* respectively. Then, one synthetic model (e.g. *Mod.R*) was chosen for the analysis. Sequential mainshocks were created accordingly, and the damage was calculated after each sequence. A total of 210 sequences composed of 44 acceleration time histories each, were generated in order to represent a lifetime of 100 years. Finally, the survival function and its corresponding Mean Time To Failure (MTTF) were calculated. For these purposes, an elastoplastic multi-mechanism soil behavior model was used with the help of the finite element code (*GEFDyn*).

The conclusions that this chapter have found are the following:

- For the site-specific seismic analysis, *Mod.R* showed a large variety of the response than *Mod.B*. The relative crest settlement of this model was mainly between *Minor* and *Moderate* damage levels.
- The cumulative damage in this study showed two responses for the embankment: i) a progressive deterioration that did not necessarily lead to drastic damages or ii) a sudden deterioration after few years.

- Based on the survival function, it was shown that after 25 years ( $MTTF = 25$  years), the embankment have 50% chance to present *Moderate* damage. Whereas it will not show *Serious* damage during its lifetime. These results prove that classical or short-term analysis are not always a good idea to know the global performance of the embankment.
- The distribution of the survival function for the *Moderate* damage level, follows a Weibull distribution whereas that of the *Serious* damage level is more likely to be represented by an exponential distribution. In addition, parameters of each distribution were calculated for each type of analysis.
- The consideration of the loading history for geo-structures is very important since the  $MTTF$  changed from 6 years to 25 years. In addition, a recovery time between each ground motion is essential in order to ensure the dissipation of the excess pore water pressure and it was shown in this study, that the  $MTTF$  is also affected.
- It is very important to pay attention to the chosen synthetic ground motion model since the performance might highly be affected. The  $MTTF$  for *Mod.B* was under estimated comparing to *Mod.R*.

It should be noted that the above conclusions are based on the results corresponding to soil behavior models and stochastic GM models adopted in this work.

### 3.10 Complements to this chapter

The work presented in this chapter was published as an article in *Soil Dynamics and Structural Engineering* Journal. Hence, it was subjected to comments and accurate critics that were out of the scope of the published paper, however, they were treated and discussed as a complement to the work. Thus, it can be interesting to provide them in the following.

- a) *What does the events of Figure 3.3 actually represent?*

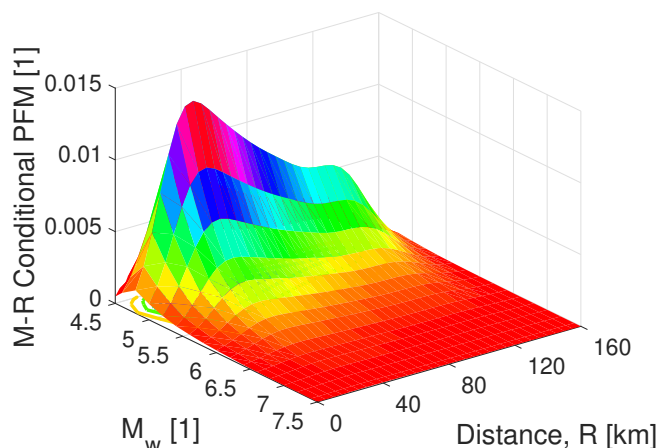


Figure 3.15: The PMF of  $M_w$  and  $R$

This work is based on the disaggregation of scenarios from a PSHA conducted by [Aristizábal et al. \(2018\)](#) in the region of Mygdonia, Greece. Figure 3.15 shows the joint Probability Mass Function (PMF) of  $M_w - R$  for the studied cite. In addition, and similar to what was mentioned in this chapter, in order to be compatible with the PSHA and the assumed working life of the embankment, the used event rate of the mainshock issued from the work of [Aristizábal et al. \(2018\)](#), is assumed to be  $\lambda = 0.44$  [events/year], which means 44 acceleration time histories during a design working life of 100 years. To be statistically representative, a large number of subsets should be used. In this work, 21 subsets compatible with the seismic hazard of the tested site were considered. Every subset contains 44 compatible acceleration time histories. Then, the 44 ground motions of each subset were randomly permuted 10 times to have a variety of sequences (which means 21x10 sequences and 21x44 mainshocks).

- b) *How was the [Rezaeian and Der Kiureghian \(2012\)](#) model used for small magnitudes? Was it modified in any way?*

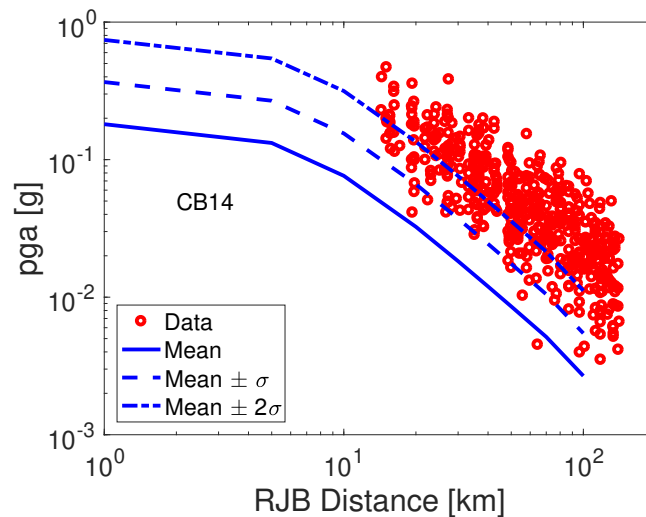


Figure 3.16: The compatible IM with the GMPE for  $M_w = 5.0$  conditioned on  $S_a$  of 0.41g

The magnitude of the tested site is between 4.5 to 7.8. Even if [Rezaeian and Der Kiureghian \(2012\)](#) model is for  $M_w$  greater than 6.0, it was verified that the obtained IMs (PGA in this case) are compatible with the selected GMPEs for lower magnitudes. Figure 3.16 is drawn for a magnitude of 5.0. It is noted from this figure, that even if the accelerations are greater than the mean values, they are close to the limit of mean +  $2\sigma$ . It should not be denied that a more complex stochastic model can be used and may probably represent the hazard context with more precision. However, as mentioned in the Introduction section of this chapter, any other stochastic model or an earthquake recurrence model is also suitable to be used under the proposed methodology.

- c) *The computed survival probabilities are in reality conditional probabilities, conditioned on the scenarios chosen (Figure 3.3). How does the survival*

*probability change if different time windows were considered?*

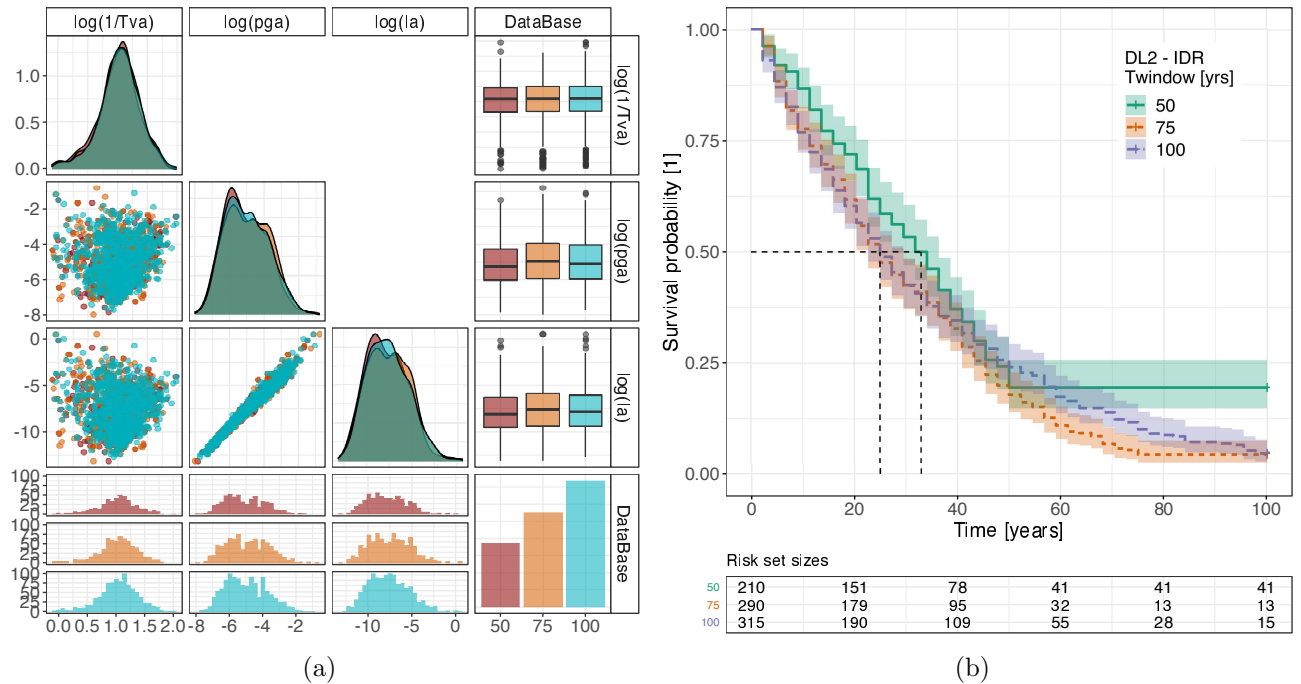


Figure 3.17: a) The logarithmic distribution of some ground motion parameters of  $Mod.R$  for the tested time windows and b) The survival analysis for a time window of 50, 75 and 100 years, adapted from the data of Lopez-Caballero et al. (2020)

One of the key objectives of the survival functions is to know if the MTTF is lower than the design time window. From the recent study conducted by Lopez-Caballero et al. (2020), data were adapted to show if the time window could affect both, the computed survival probabilities and the MTTF for a particular damage level. For this purpose, three time windows were selected: 50, 75 and 100 years. The logarithmic distribution of the IMs of the seismic input of every window is plotted in Figure 3.17a. It can be noticed that the density distribution of the databases are the same, similarly for the scatter plots. For the boxplots, clearly, the median value is slightly close for 75 and 100 years, and is smaller for 50 years. It should be mentioned that the number of data cannot be the same between the three time windows, since for a long time period, more earthquake scenarios can occur. Concerning the survival curve in Figure 3.17b, it is clear that the obtained survival curve and the MTTF for 75 and 100 years are statistically similar but for 50 years catalog length, it is too short with respect to the recurrence times of large events. This proves that the obtained survival probability is controlled by the ground motions characteristics rather than the time window.

- d) *Survival would highly depend on which earthquake happens first. If it is strongly dependent on the order in which the considered events occur, how can the average survival curve be meaningful?*

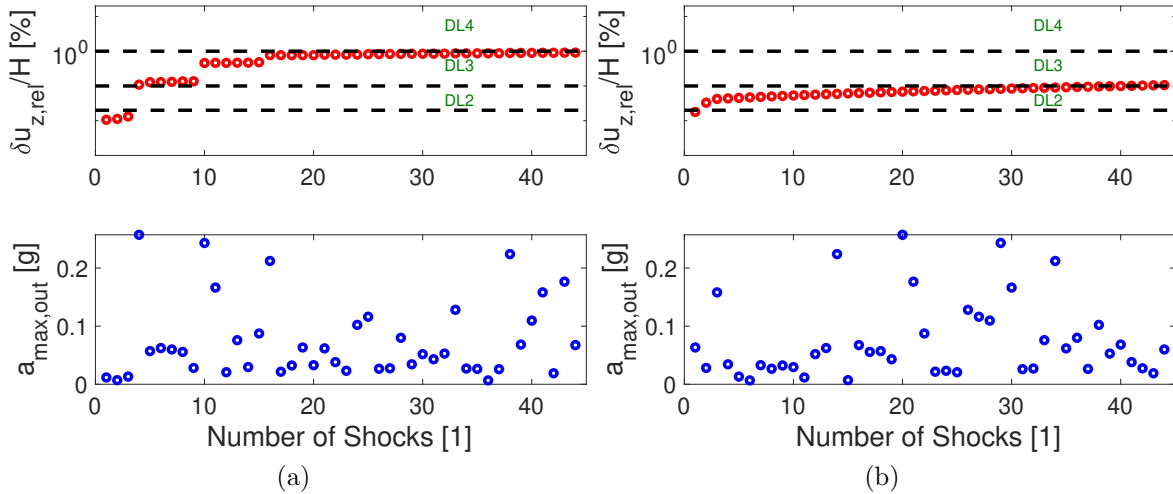


Figure 3.18: The relative crest settlement of one subset but different permutation: a) perm1 and b) perm2

It is well known that the behavior of some geo-structures highly depends on the history of the loading. In addition, the response depends on some ground motion parameters, like  $a_{max,out}$  for example (as seen previously in this chapter). But an input motion of high acceleration does not necessarily induce the same damage if it occurs at the third year than at the 80th year for example. The proof of this idea is shown in Figure 3.18. The response of the embankment for one subset (i.e. 44 acceleration time histories) with two random permutations are examined. It is clear that the response in terms of the relative crest settlement value and the level of damage is very different between each permutation: the induced damage of perm1 is higher than perm2 (can also be seen from the damage levels). It should be noted that the motions with the high acceleration occurs before 20 years for perm1 (Figure 3.18b) which resulted in an increase of the damage at the beginning of the lifetime behavior. However, these motions occurred after 20 years for perm2 (Figure 3.18a) and resulted in a minor damage all over the working life. According to that, even if the two sequences comes from the same hazard and the same subset, the induced damage can be different. This confirms that it is not only the occurrence of the event that matters but also the history of loading of the soil.

- e) *The time histories of this work are generated from the stochastic ground motion model noted Mod.R. (i.e. Seed 1). What happens to the lifetime distribution of the embankment if they were generated a second time (i.e. Seed 2) ?*

Before answering the aforementioned question, a comparison of the parameters distribution between the two seeds is shown in Figure 3.19. It should be noticed that the number of data is the same for both seeds. Clearly, there is no difference in the density distribution of their  $PGA$ ,  $PGV$ ,  $1/T_{va}$ ,  $Ia$  and  $CAV$  and a slight difference in the effective

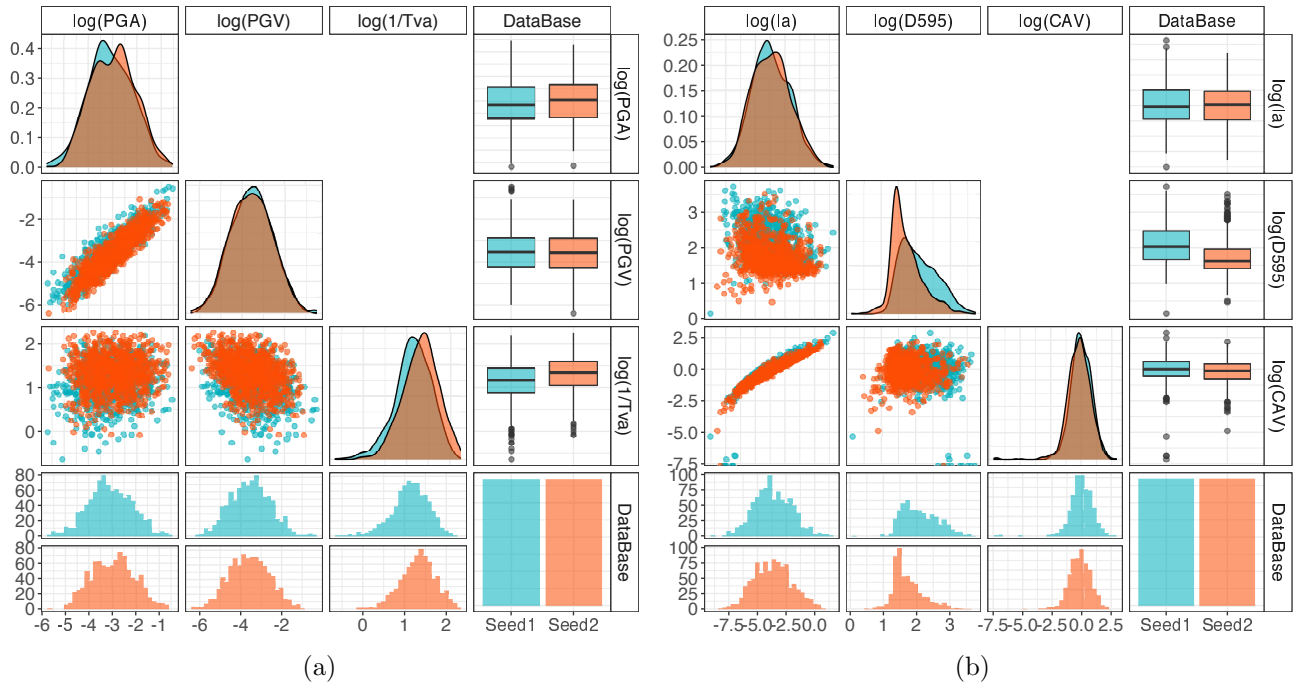


Figure 3.19: Comparison of the logarithmic distribution of some ground motion parameters for Seed 1 and 2 of *Mod.R*

duration  $D_{595}$ . Similar discussion can be made for the median value of each database extracted from the boxplots. The median value of seed 2 is less than seed 1 for the effective duration parameter. In order to verify if the slight difference in  $D_{595}$  and similarity in other parameters affect the results of the survival curve, Figure 3.20 is represented for *Moderate* and *Serious* damage levels. It can be seen in this figure that it indicates an important value, other than the MTTF, which is the *p-value*. An explanation regarding this statistical parameter is shown in Appendix G. Typically, if the *p-value*  $\leq 5\%$ , the null hypothesis is rejected, and vice versa. The null hypothesis in this case states that there is no difference in the lifetime distribution of the embankment between seed 1 and 2.

For the *Moderate* damage level (Figure 3.20a), it is clear that the lifetime distribution of both seeds is close. However, each type of record gave a different estimation of the MTTF. It seems that the slight decrease in  $D_{595}$  resulted in a decrease in the MTTF of seed 2 comparing to seed 1. In addition, and based on the *p-value* of this damage level, the lifetime distribution of seed 1 is different than that of seed 2 (i.e. the null hypothesis is rejected because *p-value*  $< 5\%$ ). Concerning the *Serious* damage level in Figure 3.20b, for both seeds the MTTF is less than the chosen working life window. In addition, they do not have similar or close lifetime distribution. Hence, these results emphasize the importance of the choice of the seed records in the risk assessment. It should be mentioned that these results are affected by the number of the sampling data used for the study. Probably a larger data might give different findings. But for instance, the effect

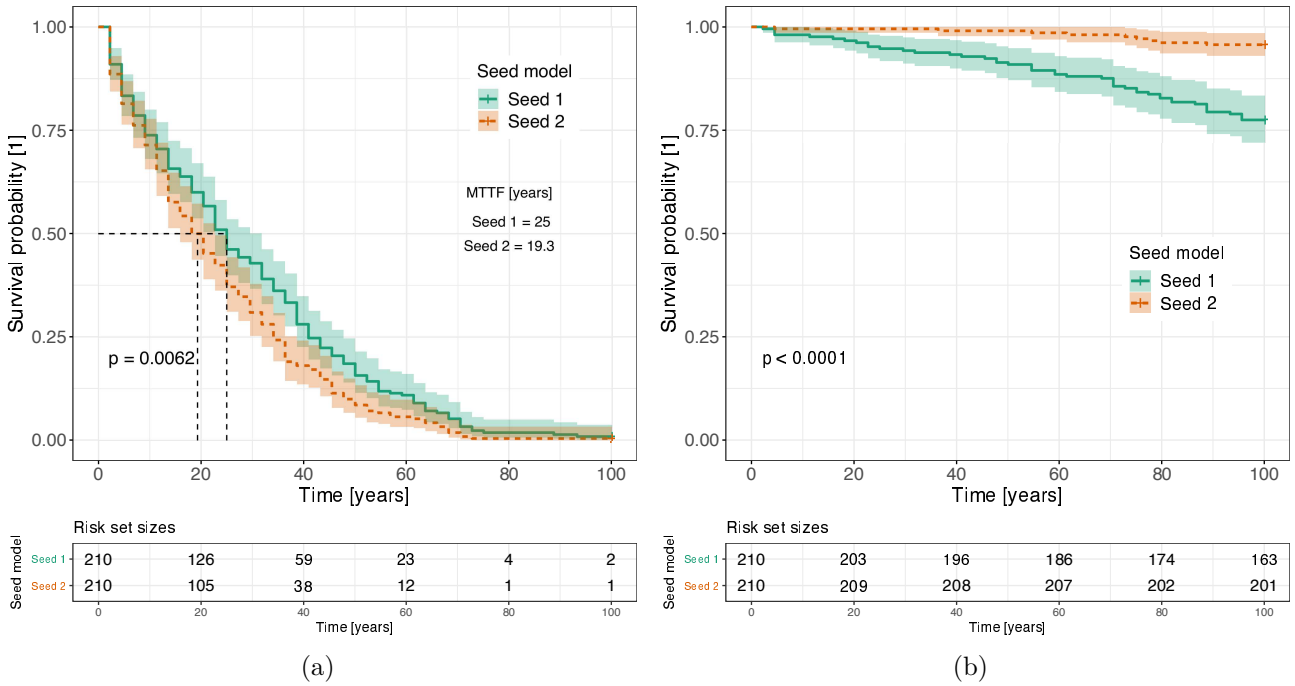


Figure 3.20: Comparison of the survival functions for each seed record for a) *Moderate* and b) *Serious* damage levels

of the seed record is important for the risk assessment of the embankment, specially for high damage levels.

f) *Does the generated sequences have different magnitude distributions?*

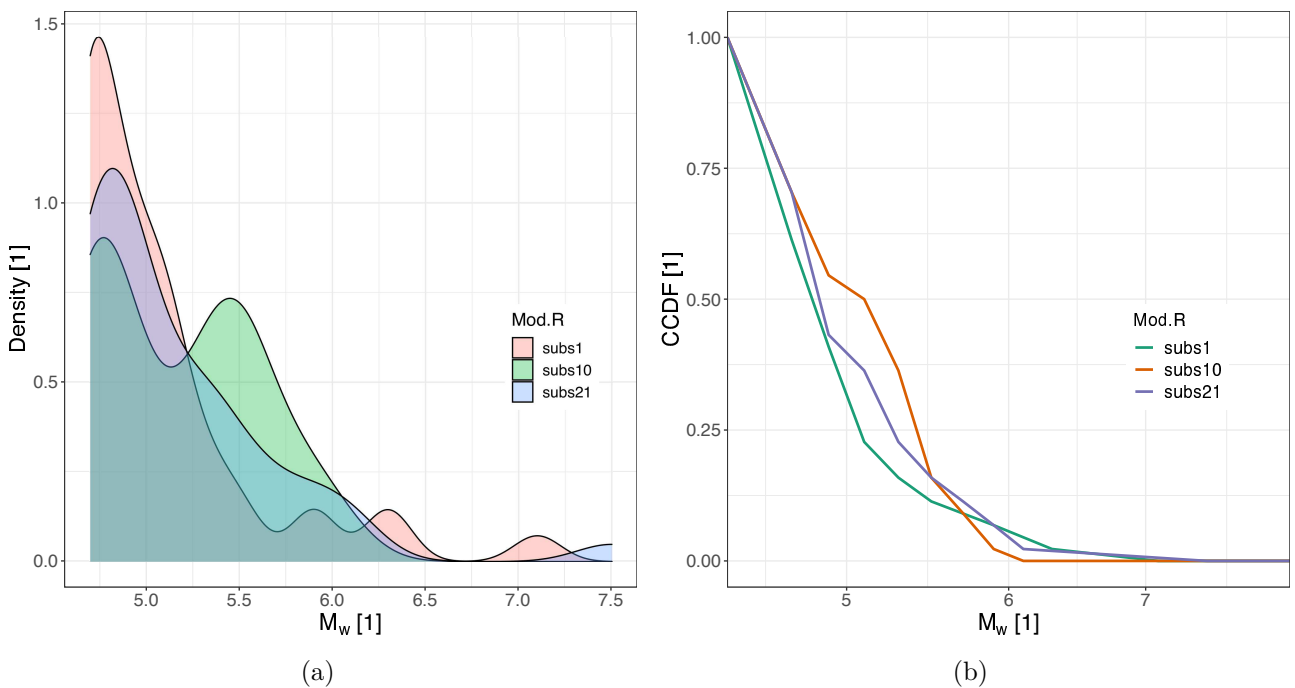


Figure 3.21: a) The density distribution function and b) the CCDF of  $M_w$  for three example sequences

To answer this question, three example sequences of different subsets were chosen. Figure 3.21 shows the density distribution function of each example. Clearly, the magnitude intervals are represented, in addition, with no similarity in the distribution of each sequence.



# Chapter 4

## Lifetime evolution of the performance of an embankment subjected to sequences of mainshocks and aftershocks

### Contents

---

<b>4.1</b>	<b>Introduction</b>	<b>96</b>
<b>4.2</b>	<b>Assumptions of this chapter</b>	<b>99</b>
<b>4.3</b>	<b>Model to generate aftershocks</b>	<b>99</b>
4.3.1	Distribution of the magnitude-frequency	100
4.3.2	Distribution of the occurrence time	101
4.3.3	Location of the aftershocks	102
4.3.4	Description of the generated aftershocks	102
<b>4.4</b>	<b>Damage measure during sequential clusters</b>	<b>104</b>
4.4.1	Relative crest settlement for sequential earthquakes	105
4.4.2	Damage index from the soil residual strength	107
<b>4.5</b>	<b>Survival functions of the tested sequences</b>	<b>109</b>
<b>4.6</b>	<b>Fragility curves evolution</b>	<b>111</b>
<b>4.7</b>	<b>Concluding remarks</b>	<b>115</b>

---

## Abstract

Structures are subjected to multiple earthquakes during their typical design working life. Moreover, earthquakes are divided into clusters of mainshocks and aftershocks. In consequence, structures can be subjected to several cluster events and thus, the induced seismic damage accumulates due to the multiple earthquakes in each cluster. In this context, the Performance Based Earthquake Engineering (PBEE) methodology presents limitations in accounting for the damage issued from multiple events because the traditional Probabilistic Seismic Hazard Analysis (PSHA) considers only mainshocks. In addition, the fragility curves represent the failure probability in one event of a given intensity.

This work studies the response of a given structure subjected to sequences of mainshocks - aftershocks during its lifetime. This chapter is a continuity of the work of [Khalil and Lopez-Caballero \(2021\)](#), presented also in Chapter 3. This means that the site of concern and its compatible PSHA are similar to the ones used in the cited work. Thus, the mainshocks are known and generated from a stochastic synthetic ground motion model. The aftershocks are generated in this chapter from the Branching Aftershock Sequence (BASS) model. The cumulative damage measure of the embankment is calculated after the tested sequences. More importantly, its lifetime distribution is estimated and compared with previous results. And finally, to be compatible with the PBEE methodology, the fragility exposure of the embankment over its lifetime was calculated as to emphasize the effect of the loading history.

This chapter is under preparation to be published in a scientific journal.

## 4.1 Introduction

In earthquake-prone regions, structures are exposed to seismic sequences that consist of mainshocks, aftershocks and foreshocks. Aftershock events are usually triggered by the mainshocks due to the change of static and dynamic stresses during the earthquake process ([Ruiz-García, 2012](#)). It was shown that aftershocks exacerbate the damage generated from the triggering mainshock and may be the reason of collapse even though they have a smaller magnitude than the triggering mainshock ([Yeo and Cornell, 2009](#); [Zhai et al., 2013](#); [Ruiz-García, 2014](#); [Wen et al., 2017](#); [Shokrabadi and Burton, 2018](#), among others). When structures are subjected to multiple deterioration over time, the assessment of their useful *Life Cycle* is interesting to estimate. Several analysis exist in order to calculate or estimate the life cycle of the structure ([Yeo and Cornell, 2009](#); [Sanchez-Silva et al., 2011](#); [Ruiz-Garcia and Negrete-Manriquez, 2011](#); [Iervolino et al., 2015](#); [Riascos-Ochoa et al., 2016](#); [Salami et al., 2019](#); [Lopez-Caballero et al., 2020](#), among others). Typically, by taking into account sequences of loading, the induced potential damage during the lifetime  $D(t)$  of the structures can be interpreted as the accumulation of the damages due to all the occurred earthquake shocks  $N(t)$  ([Sanchez-Silva et al., 2011](#); [Iervolino et al., 2015](#); [Lopez-Caballero et al., 2020](#)):

$$D(t) = \sum_{i=1}^{N(t)} D_i(t_i) \quad , \quad (4.1)$$

where  $D_i(t_i)$  is the damage accumulated until the  $i$ th shock. In practice, from the Performance Based Earthquake Engineering (PBEE) methodology, structures are designed to resist the first damaging earthquake scenario. Hence, the classical fragility curves represent the failure probability of one event of a given intensity only. This means that this framework neglects the cumulative damage and the evolution of the material properties issued from multiple events (Iervolino et al., 2020). In addition, the commonly used Probabilistic Seismic Hazard Analysis (PSHA) to select the corresponding ground motions, is intended to evaluate the hazards from discrete independent events. Thus, empirical scaling laws (i.e. Gutenberg-Richter, modified Omori's law, Bath's law) have been proposed to characterize the aftershocks occurrence (Shcherbakov et al., 2005). These laws are based on parameters that depend on the statistical properties of particular seismic sequences (Shcherbakov et al., 2005; Ruiz-García, 2012; Trevlopoulos et al., 2020). Previous works on buildings subjected to mainshock-aftershock events have been conducted (Li and Ellingwood, 2007; Hatzigeorgiou and Beskos, 2009; Ruiz-García and Negrete-Manriquez, 2011; Ruiz-García, 2012; Goda, 2012; Zhai et al., 2013; Ruiz-García, 2014; Ghosh et al., 2015; Iervolino et al., 2015; Shokrabadi and Burton, 2018; Pan and Kusunoki, 2020, among others).

In this context, researchers, have been recently interested in conducting methodologies to assess the fragility exposure of structures subjected to mainshocks-aftershocks events (Panchireddi and Ghosh, 2019; Iervolino et al., 2020; Di Sarno and Pugliese, 2020; Wen et al., 2020; Zhang et al., 2020, among others). Therefore, evaluating the seismic performance of structures subjected to sequential seismic events, specially when dealing with the aftershock occurrence, requires explicit consideration of the uncertainty in the state of the structure (Shokrabadi and Burton, 2018). For example, the known *Incremental Dynamic Analysis (IDA)* which assesses the response of structures subjected to multiple events requires the scaling of the seismic input (Shome, 1999; Vamvatsikos and Cornell, 2002; Iervolino et al., 2015, among others). Then, failure is identified once the structure exceeds a threshold limit. However, in liquefaction related problems, several aspects are essential. For example, the multi-physical aspects of the soil, its history of loading and its correlation with several intensity measures, are all important aspects that makes the IDA approach unrepresentative of the overall response of the geo-structure (Sica et al., 2008; Causse et al., 2014b; Lopez-Caballero et al., 2016; Khalil and Lopez-Caballero, 2021).

Otherwise, the *Survival Analysis* has been a used approach in geotechnical engineering to identify the relative risks of various earthquake (Nafday, 2010; Lopez-Caballero et al., 2020; Khalil and Lopez-Caballero, 2021). It is defined as the time length of the structure until the occurrence of an event of interest (i.e. equipment failure, damage, complex system) (Hosmer Jr

and Leshow, 1999; Nafday, 2010; Christodoulou and Fragiadakis, 2014; Diamoutene et al., 2016; Lopez-Caballero et al., 2020; Khalil and Lopez-Caballero, 2021). It accounts for a set of statistical methods to analyze data that has the occurrence time of an event as the outcome. It calculates the probability of survival of concerned test data and estimates its Mean Time to Failure (MTTF).

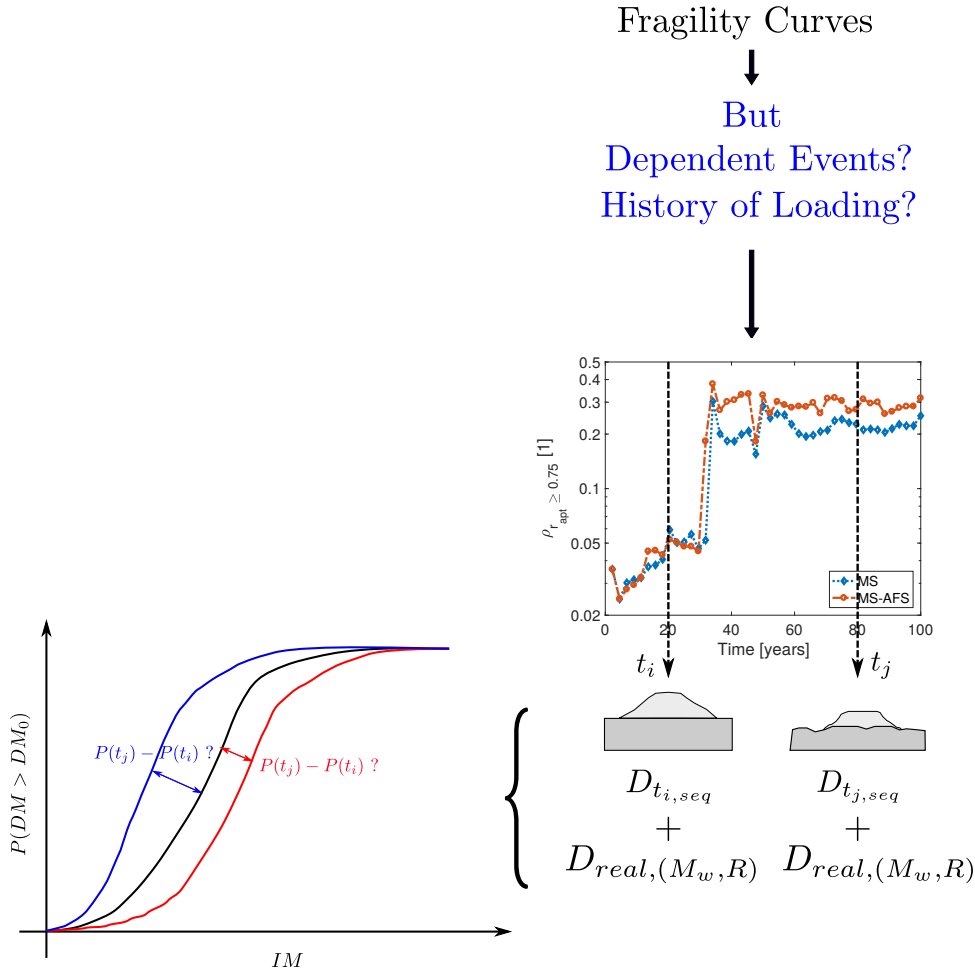


Figure 4.1: The methodology presented in this chapter

In the work of Khalil and Lopez-Caballero (2021), it was estimated the lifetime distribution of the embankment subjected to mainshock sequential events. These later were extracted from several subsets compatible with the seismic hazard of the site of concern. Each subset was compatible with the event rate of the mainshocks and the corresponding time histories were permuted many times in order to consider the randomness of the events. For the same geometry and numerical model in the work of Khalil and Lopez-Caballero (2021), the steps of this work are presented in Figure 4.1. This study will try to answer the following significant questions:

- a) How does the cumulative damage evolve during the lifetime of the embankment when subjected to sequences of mainshocks-aftershocks, comparing to sequences of only mainshocks events ? (Section 4.4)
- b) Does the aftershock occurrence affects the lifetime distribution of the embankment, as

well as its MTTF ? (Section 4.5)

- c) How do the fragility curves evolve after multiple loading histories ? Is their evolution dependent of the type of the applied load ? (Section 4.6)

In order to answer these questions, the methodology and the PSHA of the site of concern are similar to the ones presented in the work of [Khalil and Lopez-Caballero \(2021\)](#). A large number of time histories is generated using stochastic simulations from the synthetic ground motion model of [Rezaeian and Der Kiureghian \(2012\)](#). The model used to generate the aftershocks is based on the probabilistic version of the Branching Aftershock Sequences (BASS) model and is inspired from [Turcotte et al. \(2007\)](#) and [Hu et al. \(2018\)](#).

## 4.2 Assumptions of this chapter

In this chapter, the required assumptions are:

- The effect of external uncontrolled conditions (i.e. weather, rain, wind) is not considered.
- Since aging is connected to the material resistance, origin and age, it is not considered in this study.
- The computations start after the construction phase when the embankment is intact. Thus, it does not have a history of earthquake loading at the first mainshock event.
- The embankment is not subjected to any repairs during its lifetime.
- The constitutive model does not take into account the secondary consolidation or compression after each seismic loading.
- The cluster earthquakes consist of mainshocks and aftershocks only. The effect of foreshocks is not considered in this study.
- Even if the used synthetic model of [Rezaeian and Der Kiureghian \(2012\)](#) model is for  $M_w$  greater than 6.0, it was verified that the obtained intensity measures are compatible with the selected ground motion prediction equations for lower magnitudes (refer to Chapter 3).
- The original database used in the stochastic ground motion model to generate the mainshocks is not modified to generate the aftershocks (as in the work of ([Hu et al., 2018](#))).

## 4.3 Model to generate aftershocks

It is known that an earthquake event does not consist of only mainshocks, but also the occurrence of aftershocks and foreshocks. A cluster earthquake is in general composed of one mainshock with its corresponding aftershocks. The Epidemic Type Aftershock Sequence (ETAS)

model has been widely used to model the statistics of seismicity (Turcotte et al., 2007; Hu et al., 2018; Trevlopoulos et al., 2020, among others). An essential feature of the ETAS model is the magnitude dependent branching (parent-daughter) ratio. In this context, Turcotte et al. (2007) introduced Branching Aftershock Sequence (BASS) model as the self-similar limit of the ETAS model. Both approaches are based on empirical laws describing the distribution of earthquakes in magnitude, time and space. Four scaling relations are required in order to generate and identify the aftershocks distribution: 1) the Gutenberg-Richter (GR) frequency-magnitude scaling, 2) the Bath's law (or the modified version) for maximum-magnitude scaling, 3) Omori's law for power-law seismicity rate decay and 4) a spatial form of Omori's law. Both approaches utilize the concept of primary, second-order and higher-order aftershocks. The primary difference between the ETAS and the BASS model is in their use of the Bath's law to estimate the  $a$ -value of the GR relation; the BASS model uses the modified form of Bath's law instead of the productivity relation used in the ETAS model (Turcotte et al., 2007). In addition, the branching statistics in the BASS model are identical to the self-similar Tokunaga statistics of drainage networks (Turcotte et al., 2007; Yoder et al., 2013).

The following section will develop the theoretical model used to generate the corresponding aftershocks of the mainshocks found in Chapter 3. It should be recalled that the mainshocks were generated from the stochastic ground motion model of Rezaeian and Der Kiureghian (2012). As for the aftershocks generation, it is based on the BASS model to compute the distribution in magnitude and time of the aftershocks and is inspired from Turcotte et al. (2007) and Hu et al. (2018). As for the location of the aftershocks, and due to the point source of the seismic propagation (i.e. no directivity effects), an Aftershock PSHA (or APSHA) is used (Iervolino et al., 2015). It should be mentioned that only primary order of aftershocks is considered in this study. The theoretical equations will be developed first, and at the end of that, a summary of the used scaling relations for this study and their parameters will be presented.

### 4.3.1 Distribution of the magnitude-frequency

Similar to any seismic hazard model, the frequency-magnitude distribution of each sequence aftershock should satisfy the Gutenberg-Richter (GR) relation (Equation 4.2):

$$\log_{10}[N_d(\geq m_d)] = a_d - b_d m_d, \quad (4.2)$$

where  $m_d$  is the magnitude of the aftershocks,  $N_d(\geq m_d)$  is the number of the aftershocks with magnitude greater than or equal to  $m_d$ . Parameters  $a_d$  and  $b_d$  are constants (or known as  $a$ -value,  $b$ -value of the GR distribution). It should be noted that in practice, the magnitude of the largest aftershock  $\Delta m^*$  should be less than that of the triggering mainshock  $m_p$ . So

$$N_d(\geq (m_p - \Delta m^*)) = 1. \quad (4.3)$$

Considering both Equations 4.3 and 4.2, The GR relation for aftershocks will be:

$$\log_{10}[N_d(\geq m_d)] = b_d(m_p - \Delta m^* - m_d), \quad (4.4)$$

In order to terminate the sequence of aftershocks, it is necessary to specify a minimum magnitude of the aftershocks  $m_{min}$ . The total number of aftershocks  $N_{dT}$  based on Equation 4.4 is:

$$N_{dT} = N(\geq m_{min}) = 10^{b_d(m_p - \Delta m^* - m_{min})}. \quad (4.5)$$

Hence, the cumulative distribution function  $P_{Cm}$  for the magnitude of the aftershocks, is deduced from Equations 4.4 and 4.5. It is a random value between 0 and 1 and is given by:

$$P_{Cm} = \frac{N_d(\geq m_d)}{N_{dT}} = 10^{-b_d(m_d - m_{min})}. \quad (4.6)$$

In this study, the empirical parameters to calculate the aftershocks magnitude are  $m_{min} = 4.5$ ,  $b_d = 1$  and  $\Delta m^* = 1.3$ .

### 4.3.2 Distribution of the occurrence time

Knowing the magnitude of each occurring aftershock in the sequence from Equation 4.6, the time delay  $t_d$  until the occurrence of each aftershock after the triggering mainshock should be known. It should be mentioned that  $t_d$  will allow to know the sequential position of each occurring aftershock. Following the generalized form of Omori's law, the rate of aftershock occurrence  $R(t_d)$  would be:

$$R(t_d) = \frac{dN_d}{dt} = \frac{1}{\tau(1 + \frac{t_d}{c})^p}, \quad (4.7)$$

where  $\tau$ ,  $c$  and  $p$  are given parameters.  $N_d(\geq t_d)$  is the number of aftershocks that occurred after a time  $t_d$ :

$$N_d(\geq t_d) = \int_{t_d}^{\infty} \frac{dN_d}{dt} dt' = \frac{c}{\tau(p-1)(1 + \frac{t_d}{c})^{p-1}}. \quad (4.8)$$

Setting  $t_d = 0$  in Equation 4.8, the total number of aftershocks will be obtained. Hence, the cumulative distribution function  $P_{Ct}$  for the occurrence time of the aftershocks will be:

$$P_{Ct} = \frac{N_d(\geq t_d)}{N_{dT}} = \frac{1}{(1 + \frac{t_d}{c})^{p-1}}, \quad (4.9)$$

$P_{Ct}$  is a random value between 0 and 1 and the time of occurrence of the aftershock is deduced from Equation 4.9. The parameters used in this work to calculate  $t_d$  are  $\tau = 0.001$  and  $p =$

1.25.

### 4.3.3 Location of the aftershocks

Concerning the seismogenic zone of the aftershock, it is assumed that each mainshock has its corresponding aftershocks located within an area around its epicenter. The size of this area depends on the magnitude of the triggering mainshock as follows:

$$S_A = 10^{m_d - m_{min}}. \quad (4.10)$$

Within this area, considered a square, the aftershocks occur on a smaller lattice. Table 4.1 summarizes the parameters values of the scaling relations used for this study. Having the magnitude, distance and the time delay until the occurrence of every daughter earthquake, the generation of aftershocks time histories is feasible.

Scaling relations	Parameters values	References
<i>GR-Bath Parameters:</i>		
$N_{dT} = N(\geq m_{min}) = 10^{b_d(m_p - \Delta m - m_{min})}$	$b_d = 1$	Turcotte et al. (2007)
$m_d = -(1/b_d) \cdot \log(P_{Cm}) + m_{min}$	$\Delta m = 1.3$	and Hu et al. (2018)
<i>Temporal Omori:</i>		
$t_d = \tau \cdot (P_{Ct}^{-1/(p-1)} - 1)$	$p = 1.25$ $\tau = 0.001$	Turcotte et al. (2007) and Hu et al. (2018)
<i>Space APSHA:</i>		
$S_A = 10^{m_d - m_{min}}$	$m_{min} = 4.5$	Iervolino et al. (2015)

Table 4.1: The scaling relations of the magnitude, time and space distribution of the used model to generate the aftershocks

### 4.3.4 Description of the generated aftershocks

In the following, it will be described the IMs of the generated aftershocks. The median response spectra (structural damping  $\xi = 5\%$ ) of the generated mainshocks and aftershocks are shown in Figure 4.2a. It is clear that the spectral acceleration of the mainshocks is slightly higher than that of the aftershocks (Turcotte et al., 2007; Hu et al., 2018). Figure 4.2b shows a window of a sequence example. It can be seen from this figure three ideas: i) the aftershocks, if they exist, occur between two mainshocks, ii) the magnitude of the aftershocks is less than that of the principal mainshock and iii) the mainshock of larger magnitude will generate more aftershocks comparing to the one with a small magnitude (Equation 4.6).

Another illustration of the mainshock-aftershock parameters is shown in Figure 4.3. This figure considers three mainshocks (in dashed circles) with their corresponding aftershocks. Each cluster earthquake is drawn in a different shape (circle, square and diamond). Figure 4.3a shows a scatter plot of the outcrop acceleration  $a_{max,out}$ , the equivalent predominant frequency  $1/T_{va}$  and the magnitude  $M_w$ . Based on Kawase (2011), there exists a proportional relation between

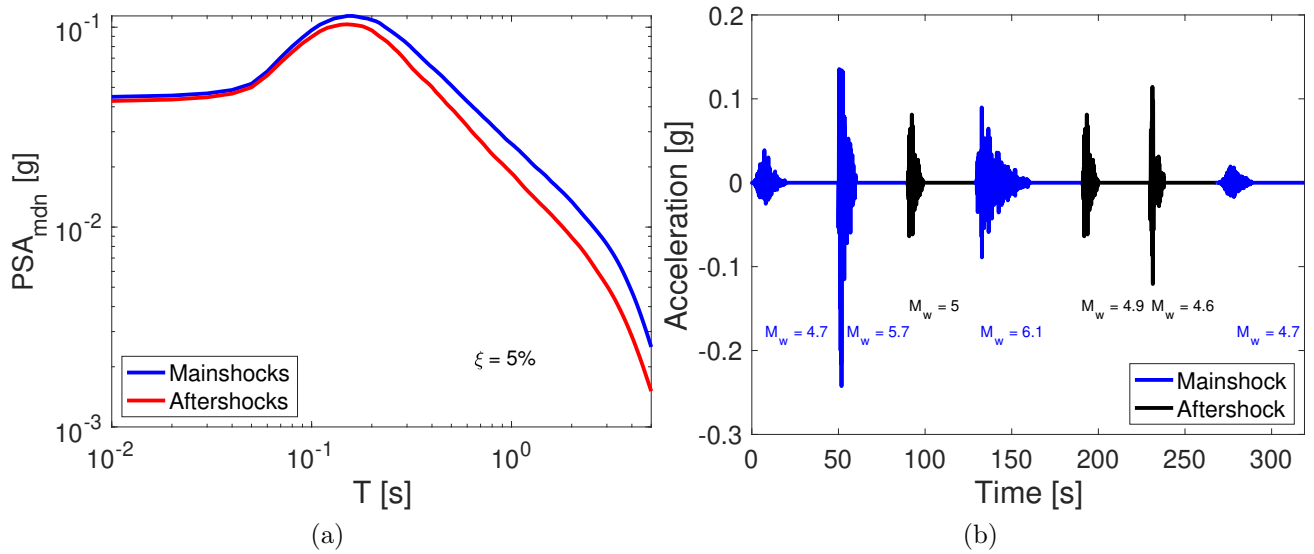


Figure 4.2: a) The response spectral of the generated aftershocks and b) a section of a sequence

the peak ground velocity  $PGV$ ,  $a_{max,out}$  and  $1/T_{va}$  and is represented as dashed lines. In addition to these parameters, Figure 4.3b shows also the variation of the source-to-site distance  $R$ .

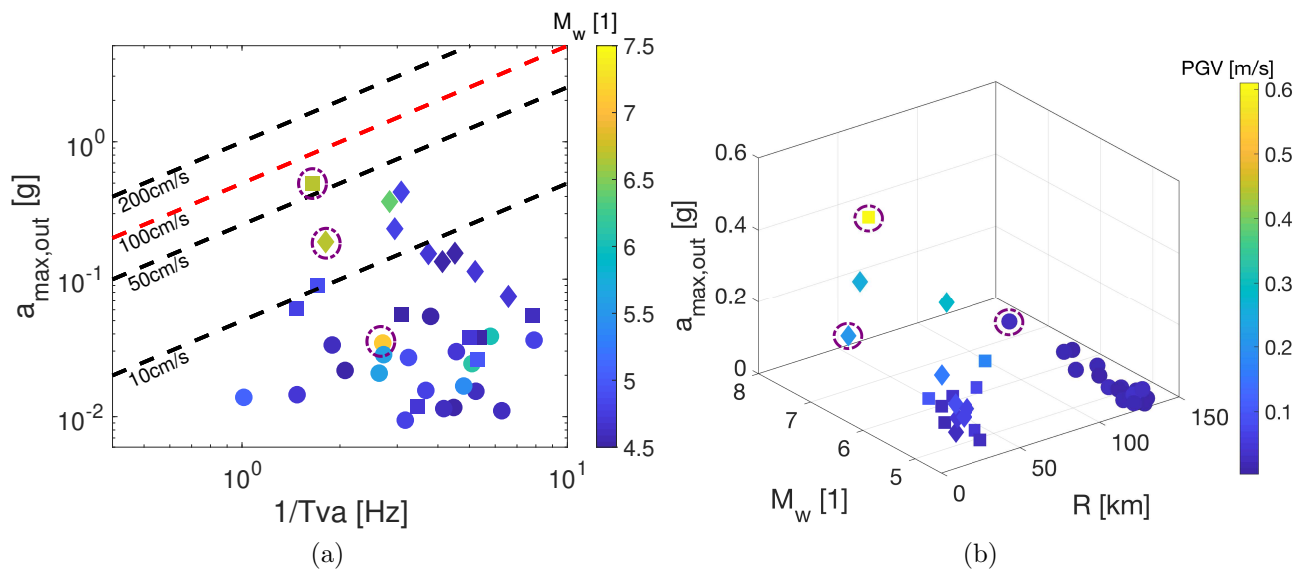


Figure 4.3: Scatter plots of some ground motion parameters of mainshocks and aftershocks with respect to a)  $M_w$  and b)  $M_w$  and  $R$

From Figure 4.3, it can be seen that the corresponding aftershocks have close values of  $a_{max,out}$  and  $1/T_{va}$  but are in general less than those of the mainshock. In addition, the magnitude of the mainshock is higher than that of the aftershocks, whereas the source-to-site distance of the aftershocks is close to that of the mainshocks.

In order to take into account all the generated Mainshocks (MS) and the Aftershocks (AFS), Figure 4.4 shows a matrix form of a logarithmic comparison of some ground motion parameters. The comparison is conducted in terms of the density functions located in the diagonal of the

matrix, the scatterplots and the histograms that are both located to the bottom left of the diagonal and finally, the boxplots that are located to the right.

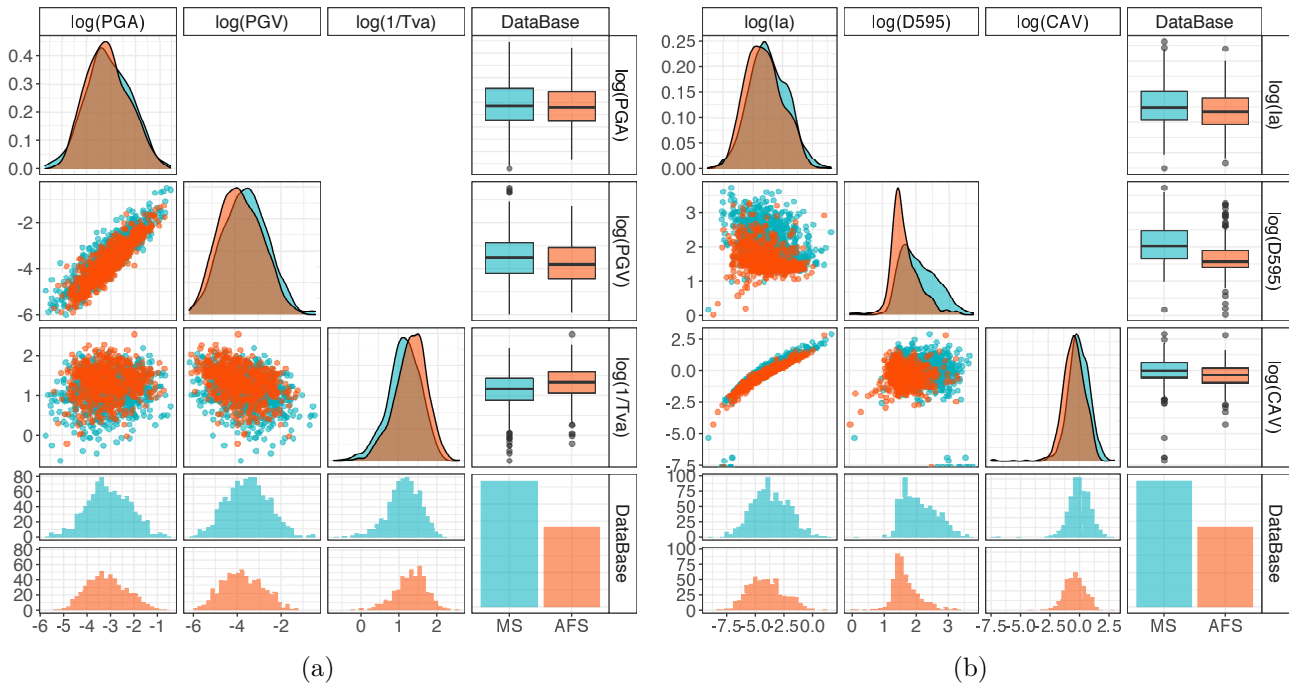


Figure 4.4: The logarithmic distribution of some ground motion parameters of the Mainshocks (MS) and the Aftershocks (AFS)

For the density distribution function of the chosen parameters, it can be seen that the distributions of MS and AFS overlap for almost all the tested parameters, except a small change in the effective duration  $D_{595}$ . For the median value of each database, it can be seen from the boxplots, that it is almost close for the two ground motions. Concerning the scatterplots and the histograms, they are useful to have an idea about the precise values or the relation between each parameter.

It was calculated in Chapter 2 global damage indices to evaluate the potential failure of the embankment. It was evaluated also in the work of [Khalil and Lopez-Caballero \(2021\)](#) (or Chapter 3) the response of the same embankment after sequences of mainshock events. It will be examined in the next section, the damage measures of the embankment subjected to the same sequences of mainshocks but with their corresponding aftershocks occurrence.

## 4.4 Damage measure during sequential clusters

The PBEE methodology provides a probabilistic description of the system-level performance of structures. It requires the calculation of an engineering demand parameter that can be related to the intensity measure of the occurred ground motions. The potential structural failure is measured either for each structural element (local) or related to the global response of the structure ([Cosenza and Manfredi, 2000](#)). However, for life cycle assessment, it is necessary to

account for the build-up of seismic losses because of the damage issued from multiple events (Ghosh et al., 2015; Iervolino et al., 2015, 2020, among others).

In this study, 210 sequential cluster events of MS-AFS are considered. It should be reminded that each sequence contains 44 acceleration time histories of mainshocks that were permuted 10 times. In order to be statistically representative of a large number of sequences, 21 subsets compatible with the seismic hazard of the site of concern were considered. In addition, to take into account the recovery time of the embankment after each principal shock, 30 seconds of no load is added after each mainshock. Chapter 3 (or Khalil and Lopez-Caballero (2021)) emphasizes the importance of the recovery time on the response of the embankment. Since the used numerical model takes into consideration the damage history of the embankment, in this section, the evolution of the global response will be examined from the damage measures presented previously in Chapter 2. Nevertheless, they will be briefly developed hereafter. All over this chapter, the notation *MS* designates *Mainshocks* and *AFS* designates *Aftershocks*.

#### 4.4.1 Relative crest settlement for sequential earthquakes

The performance of the embankment during its lifetime is evaluated from its cumulative damage measure. In the case of embankments (or dams), the damage is quantified from the percentage relative crest settlement  $\delta u_{z,rel}/H$  where  $u_{z,rel}$  is the crest settlement and  $H$  is the height of the dam with the foundation (i.e. 19 m in this case) (Lopez-Caballero and Khalil, 2018; Khalil and Lopez-Caballero, 2021). In order to classify the damage, levels are also attributed to the relative crest settlement. When  $\delta u_{z,rel}/H \leq 0.02\%$ , there is *No* damage, if  $0.02\% < \delta u_{z,rel}/H \leq 0.1\%$ , the damage is *Minor*, if  $0.1\% < \delta u_{z,rel}/H \leq 1\%$ , the damage is *Moderate* and finally if  $\delta u_{z,rel}/H > 1\%$ , the damage is *Serious*. For the sake of brevity only, Figure 4.5 shows a comparison of  $\delta u_{z,rel,cum}/H$  for two examples of MS and MS-AFS sequences in order to examine the effect of the aftershock occurrence. It should be mentioned that for each presented case in Figure 4.5, the permutation of the mainshock events is the same in both sequence types. The only difference is the aftershock occurrence.

Clearly, two typical behaviors can be identified. In Figure 4.5a the global response during the lifetime of the embankment was almost similar for the two sequences. At a point in time, when the 17th shock occurred, a small peak in the damage appears for the MS-AFS sequence. It should be noted that this shock has 3 aftershocks. On the contrary, the damage for MS-AFS sequence in Figure 4.5b, has a rapid increase in the 9th shock so that it surpassed a damage level. It should be noted that this shock produced 70 aftershocks. After it, the damage was higher for the MS-AFS sequence, until the end of the lifetime when the soil densifies and was subjected to multiple types of motions, the level of damage is the same. Thus, it should be remarked that the occurrence and the high number of aftershocks (i.e.  $N_d$ , Section 4.3) has a major importance on the lifetime behavior of the embankment.

In order to take into considerations all the tested sequences, the median estimator value of the cumulative relative crest settlement is shown in Figure 4.6. A comparison with the

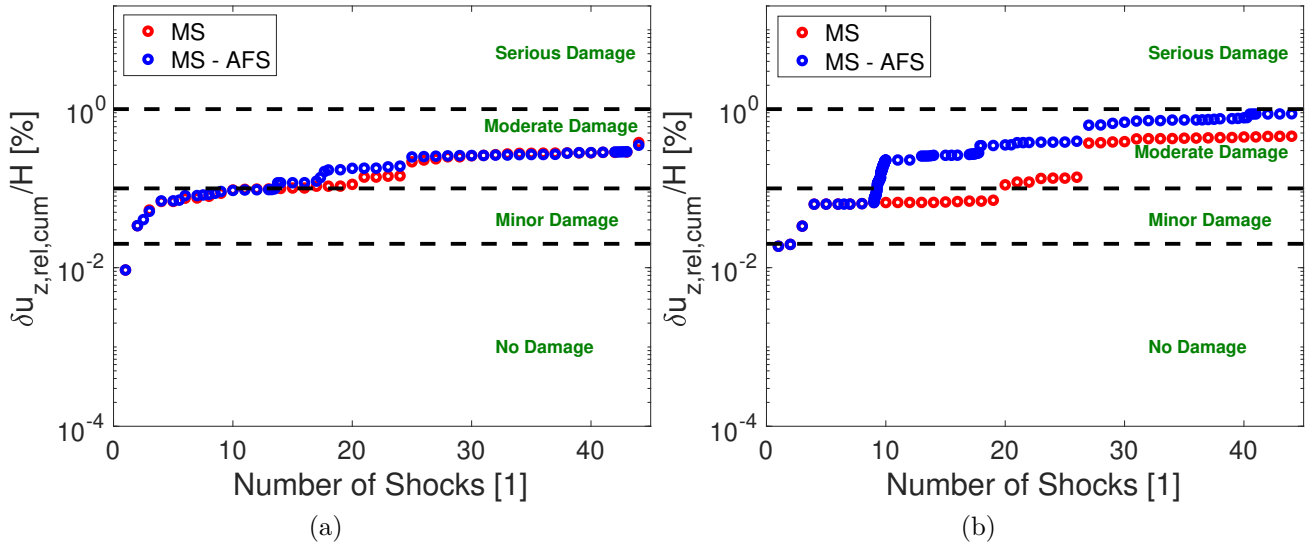


Figure 4.5: Comparison of the percentage relative crest settlement for an example of mainshock (MS) sequences and mainshocks - aftershocks (MS - AFS) sequences

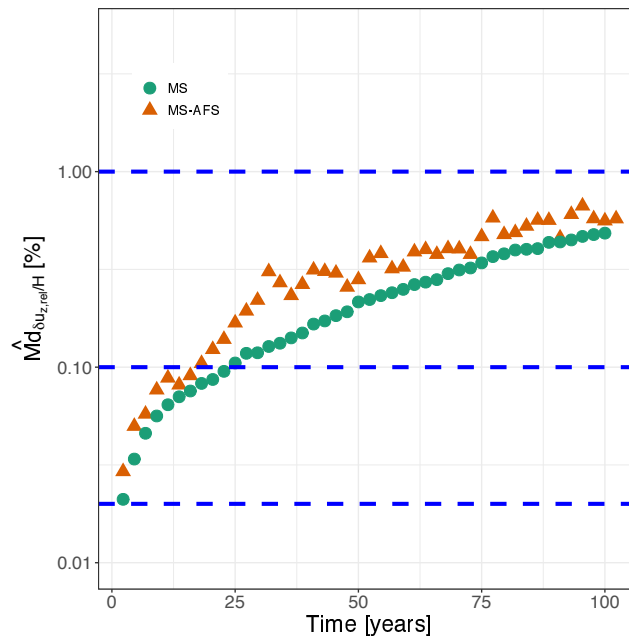


Figure 4.6: Median value of the crest settlement for the MS and MS-AFS sequences

MS sequential type appears also in this figure. Clearly, the damage during the lifetime of the embankment is not the same, whereas at the beginning and the end of the lifetime, the cumulative crest settlement is slightly different between both sequences. However, for the level of damage, no remarkable difference is noted (i.e. at the end of the lifetime, *Moderate* damage was reached for MS and MS-AFS sequences).

It can be deduced from the comparison of the MS and MS-AFS sequences, that the lifetime damage of the embankment could be affected by the occurrence and number of aftershocks. As for the level of damage, similarity between both sequences is identified. In order to understand the reason behind this behavior, a close examination a damage index related to the soil residual

strength is conducted in the next section.

#### 4.4.2 Damage index from the soil residual strength

It was previously presented and discussed in Chapter 2 that from the used soil constitutive model, the “distance to reach the critical state” can be provided through the parameter  $r_{apt}$ . The yield surface of the model (Equation 4.11) shows two parameters that control the behavior of the soil.

$$f_k(\sigma, \varepsilon_v^p, r_k) = q_k - \sin \phi'_{pp} \cdot p'_k \cdot F_k \cdot r_k . \quad (4.11)$$

$F_k$  that controls the isotropic hardening associated with the plastic volumetric strain and  $r_k$  that controls the isotropic hardening generated by the plastic shearing. These two parameters represent progressive friction mobilization in the soil, such that:

$$F_k = 1 - b \ln \left( \frac{p'_k}{p_c} \right) , \quad (4.12)$$

$$p_c = p_{co} \exp(\beta \varepsilon_v^p) . \quad (4.13)$$

$$\sin \phi'_{apt} = \frac{q_k}{p'_k \cdot F_k} , \quad (4.14)$$

$$r_{apt} = \frac{\sin \phi'_{apt}}{\sin \phi'_{pp}} . \quad (4.15)$$

$r_{apt}$  varies from 0 and reaches perfect plasticity at 1. So when  $r_{apt}$  is close to one, the critical state is reached and hence instabilities such as liquefaction, will occur. Because  $r_{apt}$  is considered as a local damage index, the failure density concept represented by  $\rho_{r_{apt}}$ , calculates the local damage exceedance in a domain of interest. Thus, it can be estimated as a global damage index. It should be reminded that technically,  $\rho_{r_{apt}}$  represents the percentage of the local integration points of a domain that have  $r_{apt} \geq 0.75$  (Lopez-Caballero and Modaresi-Farahmand-Razavi, 2013; Rapti et al., 2018) (see also Chapter 2).

It was found in Section 4.4.1 that the lifetime damage index of the embankment represented by the relative crest settlement  $\delta u_{z,rel,cum}/H$  slightly varies when the aftershocks occur. The link of this damage measure with the one related to the soil residual strength (i.e.  $\rho_{r_{apt} \geq 0.75}$ ) is shown in Figure 4.7. It should be reminded that similar to the notation of Chapter 2,  $\rho_{r_{apt} \geq 0.75}$  means  $\rho_{r_{apt} \geq 0.75}(t = t_{end})$ . In addition, the domain of interest in which this parameter is calculated is the soil shallow foundation with the embankment. Hence, the lifetime evolution of both damage indices is shown for an example of a MS sequence (Figure 4.7a) and for the same sequence with added aftershock occurrence (Figure 4.7b). The response of the embankment for this sequence example can be divided into three time intervals: before 30 years, between 30 and 60 years, and after 60 years. A discussion on each sequences will be developed and then a comparison of both types will proceed.

For the mainshock sequence in Figure 4.7a, before 30 years,  $\rho_{r_{apt} \geq 0.75}$  slightly increases when

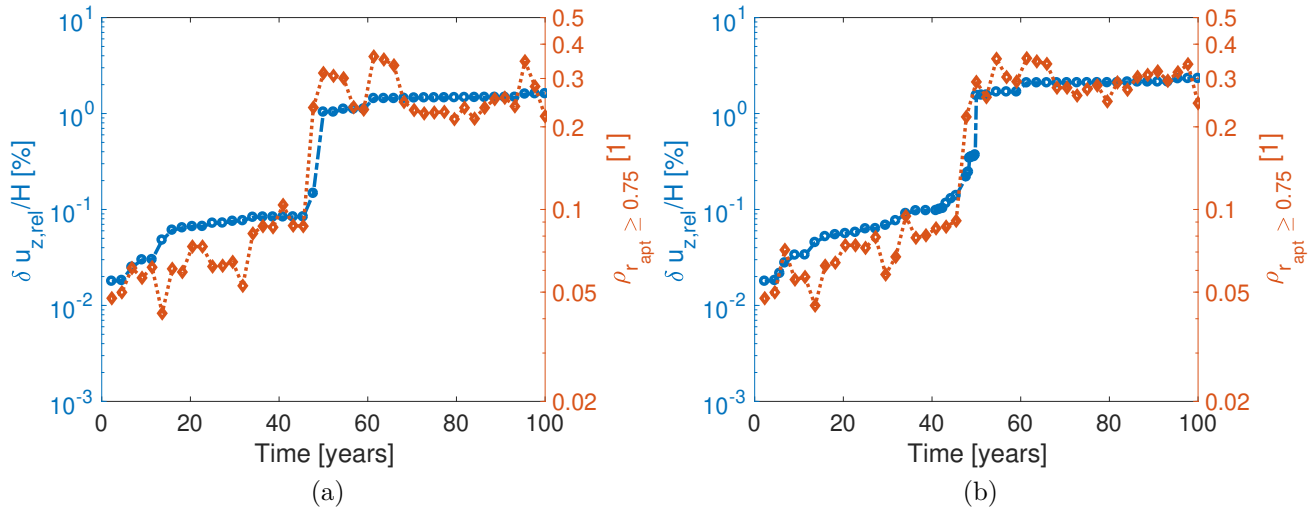


Figure 4.7: The time evolution of  $\delta u_{z,rel}/H$  and  $\rho_{r_{apt} \geq 0.75}$  for a a) MS sequence and b) a MS-AFS sequence

$\delta u_{z,rel}/H$  was also increasing. The global damage for this duration is still acceptable. It should be remarked that for one shock at 18 years, the crest settlement increases whereas  $\rho_{r_{apt} \geq 0.75}$  decreases, this means this shock did not induce many local instabilities, or on the contrary it helped the soil to dissipate the residual excess pore water pressure  $\Delta p_w$ . Between 30 and 60 years, the behavior was almost similar to the previous time interval, however, at 50 years,  $\delta u_{z,rel}/H$  increases rapidly to reach severe damages which induced instabilities in 30% of the domain of interest (i.e.  $\rho_{r_{apt} \geq 0.75} = 0.3$ ). After 60 years, both damage measures are constants. For the aftershock occurrence in this example sequence (Figure 4.7b), no change in the response for two time intervals: before 20 years and after 60 years. However, between 30 and 60 years, the aftershocks prevented the rapid increase in the crest settlement and in  $\rho_{r_{apt} \geq 0.75}$ . It is interesting to mention that for both MS and MS-AFS sequences, at the end of the lifetime duration, the level of damage is the same. This result confirms the one deduced from the lifetime evolution of the relative crest settlement and also verifies the link between both damage indices.

As to take into consideration more example sequences and the lifetime evolution of  $\rho_{r_{apt} \geq 0.75}$ , Figure 4.8 shows this parameter for two example sequences of MS and their corresponding sequences with aftershock occurrence. As expected, two typical behaviors can be identified: a similarity in the response during time, for example the sequence in Figure 4.8a, and a slight difference in the damage response specially after a severe shock (Figure 4.8b).

It can be partially concluded from this section, that the lifetime embankment failure, evaluated from two damage indices slightly differs between MS and MS-AFS sequences. The occurrence of AFS increases the damage during time, but, at the end of the working life, the damage of both sequences is slightly close and the level of damage is the same. The coming section will try to answer the second question of the Introduction section about the effect of the aftershocks occurrence on the lifetime distribution of the embankment.

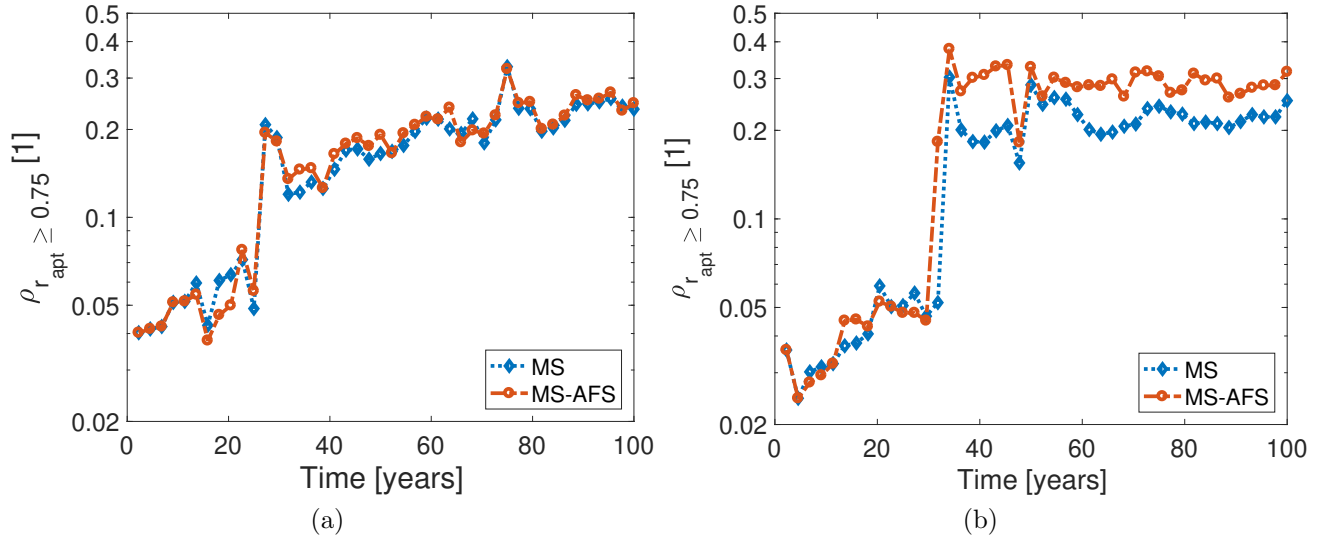


Figure 4.8: The time evolution of  $\rho_{r_{\text{apt}} \geq 0.75}$  for two examples of MS or MS-AFS sequences

## 4.5 Survival functions of the tested sequences

Survival analysis is the time needed for an event of interest to occur. It is also called the time-to-event data (Bradburn et al., 2003; Kartsonaki, 2016; Schober and Vetter, 2018, among others). Survival analysis is represented by survival functions or hazard functions. They are both inversely proportional, so when the hazard increases the survival function decreases. This later estimates the lifetime distribution of a test model and more importantly its Mean Time To Failure (MTTF, the expected time to failure for a non-repairable system). Several approaches exist in order to calculate the survivors (Hosmer Jr and Lemeshow, 1999). They can be parametric and non-parametric approaches. The commonly used method is the *Kaplan-Meier* estimator (Kaplan and Meier, 1958). It is a non parametric method that does not need any assumptions for the distribution of the survival time, or the relationship between the covariates and the survival time (refer to Khalil and Lopez-Caballero (2021) for more details).

Section 4.4 analyzed the damage measure of example sequences of MS and MS-AFS. In order to take into account all the tested sequences and evaluate their survival probability, a survival analysis is conducted to estimate the useful working life of the embankment. The survival functions for *Moderate* (DL3) and *Serious* (DL4) damage levels are shown in Figure 4.9. The MTTF and the *p-value* are indicated in this figure. Typically, if the *p-value*  $\leq 5\%$ , the null hypothesis  $H_0$  is rejected, and vice versa. Appendix G presents a detailed explanation about the statistical parameter *p-value*. The null hypothesis  $H_0$  in the case of this chapter is to state that there is no difference in the lifetime distribution of the embankment between a MS or a MS-AFS sequence. In addition, an informative risk table shows the number of sequences that did not reach the precised damage level in a specific period of time.

Concerning the *Moderate* damage (or DL3, Figure 4.9a), the MTTF of both MS and MS-AFS sequences occurs within the useful life of the embankment (i.e. 100 years). However, the

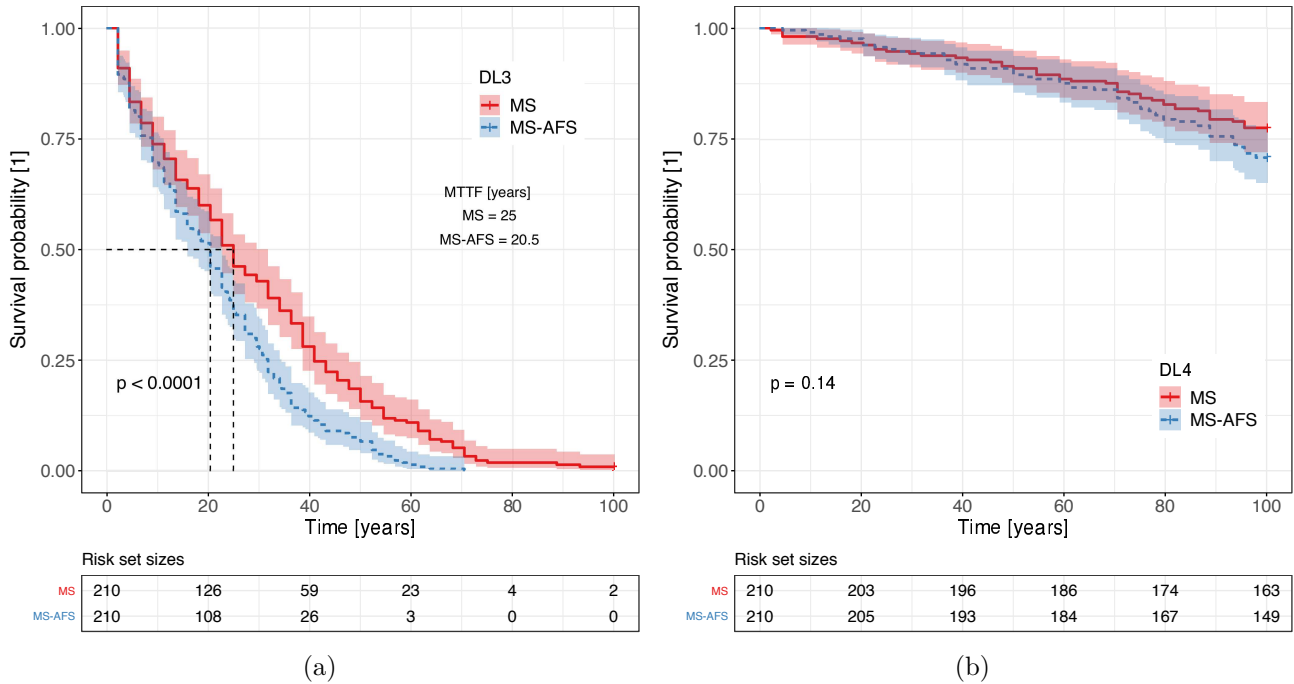


Figure 4.9: Survival functions of the two types of sequences used in this study for a) *Moderate* damage (DL3) and b) *Serious* damage (DL4)

occurrence of aftershocks decreased the MTTF of the embankment for 5 years (i.e. 20.5 years instead of 25 years for MS sequence). The risk table shows also that more sequences have reached *DL3* when the aftershocks occurred. For example, at 20 years, 126 MS sequences resisted this level of damage comparing to a decrease to 108 MS-AFS sequences that resisted it. Moreover, the  $p$ -value  $\leq 5\%$ , which means that  $H_0$  is rejected and thus, there is a difference between the lifetime distribution of the MS and MS-AFS sequences for *Moderate* damage level. As for the *Serious* damage (or DL4, Figure 4.9b), the embankment maintains its initial performance and then starts to degrade. The survival function did not reach its MTTF and the null hypothesis is accepted, thus, the two distributions are alike for this damage level. However, after 70 years, the lifetime distribution for *DL4* in the case of MS-AFS sequences is slightly different from that of the MS sequences. This remark can also be seen from the risk table. Thus, for *DL4*, the embankment might reach its MTTF for a time window greater than 100 years (e.g. 475 years). This means that for the same event rate of mainshocks, the number of shocks should be greater than 44 input motions in one sequence. Clearly, the survival probability is site and structure specific because it is controlled by the ground motions characteristics and the working life of the concerned structure.

It can be partially concluded that for the considered working life of the embankment, the aftershocks occurrence is important for small damage levels whereas it is not the case for high damage levels. This aspect was seen because the embankment for DL3, started to degrade directly after the first shock, however for DL4, it maintained its initial performance and then degraded with time.

Since the survival analysis can be interpreted as a probability of failure, the coming section will develop the classical way to calculate this probability (i.e. fragility curves) and evaluate it during the working time of the embankment.

## 4.6 Fragility curves evolution

From Section 4.5, it was found that for *Moderate* damage level, the lifetime distribution of the MS and MS-AFS sequences is not the same, on the opposite to *Serious* damage level. In this section, and because the fragility curves are commonly used for seismic loss estimation and risk management, their time evolution will be assessed. Classical fragility curves represent the failure probability of one event of given intensity (Shinozuka et al., 2000; Sáez et al., 2011; Zentner, 2017; Iervolino et al., 2020, among others). However, for life cycle assessment, it is necessary to account for the build-up of seismic losses because of the damage in multiple events. In addition, the fragility functions are developed from *independent and identically distributed* observations. Hence, it is difficult to conduct the fragility curves for the cluster earthquakes since the aftershocks depend on their corresponding mainshock. More importantly, the history of loading in the soil plays a major role in its future behavior, which emphasizes the importance of the sequential analysis (Khalil and Lopez-Caballero, 2021). In order to overcome these challenges, the evolution of the fragility curves during the lifetime of the embankment proposed in this study is summarized in Figure 4.10 (continuity of Figure 4.1).

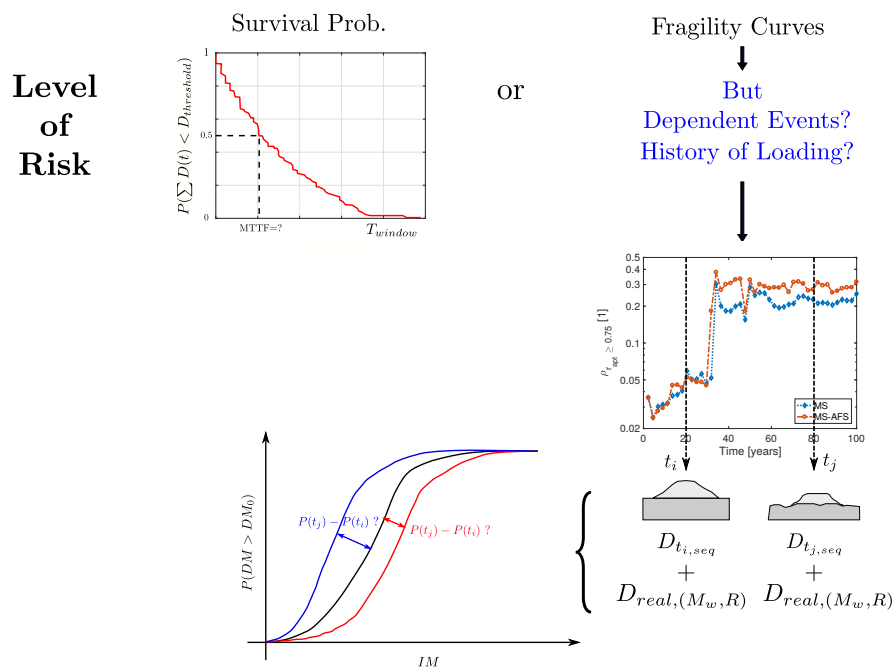


Figure 4.10: The methodology presented in this section

For different time intervals during a MS-AFS sequence, the damage state of the embankment is not the same. For each corresponding state (considered as a new initial state - site

and structure specific), the damage is calculated after a number of unchained real motions (structure-specific) in order to calculate the fragility curves. Thus, the total induced damage is the one produced from the cumulative damage at  $t = t_i$  resulted from the MS-AFS sequence added to the one produced from unchained ground motions (i.e.  $D_{tot} = D_{cum_{ms-afs}(t_i)} + D_{real}$ ). According to that, and given the IM corresponding to the real ground motions, the evolution in time of the fragility curves is calculated. In the case of this work, the real ground motions are events ranged between 5.2 and 7.6 in magnitude and a site-to-source distances from 15 to 50 km. These events correspond to the type *RM* developed in Chapter 2. The MS-AFS sequence taken as an example is shown in Figure 4.11 and the years interval after which the fragility curves will be calculated are 0, 11, 22, 45 and 100 years (dashed lines).

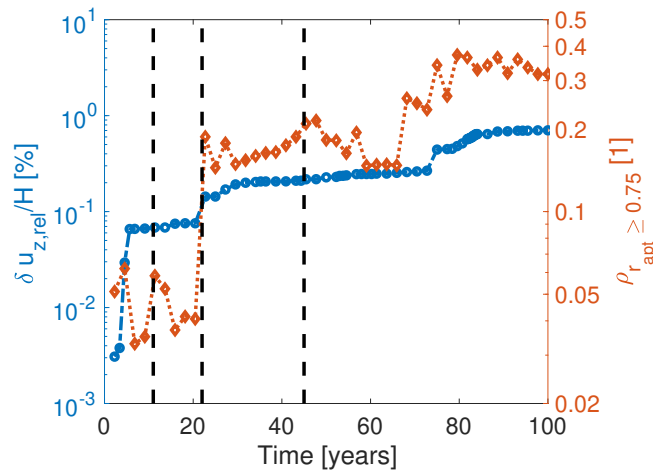


Figure 4.11: The MS-AFS sequence example and the time interval after which the fragility curves will be calculated

First, in order to examine the evolution of the global response of the embankment after each time interval, its damage measure is drawn in Figure 4.12a. It should be noted that in this figure, “NH” means “no history” and “WH” means “with history”. Taking as a reference the damage at  $t_0 = 0$ , which means when the embankment did not have a loading history, the evolution of  $\delta u_{z,rel}/H$  shows that crest settlement increases when the time increases. It is interesting to mention that for longer  $t_0$ , the history of loading delays the arrival to high values of  $\delta u_{z,rel}/H$  that are compatible with the referenced values (at  $t_0 = 0$ ).

Concerning the second damage index related to the soil’s residual strength,  $\rho_{r_{apt} \geq 0.75}$ , and its link with  $\delta u_{z,rel}/H$ , Figure 4.12b shows that for a short lifetime duration (i.e.  $t_0 = 11$  or 22 years),  $\delta u_{z,rel}/H$  and  $\rho_{r_{apt} \geq 0.75}$  were still acceptable. In addition, the results overlaps with the ones of  $t_0 = 0$ . This indicates that sometimes, the short term analysis may be enough to represent the performance of the embankment. However, for higher values of  $t_0$ , both  $\delta u_{z,rel}/H$  and the density parameter  $\rho_{r_{apt} \geq 0.75}$  showed important values with a tendency to regain the initial values at  $t_0 = 0$ . This result emphasizes the need to consider sequential analysis to understand the global performance of the structure during its lifetime.

As for the calculation of the fragility curves, two-parameter log-normal distribution functions

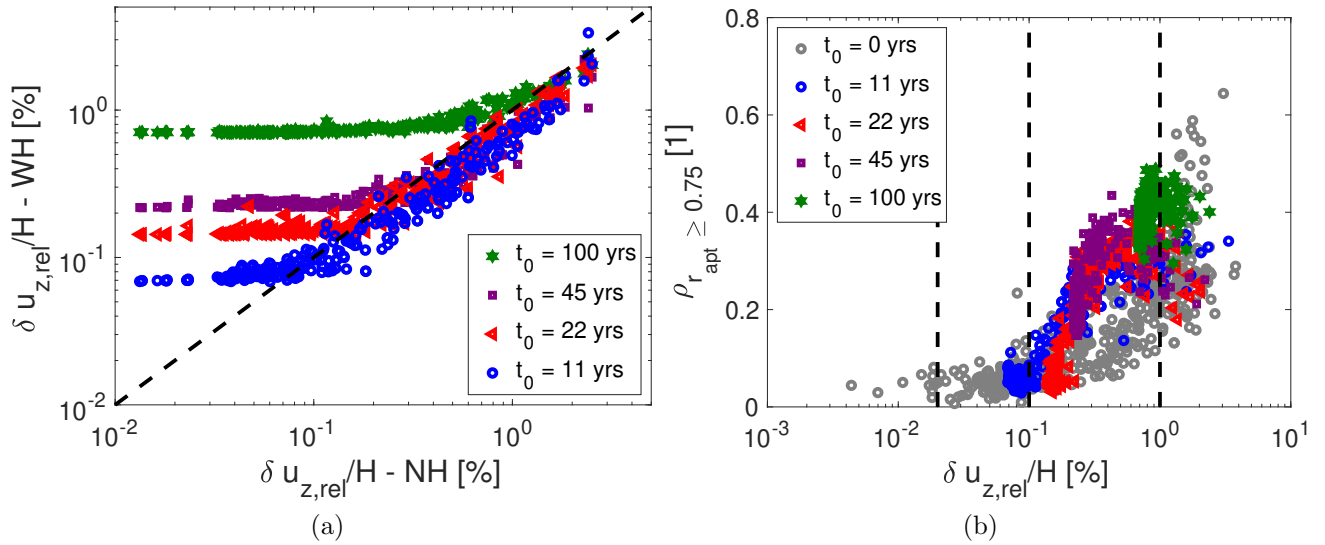


Figure 4.12: The time evolution of the crest settlement  $\delta u_{z,rel}/H$  and the density parameter  $\rho_{r_{apt}}$

are used (Equation 4.16) and are estimated from the maximum likelihood method (Shinozuka et al., 2000; Sáez et al., 2011). In addition, the quality of fit and the estimation of the confidence intervals are conducted from the methodology presented in the work of Sáez et al. (2011). More details about the computation of the fragility functions are presented in Appendix E. Considering a damage measure  $DM_0$  for given a IM of level  $im$ . It has the following form:

$$P(DM > DM_0 | IM = im) = \phi \left[ \frac{\ln im - \ln \eta_{DM|IM}}{\beta_{DM|IM}} \right], \quad (4.16)$$

where  $\phi[.]$  is the standardized normal distribution function.  $\eta_{DM|IM}$  is the median threshold value of IM required to cause the damage and  $\beta_{DM|IM}$  is the total lognormal standard deviation. One or more IMs can be used to represent the fragility curves (Lopez-Caballero and Khalil, 2018). In this study, the intensity measure is the outcrop acceleration  $a_{max,out}$ , and the damage levels are *Moderate* and *Serious*. The results are shown in Figure 4.13. The solid line in this figure shows the response of the embankment without a past history which means at  $t_0 = 0$ .

Clearly, from Figure 4.13, the fragility curves evolves with time. At 11 years, the probability of exceeding the *Moderate* damage level depends on the severity of the ground motion that happened during this time (Figure 4.13a). For example, for ground motions of accelerations less than 0.2 g, the fragility curve is lower than that at  $t_0 = 0$ . However, greater than 0.2 g and for this short time interval, the embankment reaches failure faster when it has a history of loading. It should be mentioned that the other time intervals (i.e. 22, 45 and 100 years) are not drawn for this damage level, since their probability of failure is 1. As seen in Figure 4.11, the new “initial” state of the embankment after those time intervals has already surpassed the *Moderate* damage level. Concerning the *Serious* damage level in Figure 4.13b, also for  $t_0 = 11$  years, the probability of failure depended on the severity of the ground motion. However, at 22

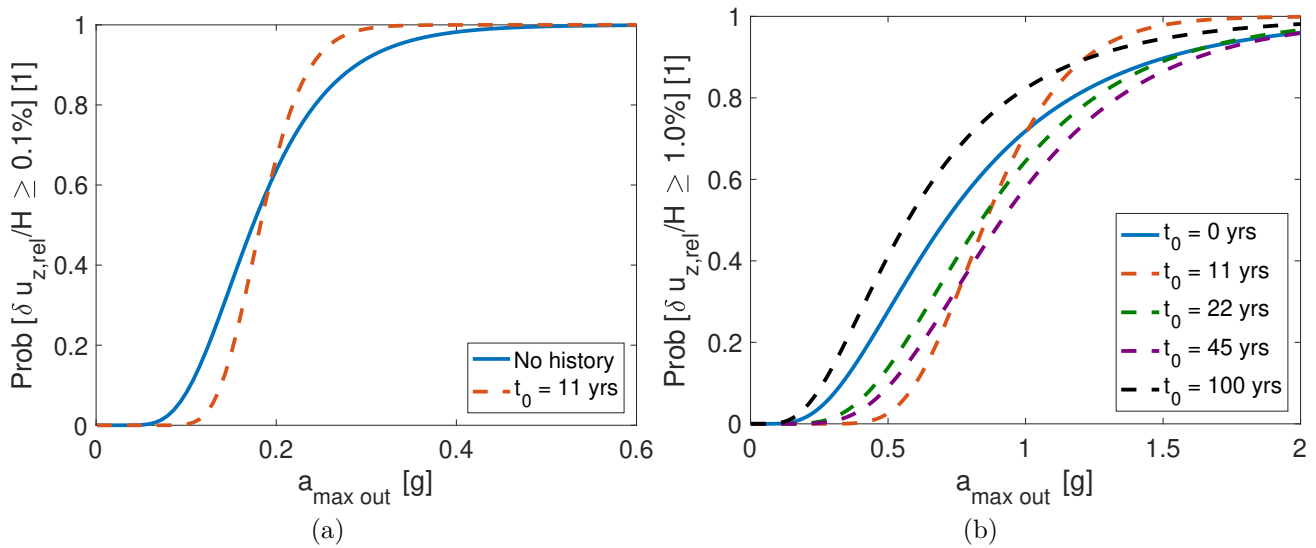


Figure 4.13: The evolution in time of the probability of exceeding the a) *Moderate* and b) the *Serious* damage level

and 45 years, the fragility curves are lower than that at  $t_0 = 0$ . Thus, it can be deduced that the embankment resisted the applied load better than the beginning of its lifetime. This result points out the importance of the soil history of loading that affects its future behavior and may result in soil densification. Nevertheless, at 100 years, the probability of failure increases, and the embankment resistance to the amount of loading decreases.

In order to take into account different sequence examples, Figure 4.14 shows the fragility curve of *Serious* damage evolution for two other example sequences having different permutations of their mainshock occurrence. First, it can be seen that the interpretation of this case is different from the one conducted for Figure 4.13b. For the same IM, in the case of sq14, the probability of failure decreases at the beginning of the lifetime indicating a soil densification, to then increase starting 43 years. However, for higher time intervals, the probability of exceeding this damage level increases. It is interesting to notice that sq14 and sq48, at almost close  $t_0$  (i.e. purple and yellow curves), showed completely opposite behavior. sq14 indicates a probability of failure close to that at  $t_0 = 0$ , however, sq48 shows an increase in this probability.

Thus, it can be deduced from these results, that the initial state of the embankment for each selected time interval is site-specific and affected by the history of loading. Otherwise, the fragility curve computation is somehow a structure-specific approach. The probability of collapse decreases if the embankment tends to densify due to its history of loading, or the opposite if its initial state was already excessively damaged. It should be reminded that the embankment during its lifetime was not subjected to any type of reinforcement or amelioration.

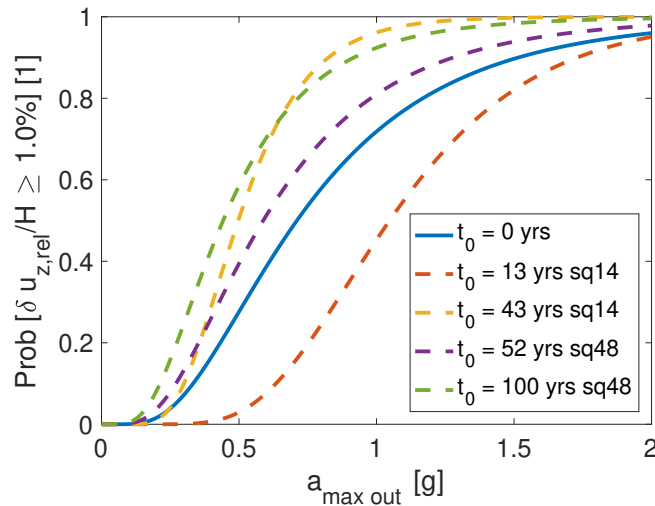


Figure 4.14: The evolution in time of the probability of exceeding the *Serious* damage level for different sequence examples

## 4.7 Concluding remarks

This chapter presents the lifetime evolution of the performance of the embankment subjected to sequential cluster events. The mainshock events were similar to the ones presented in Chapter 3 and were composed from the synthetic ground motion model of [Rezaeian and Der Kiureghian \(2012\)](#). It was first presented in this chapter the model to generate the aftershocks that is based on the probabilistic version of the BASS model and is inspired from [Turcotte et al. \(2007\)](#) and [Hu et al. \(2018\)](#). This chapter tries to answer the questions asked in the introduction as such:

- a) During sequential earthquakes, the potential failure of the embankment evaluated from its global damage measure shows that during time, the damage is higher for sequences with aftershocks (i.e. MS-AFS) than the ones without the aftershocks occurrence (i.e. MS).
- b) The survival functions with their MTTFs values, showed that the consideration of the aftershocks events is important for moderate levels of damage. However, the embankment survived high damage levels for a working life of 100 years.
- c) The evolution of the fragility curves depends on the sequence type, and more importantly the initial soil state. It should be mentioned that the fragility functions were not computed for the sequential cluster events themselves due to some challenges (i.e. dependency of the mainshock and aftershock events, the randomness of the aftershock occurrence and the soil history of loading). Instead, it was evolved for some time intervals of a sequence example, after a bundle of unchained recorded ground motions. It was shown that the probability of failure either increases or decreases from the very initial probability of failure at  $t_0 = 0$ .



# Chapter 5

## Application of a mitigation method to reduce the earthquake-induced liquefaction of an embankment

### Contents

---

<b>5.1</b>	<b>Introduction</b>	<b>118</b>
<b>5.2</b>	<b>Geometry and numerical model</b>	<b>123</b>
5.2.1	Geometry	123
5.2.2	Finite Element model	124
5.2.3	Boundary conditions	124
<b>5.3</b>	<b>Soil constitutive model</b>	<b>124</b>
<b>5.4</b>	<b>Injection technique</b>	<b>125</b>
5.4.1	Location of the injection	126
5.4.2	Injected material	126
5.4.3	Method for injection	127
<b>5.5</b>	<b>Input ground motion</b>	<b>128</b>
<b>5.6</b>	<b>Comparison of the treated and untreated cases</b>	<b>128</b>
5.6.1	Comparison based on the number of the injection zones	129
5.6.2	Comparison based on the injected material	130
5.6.3	Comparison based on the stress - strain evolution	130
<b>5.7</b>	<b>Amelioration ratio of the crest settlement</b>	<b>132</b>
<b>5.8</b>	<b>Fragility curves of the tested cases</b>	<b>134</b>
<b>5.9</b>	<b>Sensitivity analysis of the crest settlement amelioration ratio</b>	<b>136</b>
<b>5.10</b>	<b>Concluding remarks</b>	<b>138</b>

---

## Abstract

Natural biological solutions have been used to overcome the challenges of the typical soil improvement methods. From experimental studies in this field, the treated soil will increase its dilatant behavior, and a small amount of carbonate content is enough for soil amelioration. From numerical studies, the permeability and porosity of the treated material decrease, and one yield surface emphasizes the procedure.

This chapter aims to combine, from a phenomenological viewpoint, experimental and numerical results to assess a mitigation application on a liquefiable foundation of an embankment. The improvement requires the replacement of a treated material within an injection zone. The effect of the number and type of the materials, and the potential of liquefaction of the embankment are discussed. Large number of input motions is considered. Fragility curves are drawn. A sensitivity analysis is conducted to identify the ground motion parameter that controls the amelioration ratio of the crest settlement.

This chapter was submitted to the *Géotechnique* journal and cited as *Khalil, C., & Lopez-Caballero, F. (2021). Application of a mitigation method to reduce the earthquake-induced liquefaction of an embankment. Géotechnique. (Submitted)*

## 5.1 Introduction

The step change of the existing geotechnical practices to improve the soil against liquefaction has been recently focused on the choice of natural biological solutions. Previously, the typical methods required the densification or compaction of the soil with mechanical energy (Brennan and Madabhushi, 2002; Mitrani and Madabhushi, 2012; Montoya-Noguera and Lopez-Caballero, 2016, among others). It was shown that these methods may be disruptive to existing facilities and may cause extensive settlements. For this purpose, the mediated or inspired methods provide somehow a sustainable ground improvement solution with less harm to the nature. They are called the *Bio-mediated* or *Bio-inspired* processes. The latter is described by an attraction or a translation of biological solutions to develop new abiotic solutions (DeJong and Kavazanjian, 2019; DeJong et al., 2017). Whereas the *Bio-mediated* processes are managed and controlled through biological activities together with chemical reactions. It should be mentioned that the *Bio-mediated* processes, regroups three concepts: Microbial Induced Calcite Precipitation (MICP), Enzymatically Induced Calcite Precipitation (EIDP) and Microbially Induced Desaturation and Precipitation (MIDP). Researchers have collected that a treated soil with these methods will have a higher shear wave velocity, unconfined compression strength and peak friction angle than an untreated soil (Montoya and DeJong, 2015; O'Donnell, 2016; Lin et al., 2016; Gomez and DeJong, 2017; Cui et al., 2017; Lee et al., 2020; Zhang et al., 2020; Yu et al., 2020, among others). For example, in the work of O'Donnell (2016), undrained triaxial tests on Ottawa sands with  $D_r = 40\%$  and  $p'_0 = 100$  kPa were conducted. In order to evaluate

the effect of the MICP, different percentages of carbonate content were applied. The results of the referenced work are represented by the stress paths (Figure 5.1a) and the variation of the excess pore water pressure (Figure 5.1b). Moreover, it is known that soils are primarily controlled by the relative amounts of shear stress to mean stress which is also designated as the stress ratio  $\eta = q/p'$  (Been and Jefferies, 1985). Thus the variation of  $\eta$  can be considered as a dilatancy indicator because of its relation with the critical friction ratio  $M$  or the friction angle at the critical state  $\phi'_{pp}$ . Figure 5.1c shows the variation of  $\eta$  with respect to the axial strain  $\epsilon_1$  adapted from the conducted tests in the work of O'Donnell (2016). It is clear that the soil becomes more dilatant since the stress ratio reaches a peak value for small value of axial strain (Figure 5.1). Furthermore, an important finding of the cited work is that a small carbonate precipitation is able to increase the stiffness and dilatant behavior of the soil.

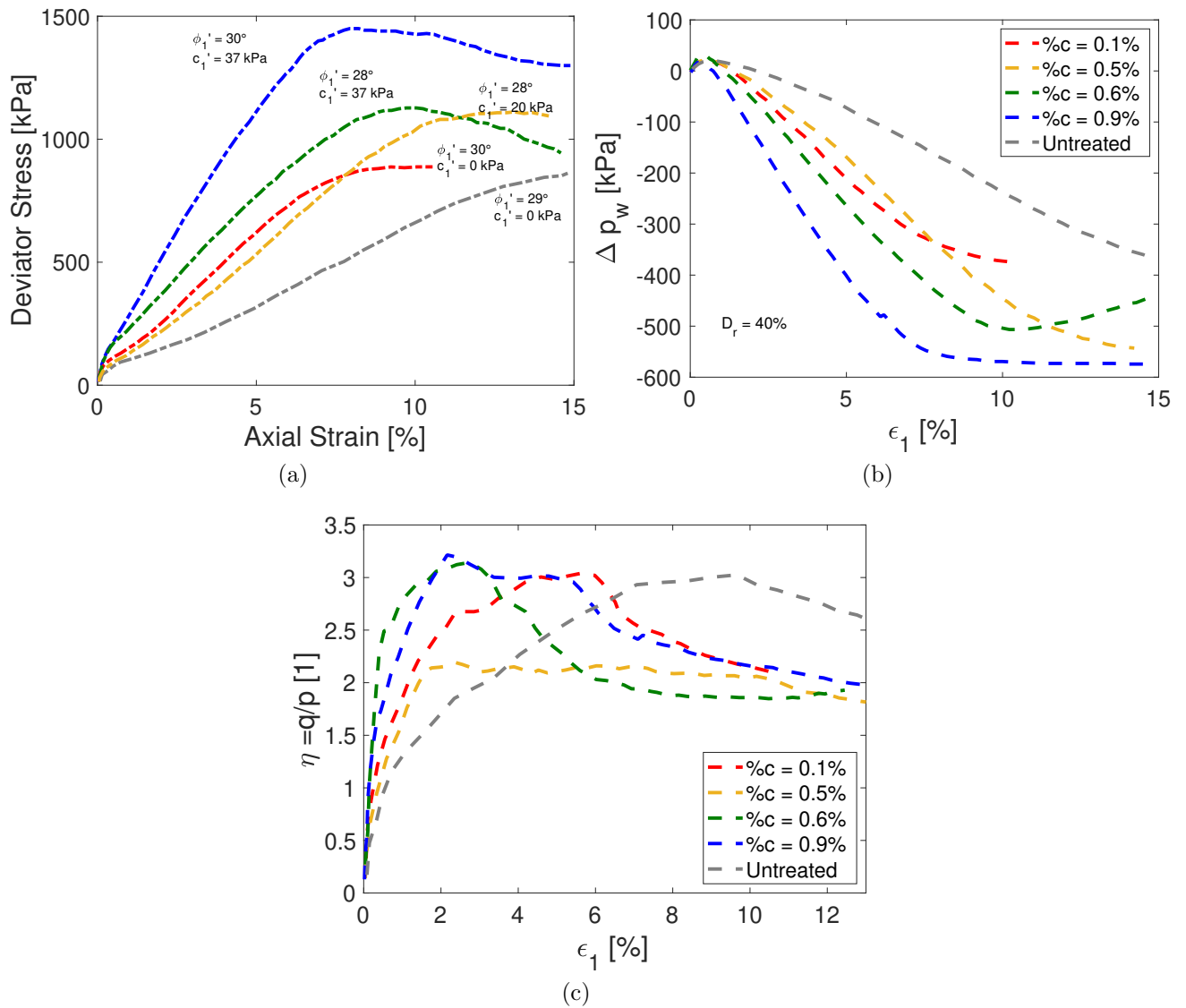


Figure 5.1: The a) deviator stress, b) excess pore pressure and c) stress ratio from undrained testing of specimens at an initial relative density of 40% and a confining stress of 100 kPa, extracted and adapted from O'Donnell (2016)

## Challenges of ground improvement technologies

Although the improvement techniques are very important in ameliorating the soil, a good attention should be made on the choice of the method because in some cases the added material could be toxic to the surrounding and will cause other problems (O'Donnell, 2016). Thus, additional costs will occur and are not appreciated by decision makers or industries. Moreover, it cannot be denied that these methods present some challenges since any change in the macro-scale performance (i.e. the addition of products) will affect the micro-scale soil conditions (i.e. between the soil particles). Also, the common challenge for soil improvement techniques is the upscaling effects due to the addition and transportation of products. So it is not easy to consider both, the durability and longevity of the process to choose the best solution with the least cost (Fauriel and Laloui, 2012).

## Numerical studies *vs* Soil improvement techniques

Modeling the Bio-mediated processes require appropriate numerical tools that take into account the coupling between the mechanics and the bio-chemo-hydraulics approaches. The focus of existing models has been mainly on the prediction of the bio-chemical processes and the precipitated calcite distribution during the process (Van Wijngaarden et al., 2011; Stumpp et al., 2011; Fauriel and Laloui, 2012; Feng and Montoya, 2016, among others). Since bacteria are living organisms, they are subjected to mechanisms that affect the transport and the removal of microbes in saturated, porous media as well as physico-chemical phenomena (Fauriel and Laloui, 2012). The majority of the mathematical models involve a simplified form of the advection-dispersion equations (Yavuz Corapcioglu and Haridas, 1984; Van Wijngaarden et al., 2011; Stumpp et al., 2011, among others). Few models consider the change in the mechanical properties due to the treatment (Van Wijngaarden et al., 2011; Fauriel and Laloui, 2012; Feng and Montoya, 2016; Gai and Sánchez, 2019, among others). For example, in the work of Gai and Sánchez (2019), a mechanical model in the framework of an elastoplastic theory and strain hardening was presented in order to model laboratory tests for the MICP process. The model was described with three yield surfaces: i) a critical state soil mechanics, ii) a MICP enhanced and iii) a sub-loading yield surfaces. The purpose behind this consideration is to be able to describe the behavior of the soil during the monotonic loading, consider the mechanical influence of the calcite precipitation and allow a smooth transition between elastic and plastic phases. It was found from this cited work that the increase in the stiffness will induce a reduction in the strain of the treated soil. In addition, the findings of their works showed that the yield surface expands from a normal to a treated state but it does not change its shape.

Also in the context of modeling soil improvement methods, a bio-chemo-mechanical coupled approach was presented in the work of Fauriel and Laloui (2012) where a nonlinear elastic model to simulate the mechanical behavior of treated soils was adopted. Two-way coupling between the hydro-mechanical system (i.e. flow, porosity, permeability stress-strain) and the bio-chemical

system (i.e. diffusion, dispersion, reaction rate) was addressed to realistically predict the MICP process and the overall system response. Concerning the mechanical responses, [Fauriel and Laloui \(2012\)](#) concluded that the effective stress change is negligible due to the precipitation of the calcium carbonate. In addition, the porosity and the permeability decrease. Thus, the bacteria accumulation will not affect the volume of the fluid, instead, it will alter the solid phase ([Van Wijngaarden et al., 2011](#); [Fauriel and Laloui, 2012](#)). Moreover, the increase in the stiffness will induce a reduction in the strain of the treated soil.

Hence, it is evident that the micro scale level (i.e. order of nanometers) is dependent on the initial assumptions as well as the boundary conditions of the numerical model. Whereas for the macro scale level (i.e. order of meters), previous works have been conducted to identify the global response of structures after treated soil profiles ([Elgamal et al., 2002](#); [Adalier and Aydingun, 2003](#); [Lopez-Caballero and Modaressi-Farahmand-Razavi, 2013](#); [Xu et al., 2013](#), among others). For example, in the work of [Montoya-Noguera and Lopez-Caballero \(2016\)](#), the effect of the spatial heterogeneity of the treated soil in a foundation is studied. It was found that the liquefaction was reduced due to spatial distribution of the treated zones. In addition, it was emphasized the importance of the mechanical behavior of the soil rather than the permeability change.

## State of art of this work

The state of art of this work is to present a soil improvement application that combines the experimental-numerical approaches presented so far. This means that, from a phenomenological point of view, this work will take into consideration the behavior changes of the treated soil proven experimentally (i.e. the dilatant behavior and amount of carbonate content) as well as the numerical results that simulated the process (i.e. the permeability decrease, the mechanical response and the unmodified yield surface). Thus, the purpose of this chapter is to numerically improve the foundation soil under a liquefiable embankment by adding treated zones and to validate the results with previous works. The methodology applied to represent the mitigation will require:

- The addition of a new material that has similar properties to a treated material with MICP. From the work of [O'Donnell \(2016\)](#), it was found that a material treated with MICP, will increase its dilatant behavior and the dilatancy of the material is proportional to the carbonate content used to mitigate the soil (Figure 5.1 extracted and adapted ([O'Donnell, 2016](#))). It should be mentioned that from the reaction network of the MICP, the calcite percentage increases with the carbonate content ([Gomez and DeJong, 2017](#)). Hence, for this chapter, two different calcite percentages (i.e. high and moderate) will be tested.
- Concerning the location of the treated zones and after recall to the existing numerical application, [Fauriel and Laloui \(2012\)](#) in their work, have found that the mechanical effect

from a treated and untreated soil is almost negligible. In addition, [Montoya-Noguera and Lopez-Caballero \(2016\)](#) have shown that the presence of the injection in the form of clusters affects the liquefaction triggering. On the other hand, it is known that the failure pattern of the embankment is a wedge shape located in the downstream side of the embankment ([Kramer, 1996](#); [Kourkoulis et al., 2010](#); [Sadeghi et al., 2014](#); [Rapti, 2016](#), among others). Hence, this study analyses two injection zones under the slope of the embankment. A comparison with an additional zone is also conducted in order to study the influence of the number of zones on the global response.

Following the Performance-Based Earthquake Engineering (PBEE) methodology, this study analyses the liquefaction triggering from a hazard analysis to a damage analysis. To account for the natural hazards, a large number of recorded input ground motions is taken. The quantifiable damage parameter of the embankment is its relative crest settlement. It is analyzed as function of some input ground motion characteristics. Fragility curves are also drawn to identify the damage measure. Finally, a sensitivity analysis is performed in order to identify the input ground motion parameter that controls the response of the crest settlement. This study is conducted on an embankment model and computed with a finite element code called GEFDyn ([Aubry et al., 1986](#)). An elasto-plastic multi-mechanism model is used to represent the soil behavior.

## Assumptions for this study

- At the beginning of the study, the embankment is considered in its virgin and stable state. It does not have a history of loading.
- The simulation of the injection process is out of the scope of this study. Instead, the response of the embankment after a mitigation procedure is assessed.
- For the treated cases, it is assumed that the embankment is constructed after a treated soil. Which means that the injections are included in the soil before the embankment construction.
- The same numerical model is used for all the tested cases (i.e. treated and untreated).
- The focus of this research is to capture the main tendencies and general features of the soil improvement processes, rather than to perfectly match the experimental or numerical observations.

This chapter is structured as follows. The first section presents the geometry and the numerical model. The soil constitutive model is developed next. The details of the injection technique in which the location, the materials and the method of injection are explained in Section INJECTION TECHNIQUE. The damage quantification and its comparison as function

of the treatment zone and the injected material are shown in a section. Then, section AMELIORATION RATIO OF THE CREST SETTLEMENT develops the results of all the tested ground motions in terms of the relative crest settlement of the embankment. Next, a section about the fragility curves of all the tested cases in this study is presented. The conducted sensitivity analysis to show the controlling ground motion parameter is developed in the last section. Finally, conclusions summarizing the obtained results are provided.

## 5.2 Geometry and numerical model

### 5.2.1 Geometry

The geometry of the model, as shown in Figure 5.2, consists of an embankment of 9 m high composed of dry dense sand. The soil foundation is composed by a loose sand of 4 m at the top of a saturated dense sand of 6 m. The bedrock is located at the bottom of the dense sand. The water table is situated at 1 m below the base of the levee that was kept dry. The levee's inclination is a slope of 1:3 (vertical: horizontal). The geometry used in the FEM was inspired by the one proposed by [Rapti et al. \(2018\)](#).

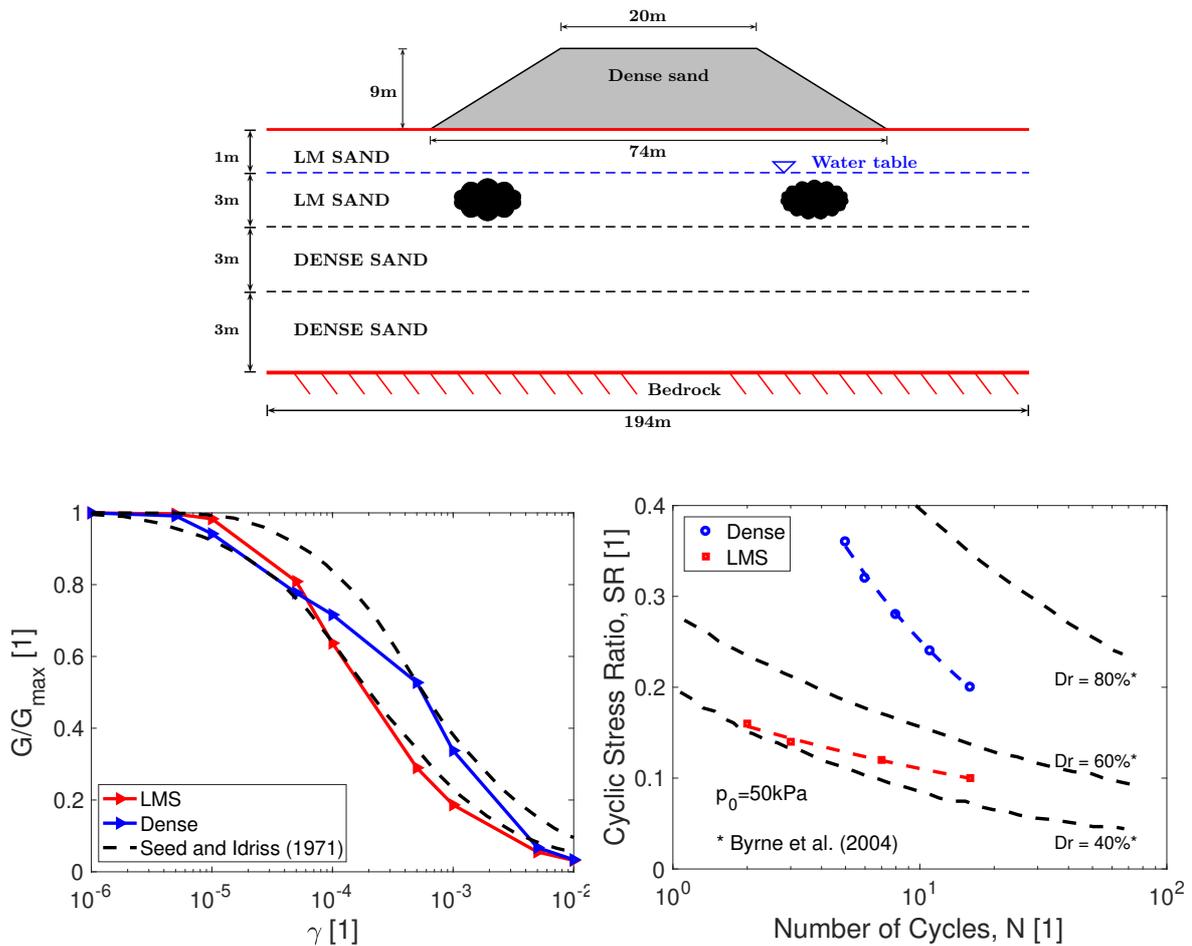


Figure 5.2: Geometry and behavior of the soil ([Lopez-Caballero and Khalil, 2018](#))

### 5.2.2 Finite Element model

The computations were carried out by the coupled FE modelling code GEFDyn (Aubry et al., 1986), using a dynamic approach derived from the  $\underline{u} - p_w$  version of the Biot's generalized consolidation theory (Zienkiewicz, 1991). An implicit Newmark numerical integration scheme with  $\gamma = 0.625$  and  $\beta = 0.375$  was assumed in the dynamic analysis (Kuhl and Crisfield, 1999). The FE model is composed of quadrilateral isoparametric elements with eight nodes for both solid displacements and fluid pressures. The element size for the soil foundation is 1.5 m horizontally by 0.5 m vertically. The FE model considers both computations; the treated and untreated cases. It is performed in three consecutive steps: i) a computation of the initial in-situ stress state due to gravity loads; ii) a sequential level-by-level construction of the embankment and iii) a seismic loading analysis in the time domain. Concerning the simulation of the injection technique, it will be more developed in its proper section.

### 5.2.3 Boundary conditions

In the analysis, equivalent boundaries have been imposed on the nodes of lateral boundaries (i.e., the normal stress on these boundaries remains constant and the displacements of nodes at the same depth in two opposite lateral boundaries are the same in all directions). They are the response of a modeled infinite semispace. Hence, only vertically incident shear waves are introduced into the domain. The model is wide enough (194 m) to ensure that the effect of the boundaries on the response of the model can be neglected and also to satisfy the free field condition at the lateral boundaries. For the half-space bedrock's boundary condition, paraxial elements simulating deformable unbounded elastic bedrock have been used (Modaresi and Benzenati, 1994). The incident waves, defined at the outcropping bedrock are introduced into the base of the model after deconvolution.

## 5.3 Soil constitutive model

A constitutive model for soils should be able to well represent the volume change in case of drained conditions or the distribution of the excess pore water pressure in case of undrained conditions (Aubry et al., 1982). In addition to the stress-relationship which controls the settlements, the use of numerical modeling best describes the non-linear soil behavior under cyclic loading. A good modeling takes into consideration essential properties: necessary data, an appropriate constitutive model and adequate parameters, in addition to the method that solves boundary value problems (Lopez-Caballero et al., 2003). The *Ecole Centrale Paris (ECP)* elastoplastic multi-mechanism model (also known as Hujoux model) is the one chosen for this study and is written in terms of effective stress (Aubry et al., 1986). The non-linearity of this model is represented by four coupled elementary plastic mechanisms: three plane-strain deviatoric plastic strain mechanisms in three orthogonal planes ( $k$  - planes) and an isotropic

one. The model follows a Coulomb type failure criterion, contemplates the existence of dilatancy/contractancy phenomena, and uses the critical state concept. The cyclic behavior is taken into account by a kinematical hardening that is based on the state variables at the last load reversal. The model is written using incremental plasticity which divides the total strain increment into an elastic and a plastic part. Refer to (Aubry et al., 1982) and (Lopez-Caballero et al., 2003), among others for further details about the ECP model.

In order to identify the behavior of the two foundation layers, the  $G/G_{max} - \gamma$  curves and the cyclic resistance ratio  $CSR$  were simulated for an initial effective stress of 50 kPa. The results are shown in Figure 5.2. Based on reference studies conducted by Seed and Idriss (1971) for  $G/G_{max} - \gamma$  curve and Byrne et al. (2004) for  $CSR$  curve, it can be seen from Figure 5.2 that the loose sand (LMS) has a small resistance to liquefaction on the opposite to the dense sand. In addition, it has a relative density close to  $D_r = 40\%$ , whereas that of the dense sand is close to  $D_r = 70\%$ . The loose layer is the one to be concerned by the injection in the following study.

## 5.4 Injection technique

The liquefaction-susceptibility of the soil during seismic activities is enhanced by the use of various improvement techniques (DeJong et al., 2010; Bradley et al., 2013; O'Donnell, 2016, among others). The *Bio-mediated* processes are managed and controlled through biological activities together with chemical reactions. Concerns about the spatial distribution of the injected material, its timing rate of injection as well as its depth in soil, are essential for an effective mitigation (DeJong et al., 2010). As developed in the introduction of this work, the choice of the treated zone is based on the existing numerical applications in this field. Fauriel and Laloui (2012) in their work found that the coupling between the mechanical and the bio-chemo-hydraulics result in a permeability decrease from the treated to the untreated soil cases. In addition, the effective stress change is almost negligible. In this context and concerning the global structural response after treatment, Montoya-Noguera and Lopez-Caballero (2016) found that the presence of the injection in the form of clusters affect the liquefaction triggering. Thus, this work will study different injection zones.

For the material type and from the work of O'Donnell (2016), a soil treated with a bio-mediated process (i.e. MICP) increases its stiffness, strength and dilatant behavior. Figure 5.1 extracted and adapted from this cited work, shows that a small carbonate content is necessary to improve the undrained response of a liquefiable soil. Moreover, the dilatancy of the material is proportional to the carbonate content used to mitigate the soil (O'Donnell, 2016). It is also remarked that the reaction network of the MICP requires the carbonate equilibrium in order to produce the calcite precipitation (Gomez and DeJong, 2017). This means that the calcite percentage increases with the carbonate content. Thus, this chapter will numerically study the response after two different injected material: one with a high calcite percentage (i.e. greater

than 2%) and another with a moderate calcite percentage (i.e. less than 1%). The location of the injection zones as well as the behavior of each material and the foundation will be discussed in this section.

### 5.4.1 Location of the injection

Based on previous works, one of the failure patterns under an embankment is the one described as a zone that starts underneath the embankment and continues vertically or inclined toward the slopes. A wedge shape will be created around the crest of the embankment (Kramer, 1996; Kourkoulis et al., 2010; Sadeghi et al., 2014, among others). Figure 5.3, extracted from the work of Rapti et al. (2018) in which the same numerical model was used, shows the distribution of the deviatoric strain at the end of an earthquake motion. It is clear that  $\varepsilon_d$  reaches its highest values below the toes of the levee, which confirms the wedge shape developed in the literature. For this reason, the injected material in this study will consider the zones under the slope of the embankment (represented as black clouds in Figure 5.2). The depth of the treatment zone should consist of the layer that is more susceptible to liquefaction (i.e. 4 m in this case) (Gopal Madabhushi, 2007). In order to verify if the increase in the injection zones

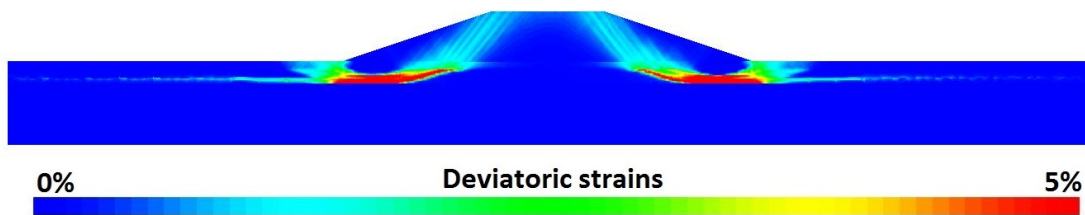


Figure 5.3: Deviatoric strain  $\varepsilon_d$  at the end of the ground motion (Rapti et al., 2018)

affects the liquefaction potential, a third zone in the middle of the liquefiable layer is added. The quantified damage developed in later on in this chapter, is compared for both cases: two injection zones and three injection zones.

### 5.4.2 Injected material

As mentioned in the introduction of this section, the improvement of the soil will consist of two different materials: greater than 2% calcite percentage and less than 1% calcite percentage. For this purpose, monotonic triaxial undrained tests will be simulated on the injected and untreated materials. The untreated material is extracted from the first foundation layer. The used initial effective stress is  $p'_0 = 50$  kPa. The results are shown as function of the stress-strain path (Figure 5.4a), the variation of the excess pore water pressure (Figure 5.4b) and the stress ratio  $\eta$  (Figure 5.4c).

It can be seen from Figure 5.4 that the foundation soil is very loose and has a contracting behavior. Whereas the treated materials, regardless of the calcite percentage, have a dilatant

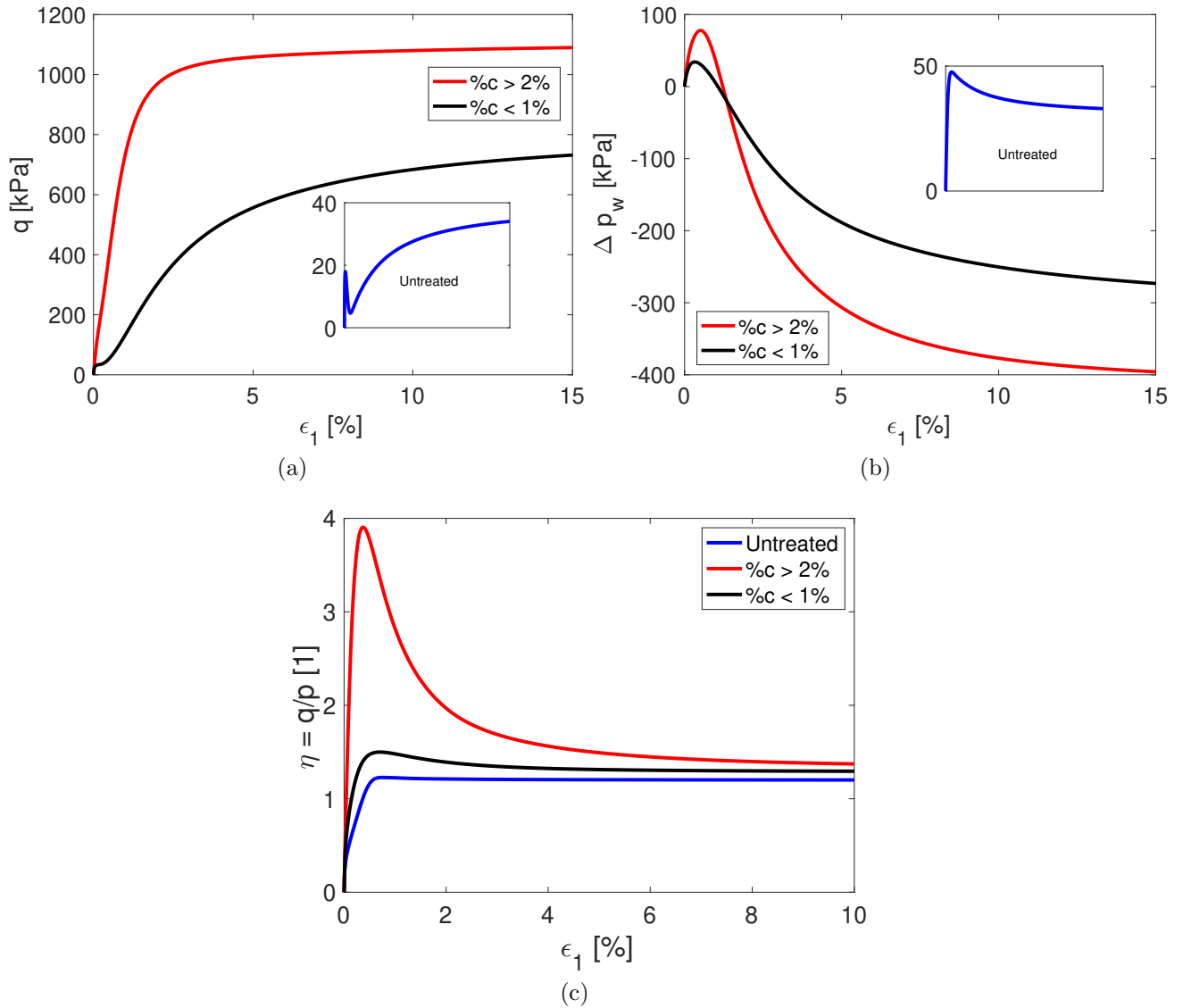


Figure 5.4: The soil behavior of the tested materials for  $p'_0 = 50$  kPa

behavior similar to a soil sample treated with bacteria reactions. In addition, it is clear from Figure 5.4c that the sample with high calcite percentage has a higher dilatancy, as shown in the work of Cui et al. (2017) with triaxial test on Ottawa sand.

### 5.4.3 Method for injection

It is known that the efficiency of the mitigation method, precisely the injected length depends on the ground porosity, geometry and depth of the treatment zone. In fractured materials for example, the heterogeneity of the soil porosity affects the injected length. In addition, it was shown that the formation of the inclusion does not take a regular shape once injected in the soil (Prabhakaran et al., 2020). Thus, in order to represent the injection method a probabilistic approach called the Power Law Distribution (Reeves et al., 2008) is used. After fixing the depth and the width of the injection zone and at every depth in the liquified layer, the material used

for treatment is "injected" horizontally following the formula (Reeves et al., 2008):

$$P(L > l) = wl^{-a} \quad (5.1)$$

where  $P$  = probability that the length of injection  $L$  exceeds the max length  $l$ ;  $w$  = a constant that depends on the minimum length taken to be 1 and  $a$  = a power law exponent taken to be equal to 1.5 in this work. As mentioned previously in this section, the foundation will be improved with different zones of injection. The discretization into mesh elements and the injection zones are shown in Figure 5.5.

After developing the necessary data to calculate the damage, the natural hazard is accounted

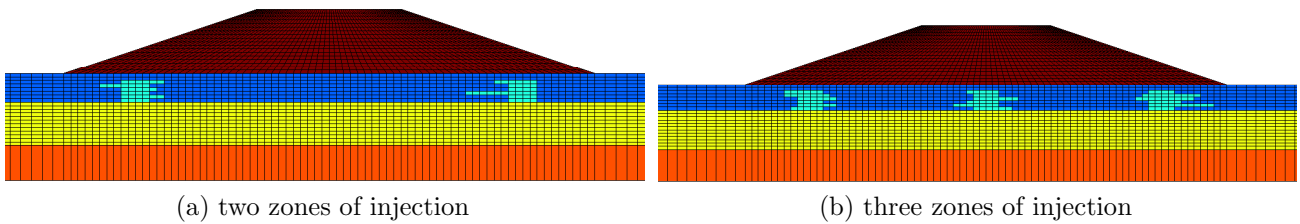


Figure 5.5: The mesh elements and the different zones of injections

for by the use of a large set of recorded input ground motions that will be developed in the following section.

## 5.5 Input ground motion

The selection of input motions for geotechnical earthquake engineering problems is important as it is strongly related to the nonlinear dynamic analysis. In this study, 271 recorded signals were chosen to represent the dynamic behavior of the model in order to represent the consistency of the seismic parameters and characteristics. Several Intensity Measures (IM) from each signal are interrelated each others (e.g. PGA, PGV,  $M_w$ ). They are extracted from a study conducted by Lopez-Caballero and Khalil (2018). The events range between 5.2 and 7.6 in magnitude. The recordings have site-to-source distances from 15 to 50 km and concern dense-to-firm soil conditions (i.e.  $360 \text{ m/s} < V_{s,30m} < 800 \text{ m/s}$ ).

## 5.6 Comparison of the treated and untreated cases

The aim of this chapter is to assess numerically the application of a mitigation method inspired from the Bio-mediated solutions for soil improvements. It is known that following these methods, the treated soil will increase its dilatant behavior (O'Donnell, 2016). Implementing the PBEE methodology in this work, the Engineering Demand Parameter (EDP) is calculated from the relative crest settlement  $\delta u_{z,rel}/H$  of the embankment after the occurrence of different input ground motions. In this section, a comparison between the untreated and treated cases

will be developed. It will consider the variation of the relative crest settlement as function of i) the number of the injection zones and ii) the injected material (i.e. dilatancy level or calcite percentage). In addition, the mechanical changes and the liquefaction potential of the embankment between the two cases will be examined. For each comparison and for the sake of brevity only, one ground motion will be taken as an example.

### 5.6.1 Comparison based on the number of the injection zones

It was shown in Section 5.4.1 that the injection zones are located under the edges of the embankment where the shear zones are localized (i.e. Figure 5.3). In order to represent this approach, this case will be designated in this chapter by *two injection zones*. However, as it might be thought that the greater the number of treatment zones, the better the response of the embankment (or the lesser the settlement), an additional injection zone in the middle of the shallow foundation layer is considered (designated by *three injection zones*). The co-seismic relative crest settlement  $u_{z,rel}$  of the two cases is calculated and is shown in Figure 5.6a. The characteristics of the motion taken as an example are also shown in this figure. Notice that  $a_{max,out}$  means the outcrop acceleration,  $I_{arias}$  means the Arias intensity and  $D_{595}$  refers to the significant duration (i.e. time elapsed from 5% to 95% of the integral of the acceleration).

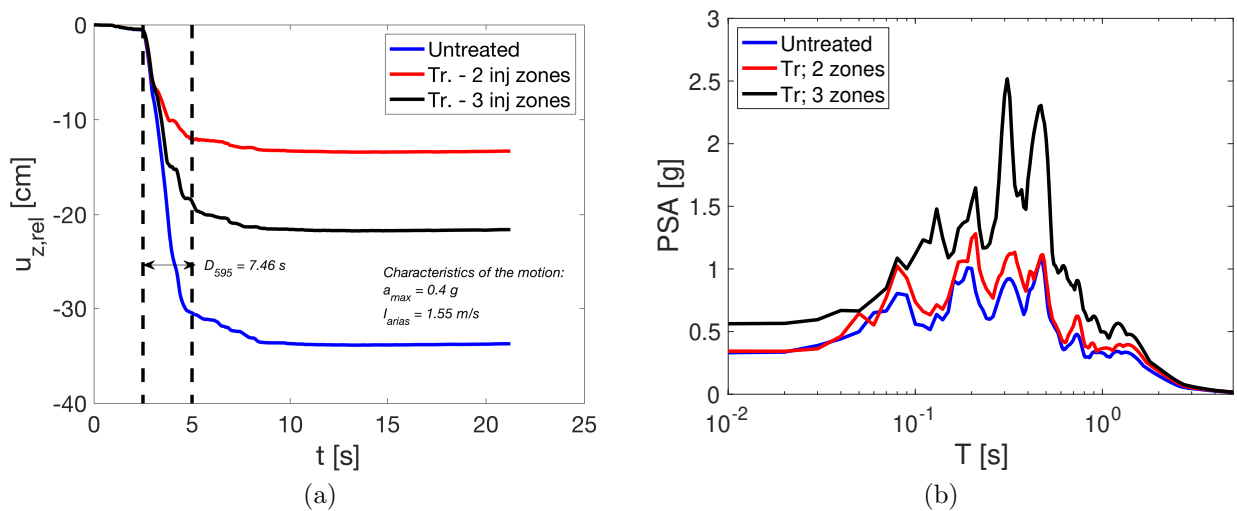


Figure 5.6: Comparison of a) the co-seismic relative crest settlement of the embankment as function of the number of the injection zones and b) the response spectral of each case

It can be seen for the three cases in Figure 5.6a, that around 2 seconds, which is the beginning of the effective duration, the crest settlement decreases rapidly. Clearly, the two injection zones reduced the settlement from 34 cm to 13 cm. By increasing the number of injection zones to three, the crest settlement was reduced to 21 cm, which is greater than the previous case. Comparing these results with those conducted by Gopal Madabhushi (2007) on a centrifuge test, they are in accordance. Although the cited study presented the densification improvement method, the theoretical concepts in both works are somehow similar: *a densified soil layer*

under a foundation reduces the settlement, and an increase in the width of this layer will give similar results (Gopal Madabhushi, 2007). Thus, other than being costly and impractical, three injection zones under the embankment does not seem to be as efficient as two zones.

In order to also verify this result, the response spectral is drawn at the crest for the three tested cases (Figure 5.6b). Clearly, there is an amplification for the case of three injection zones. This will perhaps cause the deterioration of the levee. Thus, the additional injection zone does not seem to be beneficial neither in reducing the liquefaction potential, nor the cost of construction-reparation of the embankment.

### 5.6.2 Comparison based on the injected material

It was shown by O'Donnell (2016) that a small calcite percentage is able to ameliorate the soil and change its properties. This section will present the results of the co-seismic crest settlement after injecting two different materials: i) with high calcite percentage (i.e. greater than 2%) and ii) with a moderate calcite percentage (i.e. less than 1%). The results are shown in Figure 5.7.

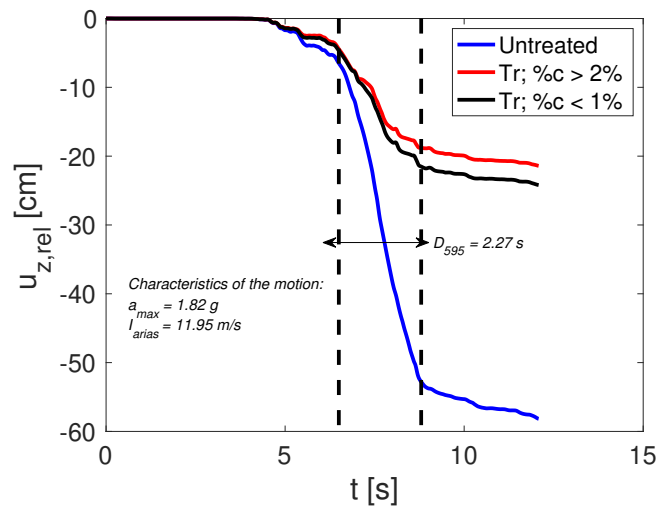


Figure 5.7: Comparison of the co-seismic relative crest settlement of the embankment as function of the injected material

As expected, and regardless of the material type, the relative crest settlement is reduced. The values using a small calcite percentage material are almost close to the ones found using a high calcite percentage. These results validate the ones found with O'Donnell (2016) that even a small calcite percentage can affect the amelioration of the soil.

### 5.6.3 Comparison based on the stress - strain evolution

In this paragraph, the mechanical behavior and the liquefaction potential of the soil will be examined. There are shown in terms of their logarithmic ratio  $\log\left(\frac{x_{tr}}{x_{untr}}\right) = \log(x_{tr}) - \log(x_{untr})$ , where  $\log(\cdot)$  is the natural logarithm of the observed variable for the treated and untreated

cases. For this purpose, a window in the foundation, under the left side of the embankment is considered. Concerning the mechanical state, Figure 5.8 shows the logarithmic ratio of the maximum shear stress  $\tau_{max}$  and strain  $\gamma_{max}$ . For the liquefaction potential, the logarithmic ratio of the excess pore water pressure  $\Delta p_w$  and the volumetric strain  $\varepsilon_v$  are shown in Figure 5.9. The location of the injections appears as dashed lines on each figure.

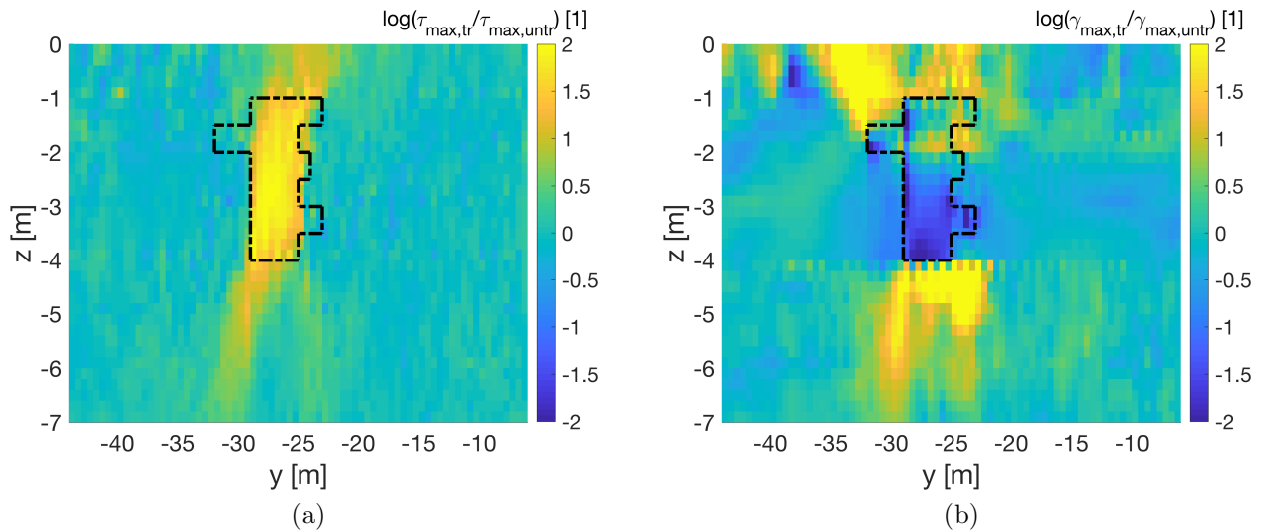


Figure 5.8: The ratio of the maximum shear a) stress and b) strain between the treated and untreated cases

From Figure 5.8a, it is clear that in the region of injection, the maximum shear stress  $\tau_{max}$  has increased from the treated phase to the untreated phase. All around the injection zone, the shear stress did not change between the two phases. As for the maximum shear strain  $\gamma_{max}$  (Figure 5.8b), it decreases from the untreated to the treated phase in the injection zone, on the opposite to what happened around. Based on these results, it can be seen that the used mitigation method decreases the deformation of the soil whereas it increases its shear loss. The localization of the shear losses is near the injection zones. Concerning the liquefaction analysis, the logarithmic ratio of the excess pore water pressure (Figure 5.9a) shows that there is partially no difference between the two phases. It looks like there exist regions where the excess pore water pressure change in the treated case is less than the untreated. In Figure 5.9b, it can be seen an uneven distribution of the volumetric strain in the analyzed zone. For example, for a depth between 2 and 4 meters, the treatment pushed the soil towards a more dilative behavior since the volume have expanded in the treated phase more than the untreated one. On the opposite, and due to the dry shallow soil,  $\varepsilon_v$  for the treated phase is higher than the untreated one between 1 and 2 meters depth.

Finally for this section, it can be partially concluded that first, the soil improvement is more efficient under the edges of the embankment (i.e. two injection zones), rather than with increasing zones (i.e. three injection zones). Second, a small percentage of calcite is able to reduce the liquefaction potential since the results of the relative crest settlement were close to

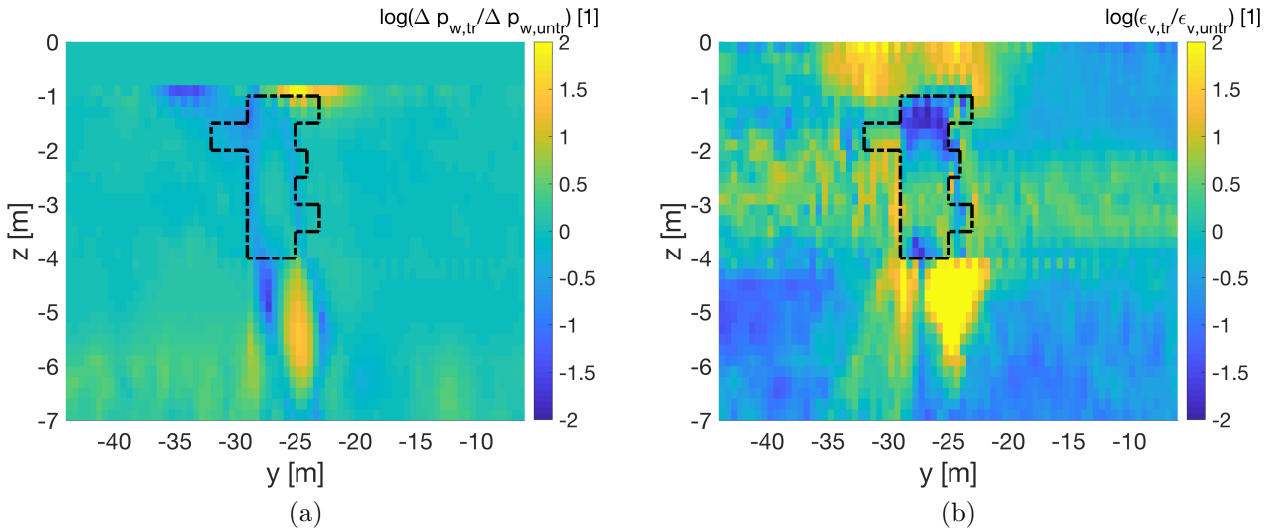


Figure 5.9: The ratio of the a) excess pore water pressure and b) the volumetric strain between the treated and untreated cases

the ones with higher calcite percentage. Third, the proposed mitigation method is efficient for decreasing the deformation, but it might affect the shear resistance of the soil. In addition, for the presented examples in this section, the proposed methodology tends to push the soil toward a dilative behavior. In order to understand the global behavior of the embankment, the focus of the coming section will be on the response of the embankment for all the tested ground motions. The material with the high calcite percentage will be analyzed in order to have a better idea on the amelioration ratio of the crest settlement.

## 5.7 Amelioration ratio of the crest settlement

In this section and following the PBEE methodology, the performance of the embankment is studied and the damage will be quantified with respect to an intensity measure. It was shown in Section 5.6 that the presented mitigation method decreases the deformation of the soil. Thus, in order to have a better estimation of the structural response, the injected material in this section will require the higher calcite percentage.

Previous works have shown that the crest settlement of the embankment is directly related to some input ground motion characteristics (i.e. the peak ground acceleration and magnitude) (Swaisgood, 2003; Lopez-Caballero and Khalil, 2018). In this work the obtained percentage crest settlement ( $\delta u_{z,rel}/H$ , where  $u_{z,rel}$  is the relative crest settlement,  $H$  is the height of the dam and the foundation which is 19 m) is compared to the peak ground acceleration at the outcropping bedrock ( $a_{max,out}$ ). The results are shown in Figure 5.10. The analysis was conducted essentially on the treated case with two injection zones comparing to the untreated case. But Figure 5.10b shows the three injection zones of selected ground motions in order to confirm the conclusion of Section 5.6. The damage levels of the percentage crest settlement

proposed by Swaisgood (2003) and modified to liquefaction occurrence by Lopez-Caballero and Khalil (2018) are also shown in this figure in the form of dashed lines; when  $\delta u_{z,rel}/H \leq 0.02\%$ , there is *No* damage, when  $0.02\% < \delta u_{z,rel}/H \leq 0.1\%$ , the damage is *Minor*, when  $0.1\% < \delta u_{z,rel}/H \leq 1\%$ , the damage is *Moderate* and when  $\delta u_{z,rel}/H > 1\%$  the damage is *Serious*. A study conducted by Lopez-Caballero and Khalil (2018) on the same numerical model with

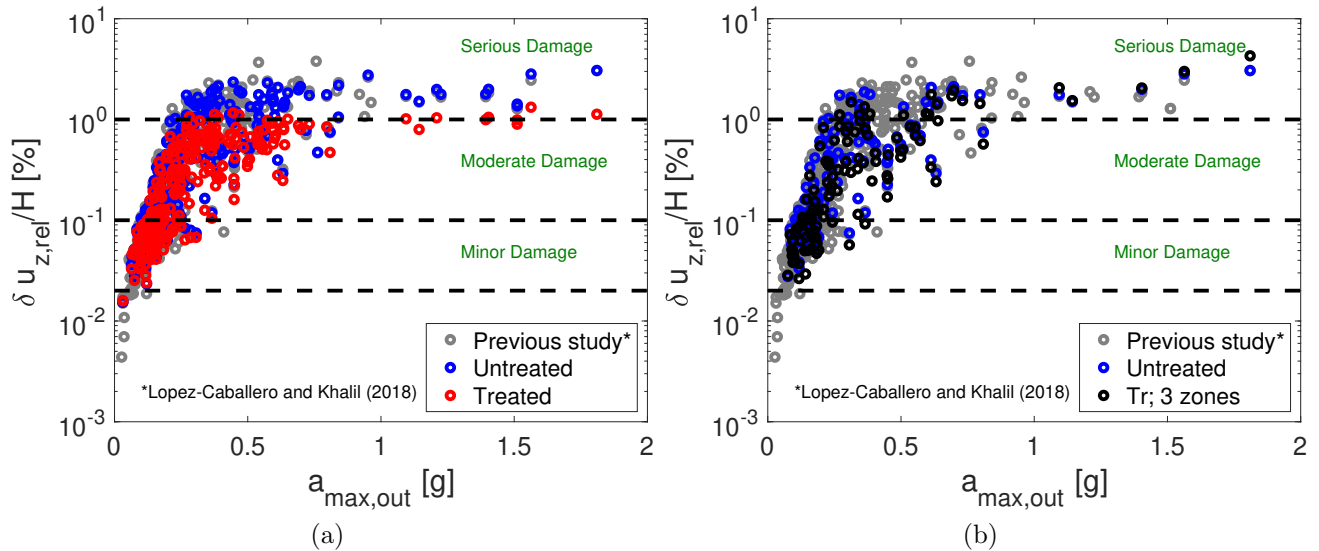


Figure 5.10: The crest settlement analysis with respect to the outcropping acceleration ( $a_{max,out}$ ) for each case study

larger element sizes (i.e.  $3.5\text{m} \times 1\text{m}$ ) is shown with grey dots in order to validate the response of this study. As expected, the results are consistent in terms of the increase of the relative crest settlement with the acceleration at the outcrop  $a_{max,out}$ . It is clear from Figure 5.10a that the percentage crest settlement is reduced comparing to the case when the soil was not treated. It is interesting to mention that in some cases, the crest settlement reduction transformed the damage from a *Serious* damage level to almost a *Moderate* damage level. However, for small values of  $a_{max,out}$ ,  $\delta u_{z,rel}/H$  is not very important since the reduction of the crest settlement is almost negligible.

Regarding the case of three injection zones (Figure 5.10b), the percentage relative crest settlement slightly decreases comparing to the untreated case. Clearly, more data are found in *Serious* damage level on the opposite to what was found for two injection zones (Figure 5.10a). Thus, the conclusion of Section 5.6 regarding the efficiency of three injection zones for the crest settlement reduction is confirmed. However, it is remarked that for some cases, specially for high values of  $a_{max,out}$ , the crest settlement at the end of the motion is equal or higher than an untreated case. This result is the consequence of the dilatant behavior of the injected material under the center of the embankment, that led to an increase in the vertical stress and a partial dissipation of the excess pore water pressure. Thus, three injection zones for the case of this study is again not a good choice. For the structural analysis of this chapter, two injection zones with a high calcite percentage material will be considered.

Furthermore, from Figure 5.10, it can be seen that for a given value of  $a_{max,out}$ , the soil presents different damage levels. It means that the response of the soil does not only depend on the outcrop acceleration but also on other ground motion characteristics. Hence, the amelioration ratio of the crest settlement (i.e.  $(\Delta u_{tr.} - \Delta u_{untr.})/\Delta u_{untr.}$ ) was found based on the variation of  $a_{max,out}$ , the equivalent predominant frequency  $1/T_{va}$  and the peak ground velocity  $PGV$ . The results are shown in Figure 5.11a. The dashed lines in this figure represent  $PGV$ . It can be seen that the amelioration of the crest settlement tends toward the upper left, in a way to be proportional with the increase in  $PGV$  (Montoya-Noguera and Lopez-Caballero, 2016). In addition, the amelioration ratio for this case is in majority greater than 40% (or 0.4 in the Figure 5.11b). The evolution of this ratio with only  $PGV$  is shown in Figure 5.11b. It is noted that the higher the  $PGV$ , the higher this ratio.

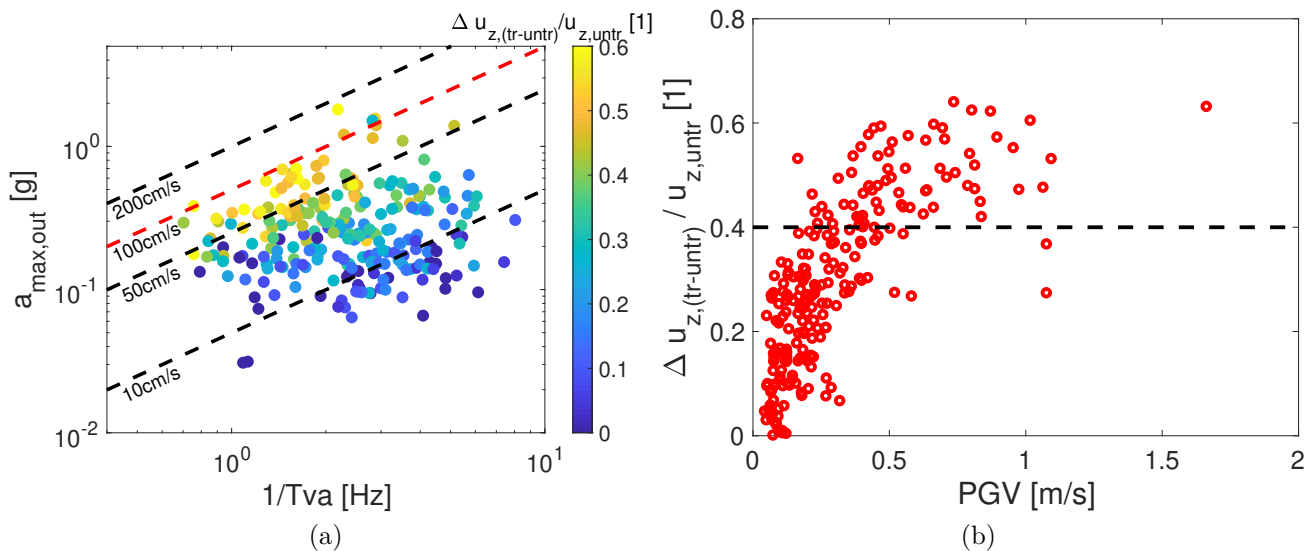


Figure 5.11: The reduction ratio of the relative crest settlement as function of a)  $a_{max,out}$  and  $1/T_{va}$  and b)  $PGV$

## 5.8 Fragility curves of the tested cases

Up to this stage of the study, it is well evident that the response of the soil depends on the characteristics of the input ground motion. More details regarding this concept will be discussed in the proceeding section. Since the performance of the embankment requires a structural and a damage analysis, the damage measures are determined from fragility curves. Fragility curves are functions that represent the probability of failure of structures given an Intensity Measure (IM) (usually the peak ground acceleration) (Shinozuka et al., 2000; Sáez et al., 2011; Zentner, 2017, among others). It is assumed that the curves can be expressed in the form of log-normal distribution functions, and the estimation of the two parameters (median  $\alpha$  and log-standard deviation  $\beta$ ) is performed by the maximum likelihood method (Shinozuka et al., 2000). In addition, Sáez et al. (2011) proposed a methodology based on the Fisher information

matrix to find the quality of fit and to estimate the confidence intervals for the two parameters controlling the fragility curves. The analytical fragility functions that represents the probability of exceeding a damage level  $D_0$  given an intensity measure  $a_k$  can be evaluated as such:

$$P(D > D_0 | a_k; \alpha, \beta) = \phi\left[\frac{1}{\beta} \ln\left(\frac{a_k}{\alpha \bar{a}}\right)\right] \quad , \quad (5.2)$$

where  $\phi[.]$  is the standardized normal distribution function and  $\bar{a}$  is the normalization of  $a_k$  to obtain a non-dimensional value of  $\alpha$ . In this work, the intensity measure is the outcrop acceleration  $a_{max,out}$ , and the damage levels are *Moderate* (i.e.  $0.1\% < \delta u_{z,rel}/H \leq 1\%$ ) and *Serious* (i.e.  $\delta u_{z,rel}/H > 1\%$ ). The fragility curves are drawn in Figure 5.12 for the untreated and all the treated cases developed in this study.

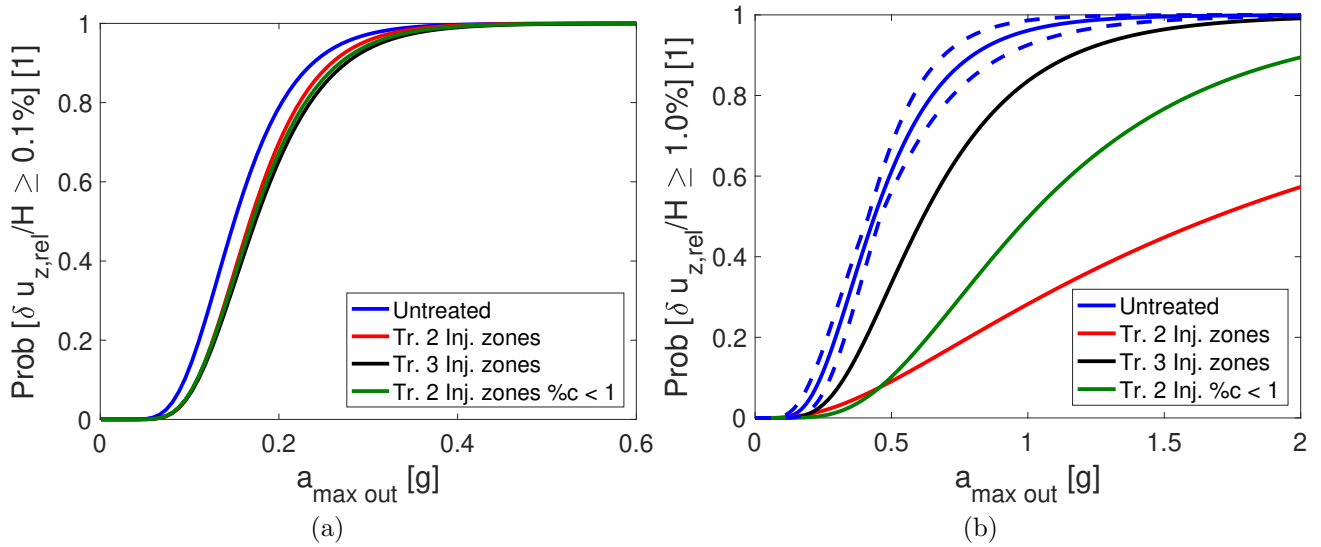


Figure 5.12: Fragility curves of two damage levels: a)  $\delta u_{z,rel}/H = 0.1$  and b)  $\delta u_{z,rel}/H = 1$

For *Moderate* damage, it is clear from Figure 5.12a that the soil improvement slightly decreases the chance of failure of the embankment. For the sake of clarity, the confidence limits of this damage level were omitted. For an acceleration of 0.2g as an example, the probability of exceeding the *Moderate* damage level is 80% (or 0.8) for an untreated case whereas it decreases to almost 70% (or 0.7) for the treated cases. Similar to what was found in previous sections, the adopted improvement methodology does not seem to be beneficial for small accelerations. As for the *Serious* damage level in Figure 5.12b, it should be remarked that the majority of the cases that have failed initially in this damage level did not do as such when the two injection zones (i.e. red curve) was applied. Thus, there was not enough data to be able to draw the confidence limits of this type of treatment. As for the three injections zones (i.e. black curve), and similar to what was analyzed in the previous section, such treatment did not decrease the soil response for high accelerations, however, not enough data were computed for this case. Nevertheless, the probability of exceeding the *Serious* damage level is less than the untreated case. As for the green curve that represents two injection zones for a less dilatant material, the

probability of exceeding this damage level decreases from 98% to 45%, which emphasizes the efficiency of the chosen improvement technique for high accelerations.

Finally, it was presented throughout this study the variation of the response with mainly the outcrop acceleration. But it was noticed that the response might be controlled with other input motion parameters. Thus, the next section will identify the ground motion parameters that best control the response of the embankment.

## 5.9 Sensitivity analysis of the crest settlement amelioration ratio

The goal of many statistical tools is to reduce high dimensional multivariate variables to a smaller number of dimensions so that the relationship between the variables will be more understood (Friendly, 2002). From previous results in this chapter, it was shown that there exists an uncertainty between the parameter of the input motions and the response of the soil. Also, in literature, it was shown that the Arias intensity at outcropping has the best influence on the liquefaction triggering (Lopez-Caballero and Modaresi-Farahmand-Razavi, 2010). In this section, the reason behind this uncertainty will be developed via a sensitivity analysis in order to identify the parameter of the input motion that best controls the amelioration ratio of the crest settlement of the embankment. The ground motion parameters are the outcrop acceleration  $a_{max,out}$ , the effective duration  $D_{595}$ , the peak ground velocity  $PGV$ , the equivalent predominant frequency  $1/Tv, a$ , the Arias intensity  $I_{a,out}$ , the cumulative absolute velocity  $CAV_5$  and the number of cycles  $N_{cyc}$ . The results are represented in the form of a correlation matrix shown in Figure 5.13. The chosen input motion parameters are indicated in the diagonal with their distribution. Each parameter occupies the corresponding row and column. The box to the right of the figure develops the chosen abbreviations. The last term of the diagonal, in the lower right (i.e. `duz_inj1`), shows the amelioration ratio of the crest settlement, which is the output analysis. The results then, are going to be analyzed based on this output. To the lower side of the diagonal are shown the scatter plots of every two parameters. For example, the graph in the position (5x3) shows the correlation between the  $PGV$  and  $I_{a,out}$ . Whereas the upper side of the diagonal shows the significance level or the correlation coefficient of each two parameters correlation. For this same example, the significance level is 0.88, located in position (3x5). Concerning the input parameter that best affects the crest settlement reduction, and from the significance levels in the 8th column, it can be seen that  $PGV$  has the higher correlation value (0.58, even if it is considered not significant). Arias intensity  $I_{a,out}$  has also a good importance and then comes  $CAV_5$  and  $a_{max,out}$  with the same influence level. It should be noted that for the case of this study, regarding the crest settlement reduction, the number of cycles of the input motion as well as the equivalent predominant frequency, did not highly affect the result. Hence, the peak ground velocity  $PGV$  is the input motion parameter that best affects the reduction

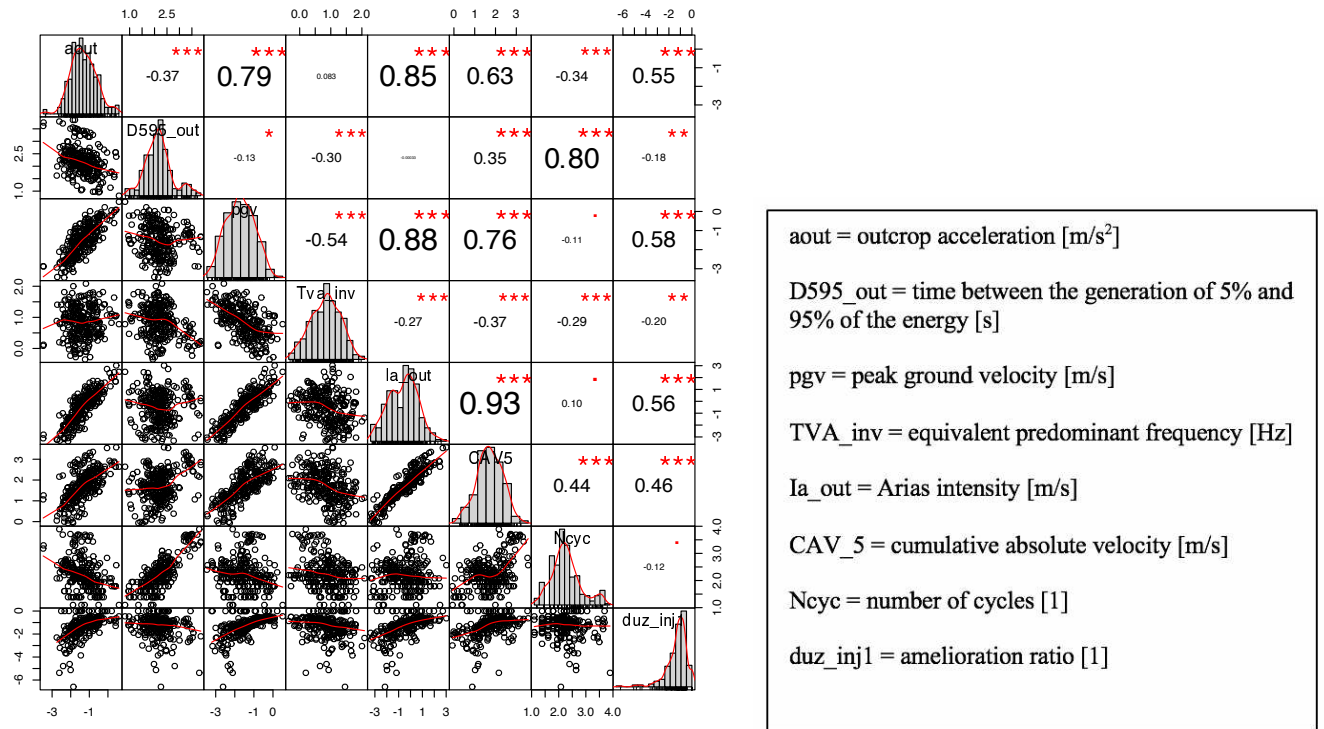


Figure 5.13: The correlation between a) the chosen input ground motion parameters and b) with respect to the reduction of the crest settlement

of the crest settlement which was previously seen in this study (i.e. Figures 5.11a and 5.11b).

## 5.10 Concluding remarks

This chapter assesses numerically the application of a mitigation method inspired from the Bio-mediated solutions for soil improvements. These methods are managed and controlled through biological activities together with chemical reactions. The adopted methodology in this work requires the injection of a new material that has similar properties to a treated material with MICP. Following the performance-based earthquake engineering methodology, this study analyses the liquefaction triggering from a hazard analysis to a damage analysis. An elastoplastic multi-mechanism soil behavior model was used with the help of a 2D finite element code (GEFDyn). The damage is quantified by the percentage relative crest settlement. A sensitivity analysis was also conducted in order to identify the input ground motion parameter that has the higher influence on the crest settlement reduction. The conclusions that this chapter have reached are the following:

- The adopted injection technique is efficient in decreasing the liquefaction potential by the decrease of the relative crest settlement.
- This methodology showed satisfying results when the acceleration of the input ground motion is very high. Whereas when the acceleration is small, the amelioration of the soil is not very essential following this methodology.
- The amelioration of the crest settlement is important when the injection zones are under the edge of the embankment, in the depth of the liquefiable foundation layer. Additional injection zones are not important for the global response.
- Even a small percentage of calcite is able to improve the soil and the crest settlement is reduced closer to the material with high calcite percentage.
- The proposed application is efficient for decreasing the soil deformation, but it might affect its shear resistance.
- Fragility curves confirmed the second conclusion. They show that the chance of failure of the embankment will decrease with this improvement technique, specially for ground motions of high accelerations.
- Based on the conducted sensitivity analysis, the peak ground velocity (PGV) is the input motion parameter that best controls the amelioration ratio of the crest settlement. Then it comes the Arias intensity and the outcrop acceleration.

# Conclusions and further research

In the context of this work, the seismic analysis of a liquefiable soil foundation-embankment system was conducted, starting from a soil sampling interpretation to a life cycle performance. An application (sometimes an adaptation) of the PBEE methodology is also assessed in this work. For this purpose, an embankment model is used, and the soil behavior is represented by an elasto-plastic multi-mechanism model. The finite element method in time domain is used as numerical tool.

Even if partial conclusions were already given through the dissertation, the main obtained results are highlighted herein and discussed in the light of their contribution to the significant questions presented in the general introduction of this document.

- 1) In this work, *virtual* laboratory tests were used in order to characterize the soil and identify its *in-situ* response. For this purpose, two sand samples (*Mat.1* and *Mat.2*) were tested. Regular and irregular loads were applied as to be consistent with the conditions of the laboratory tests and the realistic scenarios. The results have shown that *Mat.1* is a “loose” sand and has an ability to liquefy rapidly on the contrary to the second sample who was “dense” sand and had a higher resistance to liquefaction. From the simulated laboratory test, a boundary was identified as it identifies the liquefaction triggering. Based on that, and after the application of irregular loads on the soil samples, it was seen that this boundary can sometimes underestimate the resistance of the soil sample. Concerning the *in-situ* response, the results of the soil resistance show that below a field corrected boundary, the soil may liquefy whereas above it, the response will also depend on the severity of the earthquake.
- 2) Given a soil sampling characterization and a predefined seismic hazard, the co-seismic response of the embankment was calculated from a large number of real and synthetic ground motions. It was presented in this work a model parameter noted  $r_{apt}$  that indicates the local damage of a domain of interest. This parameter can be used as a criterion for estimating the local damage measure. Moreover, the failure density concept represented by the probability of exceeding  $r_{apt} \geq 0.75$ , noted as  $\rho_{r_{apt} \geq 0.75}$ , shows that it can be considered as a global damage index. The link between this latter parameter with the relative crest settlement  $\delta u_{z,rel}/H$  was shown in this study since  $\rho_{r_{apt} \geq 0.75}$  is difficult to compute without powerful numerical models and is not measured in field. Moreover, in

order to be compatible with the PBEE methodology, the link between the chosen EDP ( $\delta u_{z,rel}/H$ ) and IM ( $a_{max,out}$ ) was presented for this case study. It was shown that the global response for real and synthetic ground motions is slightly close. Concerning the fragility exposure of this case, the synthetic and real ground motions closely estimates the level of performance.

- 3) After the co-seismic analysis, the lifetime performance of the embankment was assessed through a survival analysis. For this purpose, sequential mainshocks were created from two stochastic ground motion models, and the damage was calculated after each sequence. The cumulative damage in this study showed two responses for the embankment: i) a progressive deterioration that did not necessarily lead to drastic damages or ii) a sudden deterioration after few years. From the survival function, it was shown that after 25 years (MTTF = 25 years), the embankment has 50% chance to present *Moderate* damage. Whereas it will not show *Serious* damage during its lifetime. The distribution of the survival function for the *Moderate* damage level, follows a Weibull distribution whereas that of the *Serious* damage level is more likely to be represented by an exponential distribution. It was also emphasized in this work the importance of the history of loading and the recovery time of the geo-structure since it affects its lifetime performance.
- 4) As for the aftershock occurrence, during sequential earthquakes, it was shown that the damage is higher for sequences with aftershocks (i.e. MS-AFS) than the ones without the aftershocks occurrence (i.e. MS). The survival functions with their MTTFs values, showed that the consideration of the aftershocks events is important for moderate levels of damage. However, the embankment survived high damage levels for a working life of 100 years. It was also emphasized in this work that the evolution in time of the fragility exposure is affected by the history of loading and the initial state of the embankment.
- 5) Given an unacceptable risk, it is presented in this work a mitigation application inspired from the Bio-mediated solutions for soil improvements. The adopted methodology in this paper requires the injection of a new material that has similar properties to a treated material with MICP. It was shown that the relative crest settlement decreases as the mitigation is applied, however, the soil shear resistance might be affected. It should be mentioned that the soil amelioration methodology showed satisfying results in terms of damage reduction and fragility exposure, when the acceleration of the input ground motion is very high. In addition, the amelioration of the crest settlement is important when the injection zones are under the edge of the embankment, in the depth of the liquefiable foundation layer. It was also conducted in this work a sensitivity analysis as to identify the ground motion parameter that best controls the amelioration ratio of the crest settlement. It was shown that the peak ground velocity *PGV*, then the Arias intensity and the outcrop acceleration are the main parameters.

Further research aspects can be established from this work and some of them are proposed in the following:

- The used PSHA was extracted from a previous study applied on the same site of concern. In addition, the aftershock model was adapted accordingly. A conducted PSHA from scratch on a different site can be interesting in order to validate the efficiency of the proposed methodology.
- The lifetime performance of the embankment was assessed on an intact embankment from an initial state. It is interesting to validate the performance on an actual damaged state in order to estimate its probability of survival.
- It was assumed in this study that the embankment is not ameliorated during its lifetime. It is interesting to check if the survival function can be affected if an amelioration procedure is conducted during the life cycle of the embankment.



# Appendices



# Appendix A

## ECP multimechanism model

A constitutive model for soils should be able to well represent the volume change in case of drained conditions or the distribution of the excess pore water pressure in case of undrained conditions (Aubry et al., 1982). The use of numerical modeling best describes the non-linear soil behavior under cyclic loading. A good modeling takes into consideration essential properties: necessary data, an appropriate constitutive model and adequate parameters, in addition to the method that solves boundary value problems. The ECP elastoplastic multi-mechanism model (also known as *Hujeux* model) is used to simulate the soil behavior in this work. The model is written in terms of effective stresses because when water is present, the soil mechanical behavior is determined by the contact forces between grains which depend on the total stresses but also on the pore-water pressure. One important remark of this approach is that *the true cohesion* will not be used. The ECP model can take into account a large range of deformations. A brief description will be given in the following, however, for more details, it is recommended to refer to Aubry et al. (1982), Hujeux (1985) and Lopez-Caballero and Modaressi-Farahmand-Razavi (2010), among others.

The non-linearity of this model is represented by four coupled elementary plastic mechanism: three plane-strain deviatoric plastic strain mechanism in three orthogonal planes ( $k$  - planes) and an isotropic plane. The projection of any tensor ( $\underline{t}$ ) on the  $k$  - plane including  $\underline{e}_i$  and  $\underline{e}_j$  concerns only the components  $ii$ ,  $jj$  and  $ij$ . So the mean and deviatoric stress and strains tensors are written as follows:

$$p_k = \frac{\sigma'_{ii} + \sigma'_{jj}}{2} \quad (\text{A.1})$$

$$q_k = \left[ \left( \frac{\sigma'_{ii} - \sigma'_{jj}}{2} \right) + \sigma'^2_{ij} \right]^{\frac{1}{2}} \quad (\text{A.2})$$

$$\varepsilon_{vk} = \varepsilon_{ii} + \varepsilon_{jj} \quad (\text{A.3})$$

$$\varepsilon_k = \left[ \left( \frac{\varepsilon_{ii} - \varepsilon_{jj}}{2} \right) + \varepsilon^2_{ij} \right]^{\frac{1}{2}} \quad (\text{A.4})$$

The model follows a Coulomb type failure criterion, contemplates the existence of dilatancy/contractancy phenomena, and uses the critical state concept. The cyclic behavior is

taken into account by a kinematical hardening that is based on the state variables at the last load reversal. The model is written in the concept of the incremental plasticity which divides the total strain into an elastic and a plastic part. The elastic part confirms a non-linear elasticity behavior in which the bulk  $K$  and the shear modulus  $G$  are function of the mean effective stress  $p'$ :

$$K = K_{ref} \left( \frac{p'}{p_{ref}} \right)^{n_e} \quad \text{and} \quad G = G_{ref} \left( \frac{p'}{p_{ref}} \right)^{n_e} \quad (\text{A.5})$$

where  $K_{ref}$  and  $G_{ref}$  are the bulk and shear moduli measured at the mean reference pressure ( $p_{ref}$ ) and  $n_e$  is the degree of non-linearity.

Considering the well-known sign convention of the soil mechanics which sets the positive sign to the compression forces, the yield surface of this numerical model is written in the  $k$  plane as follows:

$$f_k(\sigma, \varepsilon_v^p, r_k) = q_k - \sin \phi'_{pp} \cdot p'_k \cdot F_k \cdot r_k \quad (\text{A.6})$$

with  $\phi'_{pp}$  is the friction angle at the critical state and  $F_k$  depends on  $\varepsilon_v^p$  such that

$$F_k = 1 - b \ln \left( \frac{p'_k}{p_c} \right) \quad (\text{A.7})$$

$$p_c = p_{c0} \exp(\beta \varepsilon_v^p) \quad (\text{A.8})$$

with  $\beta$  is the plasticity compression modulus and  $p_{c0}$  is the critical stress that corresponds to the initial void ratio. The parameter  $b$  shapes the form of the yield surface in  $p' - q$  plane and varies between  $b = 0$  where it verifies the Mohr-Coulomb criterion and  $b = 1$  which will be the Cam-Clay criterion. The third variable of the yield surface which is the degree of mobilized friction angle  $r_k$  is linked to the plastic deviatoric strain  $\dot{\varepsilon}^p$ . It shows the effect of the shear hardening and decomposes its behavior into pseudo-elastic, hysteretic and mobilized domains. It is given by:

$$\dot{r}_k = \dot{\lambda}_k^p \frac{(1 - r_k)^2}{a} \quad (\text{A.9})$$

where  $\dot{\lambda}_k^p$  is the plastic multiplier of  $k$  mechanism and

$$a = a_1 + (a_2 - a_1) \alpha_k(r_k) \quad (\text{A.10})$$

with,

$$\begin{aligned} \alpha_k &= 0 & \text{if } r_k^{elas} < r_k < r_k^{hys} \\ \alpha_k &= \left( \frac{r_k - r_k^{hys}}{r_k^{mob} - r_k^{hys}} \right)^m & \text{if } r_k^{hys} < r_k < r_k^{mob} \\ \alpha_k &= 1 & \text{if } r_k^{mob} < r_k < 1 \end{aligned} \quad (\text{A.11})$$

Notice that  $a_1$ ,  $a_2$  and  $m$  are model parameters and  $r_k^{hys}$  and  $r_k^{mob}$  designates when the domain

shows hysteresis degradation. The isotropic yield surface is assumed to be :

$$f_{iso} = |p'| - d p_c r_{iso} \quad (\text{A.12})$$

with :

$$\dot{r}_{iso} = \dot{\epsilon}_{v_{iso}}^p \frac{(1 - r_{iso})^2}{c_{mon} \frac{p_c}{p_{ref}}} \quad (\text{A.13})$$

where  $d$  is a model parameter representing the distance between the isotropic consolidation line and the critical state line in the  $(e - \ln p')$  plane and  $c_{mon}$  controls the volumetric hardening. In the model, an associated flow rule in the deviatoric  $k$  plane is assumed and the Roscoe's dilatancy law is used to obtain the increment of the volumetric plastic strain in terms of the characteristic angle  $\psi$  and a constant parameter  $\alpha_\psi$  such that:

$$\dot{\epsilon}_{vk}^p = \dot{\lambda}_k^p \cdot \alpha_\psi \cdot \alpha_k(r_k) \left( \sin \psi - \frac{q_k}{p'_k} \right) \quad (\text{A.14})$$

$\psi$  is the characteristic angle and  $\alpha_\psi$  a constant parameter.



# Appendix B

## Soil parameters for the ECP model

The following appendix will present the ECP model parameters of all the soil types used in this thesis work. Table [B.1](#) presents the parameters for the soil foundation-embankment model in which *Mat.1* or *LM Sand* is also the soil sample used in the *virtual* laboratory tests of Chapter [1](#). In addition, Table [B.2](#) presents the hydraulic parameters of the soil foundation. Moreover, Table [B.3](#) presents the soil parameters used for the mitigation method in Chapter [5](#) in which the soil sample *Mat.2* of Chapter [1](#) is also presented. And finally, Table [B.4](#) shows the hydraulic parameters of the soil types used for the mitigation technique.

Parameter	<i>Mat.1</i> LM Sand	Dense Sand foundation	Dense Sand embankment
$\rho[kg/m^3]$ : Solid density	2700	2700	1755
<b><i>Elasticity</i></b>			
$G_i$ [MPa]: Shear modulus	290	1440.0	583
$K_i$ [MPa]: Bulk modulus	628	719.5	972
$n_e$ [1]: Nonlinear degree	0.5	0.47	0.6
$p'_{ref}$ [MPa]: Reference mean stress	1	1	1
<b><i>Critical State and Plasticity</i></b>			
$\beta$ [1]: Plastic compressible modulus	33	44	43
$b$ [1]: Yield surface shape	0.12	0.8	0.23
$d$ [1]: Isotropic consolidation distance	2	5	10
$\phi'_{pp}$ [°]: Friction angle	30	37	36
$p_{c,0}$ [kPa]: Initial critical stress	40	400	1200
<b><i>Flow rule and hardening</i></b>			
$a_1$ [1]: Primary plastic stiffness	0.0001	0.0002	0.0001
$a_2$ [1]: Secondary plastic stiffness	0.005	0.0004	0.01
$c^m$ [1]: Monotonic isotropic hardening	0.004	0.010	0.2
$c^c$ [1]: Cyclic isotropic hardening	0.002	0.005	0.1
$\psi$ [°]: Characteristic angle	30	37	36
$\alpha_\psi$ [1]: Volumetric parameter	1	1	1
$m$ [1]: Cyclic loading exponential	1.5	1.0	1.0
<b><i>Threshold domain</i></b>			
$r_{ela}$ [1]: Deviatoric elastic	0.03	0.005	0.001
$r_{iso}^{ela}$ [1]: Isotropic elastic	0.02	0.0001	0.0001
$r^{hys}$ [1]: Hysteretic	0.04	0.150	0.01
$r^{mob}$ [1]: Mobilized	0.8	0.90	0.9

Table B.1: Parameters for the soil foundation-embankment system

Parameter	Foundation Loose	Foundation Dense
$\rho_w[kg/m^3]$ : Fluid density	1000	1000
$n$ [1]: Porosity	0.35	0.35
$k_h$ [m/s]: Horizontal Permeability	$10^{-4}$	$10^{-5}$
$k_v$ [m/s]: Vertical Permeability	$10^{-4}$	$10^{-5}$
$H_w [Pa^{-1}]$ : Fluid Compressibility	$9.35 \cdot 10^{-8}$	$9.35 \cdot 10^{-8}$

Table B.2: Hydraulic parameters for the soil foundation

Parameter	<i>Mat.2</i>	
	%c > 2 %	%c < 1 %
$\rho[kg/m^3]$ : Solid density	2700	2700
<b><i>Elasticity</i></b>		
$G_i$ [kPa]: Shear modulus	474.0	318
$K_i$ [kPa]: Bulk modulus	546.0	462
$n_e$ [1]: Nonlinear degree	0.5	0.5
$p'_{ref}$ [kPa]: Reference mean stress	1000	1000
<b><i>Critical State and Plasticity</i></b>		
$\beta$ [1]: Plastic compressible modulus	200	28
$b$ [1]: Yield surface shape	1	0.22
$d$ [1]: Isotropic consolidation distance	2.5	5
$\phi'_{pp}$ [°]: Friction angle	39	35
$p_{c,0}$ [kPa]: Initial critical stress	1500	600
<b><i>Flow rule and hardening</i></b>		
$a_1$ [1]: Primary plastic stiffness	0.0015	0.0001
$a_2$ [1]: Secondary plastic stiffness	0.008	0.005
$c^m$ [1]: Monotonic isotropic hardening	0.03	0.004
$c^c$ [1]: Cyclic isotropic hardening	0.03	0.002
$\psi$ [°]: Characteristic angle	33	32
$\alpha_\psi$ [1]: Volumetric parameter	1	1
$m$ [1]: Cyclic loading exponential	2.6	0.9
<b><i>Threshold domain</i></b>		
$r_{ela}$ [1]: Deviatoric elastic	0.001	0.01
$r_{iso}^{ela}$ [1]: Isotropic elastic	0.0001	0.0001
$r^{hys}$ [1]: Hysteretic	0.004	0.050
$r^{mob}$ [1]: Mobilized	0.8	0.9

Table B.3: Parameters for the two injection materials

Parameter	%c > 2 %	%c < 1 %
$\rho_w[kg/m^3]$ : Fluid density	1000	1000
$n$ [1]: Porosity	0.35	0.35
$k_h$ [m/s]: Horizontal Permeability	$10^{-5}$	$10^{-5}$
$k_v$ [m/s]: Vertical Permeability	$10^{-5}$	$10^{-5}$
$H_w$ [Pa <sup>-1</sup> ]: Fluid Compressibility	$9.35 \cdot 10^{-8}$	$9.35 \cdot 10^{-8}$

Table B.4: Hydraulic parameters for the soil used for the mitigation technique



# Appendix C

## Concept of confusion matrices

In the statistics community or recently in the machine learning, it is important that the metrics represent meaningful data for predictions. The analysis of data in a confusion matrix is a measurement of the performance of a classification model. It reports how the model classifies and compares the different fault categories with respect to their actual classifications. The actual (or observed) class under test is represented by the matrix row and the classification (or prediction) of that particular class is represented under the matrix column.  $M[i][j]$  gives the number of times that an observation of class  $i$  was assigned to the prediction  $j$ . The diagonal represents the correct classifications. Three metrics are usually used to evaluate or compare predictions from a confusion matrix: the *Accuracy*, *Precision* and *Recall*. The following development will take into consideration a confusion matrix of a 2-class classification problem Figure C.1.

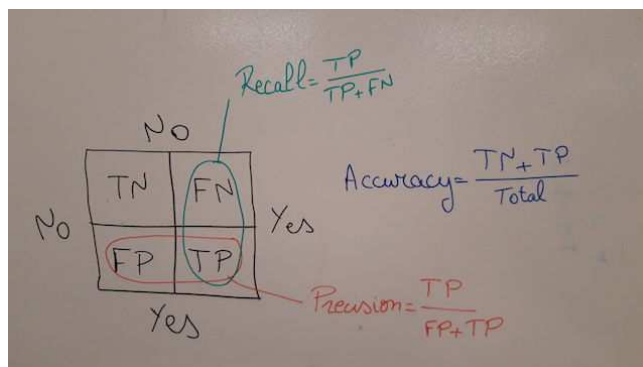


Figure C.1: Summary of the confusion matrix and its classification

Depending on each study for the meaning of the terms “positive” and “negative”, in the following study, the term “positive” means the liquefaction did not occur whereas “negative” designates the opposite. Hence, four pieces of data can be presented:

- True Negative (TN): A sample is negative and was predicted as negative.
- False Negative (FN): A sample is actually positive but was predicted as negative. FN are sometimes known as *Type I Error*.

- False Positive (FP): A sample is actually negative but was predicted as positive. FP are also known as *Type II Error*.
- True Positive (TP): A sample is actually positive and was predicted as positive.

The first metrics obtained from the above pieces of data is the *Accuracy*. It indicates how close to reality the predictions were. It is calculated as:

$$Accuracy = \frac{TN + TP}{TN + FN + FP + TP} \quad . \quad (C.1)$$

The *Recall* focuses on the data that were correctly identified (i.e. how much the prediction was correct). It should be close to 1 (or 100%) in the ideal case.

$$Recall = \frac{TP}{FN + TP} \quad . \quad (C.2)$$

The *Precision* focuses on the data are positives. It indicates from all the positive classes, how many are actually positive.

$$Precision = \frac{TP}{FP + TP} \quad . \quad (C.3)$$

Therefore, a successful predictions means high Accuracy and Recall, whereas a high Precision is not always critical.

# Appendix D

## The distribution of the ground motions used in Chapter 2

The effect of recorded and synthetic earthquakes on the response of the embankment was one of the main objectives of Chapter 2. For this purpose, the synthetic motions were compared to the real ones in terms of their ground motion parameters. Based on the density distribution of the peak ground acceleration  $PGA$ , the tested motions were divided into two groups. In Section 2.4, the distribution of some ground motion parameters ( $PGA$ ,  $PGV$ ,  $I_a$  and  $1/T_{va}$ ) was represented for the two types of motions as well as the two groups.

In this appendix, the distribution of other ground motion parameters will be presented. The ones added to the  $PGA$  are the effective duration  $D_{595}$  and the cumulative absolute velocity  $CAV$ . The results are shown in a matrix form in Figures D.1 and D.2. The comparison is conducted in terms of the density functions located in the diagonal of the matrix, the scatterplots and the histograms that are both located to the bottom left of the diagonal and finally, the boxplots that are located to the right.

For the comparison of the two types of motions (Figure D.1), it is clear that the effective duration of the synthetic motions is higher than that of the real motions. As for the cumulative absolute velocity, there is a slight difference between the two types.

Concerning the comparison of the ground motion parameters as function of the two classified groups from Chapter 2, it is seen in Figures D.2a and D.2b that each group overlaps similar data intervals. It should be recalled that with larger synthetic data, the results of this study would be more interesting. As for the second group that has same number of data (Figure D.2c), it is clear that the distribution of their parameters are somehow close.

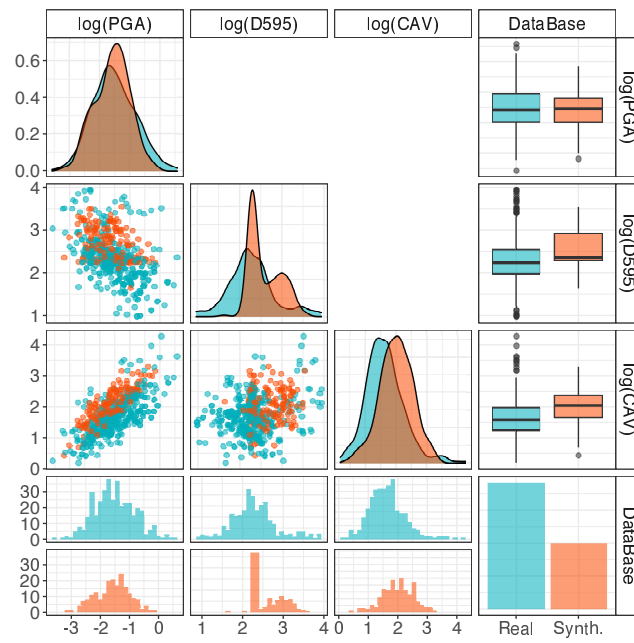


Figure D.1: The logarithmic distribution of some ground motion parameter ( $PGA$ ,  $D_{595}$  and  $CAV$ ) of the real and synthetic ground motions

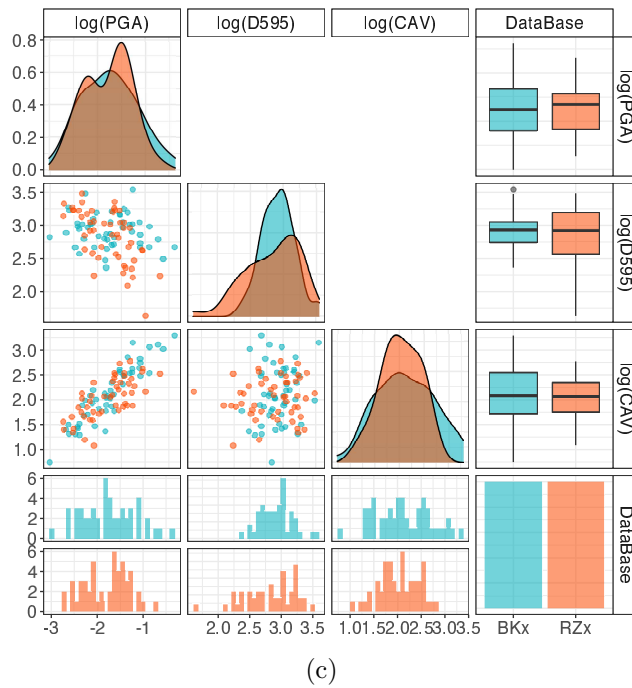
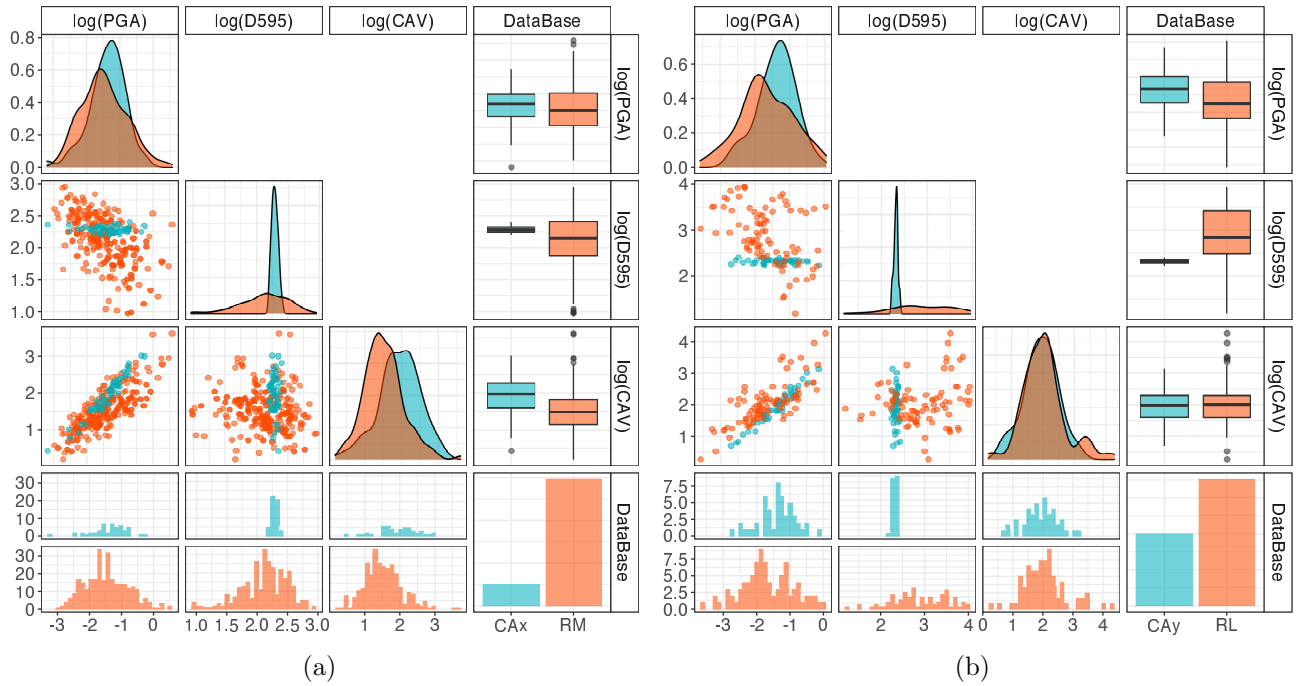


Figure D.2: The logarithmic distribution of some ground motion parameter ( $PGA$ ,  $D_{595}$  and  $CAV$ ) for the group of a) & b)  $CAx$ ,  $CAy$ ,  $RM$  and  $RL$  and c)  $RZx$ ,  $BKx$



# Appendix E

## Analytical fragility curves

The development of seismic vulnerability in the form of fragility curves is a useful approach when the information accounts for many uncertainty sources (Shinozuka et al., 2000). Fragility curves are functions that represent the probability of failure of structures given an Intensity Measure (IM) (Shinozuka et al., 2000; Porter et al., 2007; Sáez et al., 2011; Zentner, 2017, among others). It is assumed that the curves can be expressed in the form of log-normal distribution functions, and the estimation of the two parameters (median  $\alpha$  and log-standard deviation  $\beta$ ) is performed by the maximum likelihood method (Shinozuka et al., 2000). This appendix will develop the used methodology to calculate the fragility curves of this work. The procedure presented follows the one adopted by Shinozuka et al. (2000) or Sáez et al. (2011). It is recommended to be familiar with some statistical concepts such as the nature of statistical models, probability mass functions, and statistical independence.

The fundamental interpretation of a fragility curve suggests that the structure will sustain a precised damage state with a probability  $F(\underline{\theta})$  and will not sustain this designated damage state with a probability of  $1 - F(\underline{\theta})$ .  $\theta$  is the parameters that describes  $F(\underline{\theta})$ . Thus, this probabilistic phenomena can be described as a Bernoulli experiment which is an action that has only two possible outcomes: failure or success (i.e. sustain or collapse). As it is commonly used, in what follows, the random variables will be denoted by capital letters and their realization with small letters. Thus,  $Y$  is denoted as the random variable that follows the Bernoulli distribution and  $y$  is its realization which is equal to 1 for a success and 0 for a failure. The discrete density function (in other terms the probability mass function) representing the fragility curves  $F(\cdot)$  is the following:

$$f(y, \underline{\theta}) = [F(\underline{\theta})]^y [1 - F(\underline{\theta})]^{1-y} \quad . \quad (\text{E.1})$$

A sequence of Bernoulli trials occurs when a Bernoulli experiments is performed several independent times and that the probability of success remains the same from a trial to another.

Thus, the likelihood function for the present purpose is expressed as follows:

$$L = \prod_{k=1}^N [F(\underline{\theta})]^{y_k} [1 - F(\underline{\theta})]^{1-y_k} \quad . \quad (\text{E.2})$$

The fragility curves being the probability of exceeding a damage state  $d$  for a given IM (usually PGA, denoted here as  $a_k$ ), the analytic form of the fragility curve, under a log-normal assumption, will be:

$$F(d|a_i; \alpha, \beta) = \phi\left[\frac{1}{\beta} \ln\left(\frac{a_i}{\alpha \bar{a}}\right)\right] \quad , \quad (\text{E.3})$$

where  $\phi[\cdot]$  is the standardized normal distribution function and  $\bar{a}$  is the normalization of  $a_i$  for the purpose to obtain a non dimensional value of  $\alpha$ .

Maximizing the likelihood  $L$  will lead to the estimation of the parameters  $\alpha$  and  $\beta$ . To facilitate the maximization, equation E.2 can be transformed into:

$$\ln L = \sum_{k=1}^n [y_k \ln F(a_k) + (1 - y_k) \ln(1 - F(a_k))] \quad . \quad (\text{E.4})$$

Hence, maximizing the above equation and assuming the concave form of the curve, means to set:

$$\frac{\partial \ln L}{\partial \alpha} = \frac{\partial \ln L}{\partial \beta} = 0 \quad . \quad (\text{E.5})$$

And finally to find:

$$\sum_{k=1}^n I_{\alpha}(y_k) = 0 \quad , \quad (\text{E.6})$$

$$\sum_{k=1}^n I_{\beta}(y_k) = 0 \quad , \quad (\text{E.7})$$

where

$$I_{\alpha}(y_k) = \frac{\phi'(a_k)}{\alpha \beta} \left[ -\frac{y_k}{F(a_k)} + \frac{1 - y_k}{1 - F(a_k)} \right] \quad , \quad (\text{E.8})$$

$$I_{\beta}(y_k) = \frac{\phi'(a_k)}{\beta^2} \ln\left(\frac{a_k}{\alpha \bar{a}}\right) \left[ -\frac{y_k}{F(a_k)} + \frac{1 - y_k}{1 - F(a_k)} \right] \quad . \quad (\text{E.9})$$

The aforementioned system of equations can be solved using standard optimization algorithms. The solution will lead to find the estimated parameters, denoted as  $\hat{\alpha}$  and  $\hat{\beta}$ .

## Sampling evaluation

It should be recalled that the purpose behind the use of fragility functions is to find the probability of exceeding a damage state given a large number of a specific IM. In order to verify if the amount of information used is enough to reach the exact solution (i.e. if the n-sampling was enough in number and quality to let  $\hat{\alpha}$  and  $\hat{\beta}$  be close to the exact values), Fisher information matrix will be used (Fisher et al., 1920). The Fisher information matrix controls the amount of information provided by the selection of ground motions. It is a way of measuring the amount of information  $I_{i,j}(\theta)$  that an observable random variable  $Y$  carries about an unknown parameter of a distribution that models  $Y$ . Formally, it is the variance of the score, or the expected value of the observed information. Hence, it can be written as:

$$I_{i,j}(\theta) = Cov\left[\frac{\partial \ln L}{\partial \theta_i}, \frac{\partial \ln L}{\partial \theta_j}\right] \quad (\text{E.10})$$

$$= E\left[\frac{\partial \ln L}{\partial \theta_i} \cdot \frac{\partial \ln L}{\partial \theta_j}\right] - E\left[\frac{\partial \ln L}{\partial \theta_i}\right] E\left[\frac{\partial \ln L}{\partial \theta_j}\right] \quad , \quad (\text{E.11})$$

where  $Cov[\cdot]$  denotes the covariance and  $E[\cdot]$  the expected value. Developing Equation E.10 to find the expected value with respect to  $\alpha$  will lead to:

$$E\left[\frac{\partial \ln L}{\partial \alpha}\right] = E\left[\sum_{i=1}^n I_{\alpha}(Y_i)\right] = nE[I_{\alpha}(Y)] \quad . \quad (\text{E.12})$$

Recalling the properties of the discrete density function, the expected value can be approximated by the mean as:

$$E[I_{\alpha}(Y)] \approx \frac{1}{n} \sum_{i=1}^n I_{\alpha}(y_i; \alpha, \beta) \quad . \quad (\text{E.13})$$

If in Equation E.12 the estimators  $\hat{\alpha}$  and  $\hat{\beta}$  were used, the expected value with respect to  $\alpha$  will be zero (findings of Equation E.6). Similar analysis can be done to the expected value with respect to  $\beta$ , this will reform the Fischer matrix information into one term:

$$\hat{I}_{i,j}(\theta) = E\left[\frac{\partial \ln L}{\partial \theta_i} \cdot \frac{\partial \ln L}{\partial \theta_j}\right] \quad . \quad (\text{E.14})$$

Developing the cross parameter term  $\hat{I}_{\alpha,\beta}$

$$E\left[\frac{\partial \ln L}{\partial \alpha} \cdot \frac{\partial \ln L}{\partial \beta}\right] = nE[I_{\alpha}(Y)I_{\beta}(Y)] + \frac{n!}{(n-2)!} E[I_{\alpha}(Y)] \cdot E[I_{\beta}(Y)] \quad , \quad (\text{E.15})$$

where  $!$  denotes the factorial.

Assuming a large number of samples and using the maximum likelihood estimators (results of Equations E.6), the components of the Fisher information matrix as function of the estimator

terms will be:

$$\hat{I}_{\alpha,\alpha} = \sum_{k=1}^n \left( \frac{\phi'(a_k)}{\hat{\alpha}\hat{\beta}} \right)^2 \left[ -\frac{y_k}{F(a_k)} + \frac{1-y_k}{1-F(a_k)} \right]^2, \quad (\text{E.16})$$

$$\hat{I}_{\alpha,\beta} = \sum_{k=1}^n \frac{(\phi'(a_k))^2}{\hat{\alpha}\hat{\beta}^3} \ln \frac{a_k}{\hat{\alpha}\hat{a}} \left[ -\frac{y_k}{F(a_k)} + \frac{1-y_k}{1-F(a_k)} \right]^2, \quad (\text{E.17})$$

$$\hat{I}_{\beta,\beta} = \sum_{k=1}^n \left( \frac{\phi'(a_k)}{\hat{\beta}^2} \right)^2 \left( \ln \frac{a_k}{\hat{\alpha}\hat{a}} \right)^2 \left[ -\frac{y_k}{F(a_k)} + \frac{1-y_k}{1-F(a_k)} \right]^2. \quad (\text{E.18})$$

## Confidence interval - Cramer Rao Bounds

To this point of the development, the estimator parameters have been identified and the sampling has been evaluated. Now, given an estimation problem, the variance of the best possible estimator should be known. Cramer Rao provided a lower bound for the estimation error variance, which is:

$$\text{Var}[\hat{\theta}] \geq \frac{1}{I(\theta)}, \quad (\text{E.19})$$

where  $\hat{\theta}$  is the unbiased estimator of  $\theta$  and  $\text{Var}[\cdot]$  is the variance. In the case of multiple parameters, and if  $\Theta$  denotes the estimator of a function of  $\theta$ , the Cramer Rao bounds of the covariance matrix of  $\Theta$  is:

$$\text{Cov}[\Theta] \geq \frac{\partial \underline{\psi}(\underline{\theta})}{\partial \underline{\theta}} [I(\underline{\theta})]^{-1} \left( \frac{\partial \underline{\psi}(\underline{\theta})}{\partial \underline{\theta}} \right)^T. \quad (\text{E.20})$$

If  $\underline{\Theta}$  is an unbiased estimator of  $\theta$  (so  $\underline{\psi}(\underline{\theta}) = \underline{\theta}$ ), then the inverse of the Fisher information matrix gives the Cramer Rao bounds which means:

$$\text{Cov}[\underline{\Theta}] \geq [I(\underline{\theta})]^{-1} \quad (\text{E.21})$$

Finally, in the concept of this work, the fragility curves are associated with the probability of exceeding a damage state. Thus, the number of ground motions should be large enough to diversify the response and reach all damage levels.

# Appendix F

## Evaluation of a statistical test from the *p-value*

In statistics, the *p-value* (or probability value) is the result of the significance of a test. The objective of a statistical test is to determine if the probability that a given variable under test (VT) fits in the distribution that is predicted or defined from the null hypothesis  $H_0$ . When the VT distribution is known, the *p-value* would be the distribution function of the VT. In the opposite case, the identification of the *p-value* would be calculated from statistical software. In general, the *p-value* is defined as the probability of obtaining results at least as extreme as the observed results of a statistical hypothesis test, assuming that the null hypothesis  $H_0$  is correct.

Typically, a statistical test with a limited number of sampling requires i) a scientific question with its answer and ii) the desire to generalize the answer to a bigger sampling. Thus the decision regarding the acceptance or the rejection of the hypothesis  $H_0$  require a threshold (or risk) value:

- the risk  $\alpha$  that consists in rejecting  $H_0$  although it could have been true
- the risk  $\beta$  that consists in accepting  $H_0$  although it could have been false

Table F.1: The statistical risks after a test

		Reality	
		$H_0$ true	$H_0$ false
Decision	$H_0$ accepted	Good decision (1 - $\alpha$ )	Error $\beta$
	$H_0$ rejected	Error $\alpha$	Good decision (1 - $\beta$ )

The conclusion of a statistical test is the decision of Table F.1:  $H_0$  is either accepted or rejected. For the first case, the difference between the reality and the decision is not significant and the hypothesis form is correct for the chosen sampling. But with this choice, the risk of error is  $\beta$ . For the second case, the difference is significant and the hypothesis form is not

correct for the given sampling. But the error that this result is false would be  $\alpha$ . It should be mentioned that  $\alpha$  and  $\beta$  are independent. In addition, and so that the statistical test has a meaning, it was considered that the null hypothesis is usually a hypothesis of “no difference”.

Relatedly, the risk  $\alpha$  is equivalent to the *p-value*. It can another definition as to be the threshold value that decides if  $H_0$  can be accepted or rejected. The procedure will take the form of:

$$\begin{array}{lll} p \leq \alpha_{th} & H_0 \text{ is rejected} & p\text{-value is significant} \\ p > \alpha_{th} & H_0 \text{ is accepted} & p\text{-value is not significant} \end{array}$$

The threshold value of  $\alpha$  is fixed to 5%. It is chosen randomly and comes from the ratio of 1 shilling / 1 sterling of the English bookmakers. Based on the type of the test the  $\alpha_{th}$  can take a different value. For example, for the diagnosis of the lungs cancer, the researcher that would like to know if the machine is as good as a doctor who is doing the test, the threshold value of  $\alpha$  can be fixed to 10%. Nevertheless, the  $\alpha_{th}$  of a test should be set in advance and before realizing the test. For more details regarding the statistical tests, it is recommended to refer to the book of [Millot \(2011\)](#) where the aforementioned information were extracted.

# Appendix G

## Thesis summary in french

Pour la conception d'une structure, et dans le but de considérer sa capacité à résister aux tremblements de terre, le Pacific Earthquake Engineering Research Center a proposé une méthodologie probabiliste prenant en compte les caractéristiques sismiques du site, l'évolution du dommage de la structure et sa vulnérabilité. L'élément essentiel de cette méthodologie est l'évaluation fiable du potentiel de dommages sismiques. Cependant, cette méthodologie présente encore une faiblesse concernant l'analyse du cycle de vie d'une structure à cause de la quantification des dommages à partir des événements indépendants. Ainsi, cette thèse cherche à simuler numériquement le cycle de vie d'une structure. Pour cela, un modèle de remblai est utilisé (voir Figure G.1) ainsi qu'un modèle élasto-plastique multi-mécanisme afin de représenter le sol, développé dans l'Annexe A.

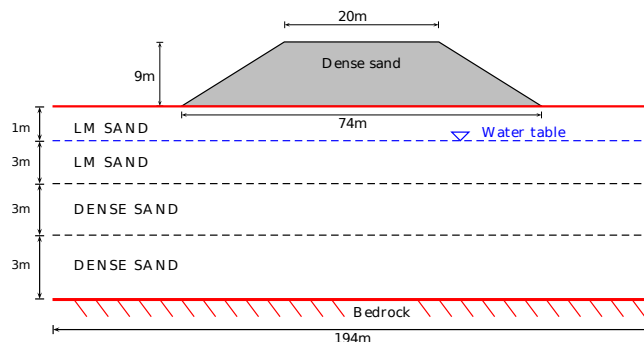


Figure G.1: Le modèle de remblai utilisé dans le cadre de cette thèse

Etant une étape indispensable en ingénierie, des essais en laboratoire *virtuel* ont été réalisés pour identifier le comportement du sol, localiser son état critique et déterminer sa résistance. Ces essais virtuels cherchaient à reproduire des essais effectués en laboratoire *réel* sur des échantillons de sol. Pour ce but, deux matériaux ont été pris en compte, qui ont été désignés dans cette thèse par *Mat.1* et *Mat.2*. Le comportement de ces deux matériaux a été étudié par des essais monotones et cycliques. L'importance de l'état initial des matériaux, ainsi que sa stabilité locale ont été identifiées par un paramètre numérique issu de la loi de comportement

utilisé (i.e.  $r_{apt}$ ).

De plus, la réponse dynamique d'une colonne de sol a été évaluée afin de comparer la précision entre les prédictions issues des tests de laboratoire et celles obtenues sur le terrain concernant la résistance des sols. Cette comparaison a eu lieu à l'aide des matrices de confusions dont une explication du concept est présenté dans l'Annexe C. Toutes ces idées faisait partie du Chapitre 1. Ce chapitre conclue que les essais de laboratoire sont capables parfois de sous-estimer la réponse réelles d'une structure, d'où l'importance des simulations numérique 2D.

Cette thèse traitant le comportement non linéaire du sol, une base de donnée sismique importante est nécessaire pour estimer précisément la défaillance potentielle du remblai. D'où le contenu du Chapitre 2 qui compare la réponse du remblai dans le cas de l'utilisation des signaux réels et synthétiques. Ces signaux ont été choisis comme chocs principaux uniquement afin de suivre la méthodologie de Performance Based Earthquake Engineering (PBEE). La rupture potentielle du remblai a été évaluée à partir d'indices de dommages globaux et locaux. Une approche spécifique considérant la structure et le site a été développée. Et finalement dans ce chapitre, pour être compatible avec le PBEE, des fonctions de fragilités ont été calculées pour savoir la probabilité de dépassé une limite de dommage.

En réalité, une structure n'étant pas soumise, au cours de sa vie, qu'à un seul mais plusieurs évènements sismiques dépendants, une analyse du cycle de vie du remblai a été menée afin d'estimer la distribution de la durée de vie du remblai et de calculer sa probabilité de survie suite aux évènements séquentiels de chocs principaux. Pour ce faire, des modèles synthétiques de mouvement du sol ont été utilisés (*Mod.R* et *Mod.B*), tenant compte des aléas sismiques du site considéré. Les effets des différents types de séquences sismiques et de modèles ont été évalués. Ces idées faisait partie du Chapitre 3. La conclusion de ce chapitre était que le dommage cumulés du remblai (aussi dis le dommage tout au long du cycle de vie) a montré deux comportements: soudain et progressive. De plus, le remblais utilisé a 50% chance qu'après 25 ans il montre des dommages modérés. Et finalement, ce chapitre a insisté sur l'importance de l'état initial du sol, de son histoire de chargement et ainsi sur le type de chargement utilisé.

Dans le Chapitre 4, afin de s'approcher de scénarios réalistes, les effets des répliques sont prises en compte dans l'analyse du cycle de vie. Le risque de dommage ainsi que la probabilité de survie ont été calculés. Aussi, l'évolution temporelle des fonctions de fragilité a également été évaluée. Ce chapitre conclue sur l'importance des répliques pour la réponse sismiques et surtout dans ce qui concerne la durée de vie utile de la structure en question, vue que ca peut augmenter la probabilité de survie.

Finalement, une hypothèse de cette thèse était que le remblai ne subissait aucune réparation et le sol aucune amélioration. Pour revenir sur cette hypothèse, une méthode d'amélioration

naturelle (MICP) a été appliquée au remblai. L'évolution de sa performance ainsi que le changement de comportement du sol ont été analysés dans le Chapitre 5, qui a montré que la méthodologie d'amélioration du sol utilisée est efficace sur la diminution du tassement de la crête du remblai. Le plus important, et à partir des fonctions de fragilité, la probabilité de faillance du remblai a diminué suite à cette méthode.

Cette thèse entre dans le cadre d'un projet national français appelé ISOLATE. Elle peut être vue comme une étude référence pour l'évaluation sismique de structures de type remblai soumises à des séismes et fournir un cadre de calcul performant accessible aux ingénieurs. Les différentes thématiques abordées dans cette thèse sont résumé dans la Figure G.2 qui fait aussi partie de l'Introduction générale.

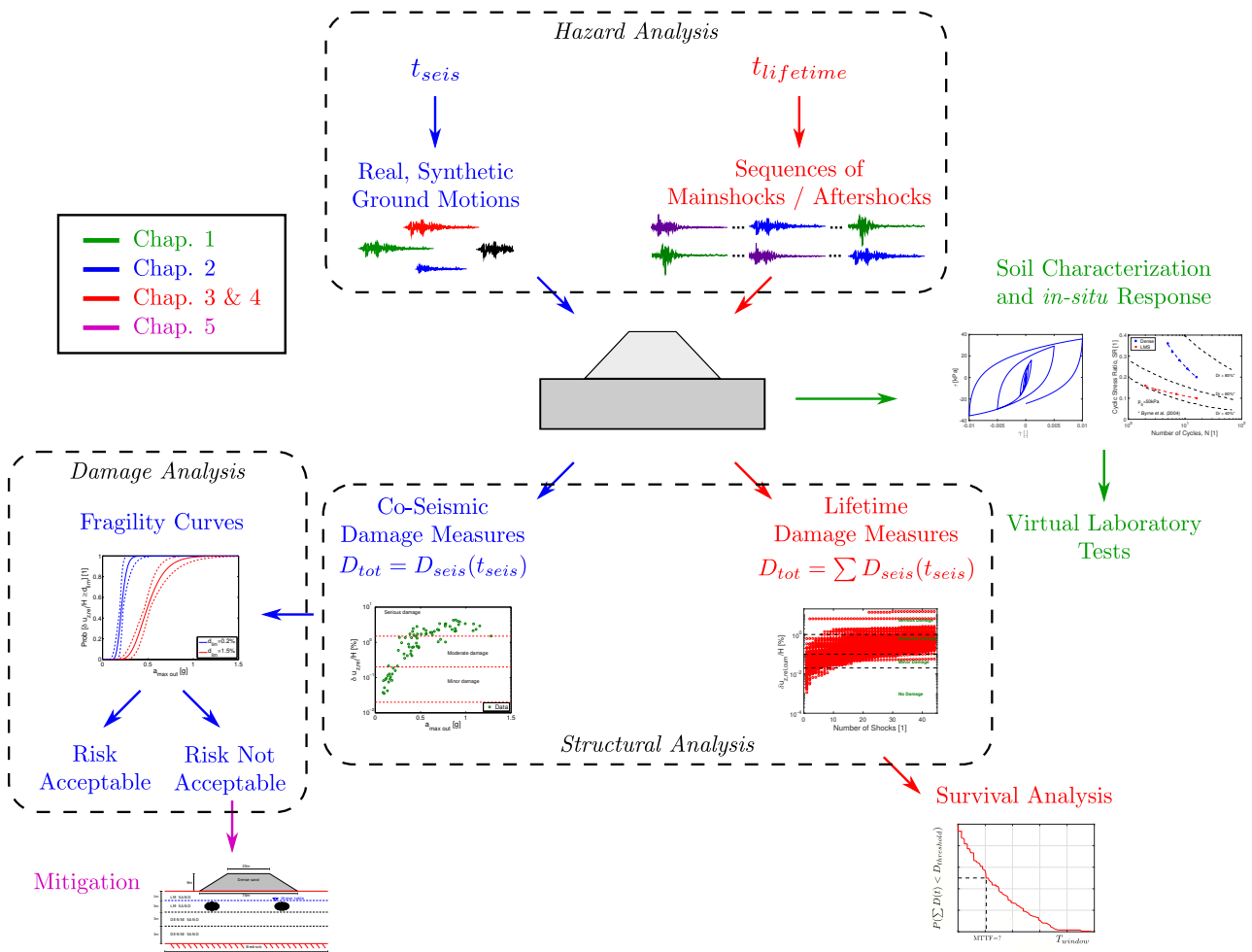


Figure G.2: Figure qui résume les différentes thématiques abordées dans cette thèse



# Bibliography

- Adalier, K. and Aydingun, O. (2003). Numerical analysis of seismically induced liquefaction in earth embankment foundations. part ii. application of remedial measures. *Canadian Geotechnical Journal*, 40(4):766–779.
- Akkar, S., Sandikkaya, M., and Bommer, J. J. (2014). Empirical ground-motion models for point-and extended-source crustal earthquake scenarios in europe and the middle east. *Bulletin of earthquake engineering*, 12(1):359–387.
- Argyroudis, S. and Kaynia, A. M. (2015). Analytical seismic fragility functions for highway and railway embankments and cuts. *Earthquake Engineering & Structural Dynamics*, 44(11):1863–1879.
- Aristizábal, C., Bard, P.-Y., Beauval, C., and Gómez, J. (2018). Integration of site effects into probabilistic seismic hazard assessment (PSHA): A comparison between two fully probabilistic methods on the euroseistest site. *Geosciences*, 8(8):285.
- Aubry, D., Chouvet, D., Modaressi, A., and Modaressi, H. (1986). Gefdyn: Logiciel d’analyse de comportement mécanique des sols par éléments finis avec prise en compte du couplage sol-eau-air. *Manuel scientifique, Ecole Centrale Paris, LMSS-Mat*.
- Aubry, D., Hujeux, J., Lassoudiere, F., and Meimon, Y. (1982). A double memory model with multiple mechanisms for cyclic soil behaviour. In *Proceedings of the Int. Symp. Num. Mod. Geomech*, pages 3–13.
- Baker, J. W. and Allin Cornell, C. (2005). A vector-valued ground motion intensity measure consisting of spectral acceleration and epsilon. *Earthquake Engineering & Structural Dynamics*, 34(10):1193–1217.
- Bazzurro, P. and Allin Cornell, C. (1999). Disaggregation of seismic hazard. *Bulletin of the Seismological Society of America*, 89(2):501–520.
- Been, K. and Jefferies, M. G. (1985). A state parameter for sands. *Géotechnique*, 35(2):99–112.
- Biarez, J. and Hicher, P. Y. (1994). *Elementary mechanics of soil behaviour: saturated remoulded soils*. AA Balkema, Rotterdam, Netherlands.

- Bommer, J. J. (2002). Deterministic vs. probabilistic seismic hazard assessment: an exaggerated and obstructive dichotomy. *Journal of Earthquake Engineering*, 6(spec01):43–73.
- Bonilla, L. F., Archuleta, R. J., and Lavallée, D. (2005). Hysteretic and dilatant behavior of cohesionless soils and their effects on nonlinear site response: Field data observations and modeling. *Bulletin of the Seismological Society of America*, 95(6):2373–2395.
- Boore, D. M. (1996). *SMSIM: Fortran programs for simulating ground motions from earthquakes: Version 1.0*. Citeseer.
- Boore, D. M. (2003). Simulation of ground motion using the stochastic method. *Pure and applied geophysics*, 160(3-4):635–676.
- Borozan, J., Costa, P. A., Romão, X., Quintero, J., and Da Fonseca, A. V. (2017). Numerical modelling of the dynamic response of liquefiable deposits in the presence of small scale buildings. In *Computational methods in structural dynamics and earthquake engineering (COMPdyn) conference, Crete Island, Greece, 15-17 June 2017*.
- Bradburn, M. J., Clark, T. G., Love, S., and Altman, D. (2003). Survival analysis part ii: multivariate data analysis—an introduction to concepts and methods. *British journal of cancer*, 89(3):431–436.
- Bradley, B. A., Araki, K., Ishii, T., and Saitoh, K. (2013). Effect of lattice-shaped ground improvement geometry on seismic response of liquefiable soil deposits via 3-d seismic effective stress analysis. *Soil Dynamics and Earthquake Engineering*, 48:35–47.
- Brennan, A. and Madabhushi, S. (2002). Effectiveness of vertical drains in mitigation of liquefaction. *Soil Dynamics and Earthquake Engineering*, 22(9):1059 – 1065.
- Byrne, P. M., Park, S.-S., Beaty, M., Sharp, M., Gonzalez, L., and Abdoun, T. (2004). Numerical modeling of liquefaction and comparison with centrifuge tests. *Canadian Geotechnical Journal*, 41(2):193–211.
- Campbell, K. W. and Bozorgnia, Y. (2008). NGA ground motion model for the geometric mean horizontal component of PGA, PGV, PGD and 5% damped linear elastic response spectra for periods ranging from 0.01 to 10 s. *Earthquake Spectra*, 24(1):139–171.
- Casagrande, A. (1936). Characteristics of cohesionless soils affecting the stability of slopes and earth fills. *J. Boston Society of Civil Engineers*, 23(1):13–32.
- Castiglia, M. and Santucci de Magistris, F. (2018). Prediction of the number of equivalent cycles for earthquake motion. *Bulletin of Earthquake Engineering*, 16(9):3571–3603.
- Castro, G., Enos, J. L., France, J. W., and Poulos, S. J. (1982). Liquefaction induced by cyclic loading. *NASA STI/Recon Technical Report N*, page 13308.

- Causse, M., Laurendeau, A., Perrault, M., Douglas, J., Bonilla, L. F., and Guéguen, P. (2014a). Eurocode 8-compatible synthetic time-series as input to dynamic analysis. *Bulletin of earthquake engineering*, 12(2):755–768.
- Causse, M., Laurendeau, A., Perrault, M., Douglas, J., Bonilla, L. F., and Guéguen, P. (2014b). Eurocode 8-compatible synthetic time-series as input to dynamic analysis. *Bulletin of Earthquake Engineering*, 12(2):755–768.
- Chandra, J., Guéguen, P., Steidl, J. H., and Bonilla, L. F. (2015). In situ assessment of the  $G$ - $\gamma$  curve for characterizing the nonlinear response of soil: Application to the garner valley downhole array and the wildlife liquefaction array. *Bulletin of the Seismological Society of America*, 105(2A):993–1010.
- Christodoulou, S. E. and Fragiadakis, M. (2014). Vulnerability assessment of water distribution networks considering performance data. *Journal of Infrastructure Systems*, 21(2):04014040.
- Clark, T., Bradburn, M., Love, S., and Altman, D. (2003). Survival analysis part i: basic concepts and first analyses. *British journal of cancer*, 89(2):232.
- Cosenza, E. and Manfredi, G. (2000). Damage indices and damage measures. *Progress in Structural Engineering and Materials*, 2(1):50–59.
- Cruz, N., Figueiredo, S., and Viana da Fonseca, A. (2004). Deriving geotechnical parameters of residual soils from granite by interpreting DMT+ CPTU tests. *Geotechnical and Geophysical Site Characterization (ed. by A. Viana da Fonseca, PW Mayne)*, 2:1799–1803.
- Cubrinovski, M. (2011). Seismic effective stress analysis: Modelling and application. In *5th International Conference on Earthquake Geotechnical Engineering*, pages 10–13. University of Canterbury. Civil and Natural Resources Engineering.
- Cui, M.-J., Zheng, J.-J., Zhang, R.-J., Lai, H.-J., and Zhang, J. (2017). Influence of cementation level on the strength behaviour of bio-cemented sand. *Acta Geotechnica*, 12(5):971–986.
- Da Fonseca, A. V., Ferreira, C., Ramos, C., and Molina-Gómez, F. (2019). The geotechnical test site in the greater lisbon area for liquefaction characterisation and sample quality control of cohesionless soils. *AIMS Geosciences*, 5(2):325–343.
- Da Fonseca, A. V., Silva, S. R., and Cruz, N. (2010). Geotechnical characterization by in situ and lab tests to the back-analysis of a supported excavation in Metro do Porto. *Geotechnical and Geological Engineering*, 28(3):251–264.
- Darve, F. and Laouafa, F. (2000). Instabilities in granular materials and application to landslides. *Mechanics of Cohesive-frictional Materials*, 5(8):627–652.

- Dashti, S., Bray, J. D., Pestana, J. M., Riemer, M., and Wilson, D. (2010). Mechanisms of seismically induced settlement of buildings with shallow foundations on liquefiable soil. *Journal of Geotechnical and Geoenvironmental Engineering*, 136(1):151–164.
- De Silva, F. (2020). Influence of soil-structure interaction on the site-specific seismic demand to masonry towers. *Soil Dynamics and Earthquake Engineering*, 131:106023.
- DeAlba, P., Chang, C. K., and Seed, H. B. (1975). Determination of soil liquefaction characteristics by large-scale laboratory tests. Report EERC-75-14, Earthquake Engineering Research Center, University of California, Berkeley, CA.
- DeJong, J. T., Burrall, M., Wilson, D. W., and Frost, J. D. (2017). A bio-inspired perspective for geotechnical engineering innovation. In *Geotechnical Frontiers 2017*, pages 862–870.
- DeJong, J. T. and Kavazanjian, E. (2019). *Bio-mediated and Bio-inspired Geotechnics*, pages 193–207. Springer International Publishing, Cham.
- DeJong, J. T., Mortensen, B. M., Martinez, B. C., and Nelson, D. C. (2010). Bio-mediated soil improvement. *Ecological Engineering*, 36(2):197–210.
- Di Sarno, L. and Pugliese, F. (2020). Seismic fragility of existing RC buildings with corroded bars under earthquake sequences. *Soil Dynamics and Earthquake Engineering*, 134:106169.
- Diamoutene, A., Barro, D., Somda, S. M. A., Nouredine, F., and Kamsu-Foguem, B. (2016). Survival analysis in living and engineering sciences. *JP Journal of Biostatistics*, 13(2):223–238.
- Dobry, R., Ladd, R. S., Yokel, F. Y., Chung, R. M., and Powell, D. (1982). Prediction of pore water pressure buildup and liquefaction of sands during earthquakes by the cyclic strain method. Building science series 138, National Bureau of Standards.
- Douglas, J., Gehl, P., Bonilla, L. F., Scotti, O., Régnier, J., Duval, A.-M., and Bertrand, E. (2009). Making the most of available site information for empirical ground-motion prediction. *Bulletin of the Seismological Society of America*, 99(3):1502–1520.
- Duncan, J. M. (1996). State of the art: limit equilibrium and finite-element analysis of slopes. *Journal of Geotechnical Engineering*, 122(7):577–596.
- Elgamal, A.-W., Parra, E., Yang, Z., and Adalier, K. (2002). Numerical analysis of embankment foundation liquefaction countermeasures. *Journal of Earthquake Engineering*, 6(4):447–471.
- Eurocode, E. (1994). 1: 1995 basis of design and actions on structures—part 1: Basis of design.
- Fasano, G., De Sarno, D., Bilotta, E., and Flora, A. (2019). Design of horizontal drains for the mitigation of liquefaction risk. *Soils and Foundations*, 59(5):1537–1551.

- Fauriel, S. and Laloui, L. (2012). A bio-chemo-hydro-mechanical model for microbially induced calcite precipitation in soils. *Computers and Geotechnics*, 46:104–120.
- Feng, K. and Montoya, B. M. (2016). Influence of confinement and cementation level on the behavior of microbial-induced calcite precipitated sands under monotonic drained loading. *Journal of Geotechnical and Geoenvironmental Engineering*, 142(1):04015057.
- Ferreira, C., Da Fonseca, A. V., Ramos, C., Saldanha, A. S., Amoroso, S., and Rodrigues, C. (2020). Comparative analysis of liquefaction susceptibility assessment methods based on the investigation on a pilot site in the greater lisbon area. *Bulletin of Earthquake Engineering*, 18(1):109–138.
- Fisher, R. A. et al. (1920). A mathematical examination of the methods of determining the accuracy of an observation by the mean error, and by the mean square error. (80):758–770.
- Friendly, M. (2002). Corrgrams: Exploratory displays for correlation matrices. *The American Statistician*, 56(4):316–324.
- Gai, X. and Sánchez, M. (2019). An elastoplastic mechanical constitutive model for microbially mediated cemented soils. *Acta Geotechnica*, 14(3):709–726.
- Ghosh, J., Padgett, J. E., and Sánchez-Silva, M. (2015). Seismic damage accumulation in highway bridges in earthquake-prone regions. *Earthquake Spectra*, 31(1):115–135.
- Goda, K. (2012). Nonlinear response potential of mainshock–aftershock sequences from japanese earthquakes. *Bulletin of the Seismological Society of America*, 102(5):2139–2156.
- Gomes, R. C., Santos, J. A., Modaressi-Farahmand-Razavi, A., and Lopez-Caballero, F. (2016). Validation of a strategy to predict secant shear modulus and damping of soils with an elastoplastic model. *KSCCE Journal of Civil Engineering*, 20(2):609–622.
- Gomez, M. G. and DeJong, J. T. (2017). *Engineering Properties of Bio-Cementation Improved Sandy Soils*, pages 23–33.
- Gomez-Martinez, F., Millen, M. D., Costa, P. A., Raomao, X., and Da Fonseca, A. V. (2018). Potential relevance of differential settlements in earthquake-induced liquefaction damage assessment. In *16th European Conference on Earthquake Engineering, Thessaloniki*.
- Gopal Madabhushi, S. P. (2007). Ground improvement methods for liquefaction remediation. *Proceedings of the Institution of Civil Engineers - Ground Improvement*, 11(4):195–206.
- Hamadi, K., Modaressi-Farahmand Razavi, A., and Darve, F. (2008a). Bifurcation and instability modelling by a multimechanism elasto-plastic model. *International Journal for Numerical and Analytical Methods in Geomechanics*, 32(5):461–492.

- Hamadi, K., Razavi, A. M.-F., and Darve, F. (2008b). Caractérisation numérique du phénomène de localisation des déformations dans des essais biaxiaux sur sable. *European Journal of Environmental and Civil Engineering*, 12(6):651–671.
- Hancock, J. and Bommer, J. J. (2005). The effective number of cycles of earthquake ground motion. *Earthquake Engineering & Structural Dynamics*, 34(6):637–664.
- Hatzigeorgiou, G. D. and Beskos, D. E. (2009). Inelastic displacement ratios for SDOF structures subjected to repeated earthquakes. *Engineering Structures*, 31(11):2744 – 2755.
- Hill, R. (1958). A general theory of uniqueness and stability in elastic-plastic solids. *Journal of the Mechanics and Physics of Solids*, 6(3):236 – 249.
- Hosmer Jr, D. W. and Lemeshow, S. (1999). Applied survival analysis: regression modelling of time to event data. *Eur Orthodontic Soc*, pages 561–2.
- Hosmer Jr, D. W., Lemeshow, S., and May, S. (2008). *Applied survival analysis: regression modeling of time-to-event data*, volume 618. Wiley-Interscience.
- Hu, S., Gardoni, P., and Xu, L. (2018). Stochastic procedure for the simulation of synthetic main shock-aftershock ground motion sequences. *Earthquake Engineering & Structural Dynamics*, 47(11):2275–2296.
- Huang, S. L. and Yamasaki, K. (1993). Slope failure analysis using local minimum factor-of-safety approach. *Journal of Geotechnical Engineering*, 119(12):1974–1989.
- Huang, Y., Yashima, A., Sawada, K., and Zhang, F. (2008). Numerical assessment of the seismic response of an earth embankment on liquefiable soils. *Bulletin of Engineering Geology and the Environment*, 67(1):31–39.
- Hujeux, J. (1985). Une loi de comportement pour le chargement cyclique des sols. *Génie parasismique*, pages 287–302.
- Iervolino, I., Chioccarelli, E., and Suzuki, A. (2020). Seismic damage accumulation in multiple mainshock-aftershock sequences. *Earthquake Engineering & Structural Dynamics*, 49(10):1007–1027.
- Iervolino, I., Giorgio, M., and Polidoro, B. (2015). Reliability of structures to earthquake clusters. *Bulletin of Earthquake Engineering*, 13(4):983–1002.
- Isbiliroglu, L. (2018). *Strategy for Selecting Input Ground Motion for Structural Seismic Demand Analysis*. Theses, Université Grenoble Alpes.
- Ishihara, K. (1993). Liquefaction and flow failure during earthquakes. *Géotechnique*, 43(3):351–451.

- Ishihara, K., Tatsuoka, F., and Yasuda, S. (1975). Undrained deformation and liquefaction of sand under cyclic stresses. *Soils and Foundations*, 15(1):29 – 44.
- Jungmeier, G., Hingsamer, M., Steiner, D., Kaltenecker, I., Kleinegris, D., van Ree, R., and de Jong, E. (2016). The approach of life cycle sustainability assessment of biorefineries. In *EUBCE 2016: 24th European Biomass Conference and Exhibition*.
- Kaplan, E. L. and Meier, P. (1958). Nonparametric estimation from incomplete observations. *Journal of the American Statistical Association*, 53(282):457–481.
- Karimi, Z., Dashti, S., Bullock, Z., Porter, K., and Liel, A. (2018). Key predictors of structure settlement on liquefiable ground: a numerical parametric study. *Soil Dynamics and Earthquake Engineering*, 113(1):286–308.
- Kartsonaki, C. (2016). Survival analysis. *Diagnostic Histopathology*, 22(7):263 – 270. Mini-Symposium: Medical Statistics.
- Kawase, H. (2011). Strong motion characteristics and their damage impact to structures during the off pacific coast of tohoku earthquake of march 11, 2011: How extraordinary was this M9.0 earthquake. In *4th IASPEI/IAEE International Symposium: Effects of Surface Geology on Seismic Motion*. University of California Santa Barbara.
- Khalil, C. and Lopez-Caballero, F. (2021). Survival analysis of a liquefiable embankment subjected to sequential earthquakes. *Soil Dynamics and Earthquake Engineering*, 140:106436.
- Khalil, C., Rapti, I., and Lopez-Caballero, F. (2017). Numerical evaluation of fragility curves for earthquake-liquefaction-induced settlements of an embankment. In *Geo-Risk 2017, Denver*, pages 21–30.
- Kokusho, T. (1980). Cyclic triaxial test of dynamic soil properties for wide strain range. *Soils and Foundations*, 20(2):45–60.
- Kourkoulis, R., Anastasopoulos, I., Gelagoti, F., and Gazetas, G. (2010). Interaction of foundation- structure systems with seismically precarious slopes: Numerical analysis with strain softening constitutive model. *Soil Dynamics and Earthquake Engineering*, 30(12):1430–1445.
- Koutsourelakis, S., Prevost, J. H., and Deodatis, G. (2002). Risk assessment of an interacting structure-soil system due to liquefaction. *Earthquake Engineering & Structural Dynamics*, 31(4):851–879.
- Kramer, S. L. (1996). *Geotechnical earthquake engineering*. Pearson Education.
- Kuhl, D. and Crisfield, M. A. (1999). Energy-conserving and decaying algorithms in non-linear structural dynamics. *International Journal for Numerical Methods in Engineering*, 45(5):569–599.

- Ladd, R. S. (1974). Specimen preparation and liquefaction of sands. *Journal of Geotechnical Engineering Division*, 100(10):1180–1184.
- Lade, P. (1994). Instability and liquefaction of granular materials. *Computers and Geotechnics*, 16(2):123 – 151.
- Lade, P. V. and Ibsen, L. B. (1997). A study of the phase transformation and the characteristic lines of sand behaviour. In *Proc. Int. Symp. on Deformation and Progressive Failure in Geomechanics, Nagoya*, pages 353–359.
- Lai, C., Bozzoni, F., Meisina, C., Poggi, V., Zuccolo, E., Bonì, R., Conca, D., Famà, A., and Cosentini, R. (2019a). Mapping the liquefaction hazard at different geographical scales. In *Proceedings of the VII ICEGE 7th international conference on earthquake geotechnical engineering, Rome, Italy*, pages 17–20.
- Lai, C., Conca, D., Bozzoni, F., Bonì, R., and Meisina, C. (2019b). Earthquake-induced soil liquefaction risk: macrozonation of the european territory taking into account exposure. In *Proceedings of the IABSE Symposium, Guimaraes, Portugal*.
- Lee, M., Gomez, M. G., Kortbawi, M. E., and Ziotopoulou, K. (2020). *Examining the Liquefaction Resistance of Lightly Cemented Sands Using Microbially Induced Calcite Precipitation (MICP)*, pages 53–64.
- Li, Q. and Ellingwood, B. R. (2007). Performance evaluation and damage assessment of steel frame buildings under main shock-aftershock earthquake sequences. *Earthquake Engineering & Structural Dynamics*, 36(3):405–427.
- Lilliefors, H. W. (1967). On the kolmogorov-smirnov test for normality with mean and variance unknown. *Journal of the American Statistical Association*, 62(318):399–402.
- Lin, H., Suleiman, M. T., Brown, D. G., and Kavazanjian, E. (2016). Mechanical behavior of sands treated by microbially induced carbonate precipitation. *Journal of Geotechnical and Geoenvironmental Engineering*, 142(2):04015066.
- Lopez-Caballero, F., Aristizábal, C., and Sánchez-Silva, M. (2020). A model to estimate the lifetime of structures located in seismically active regions. *Engineering Structures*, 215:110662.
- Lopez-Caballero, F. and Khalil, C. (2018). Vulnerability assessment for earthquake liquefaction-induced settlements of an embankment using gaussian processes. *ASCE-ASME Journal of Risk and Uncertainty in Engineering Systems, Part A: Civil Engineering*, 4(2):04018010.
- Lopez-Caballero, F., Modarelli, A., and Elmi, F. (2003). Identification of an elastoplastic model parameters using laboratory and in-situ tests. *Deformation Characteristics of Geomaterials ISLyon*, 3:1183–1190.

- Lopez-Caballero, F. and Modaressi-Farahmand-Razavi, A. (2010). Assessment of variability and uncertainties effects on the seismic response of a liquefiable soil profile. *Soil Dynamics and Earthquake Engineering*, 30(7):600–613.
- Lopez-Caballero, F. and Modaressi-Farahmand-Razavi, A. (2013). Numerical simulation of mitigation of liquefaction seismic risk by preloading and its effects on the performance of structures. *Soil Dynamics and Earthquake Engineering*, 49:27 – 38.
- Lopez-Caballero, F., Modaressi-Farahmand-Razavi, A., and Modaressi, H. (2007). Nonlinear numerical method for earthquake site response analysis I - elastoplastic cyclic model and parameter identification strategy. *Bulletin of Earthquake Engineering*, 5(3):303–323.
- Lopez-Caballero, F., Modaressi-Farahmand-Razavi, A., and Stamatopoulos, C. A. (2016). Numerical evaluation of earthquake settlements of road embankments and mitigation by preloading. *International Journal of Geomechanics*, 16(5):C4015006.
- López-Querol, S. and Blázquez, R. (2006). Identification of failure mechanisms of road embankments due to liquefaction : optimal corrective measures at seismic sites. *Canadian Geotechnical Journal*, 43(9):889–902.
- Lu, N., Sener-Kaya, B., Wayllace, A., and Godt, J. W. (2012). Analysis of rainfall-induced slope instability using a field of local factor of safety. *Water Resources Research*, 48(9).
- Luco, N. and Cornell, C. A. (2007). Structure-specific scalar intensity measures for near-source and ordinary earthquake ground motions. *Earthquake Spectra*, 23(2):357–392.
- Maharjan, M. and Takahashi, A. (2014). Liquefaction-induced deformation of earthen embankments on non-homogeneous soil deposits under sequential ground motions. *Soil Dynamics and Earthquake Engineering*, 66:113–124.
- Millot, G. (2011). *Comprendre et réaliser les tests statistiques à l'aide de R*.
- Mitrani, H. and Madabhushi, S. P. G. (2012). Rigid containment walls for liquefaction remediation. *Journal of Earthquake and Tsunami*, 6(04):1250017.
- Modaressi, H. and Benzenati, I. (1994). Paraxial approximation for poroelastic media. *Soil Dynamics and Earthquake Engineering*, 13(2):117 – 129.
- Montoya, B. M. and DeJong, J. T. (2015). Stress-strain behavior of sands cemented by microbially induced calcite precipitation. *Journal of Geotechnical and Geoenvironmental Engineering*, 141(6):04015019.
- Montoya-Noguera, S. and Lopez-Caballero, F. (2016). Numerical modeling of discrete spatial heterogeneity in seismic risk analysis: application to treated ground soil foundation. *Georisk: Assessment and Management of Risk for Engineered Systems and Geohazards*, 10(1):66–82.

- Montoya-Noguera, S., Zhao, T., Hu, Y., Wang, Y., and Phoon, K.-K. (2019). Simulation of non-stationary non-Gaussian random fields from sparse measurements using bayesian compressive sampling and karhunen-loève expansion. *Structural Safety*, 79:66 – 79.
- Nafday, A. M. (2010). Soil liquefaction modelling by survival analysis regression. *Georisk*, 4(2):77–92.
- Nakagawa, T. (2007). *Shock and damage models in reliability theory*. Springer Science & Business Media.
- National Academies of Sciences, E. and Medicine (2016). *State of the Art and Practice in the Assessment of Earthquake-Induced Soil Liquefaction and Its Consequences*. The National Academies Press, Washington, DC.
- Nieslony, A. (2009). Determination of fragments of multiaxial service loading strongly influencing the fatigue of machine components. *Mechanical Systems and Signal Processing*, 23(8):2712–2721.
- Oblak, A., Kosič, M., Viana Da Fonseca, A., and Logar, J. (2020). Fragility assessment of traffic embankments exposed to earthquake-induced liquefaction. *Applied Sciences*, 10(19):6832.
- O'Donnell, S. (2016). *Mitigation of earthquake-induced soil liquefaction via microbial denitrification: A two-stage process*. Thesis, Arizona State University.
- Pan, H. and Kusunoki, K. (2020). Aftershock damage prediction of reinforced-concrete buildings using capacity spectrum assessments. *Soil Dynamics and Earthquake Engineering*, 129:105952.
- Pan, K. and Yang, Z. X. (2018). Effects of initial static shear on cyclic resistance and pore pressure generation of saturated sand. *Acta Geotechnica*, 13(2):473–487.
- Panchireddi, B. and Ghosh, J. (2019). Cumulative vulnerability assessment of highway bridges considering corrosion deterioration and repeated earthquake events. *Bulletin of earthquake engineering*, 17(3):1603–1638.
- Papadopoulou, A. I. and Tika, T. M. (2016). The effect of fines plasticity on monotonic undrained shear strength and liquefaction resistance of sands. *Soil Dynamics and Earthquake Engineering*, 88:191 – 206.
- Pitilakis, K. (2004). Site effects. In *Recent advances in earthquake geotechnical engineering and microzonation*, pages 139–197. Springer.
- Pitilakis, K., Riga, E., and Anastasiadis, A. (2012). Design spectra and amplification factors for Eurocode 8. *Bulletin of Earthquake Engineering*, 10(5):1377–1400.

- Porter, K., Kennedy, R., and Bachman, R. (2007). Creating fragility functions for Performance-Based Earthquake Engineering. *Earthquake Spectra*, 23(2):471–489.
- Porter, K. A. (2003). An overview of PEER’s performance-based earthquake engineering methodology. In *9th international conference on applications of statistics and probability in civil engineering*. San Francisco.
- Pousse, G., Bonilla, L. F., Cotton, F., and Margerin, L. (2006). Nonstationary stochastic simulation of strong ground motion time histories including natural variability: Application to the K-net japanese database. *Bulletin of the Seismological Society of America*, 96(6):2103–2117.
- Prabhakaran, A., Kyungtae, K., Ebeido, A., Jahed Orang, M., Motamed, R., Elgamal, A., and Frazao, C. (2020). Polymer injection and associated site liquefaction remediation mechanisms. In *17WCEE: 17th World Conference on Earthquake Engineering, Sendai, Japan*.
- Ramirez, J., Barrero, A. R., Chen, L., Dashti, S., Ghofrani, A., Taiebat, M., and Arduino, P. (2018). Site response in a layered liquefiable deposit: evaluation of different numerical tools and methodologies with centrifuge experimental results. *Journal of Geotechnical and Geoenvironmental Engineering*, 144(10):04018073.
- Ramos, C., Ferreira, C., Molina-Gómez, F., and da Fonseca, A. V. (2019). Critical state lines of portuguese liquefiable sands. In *7th International Symposium on Deformation Characteristics of Geomaterials (IS-Glasgow 2019)*, volume 92, page 06003. EDP Sciences.
- Ranjesh, S. H., Hamadani, A. Z., and Mahmoodi, S. (2019). A new cumulative shock model with damage and inter-arrival time dependency. *Reliability Engineering & System Safety*, 192:106047.
- Rapti, I. (2016). *Numerical modeling of liquefaction-induced failure of geotechnical structures subjected to earthquakes*. Theses, Université Paris-Saclay - CentraleSupélec.
- Rapti, I., Lopez-Caballero, F., Modaressi-Farahmand-Razavi, A., Foucault, A., and Voldoire, F. (2018). Liquefaction analysis and damage evaluation of embankment-type structures. *Acta Geotechnica*, 13(5):1041–1059.
- Rathje, E. M. and Saygili, G. (2011). Estimating fully probabilistic seismic sliding displacements of slopes from a pseudoprobabilistic approach. *Journal of Geotechnical and Geoenvironmental Engineering*, 137(3):208–217.
- Reeves, D. M., Benson, D. A., and Meerschaert, M. M. (2008). Transport of conservative solutes in simulated fracture networks: 1. synthetic data generation. *Water resources research*, 44(5).
- Rezaeian, S. (2010). *Stochastic modeling and simulation of ground motions for performance-based earthquake engineering*. PhD thesis, UC Berkeley.

- Rezaeian, S. and Der Kiureghian, A. (2012). Simulation of orthogonal horizontal ground motion components for specified earthquake and site characteristics. *Earthquake Engineering & Structural Dynamics*, 41(2):335–353.
- Riascos-Ochoa, J., Sánchez-Silva, M., and Klutke, G.-A. (2016). Modeling and reliability analysis of systems subject to multiple sources of degradation based on lévy processes. *Probabilistic Engineering Mechanics*, 45:164–176.
- Rios, S., Millen, M., Quintero, J., and Da Fonseca, A. V. (2020). Physically-based object-oriented databases for geotechnical engineering. In Correia, A. G., Tinoco, J., Cortez, P., and Lamas, L., editors, *Information Technology in Geo-Engineering*, pages 256–267. Springer International Publishing.
- Roscoe, K. H., Schofield, A. N., and Wroth, C. P. (1958). On the yielding of soils. *Géotechnique*, 8(1):22–53.
- Ruiz-García, J. (2012). Mainshock-aftershock ground motion features and their influence in building’s seismic response. *Journal of Earthquake Engineering*, 16(5):719–737.
- Ruiz-García, J. (2014). Discussion on “effects of multiple earthquakes on inelastic structural response”. *Engineering Structures*, 58:110–111.
- Ruiz-Garcia, J. and Negrete-Manriquez, J. C. (2011). Evaluation of drift demands in existing steel frames under as-recorded far-field and near-fault mainshock-aftershock seismic sequences. *Engineering Structures*, 33(2):621 – 634.
- Rychlik, I. (1987). A new definition of the rainflow cycle counting method. *International Journal of Fatigue*, 9(2):119–121.
- Sabetta, F. and Pugliese, A. (1996). Estimation of response spectra and simulation of non-stationary earthquake ground motions. *Bulletin of the Seismological Society of America*, 86(2):337–352.
- Sadeghi, H., Kimoto, S., Oka, F., and Shahbodagh, B. (2014). Dynamic analysis of river embankments during earthquakes using a finite deformation FE analysis method. In *14th International Conference of the International Association for Computer Methods and Advances in Geomechanics*, number 2011, pages 637–642.
- Sáez, E., Lopez-Caballero, F., and Modaressi-Farahmand-Razavi, A. (2011). Effect of the inelastic dynamic soil-structure interaction on the seismic vulnerability assessment. *Structural Safety*, 33(1):51 – 63.
- Salami, M. R., Kashani, M. M., and Goda, K. (2019). Influence of advanced structural modeling technique, mainshock-aftershock sequences, and ground-motion types on seismic fragility of low-rise RC structures. *Soil Dynamics and Earthquake Engineering*, 117:263 – 279.

- Sanchez-Silva, M., Klutke, G.-A., and Rosowsky, D. V. (2011). Life-cycle performance of structures subject to multiple deterioration mechanisms. *Structural Safety*, 33(3):206 – 217.
- Sassa, S. and Yamazaki, H. (2016). Simplified liquefaction prediction and assessment method considering waveforms and durations of earthquakes. *Journal of Geotechnical and Geoenvironmental Engineering*, 143(2):04016091.
- Schober, P. and Vetter, T. R. (2018). Survival analysis and interpretation of time-to-event data: The tortoise and the hare. *Anesthesia and analgesia*, 127(3):792.
- Schofield, A. and Wroth, P. (1968). *Critical state soil mechanics*. McGraw-hill.
- Schwab, P. and Lestuzzi, P. (2007). Assessment of the seismic non-linear behavior of ductile wall structures due to synthetic earthquakes. *Bulletin of Earthquake Engineering*, 5(1):67–84.
- Seed, H. B. and Idriss, I. M. (1971). Simplified procedure for evaluating soil liquefaction potential. *Journal of Soil Mechanics & Foundations Div*, 97(9):1249–1273.
- Seed, H. B., Idriss, I. M., and Arango, I. (1983). Evaluation of liquefaction potential using field performance data. *Journal of Geotechnical Engineering - ASCE*, 109(3):458–482.
- Seed, H. B., Martin, P. P., and Lysmer, J. (1976). Pore-water pressure changes during soil liquefaction. *Journal of Geotechnical Engineering - ASCE*, 102(4):323–346.
- Semblat, J.-F., Reiffsteck, P., Foerster, E., Lopez-Cabellero, F., Canou, J., Esnault-Filet, A., and Voltaire, F. (2019). Caractériser et prévenir la liquéfaction des sols sous les ouvrages : le projet ISOLATE. In *10ème Colloque National de Génie Parasismique AFPS 2019*, Strasbourg, France.
- Sextos, A. G., Pitilakis, K. D., and Kappos, A. J. (2003). Inelastic dynamic analysis of rc bridges accounting for spatial variability of ground motion, site effects and soil-structure interaction phenomena. part 1: Methodology and analytical tools. *Earthquake Engineering & Structural Dynamics*, 32(4):607–627.
- Seyedi, D., Gehl, P., Douglas, J., Davenne, L., Mezher, N., and Ghavamian, S. (2010). Development of seismic fragility surfaces for reinforced concrete buildings by means of nonlinear time-history analysis. *Earthquake Engineering & Structural Dynamics*, 39(1):91–108.
- Sfahani, M. G., Guan, H., and Loo, Y.-C. (2015). Seismic reliability and risk assessment of structures based on fragility analysis – a review. *Advances in Structural Engineering*, 18(10):1653–1669.
- Shcherbakov, R., Turcotte, D. L., and Rundle, J. B. (2005). Aftershock statistics. *Pure and Applied Geophysics*, 162(6-7):1051–1076.

- Shinozuka, M., Feng, M. Q., Lee, J., and Naganuma, T. (2000). Statistical analysis of fragility curves. *Journal of Engineering Mechanics*, 126(12):1224–1231.
- Shokrabadi, M. and Burton, H. V. (2018). Risk-based assessment of aftershock and mainshock-aftershock seismic performance of reinforced concrete frames. *Structural Safety*, 73:64 – 74.
- Shome, N. (1999). *Probabilistic Seismic Demand Analysis of Nonlinear Structures*. Stanford University.
- Sica, S., Pagano, L., and Modaressi, A. (2008). Influence of past loading history on the seismic response of earth dams. *Computers and Geotechnics*, 35(1):61 – 85.
- Sladen, J. A., D'Hollander, R. D., and Krahn, J. (1985). The liquefaction of sands, a collapse surface approach. *Canadian Geotechnical Journal*, 22(4):564–578.
- Stamatopoulos, C. A., Lopez-Caballero, F., and Modaressi-Farahmand-Razavi, A. (2015). The effect of preloading on the liquefaction cyclic strength of mixtures of sand and silt. *Soil Dynamics and Earthquake Engineering*, 78:189–200.
- Stewart, J. P., Chiou, S.-J., Bray, J. D., Graves, R. W., Somerville, P. G., and Abrahamson, N. A. (2002). Ground motion evaluation procedures for performance-based design. *Soil Dynamics and Earthquake Engineering*, 22(9-12):765–772.
- Stumpff, C., Lawrence, J. R., Hendry, M. J., and Maloszewski, P. (2011). Transport and bacterial interactions of three bacterial strains in saturated column experiments. *Environmental Science & Technology*, 45(6):2116–2123.
- Swaigood, J. (2003). Embankment dam deformations caused by earthquakes. In *PCEE 2003: 7th Pacific Conference on Earthquake Engineering, University of Canterbury, Christchurch, New Zealand, Conference Handbook*, page Paper 014. New Zealand Society for Earthquake Engineering.
- Tatsuoka, F., Iwasaki, T., Tokida, K.-I., Yasuda, S., Hirose, M., Imai, T., and Kon-No, M. (1980). Standard penetration tests and soil liquefaction potential evaluation. *Soils and Foundations*, 20(4):95–111.
- Tiznado, J. C., Dashti, S., Ledezma, C., Wham, B. P., and Badanagki, M. (2020). Performance of embankments on liquefiable soils improved with dense granular columns: Observations from case histories and centrifuge experiments. *Journal of Geotechnical and Geoenvironmental Engineering*, 146(9):04020073.
- Trevlopoulos, K., Guéguen, P., Helmstetter, A., and Cotton, F. (2020). Earthquake risk in reinforced concrete buildings during aftershock sequences based on period elongation and operational earthquake forecasting. *Structural Safety*, 84:101922.

- Turcotte, D. L., Holliday, J. R., and Rundle, J. B. (2007). BASS, an alternative to ETAS. *Geophysical Research Letters*, 34(12):L12303.
- Ueng, T., Wu, M., Lin, C., and Yu, R. (2000). Pore water pressure changes in sands under earthquake loading. In *Proceedings of the 12th World Conference on Earthquake Engineering, Auckland, New Zealand*, volume 30.
- Vamvatsikos, D. and Cornell, C. A. (2002). Incremental dynamic analysis. *Earthquake Engineering & Structural Dynamics*, 31(3):491–514.
- Van Wijngaarden, W. K., Vermolen, F. J., van Meurs, G. A. M., and Vuik, C. (2011). Modelling biogrout: a new ground improvement method based on microbial-induced carbonate precipitation. *Transport in Porous Media*, 87(2):397–420.
- Wang, Z., Zentner, I., and Zio, E. (2020). Accounting for uncertainties of magnitude - and site-related parameters on neural network-computed ground-motion prediction equations. *Bulletin of the Seismological Society of America*, 110(2):629–646.
- Watson-Lamprey, J. and Abrahamson, N. (2006). Selection of ground motion time series and limits on scaling. *Soil Dynamics and Earthquake Engineering*, 26(5):477 – 482.
- Wen, W., Ji, D., and Zhai, C. (2020). Cumulative damage of structures under the mainshock-aftershock sequences in the near-fault region. *Journal of Earthquake Engineering*, pages 1–15.
- Wen, W., Zhai, C., Ji, D., Li, S., and Xie, L. (2017). Framework for the vulnerability assessment of structure under mainshock-aftershock sequences. *Soil Dynamics and Earthquake Engineering*, 101:41–52.
- Wu, G. (2014). Seismic design of dams. *Encyclopedia of Earthquake Engineering*, pages 1–18.
- Xenaki, V. and Athanasopoulos, G. (2003). Liquefaction resistance of sand-silt mixtures: an experimental investigation of the effect of fines. *Soil Dynamics and Earthquake Engineering*, 23(3):1–12.
- Xia, Z.-F., Ye, G.-L., Wang, J.-H., Ye, B., and Zhang, F. (2010). Fully coupled numerical analysis of repeated shake-consolidation process of earth embankment on liquefiable foundation. *Soil Dynamics and Earthquake Engineering*, 30(11):1309–1318.
- Xu, L.-Y., Cai, F., Wang, G.-X., Ugai, K., Wakai, A., Yang, Q.-Q., and Onoue, A. (2013). Numerical assessment of liquefaction mitigation effects on residential houses: Case histories of the 2007 Niigata Chuetsu-offshore earthquake. *Soil Dynamics and Earthquake Engineering*, 53:196–209.

- Yamamoto, Y. and Baker, J. W. (2013). Stochastic model for earthquake ground motion using wavelet packets. *Bulletin of the Seismological Society of America*, 103(6):3044–3056.
- Yasuda, S., Yoshida, N., Adachi, K., Kiku, H., and Ishkawa, K. (2017). Simplified evaluation method of liquefaction-induced residual displacement. *Journal of Japan Association for Earthquake Engineering*, 17(6):1–20.
- Yavuz Corapcioglu, M. and Haridas, A. (1984). Transport and fate of microorganisms in porous media: A theoretical investigation. *Journal of Hydrology*, 72(1):149–169.
- Yeo, G. L. and Cornell, C. A. (2009). Building life-cycle cost analysis due to mainshock and aftershock occurrences. *Structural Safety*, 31(5):396–408.
- Yoder, M. R., Van Aalsburg, J., Turcotte, D. L., Abaimov, S. G., and Rundle, J. B. (2013). Statistical variability and tokunaga branching of aftershock sequences utilizing bass model simulations. *Pure and Applied Geophysics*, 170(1):155–171.
- Youd, T. L. and Idriss, I. M. (2001). Liquefaction resistance of soils: summary report from the 1996 NCEER and 1998 NCEER/NSF workshops on evaluation of liquefaction resistance of soils. *Journal of Geotechnical and Geoenvironmental Engineering*, 127(4):297–313.
- Yu, T., Souli, H., Péchaud, Y., and Fleureau, J.-M. (2020). Optimizing protocols for microbial induced calcite precipitation (micp) for soil improvement-a review. *European Journal of Environmental and Civil Engineering*, pages 1–16.
- Zentner, I. (2017). A general framework for the estimation of analytical fragility functions based on multivariate probability distributions. *Structural Safety*, 64:54 – 61.
- Zentner, I. and Poirion, F. (2012). Enrichment of seismic ground motion databases using karhunen-loève expansion. *Earthquake Engineering & Structural Dynamics*, 41(14):1945–1957.
- Zeybek, A. and Madabhushi, S. P. G. (2019). Simplified procedure for prediction of earthquake-induced settlements in partially saturated soils. *Journal of Geotechnical and Geoenvironmental Engineering*, 145(11):04019100.
- Zhai, C.-H., Wen, W.-P., Chen, Z., Li, S., and Xie, L.-L. (2013). Damage spectra for the mainshock–aftershock sequence-type ground motions. *Soil Dynamics and Earthquake Engineering*, 45:1–12.
- Zhang, L., Goda, K., De Luca, F., and De Risi, R. (2020). Mainshock-aftershock state-dependent fragility curves: A case of wood-frame houses in british columbia, canada. *Earthquake Engineering & Structural Dynamics*, 49(9):884–903.

---

Zhao, T., Montoya-Noguera, S., Phoon, K.-K., and Wang, Y. (2018). Interpolating spatially varying soil property values from sparse data for facilitating characteristic value selection. *Canadian Geotechnical Journal*, 55(2):171–181.

Zienkiewicz, C. (1991). The finite element method; solid and fluid mechanics. *Dynamics and Non-Linearity*, 2:219.

**Title:** Seismic analysis of a liquefiable soil foundation-embankment system: Life Cycle performance and Mitigation

**Keywords:** life cycle, PBEE, mainshocks, aftershocks, potential failure

**Abstract:** The main goal of the performance-based design is the probabilistic evaluation of the system-level performance of structures due to earthquakes. A framing equation was proposed by the PEER Center based on the convolution of different design levels. However, this methodology presents a weakness in assessing a Life-Cycle analysis because the potential damage is calculated from independent major events. This thesis assesses numerically a life-cycle seismic analysis of an earth structure. An embankment is used, and the soil behavior is represented from an elasto-plastic multi-mechanism model with a FE code. First, real and synthetic earthquakes were used as inputs for dynamic analysis in order to identify the co-seismic response of the embankment. Then, a life-cycle analysis is conducted in order to estimate the lifetime damage of the embankment and calculate its probability of survival due to sequential events. The evolution in time of the fragility functions was also calculated. Finally, a natural biological mitigation method to ameliorate the soil was applied on the embankment to identify the evolution of its performance.

**Titre:** Analyse sismique d'un remblai et sa fondation liquéfiabale: Cycle de vie et Mitigation

**Mots clés:** cycle de vie, PBEE, chocs principaux, répliques, potentiel de dommages

**Résumé:** Pour la conception d'une structure, et dans le but de considérer sa capacité à résister à des tremblements de terre, le PEER a proposé une méthodologie probabiliste prenant en compte différents niveaux de conceptions. Cependant, cette méthodologie considère seulement des événements indépendants. Ainsi, cette thèse cherche à simuler numériquement le cycle de vie d'une structure. Pour cela, un modèle de remblai est utilisé ainsi qu'un modèle élasto-plastique multi-mécanisme pour le sol. Premièrement, des signaux d'entrées réels et synthétiques ont été utilisés pour identifier la réponse du remblai. De plus, une analyse du cycle de vie est menée afin d'estimer la distribution de la durée de vie du remblai et de calculer sa probabilité de survie en raison d'événements séquentiels. En outre, l'évolution temporelle des fonctions de fragilité a également été calculée. Finalement, une méthode d'amélioration naturelle du sol a été appliquée sur le remblai pour voir l'évolution de sa performance.